UMFORMTECHNIK
UTS
SIEGEN

Forschungsberichte des
Lehrstuhls für Umformtechnik
Univ.-Prof. Dr.-Ing. Bernd Engel (Hrsg.)

15

Peter Frohn-Sörensen

Process Development of Incremental Swivel Bending – ISB

universi
UNIVERSITÄTSVERLAG SIEGEN

Peter Frohn-Sörensen

Process Development of Incremental Swivel Bending – ISB

Forschungsberichte des Lehrstuhls für Umformtechnik
Univ.-Prof. Dr.-Ing. Bernd Engel (Hrsg.)
BAND 15

universi
UNIVERSITÄTSVERLAG SIEGEN

Bibliografische Information der Deutschen Nationalbibliothek
Die Deutsche Nationalbibliothek verzeichnet diese Publikation in der Deutschen Nationalbibliografie; detaillierte Daten sind im Internet abrufbar über: **http://dnb.dnb.de**

Impressum

Druck und Bindung:
UniPrint, Universität Siegen

Gedruckt auf alterungsbeständigem holz- und säurefreiem Papier

Siegen 2023: univers*i* – Universitätsverlag Siegen
www.universi.uni-siegen.de

ISBN 978-3-96182-145-7
ISSN 2191-0030

doi.org/10.25819/ubsi/10305

Process Development of Incremental Swivel Bending - ISB

Verfahrensentwicklung des inkrementellen Schwenkbiegens

DISSERTATION

zur Erlangung des akademischen Grades eines Doktors
der Ingenieurwissenschaften

vorgelegt von
Dipl.-Ing. Peter Frohn-Sörensen

eingereicht bei der Naturwissenschaftlich-Technischen Fakultät
der Universität Siegen
Siegen 2021

Betreuer und erster Gutachter	Univ.-Prof. Dr.-Ing. Bernd Engel Universität Siegen
Zweiter Gutachter	Prof. Dr.-Ing. Dipl.-Wirtsch.-Ing. Peter Groche Technische Universität Darmstadt
Tag der mündlichen Prüfung	08. Juni 2022

für Gesa und Alva,

für meine Familie

Vorwort

Die vorliegende Arbeit entstand im Rahmen meiner Tätigkeit als wissenschaftlicher Mitarbeiter am Lehrstuhl für Umformtechnik Siegen, dem UTS. Für die konstruktive Betreuung meiner Arbeit, die familiäre Lehrstuhlatmosphäre und die eingeräumten wissenschaftlichen Freiräume gilt meinem Doktorvater und Erstprüfer Prof. Bernd Engel besonderer Dank. Prof. Peter Groche danke ich für das großartige Feedback zu meiner Arbeit und die Übernahme des Zweitgutachtens dieser Dissertation. Bei der Prüfungskommission unter dem Vorsitz von Prof. Martin Manns und dem Beisitz von Prof. Axel v. Hehl bedanke ich mich sehr herzlich für die Unterstützung meiner Promotionsprüfung.

Während meiner Zeit am Lehrstuhl wurde ich von dem gesamten Team unterstützt und ich möchte mich für die großartige Zeit bedanken. In Bezug auf die vorliegende Arbeit möchte ich insbesondere die fachlichen Diskussionen mit Dr. Sebastian Groth, Christopher Heftrich, Jan Böcking und Jonas Reuter hervorheben. Für die Unterstützung bei der Erstellung des Manuskripts bedanke ich mich bei Dr. Linda Borchmann, Muhammad Ali Kaleem und Michael Schiller. Für die Unterstützung bei der Durchführung meiner Experimente bedanke ich mich herzlich bei Dr. Rainer Steinheimer und Henning Reichmann. Bei der Fertigung von Prüfständen, Materialproben und Umformwerkzeugen habe ich stets gute Unterstützung und Zuarbeit von unserer Fachbereichswerkstatt unter der Leitung von Friedhelm Stahl und später von Michael Schöttes samt ihrem Team bekommen. Für alle administrativen Belange und die Bereitstellung der nötigen Infrastruktur meines Arbeitsplatzes bedanke ich mich bei Hannelore Loos und Sabine Becker sowie bei unseren Systemadministratoren Reinhold Thor und Wolfgang Bürger. Auch bei allen Studierenden, die am Gelingen dieser Arbeit im Rahmen ihrer Abschlussarbeiten oder ihrer Tätigkeit am Lehrstuhl beigetragen haben, bedanke ich mich sehr herzlich, insbesondere bei Steffen Gabsa, Jan Eric Färber und Nils Tröps. Des Weiteren bedanke ich mich bei den auf gesonderter Seite aufgeführten Kollaboratoren anderer Institute, deren Unterstützung wiederum im Manuskript selbst hervorgehoben ist. Besondere namentliche Erwähnung gebührt den Kollegen vom Automotive Center Südwestfalen im Zuge des im letzten Kapitel beschriebenen Anwendungsfalls im Einzelnen Dr. Sebastian Kersten, Johannes Klinke, Manfred Riedel und Christoph Stötzel.

Schlussendlich bedanke ich mich bei meiner Frau Gesa, meiner Tochter Alva und meinen Eltern Andreas und Claudia für die zur Entstehung meiner Dissertation eingeräumte, stetige Geduld und Unterstützung sowie meine der Promotion vorangegangene schulische und berufliche Ausbildung. Ihr habt alle maßgeblich zum Gelingen dieser Arbeit beigetragen!

Siegen, im April 2023 Peter Frohn-Sörensen

Abstract

Flexible metal forming processes advance in association with the megatrend of mass customization. Kinematic processes provide high potential for product variations and production on demand, given by their degrees of freedom and a geometrically independent tooling. Incremental forming processes add up another variable by a freely adjustable density of incremental steps. Yet, both processes require an in-depth understanding to determine the process parameters in relation to the dimensional properties of the product. Incremental Swivel Bending (ISB) is a promising profile bending process which has been suggested in the past for a flexible production of structural parts from high-strength steels in the context of highly variable production demands with respect to derivatives as well as lot sizes. This thesis presents the development of a holistic analytical model to layout the kinematic process parameters of ISB, which is validated by numerical and practical bending increments. The results demonstrate the application of the process layout for incremental profile bending of variable arcs from a variety of high-strength materials. A solution for the characteristic optimization problem of incremental forming processes is developed for the key question if a target geometry should be manufactured in large but coarse steps or by rather small but numerous steps. In the light of a future-oriented highly variable production, the number of reconfigurations of the process parameters for flexible manufacturing technologies such as ISB will severely increase. The presented work provides a process model to layout these parameters for given product variants without the needs for empirical trial and error approaches. This allows to save time and preserve material resources in an industrial application of the ISB process.

Keywords: Profile Bending, Incremental Forming, Mass Customization, Analytic Modelling, Finite Elements Method

Resümee

Die Entwicklung flexibler Umformprozesse wird durch den Megatrend der personalisierten Massenproduktion und den damit verbundenen immer kleineren Stückzahlen einzelner Produktderivate bis hin zum Unikat angetrieben. Kinematische Verfahren bieten aufgrund ihrer Freiheitsgrade und den geometrisch unspezifischen Werkzeugen ein hohes Potenzial für Produktvarianten. Durch die frei wählbare Dichte von Umformschritten besitzen inkrementelle Umformverfahren darüber hinaus noch eine weitere Prozessvariable. Beide Arten von Verfahren – kinematische und inkrementelle – erfordern ein tiefes Prozessverständnis, um die Verfahrensparameter in Abhängigkeit der Produktgeometrie auszulegen. Das Inkrementelle Schwenkbiegen (ISB) ist ein vielversprechendes Profilbiegeverfahren, das für die flexible Fertigung von Strukturteilen aus hochfesten Stählen im Rahmen einer variantenintensiven Fertigung vorgesehen ist. In dieser Arbeit wird die Entwicklung eines ganzheitlich analytischen Modells zur Auslegung der kinematischen Prozessparameter vorgestellt und durch numerische und praktische Biegeversuche validiert. Den wesentlichen Kern der Verfahrensbeschreibung stellt dabei die plasto-mechanische Modellierung des reibschlüssigen Umformens dar. Die Ergebnisse zeigen die Anwendbarkeit der Prozessauslegung auf das inkrementelle Profilbiegen von variablen Bögen aus verschiedenen hochfesten Werkstoffen. Für das charakteristische Optimierungsproblem bei inkrementellen Umformprozessen der lokal entstehenden Dehnung wird ein Lösungsansatz abgeleitet, ob die Geometrie eines herzustellenden Produkts in großen, groben Schritten oder in kleinen, zahlreichen Hüben gefertigt werden sollte. Im Hinblick auf eine individualisierte, flexible Produktion wird die Anzahl notwendiger Neukonfigurationen der Prozessparameter zukunftsweisender Fertigungstechniken wie dem ISB stark zunehmen. Die vorliegende Arbeit stellt ein Prozessmodell zur Verfügung, mit dem die Parameter für jede Produktvariante ausgelegt werden können, ohne dass empirische Trial-and-Error Ansätze erforderlich sind. Dies ermöglicht hohe Zeit- und Materialersparnisse in der industriellen Anwendung des ISB-Verfahrens.

Schlagworte: Profilbiegen, Inkrementelle Umformung, Massenpersonalisierung, Analytische Prozessmodellierung, Finite Elemente Methode

Table of Contents

Nomenclature

Notation

SWIFT	Company, product and person names are written in capital letters
eq01	Equations are numbered consecutively and abbreviated eq.
(Jirkova and Kucerova 2016)	References to literature are given in parentheses by authors' family names and year of publication.

Latin Symbols (alphabetic)

Symbol	Unit	Denotation
A	square millimeter	Cross section area
A_0	square millimeter	Initial cross section area
A_1	square millimeter	Plastically deformed cross section area
A_{comp}	square millimeter	Cross section area, fraction underlying compressive stress distribution
A_c	square millimeter	Contact area
$A_{c,0}$	square millimeter	Initial contact area
$A_{c,1}$	square millimeter	Actual contact area (after plastic material deformation)
A_G	percent elongation	Uniform tensile elongation
A_{piston}	square millimeter	Surface area of a hydraulic piston
A_{ten}	square millimeter	Cross section area, fraction underlying tensile stress distribution
B		Bending factor
bi		Inner edge of a profile bottom
bo		Outer edge of a profile bottom
c		Inclination parameter for kinetic friction
c_0		Inclination factor for static friction
C_H	Megapascal	Stress parameter of HOLLOMON's hardening law
C_{S1}	Megapascal	Stress parameter of SWIFT's hardening law
C_{S2}		Strain parameter of SWIFT's hardening law
C_{S3}		Exponential parameter of SWIFT's hardening law
E	Megapascal	YOUNG's Modulus of elasticity
F_d	kilonewton	Longitudinal drawing force of friction experiments
f_f	Hz	fundamental resonant frequency

F_{fric}	kilonewton	Longitudinal reaction force of friction
fi		Inner flange of a hat-shaped profile
F_i	kilonewton	Contact force vectors
FLD_0		Limit strain parameter of KEELER's FLC model
F_{max}	kilonewton	Force maximum during tensile testing
F_N	kilonewton	Clamping force
$F_{N,min}$	kilonewton	Least clamping force to transmit the forming force or bending moment at uniform tensile elongation
$F_{N,max}$	kilonewton	Clamping force for reaching uniform tensile elongation at the processed material
$F_{N,norm}$		Clamping force, normalized by σ_N / R_e
$F_{N,yield}$	kilonewton	Clamping force for reaching material's yield stress at the processed material
fo		Outer flange of a hat-shaped profile
F_x	kilonewton	Longitudinal forming force
F_{ys}	kilonewton	Longitudinal force at yield sheath
g	millimeter	Tool gap between clamping units
G	Pascal	Shear modulus
h	millimeter	Profile height (within the bending plane)
h_0	millimeter	Initial profile height (within the bending plane)
$h_{0,comp}$	millimeter	Initial profile height underlying compressive elastic forming
$h_{0,ten}$	millimeter	Initial profile height underlying tensile elastic forming
h_1	millimeter	Actual profile height (after plastic material deformation)
$h_{1,comp}$	millimeter	Actual profile height underlying compressive plastic forming
$h_{1,ten}$	millimeter	Actual profile height underlying tensile plastic forming
$h_{y,comp}$	millimeter	Lateral location where yield criterion is prevalent within the tensile area of the bending stress distribution
$h_{y,ten}$	millimeter	Lateral location where yield criterion is prevalent within the compressive area of the bending stress distribution
k	Megapascal	Shear strength
k_{EBH}		Neutral axis shift factor
k_f	Megapascal	Flow stress or hardening stress

$k_{f,i}$	Megapascal	Flow stress or hardening stress at the incremental index i
i		Incremental index
l_0	millimeter	Initial length or length of a sheet metal strip
L_0	millimeter	Gauge length of uniaxial tensile tests
l_1	millimeter	Length after plastic deformation
l_c	millimeter	Clamping length
$l_{c,0}$	millimeter	Initial tool contact length between tool and strip material
$l_{c,1}$	millimeter	Actual tool contact length between tool and strip material
l_{draw}	millimeter	Travel during a strip drawing friction experiment
$l_{draw,1}$	millimeter	Travel during the first phase of a strip drawing experiment
$l_{draw,2}$	millimeter	Travel during the second phase of a strip drawing experiment
$l_{draw,3}$	millimeter	Travel during the third phase of a strip drawing experiment
l_{la}	millimeter	Lever arm corresponding to M_{fric}
m	Megapascal	Inclination parameter of bilinear work hardening model
M_i	Newton-millimeter	Plasto-mechanical or imaginary bending moment
m_{ff}		Empirical coefficient for the friction factor model
M_{fric}	Newton-millimeter	Friction moment
$M_{fric,max}$	Newton-millimeter	Maximum feasible friction moment a tool surface can transmit
m_{plate}	Kilogram	Mass of a sheet metal plate
M_{SB}	Newton-millimeter	Springback Moment
M_{ys}	Newton-millimeter	In-plane bending moment at yield sheath
M_z	Newton-millimeter	In-plane bending moment
$M_{z,comp}$	Newton-millimeter	In-plane bending moment, fraction underlying compressive stress distribution
$M_{z,comp,el}$	Newton-millimeter	Elastic in-plane bending moment, fraction underlying compressive stress distribution
$M_{z,comp,pl}$	Newton-millimeter	Plastic in-plane bending moment, fraction underlying compressive stress distribution
$M_{z,el}$	Newton-millimeter	Elastic in-plane bending moment
$M_{z,max}$	Newton-millimeter	In-plane bending moment when reaching uniform tensile elongation at the outer fiber(s) of a metallic strip
$M_{z,n}$	Newton-millimeter	In-plane bending moment standardized for $M_{z,max}$ at $o = 0$

$M_{z,ten}$	Newton-millimeter	In-plane bending moment, fraction underlying tensile stress distribution
$M_{z,ten,el}$	Newton-millimeter	Elastic in-plane bending moment, fraction underlying tensile stress distribution
$M_{z,ten,pl}$	Newton-millimeter	Plastic in-plane bending moment, fraction underlying tensile stress distribution
$M_{z,yield}$	Newton-millimeter	Minimum in-plane bending moment for reaching yield stress
n		Hardening exponent
n_{ISB}		Number of incremental bending sequences
n_s		Coefficient for the friction model of SHAW
o		Bending axis offset
p	Megapascal	Contact pressure
p_{clamp}	Megapascal	Pressure of the external hydraulic power unit during a strip drawing experiment
q_1		Substitution variable for square clearing
$Q2$		Substitution variable for square clearing
R	millimeter	Radius
R^2		Coefficient of determination
Ra	micrometer	Arithmetic surface roughness
$Ra_{0°}$	micrometer	Arithmetic surface roughness, longitudinal direction
$Ra_{90°}$	micrometer	Arithmetic surface roughness, lateral direction
R_c	millimeter	Corner or edge radius of a profile cross-section
R_{cl}	millimeter	Bending radius at a profile's centerline
R_e	Megapascal	Yield strength
R_{eH}	Megapascal	Highest local yield stress (LÜDERS strain)
R_i	Megapascal	Yield strength after i work hardening steps
R_{eL}	Megapascal	Lowest local yield stress (LÜDERS strain)
R_{ex}	millimeter	Bending radius at a profile's extrados
R_{in}	millimeter	Bending radius at a profile's intrados
R_m	Megapascal	Ultimate tensile strength
$R_{p0.2}$	Megapascal	0.2% offset yield strength
R_{th}	millimeter	Theoretical bending radius at neutral axis
s	millimeter	Sheet metal thickness

s_0	millimeter	Initial sheet metal thickness
s_1	millimeter	Actual sheet metal thickness
S_1		Substitution associated with frictional force transmission
S_2		Substitution associated with stiffness
$S_{3,c}$		Substitution for the cubic offset terms associated with compression
$S_{3,t}$		Substitution for the cubic offset terms associated with tension
SP		Number of superposed forming zones in the incremental sequence
$SP_{crit,l}$		Lower critical number of superposed forming zones
$SP_{crit,u}$		Upper critical number of superposed forming zones
t	Seconds	Time
T_1		Correction factor for resonant frequency
v_{rel}	Millimeter per Second	Relative velocity
W		Wall thickness factor
wi		Inner wall of a hat-shaped profile
wo		Outer wall of a hat-shaped profile
x		Longitudinal coordinate
y		Lateral coordinate
z		(Surface-) normal coordinate

Greek Symbols (alphabetic)

Symbol	Unit	Denotation
α	degree	Total or accumulated bending angle
γ	degree	Forming zone angle
γ_{ult}	degree	Maximum or threshold forming zone angle (given by the ratio between tool length $l_{c,0}$ and blank width h_0)
δ	degree	Incremental bending angle, as applied by the ISB tool
δ_M	degree	Maximum bending angle of an ISB tool
δ_{SB}	degree	Incremental springback angle
$\delta_{SB,i}$	degree	Incremental springback angle at the incremental index i
δ_u	degree	Unloaded incrementally bent angle
$\delta_{u,i}$	degree	Unloaded incrementally bent angle at the incremental index i

$\delta_{u,s}$	degree	Average incremental bending angles after release of force
Δf	millimeter	Incremental feeding distance
$\Delta f_{crit,l}$	millimeter	Lower critical incremental feeding distance
$\Delta f_{crit,u}$	millimeter	Upper critical incremental feeding distance
Δl	millimeter	Tool stroke [mm]
Δ_s	millimeter	Thinning
ε	percent elongation	Engineering strain
ε_{el}	percent elongation	Elastic strain
ε_{eq}	percent elongation	Equivalent strain
ε_f	percent elongation	Fracture strain
ε_x	percent elongation	Longitudinal strain
$\varepsilon_{x,\Delta,max}$	percent elongation	longitudinal strain maximum of the sandglass-type strain assumption
$\varepsilon_{x,comp}$	percent elongation	Compressive longitudinal strain at the intrados
$\varepsilon_{x,comp,ecc}$	percent elongation	Compressive longitudinal strain at the intrados with fully eccentric bending axis position (o = - 0.5)
$\varepsilon_{x,ten}$	percent elongation	Tensile longitudinal strain at the intrados
$\varepsilon_{x,ten,ecc}$	percent elongation	Tensile longitudinal strain at the intrados with fully eccentric bending axis position (o = 0.5)
$\varepsilon_{x,u}$	percent elongation	remaining longitudinal strain of the unloaded incremental bending angle
$\varepsilon_{x,R}$	percent elongation	Reversing longitudinal strain
ε_y	percent elongation	Lateral or transverse strain over width
ε_z	percent elongation	(Surface-) normal strain over thickness
φ		True strain
φ_1		Major true strain
$\varphi_{1,opt}$		Major true strain obtained from optical strain measurement
φ_1'		Major true strain rate
φ_2		Minor true strain
$\varphi_{2,opt}$		Minor true strain obtained from optical strain measurement
φ_{eq}		Equivalent true strain
φ_x		Longitudinal true strain
$\varphi_{x,ex}$		Longitudinal strain maximum at the extrados
$\varphi_{x,i}$		Maximum longitudinal strain at the incremental index i

$\varphi_{x,max}$		Longitudinal strain limit given by a failure criterion
$\varphi_{x,s}$		Accumulated maximum longitudinal strain of the incremental sequence
φ_y		Transversal true strain over width
φ_z		(Surface-) normal true strain true strain over thickness
κ	millimeter $^{-1}$	Curvature
κ_{ex}	millimeter $^{-1}$	Curvature at the extrados
κ_{in}	millimeter $^{-1}$	Curvature at the intrados
κ_{NF}	millimeter $^{-1}$	Curvature at the (strain-) neutral fiber
λ	millimeter	Angular gap between the stationary and rotatory clamping tools
μ		General or kinetic coefficient of friction
μ_{ini}		Initial kinetic friction coefficient of the linear regression model
μ_0		Static friction coefficient
$\mu_{0,ini}$		Initial static friction coefficient of the linear regression model
ν		(Elastic) POISSON ratio
ρ		Strain ratio
σ	Megapascal	(Engineering) stress
σ_{eq}	Megapascal	Equivalent stress
σ_N	Megapascal	Normal pressure
$\sigma_{N,0}$	Megapascal	Initial normal pressure
$\sigma_{N,1}$	Megapascal	Actual normal pressure after plastic material deformation
σ_x	Megapascal	Longitudinal stress
σ_{xy}	Megapascal	Shear stress in the x-y plane (c.f. τ_{fric})
σ_y	Megapascal	Lateral stress over width
σ_{yz}	Megapascal	Shear stress in the y-z plane
σ_z	Megapascal	(Surface-) normal stress over thickness
σ_{zx}	Megapascal	Shear stress in the z-x plane
τ_{fric}	Megapascal	Friction shear stress
$\tau_{fric,max}$	Megapascal	Maximum transferrable shear stress of the tribological system

Abbreviations

Abbreviation	Denotation

1D	One-dimensional
2D	Two-dimensional or planar
3D	Three-dimensional or spatial
3RPB	Three roll push bending
AG	"Aktiengesellschaft", public limited company, plc.
AHSS	Advanced high strength steel
acs	AUTOMOTIVE CENTER SÜDWESTFALEN GmbH
a.k.a.	Also known as
AlSi	Aluminum-silicon sheet metal surface coating system
ASTM	AMERICAN SOCIETY FOR TESTING AND MATERIALS
BAC	Bearing area curve, a.k.a. ABBOTT – FIRESTONE curve
BMWi	GERMAN FEDERAL MINISTRY FOR ECONOMIC AFFAIRS AND ENERGY
CAD	Computer aided design
CI	Interval of confidence
COMTES	Czech steel research center
CVD	Chemical vapor deposition
DA	Digital / analogue
DIC	Digital image correlation
DIN	"DEUTSCHES INSTITUT FÜR NORMUNG" German Institute for Standardization
DLC	Diamond-like coating
DoE	Design of experiments
DP	Dual Phase
DPB	Die-Push-Bending
EN	"Europäische Norm" European technical standard
ESB	EUROPEAN STEEL BUSINESS
et al.	and others
FE	Finite element
FEM	Finite elements method
FLC	Forming Limit Curve
FLD	Forming Limit Diagram in the φ_1 - φ_2 area
GmbH	"Gesellschaft mit beschränkter Haftung", limited liability company, ltd.
GTM	GASSMANN THEISS MESSTECHNIK
HRC	ROCKWELL hardness
IPF	Incremental Profile Forming

ISB	Incremental Swivel Bending
ISO	INTERNATIONAL ORGANIZATION FOR STANDARDIZATION
LEOBEN	Chair of Metal Forming at the Montanuniversity Leoben
N/A	Not available
OEM	Original equipment manufacturer
OSM	Optical strain measurement
Q-P	Quenching and Partitioning
PA-CVD	Plasma activated chemical vapor deposition
PVD	Physical vapor deposition
R&D	Research and development
RDB	Rotary draw bending
RDBM	Rotary draw bending machine
SPIF	Single point incremental forming
TENIFER	Surface treatment, where nitro-carburation is applied by a salt bath
TiN	Titanium nitride
TSS	Torque Superposed Spatial
UHSS	Ultra-high strength steel
UTG	CHAIR OF METALFORMING AND CASTING at the University Munich
UTS	Forming Technology at the University of Siegen
VDI	"VEREIN DEUTSCHER INGENIEURE", Association of German Engineers

Collaborator Contacts

Automotive Center Südwestfalen, **Mr. Christoph Stötzel**, Kölner Straße 125, 57439 Attendorn, Germany. TEL.: +49 (0)2722 9784 500, URL: www.acs-innovations.de

Chair for Metal Forming, **Professor Martin Stockinger**, Franz Josef Straße 18, 8700 Leoben, Austria. TEL.: +43 (0)3842 402 5601, URL: www.metalforming.at

Chair of Metalforming and Casting, **Professor Wolfram Volk**, Technical University of Munich, Walther-Meißner-Straße 4, 85748 Garching, Germany. TEL: +49 (0)89 2 89 13791, URL: https://www.mw.tum.de/utg/

Chair of Materials Science, **Professor Martin Franz-Xaver Wagner**, Technical University of Chemnitz, Erfenschlager Straße 73, 09125 Chemnitz, Germany, TEL: +49 (0)371 531-36153. URL: https://www.tu-chemnitz.de/mb/LWW/

Regional Technological Institute, **Dr.-Ing. Hana Jirková, Ph.D.**, University of West Bohemia: Univerzitní 8, 306 14 Pilsen, Czech Republic, TEL: +420 377 638 782. URL: https://rti.zcu.cz/

Outokumpu Nirosta GmbH, **Mr. Stefan Lindner**, Oberschlesienstraße 16, 47807 Krefeld, Germany. URL: https://www.outokumpu.com/en/locations/krefeld

1 Introduction

The flexibility in manufacturing is a crucial prerequisite for agile production and its prominence has been on the rise since 1990's (Andersen, Brunoe, and Nielsen 2015). Product individualization and mass customization are some of the key drivers associated with the fourth industrial revolution (Wang et al. 2017). In addition to the core aspects of production plants, machines and workplaces, the methodology of agile manufacturing also concerns product development, design software, process planning and production control (Gunasekaran 1998). The conventional production techniques provide high accuracy and reliability for mass production up to several million identical parts. Largely due to the shape oriented tooling, these processes lack flexibility for economically achievable lot sizes and feasible variations of product geometry or material (Yang et al. 2018). In the context of metal forming, kinematic forming methods are promising techniques to overcome the restrictions associated with geometry-specific tools. This is achieved by versatile tools and therefore these kinematic forming methods have universal applicability (Chatti 1998). Owing to inherent manufacturing flexibility, both in terms of feasible lot sizes and product variations, these kinematic forming processes have recently been in focus of research and industry. To layout the geometry manufactured by such a kinematic method, process models are required which link the processing and material parameters with the geometrical product parameters. For example, three roll bending is such a forming method in which the bending radius of a profile is determined by the movement and positioning of the bending roll and the longitudinal feed of the profile (Kersten 2013).

In contrast to continuous kinematic forming processes, incremental techniques feature generic tools that generally have a very small contact area and a forming zone which moves repeatedly over the workpiece to shape the geometry (Duflou et al. 2018). Although open-die forging might be the most prominent and oldest example of incremental forming and belongs to the group of bulk forming methods (Franzke, Recker, and Hirt 2008) yet, sheet metal forming methods with incremental kinematics have emerged more recently in the context of automated industrialization. Keeping in view the on-going research, single point incremental forming (SPIF) directly competes with deep drawing by providing strong advantages in terms of flexibility. SPIF facilitates shaping beyond conventional forming limits associated with sheet metal forming (Jeswiet et al. 2005). In addition, incremental sheet metal forming processes are also found amongst bending techniques. Out-of-plane bending is applied in industry in the bumping process on press brakes, where individual parts are formed for heavy industrial applications in a successive approach (Vorkov et al. 2018). In case of incremental in-plane bending, only few techniques are known till-to-date for example power shaping “Kraftformen”. Up till now, these processes had only been modeled using empirical approaches (Scherer 2014). Despite the high potential of manufacturing flexibility achievable by incremental in-

plane bending techniques, mechanical models that would allow an in-depth process understanding and layout are not available till-to-date.

In this thesis, a layout method for Incremental Swivel Bending (ISB) is presented. ISB is an incremental in-plane bending process, which features a generic tooling to process flat strips from sheet metals. It was patented by SCHWARZ and ENGEL (2009). Moreover, profiles with an open symmetric and asymmetric cross sections are also processible by ISB using a segmented bending mandrel. Prior to this thesis, ISB has been shown by empirical approaches as a flexible method to manufacture profile-based automotive structural components from high strength steels (Engel, Frohn, Hillebrecht, and André Knappe 2017). The present investigations advance beyond this level of technology by providing an analytical description of the ISB process in self-containing mechanical equations. Therefore, a methodological approach has been devised to layout the kinematic, incremental forming process into systematically divided consecutive steps. Each of the following steps is targeting for a specific process parameter of the ISB technique:

i) the clamping pressure applied by the forming machine,
ii) the size of the forming zone and local straining caused by bending increments,
iii) the positioning of the bending axis connected to a global straining model and
iv) the density of incremental steps and the resulting curvature.

The layout of the ISB process eventually leads to a question; Should the process sequence be arranged into few but large forming steps or rather be divided into large number of fine sequences? Both perspectives bring specific advantages and disadvantages while keeping in view technological and economic considerations. In the scope of the presented layout method, an optimum level is determined in terms of strain caused by the ISB parameterization.

The findings of this thesis allow to determine the processing parameters for a given target geometry belonging to a specific sheet metal material, in particular high-strength steels. Forming processes for such materials are especially in demand since they offer high potential in lightweight applications and manufacturing components of superior strength. However, high strength-steels are difficult to process in continuous forming methods due to their limited ductility. Incremental forming methods potentially go beyond this level by breaking down the total deformation into fractions (Allwood, Shouler, and Tekkaya 2007). Regarding the process parameters (i-iv) ante, ISB provides multiple degrees of freedom. However, these degrees of freedom need to be applied purposefully within the framework of a process layout for avoiding an empirical process operation. From an economical point of view, a flawless ISB process is most suitable for profitable manufacturing of variants, small batch size products and prototypes of components. Due to the indistinct tooling of the bending process, a

universal applicability is achieved. As a result, fixed costs associated with tooling for individual parts production are almost eliminated.

The present thesis systematically develops the process layout for ISB. It is divided into three main parts to achieve this goal. First, the very basic mechanical relations of forming under frictional engagement are derived for a tensile stretching process. Dry static friction coefficients are determined to allow a comparison between modelling and validation experiments. Secondly, in-plane bending is modelled correspondingly to determine the size of the angular forming zone which results from this process. This analytical foundation leads to the derivation of a process window for ISB, which is located in between the relation of applied clamping pressure and incremental bending angle. As the process bears considerable degrees of freedom, these need to be linked overarching the individual process models. A layout framework is thus presented in third part of the thesis, which takes the incremental processing sequence into account. At the end, the ISB process layout is applied to manufacture a longitudinal member of an electric car as an industrial use-case. Before the above-mentioned parts of this thesis begin, its main Objective is summarized and the process development methodology of LANGE (2002) is applied to the ISB process.

2 State of Research and Technology

2.1 Flexible metal forming processes

Modern market requirements raise the need for flexible manufacturing technologies, which can adapt themselves to changing product characteristics or production volumes under economically feasible conditions (Koren et al. 1999; Wang et al. 2017). The paradigm shift in production industry not only concerns individual manufacturing processes but it affects the whole facility's organization. This shift is generally addressed by the universal regime of reconfigurability (Andersen et al. 2015). In metal forming processes, flexibility means that the forming tools are independent from specific and fixed geometry of products (Cao et al. 2019). Moreover, YANG et al. (2018) define flexibility with respect to the following four dimensions:

1. economically feasible lot sizes,
2. achievable shape complexity,
3. degree of freedom provided by the forming process and
4. achievable physical process and product variations.

By the abovementioned systematic point of view, the general restrictions associated with conventional forming processes utilized in mass production become evident. Forming methods such as deep drawing provide an accurate, fast and reliable production of complex products. However, these advantages are achieved by highly specialized and expensive tools having fixed and non-changeable geometries. Any change of product geometry or even product material might lead to the requirement of a whole new forming tool. YANG et al. (2018) therefore encouraged the development of flexible metal forming methods to enhance individualized and on-demand manufacturing within scope of respective industry's production capabilities. CHATTI (1998) proposed kinematic forming methods for the production of a wide range of individualized products because a low geometric dependence exists between the forming tools and the shape of the part. This low dependence is a key criterion for achieving production flexibility.

With the overarching objective to achieve flexibility in metal forming, kinematic forming processes are focused in recent investigations, for example the publications of ENGEL, KERSTEN, and ANDERS (2011); GROTH, ENGEL, and LANGHAMMER (2018) on three roll push bending (3RPB). In addition, multiple approaches have been developed to break the restrictions of geometrical shape dependency between products and tools by subdividing the active die faces into multiple segments according to the forming zone. The paper of SELMI and SALAH (2012) is one out of many examples of the multipoint flexible forming process which breaks up a conventional stamping tool in a large number of individual pistons. HEFTRICH, STEINHEIMER, and ENGEL (2018) presented a methodology to make the rotary draw bending (RDB) process more flexible by geometrically reducing the tool surfaces.

Due to the absence of a substantial geometric relation between the tool and the finished product's geometry, kinematic forming methods require process models to layout the emerging geometry by means of provided degrees of freedom.

Incremental forming processes may possess similar characteristics like kinematic forming techniques due to the similarity in a large number of degrees of freedom and the utilization of indistinct tooling. With regard to manufacturing flexibility, they yet add up another degree of freedom due to the free arrangement of forming steps. The complicated layout of these degrees of freedom may be the reason that very few incremental forming processes are presently found in industrial environments despite their large potential for agile production (Ambrogio et al. 2005; Gatea, Ou, and McCartney 2016). Relatively sparsely addressed in research, there are yet some approaches, which consider to lay out the size, overlapping and sequence optimization of incremental processes. CARETTE, VANHOVE, and DUFLOU (2018) suggest applying a harmonic-based approach to optimize the forming paths in single point incremental forming (SPIF). In SPIF, a hollow open geometry is formed sequentially by a generic "point" tool with rounded tip being mounted on a robotic arm, c.f. (Duflou et al. 2018).

2.2 Kinematic profile bending processes with independent tooling

Two significant standards (DIN 8586 and VDI 3430) exist in literature and these standards are also relevant to categorize the bending technologies. According to DIN 8586, bending processes are divided into longitudinal and rotatory movement of tools. In addition, the technical standard VDI 3430 distinguishes in relation to the degree of shape relation between the utilized tools and the emerging product geometry. The latter correlates to kinematic forming processes and same is briefly explained in the preceding section.

Shape related bending processes hold the desired geometry in their contact surfaces in order to support the working piece as closely as possible. This approach in general delivers high reliability, reproducibility and shortens in-cycle time but the flexibility level of producing variants is significantly low. In this regard, rotary draw bending RDB establishes itself as one of the most common profile bending techniques and is well-established in production industries such as automotive (Flehmig, Blümel, and Kibben 2001; Hartl 2005; Hinkel 2013).

In contrast, kinematic profile bending processes, also known as free-form bending or free-bending, mainly define the product geometry by careful selection of the right combination of process parameters (Gantner et al. 2005; Gerlach 2010). The shape of a tool solely holds the function of supporting the cross section of the semi-finished product, for instance a sheet metal profile. If the bending geometry is defined by the position, motion and forces which are applied to the tools, a high level of flexibility results by means of physical product variations (Groth, Engel, and Frohn 2018; Kersten 2013). For this reason, process models are in demand because they correlate the kinematic

parameters to the resulting geometry and thus they avoid lengthy trials and errors and also enable the flexibility towards the economic production of small batch sizes. For example, GROTH (2020) presented an approach to determine the kinematic parameters of free-form bending. ANCELLOTTI et al. (2019) demonstrated the purposeful application of 3RPB and RDB for producing a complex and spatial bending product based on a rectangular tube.

For open profiles, Die-Push-Bending (DPB), a.k.a. Hexabend, has gained considerable attention in research and industry (Neugebauer et al. 2002). In this process, a profile is fully encompassed in a guiding die. A second die, denoted bending die, is allowed to rotate freely perpendicular to the orientation of the profile. The bending die is displaced laterally while the profile is pushed longitudinal to achieve a flexibly adjustable curvature. GROTH and ENGEL (2018) added a torsion unit to the DPB process which is capable of twisting the guiding die for bending spatially curved profiles or for compensating torsions.

At the Institute of Forming Technology and Lightweight Components in Dortmund, another combined bending process was presented by CHATTI et al. (2010). The torque superimposed spatial (TSS) bending device guides and feeds a profile similar to DPB and 3RPB, while a bending unit of rolls adds curvature by lateral displacement. In addition, the guiding unit, which consists of several rolls, can twist with reference to the longitudinal axis so as to produce spatially curved profile geometries. STAUPENDAHL and TEKKAYA (2017) provided a mathematical process model for this bending technique.

2.2.1 Incremental Bending Processes

Three major groups of incremental bending techniques are distinguished.

Bending during incremental bulk metal forming

Firstly, bending can be achieved by bulk metal forming processes. WOLFGARTEN and HIRT (2016) presented a technique in which a manipulator successively bends a bulk working piece during open die forging by taking advantage of a reduction of bending moment by orthogonal compressive stress superposition. On a smaller process scale and in cold forming conditions, JIN, KUBOKI, and MURATA (2005) investigated an incremental in-plane bending process, which is intended for the production of micro machine components such as springs. A laterally inclined punch repeatedly strokes a strip metal with interchanging feeding increments to achieve plane curved parts by bulk deformation.

Incremental sheet metal bending techniques

The second group of incremental techniques comprises of sheet metal bending. A press brake is operated repeatedly to bend a blank from sheet metal to achieve large radii, for example for the individual production of pipeline components. This process, also known as bumping, was modelled by VORKOV et al. (2015) in an numerical approach to simulate the consecutive bending procedure. In

addition, an analytical model for a single bend was developed and subjected to a grey box approach (Vorkov et al. 2018; Vorkov, Afonso Da Costa Rodrigues, and Duflou 2019). A similar incremental out of plane bending process is conducted on swivel bending machines. In order to achieve large radii at cylindrical or conical hulls, the machine is operated in a sequence of multiple bends and strokes. FROHN-SÖRENSEN, HOCHSTRATE, et al. (2020) provided an analytical model to describe the emerging geometry by calculating the loaded bending radius according to the position of the bending tools. Subsequently, the unloaded springback radius is determined and the circular approximation of the incremental sequence is determined trigonometrically under consideration of the repeating incremental feeding stroke.

The process denoted “Kraftformer”, which may be translated as power- or force-forming, is capable for force fitted incremental in-plane bending. The method dates back to the patent of ECKOLD (1958). Due to existing need for small batches and individual parts, Kraftformen is preferably applied in the industrial branches of aviation, boat and yacht building, railway carriage construction and classic car restoration. Presently, the ECKOLD GmbH & Co. KG provides manual as well as automated applications of the process, see Figure 1.

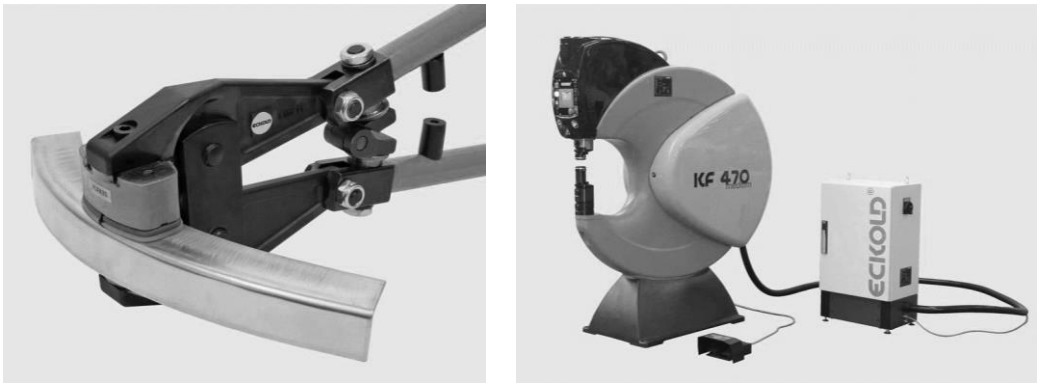

a) b)

Figure 1: ECKOLD "Kraftformer" incremental forming method in a) manual and b) automated application. Source: ECKOLD GmbH & Co. KG.

ECKOLD’s Kraftformer is capable of performing a variety of in-plane forming processes, i.e., compression, stretching, bending and out-of-plane bulging for larger cylindrical, conical or spherical surfaces. For all these operations, a pair of clamping elements are loaded perpendicularly to the blank plane for force-fitted forming. In detail, the active die faces of the clamping tools for compression or stretching are pressed against the blank plane. With the help of integrated inclined levers which are in accordance with the forming direction, the clamping force is redirected towards the blank surface resulting in compressive or tensile stresses. SCHERER (2014) provided two layout approaches for forming a specific geometry with the power forming process. Firstly, a numerical model is developed, which predicts the product shape resulting from the process parameters. The iterative approximations

lead towards the target geometry however the process was quite time consuming considering the available computer technology at the time of SCHERER's thesis. Therefore, he established a second approach, where experiments on individual forming steps are mathematically approximated by regression in between forming parameters and resulting corresponding geometrical product properties. He obtains a good correlation for stretching whereas the compressive operation could not be approximated by this approach due to the considerable influence of buckling effects. For bending, SCHERER introduces a novel parameter, the incremental density of multiple forming steps. Under consideration of this incremental density, he was able to provide a regression between the processing parameters of the incremental bending method of power forming. Even if unknown, some marginal manufacturing influences remain an open issue.

Incremental profile bending techniques

The last group of incremental bending methods includes those applied to bending profiles. According to BECKER, TEKKAYA, and KLEINER (2014), the Incremental Profile Forming (IPF) process comprises kinematic roll bending of tube profiles and a perpendicular spinning unit for incremental elastic or plastic compression of the cross section adjustments. By this method, two major advantages are obtained; Firstly, the bending moment is significantly reduced by the superposition of compressive stress, which also contributes to fewer springback and therefore an improved manufacturing accuracy, as proven by NAZARI et al. (2018). Secondly, if plastic cross sectional deformation is adjusted by the incremental spinning unit, mechanically tailored tubes are obtained with respect to variable diameters and thicknesses.

The methodology of this thesis encompasses development of an Incremental Swivel Bending process which belongs to the last group of incremental bending techniques and is explained in detail in the following section.

2.2.2 Incremental Swivel Bending

SCHWARZ and ENGEL (2009) introduced Incremental Swivel Bending (ISB) as a flexible bending technology to achieve a highly variable production of derivatives with the aim of process application in automotive industry. In this invention, the process contained two clamping units in which one is a stationary unit (7,8) and the other one is a rotatory unit (10) for bending of curved sections (4), see Figure 2.

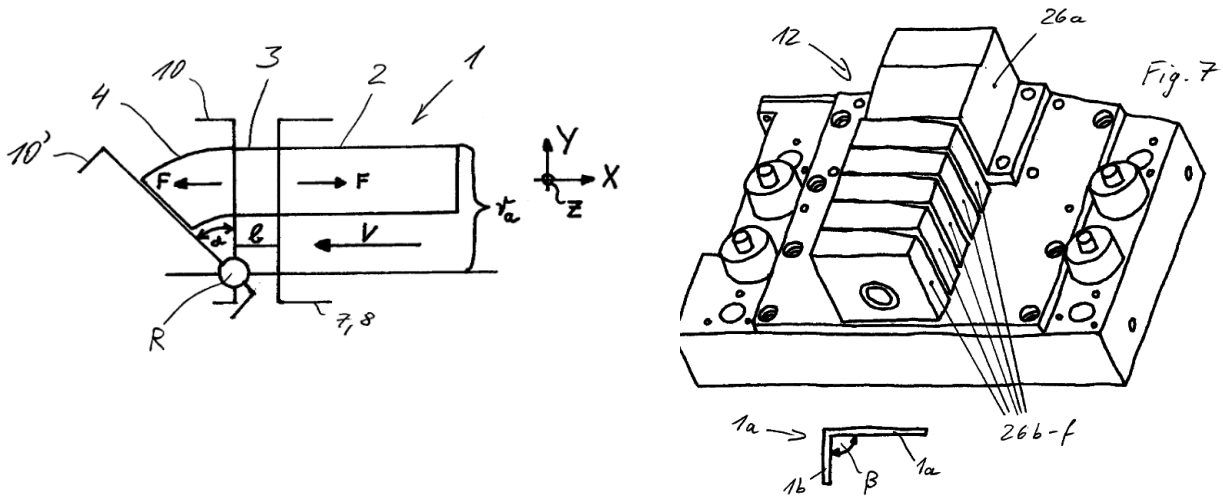

a) b)

Figure 2: Concept sketches of the ISB process according to SCHWARZ and ENGEL (2009) showing a) the functional principle of the profile bending method and b) a first draft idea of a segmented mandrel in the rotatory clamping unit.

In order to ensure the intended high degree of manufacturing flexibility, the forming operation is conducted by an indistinct tool working under the principle of frictional engagement. The bending axis (R) of the ISB tool is shiftable in lateral direction. Thereby, the ratio of compressive and tensile shares of the bending strain distribution is influenced. For profile bending, the ISB process features a segmented mandrel (26a-f). As an incremental forming process, the ISB technique operates in repeating sequences, which are divided into four basic steps as represented in Figure 3. Initially, a press commonly loads the clamping units, which are enclosed in a stamping tool frame by the clamping force $\boldsymbol{F}_{\mathrm{N}}$ (1). These units might hold a segmented mandrel for profile bending. Under the influence of the clamping load, the rotatory clamping unit pivots around the bending axis by the incremental bending angle $\boldsymbol{\delta}$, to form an incremental step under frictional engagement (2). During this step, the lateral position of the bending axis relates to the offset factor $\boldsymbol{o}$ and determines the resulting strain distribution, as indicated in Figure 3 b). Subsequently, the clamping force is released and the ISB tool is opened. The rotatory clamping unit pivots in its initial position (3) to reset the bending tools. In the last step, the profile is positioned longitudinally by the incremental feeding distance $\boldsymbol{\Delta f}$ (4). This fundamental procedure is repeated by the number of sequences $\boldsymbol{n}_{\mathrm{ISB}}$ until the process reaches the desired cumulated bending angle α of the arc.

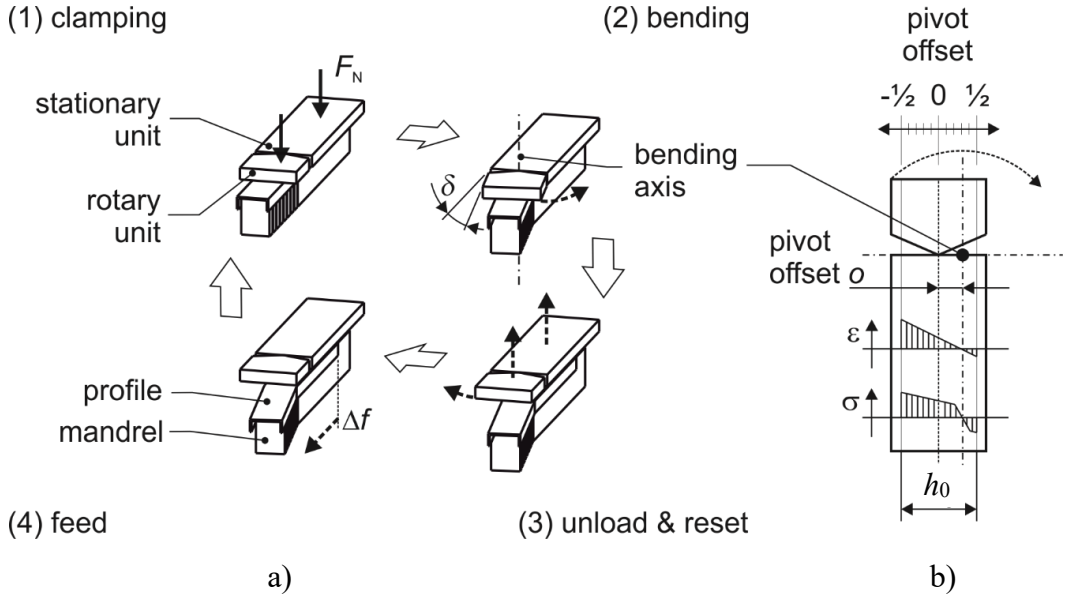

Figure 3: Schematic representation of ISB showing a) the process sequence divided into four consecutive steps with relevant incremental process parameters and b) the influence of the laterally shiftable bending axis on the tensile/compressive strain ε and stress σ distributions of the bending procedure.

In ISB, the lateral position of the bending axis can be shifted to influence the bending strain distribution. The dimensionless factor o relates the position of the bending axis to the profile height h_0. At $o = -½$, the bending axis lies at the extrados, which results in a purely compressive bending operation. Vice versa, $o = +½$ represents the axis' position at the intrados, thus causing purely tension within bending. At a axis position when o is adjusted to zero, a balanced strain distribution is achieved which is similar to a regular bending operation.

In its most elementary form, ISB allows to bend in-plane metallic sheets. Moreover, profiles featuring open symmetric and asymmetric cross sections are processible by ISB. The profile surfaces oriented parallel to the bending plane are firmly clamped and formed by the process. All other surfaces of the profile (e.g., surfaces oriented perpendicular to the bending plane) experience free deformation without clamping. At the extrados, the outer profile areas are significantly stretched in longitudinal direction. To avoid cross-sectional deformations, which typically occur during profile bending as described by PAULSEN and WELO (2001), a segmented mandrel helps to support the unclamped areas of the profile.

Even before release of the first idea of SCHWARZ and ENGEL (2009), an initial prototype ISB tool was designed and manufactured as it may be seen in the work of DUBRATZ (2006). Enclosed in a tool frame guided by six pistons, this tool prototype is operated on a try-out press, see Figure 4. The tool features a lateral hydraulic piston mounted on its side to induce the bending force, which is transferred

to the rotatory clamping unit by a lever. The rotatory clamping unit itself is assembled in yet another guided frame, with an additional degree of freedom to pivot about the bending axis (Figure 4c).

a) b) c)

Figure 4: Early stage of the ISB research tool prototype showing a) the upper and lower stationary clamping unit, b) the guiding part of the mandrel in the stationary unit and c) the rotatory clamping unit, pivoted by the maximum tool angle.

Subsequently to DUBRATZ (2006), MATHES (2007) investigated how to operate the ISB tool for bending L and U shaped profiles with small profile walls made from mild drawing steels. Concluding his experiments on the ISB tool for profile bending, MATHES provided a number of tool optimizations. In particular, he provided an improved mandrel design and the first finite element model of an ISB process capable of calculating a singular bending increment. His future prospects for the ISB technology were to set the segmented mandrel into operation and to ensure a central application of the clamping force.

2.3 Modelling of bending processes

According to the technical standard VDI3430, a profile arch is defined by two dimensionless geometrical factors:

1) The bending factor B refers to the geometry of the centerline and is defined as

$$B = \frac{R_{th}}{h_0} \qquad \text{(eq. 1)}$$

Here, R_{th}, the theoretical bending radius at the strain-neutral fiber according to FRANZ (1988) is – in standard situations[1] – located closely to the centerline radius R_{cl} and the profile height h_0.

[1] No longitudinal strain superposition such as e.g., applied by SELTER (2017) and no lateral shifting of the neutral fiber toward intrados due to very tight bending radii, e.g., described by ENGEL and HASSAN (2015).

2) The wall thickness factor *W* refers to the geometry of the profile and follows

$$W = \frac{h_0}{s_0} \qquad \text{(eq. 2)}$$

Here s_0 is the initial sheet metal thickness.

Above mentioned both factors comprehensively describe the challenge of a bending task, here *B* indicates the tightness and *W* indicates wall thinness of given relations and hence vulnerability to wrinkling. In bending, the typical strain distribution was identified by KHODAYARI (1993) as linear distribution over profile height h_0 with a transition through zero at the neutral fiber. Tensile straining occurs at the extrados while compression is caused at the intrados. Under the involvement of the lateral coordinate *y*, as used e.g., by ENGEL and HASSAN (2015; GERLACH (2010), the distribution of strain ε follows the function

$$\varepsilon(y) = \frac{\mathrm{y}}{R_{th}}. \qquad \text{(eq. 3)}$$

Accordingly, the stress distribution follows the elastic-plastic stress-strain relation over profile height. Following ENGEL, GERLACH, and CORDES (2008), the mechanical calculation of bending moment follows the ideal consideration of elastic and plastic deformation of the profile and is also called imaginary bending moment. It is calculated by integrating bending typical stress distribution over the area of cross section *A*. For the mechanical bending moment M_i, the relation

$$M_i = \int_A \sigma(y) \cdot y \cdot dA \qquad \text{(eq. 4)}$$

is obtained.

2.4 Steels, mechanical characterization and material modelling

The mechanical deformation behavior of materials needs to be parameterized in a uniform way for the implementation in forming process models such as numerical or analytical methods. For this purpose, testing procedures and necessary material specimens are standardized. During continuous, quasi-static and global elastic plastic deformation, the behavior is described by mechanical material properties which are obtained from uniaxial tensile testing.

2.4.1 Uniaxial tensile test

The uniaxial tensile test is standardized according to DIN EN ISO 6892. It requires dumbbell-shaped specimen geometries with defined clamping areas at both ends, where longitudinal tensile force is applied by the testing assembly, and a tapered, parallel gauge length L_0 is kept in between the clamping areas. Commonly, proportional specimen geometries are used, where L_0 and the initial cross section A_0 stand in a given proportional ratio of $L_0 = 5.65 \cdot \sqrt{A_0}$. Any factor divergent from this value must be indexed at the tested values, in particular fracture strain ε_f.

From the sensor signals of the uniaxial tensile test procedure, force over elongation curves are obtained. Under consideration of the initial specimen geometry, engineering stress over strain curves are calculated. From these curves, mechanical material parameters are determined at distinct locations, Figure 5.

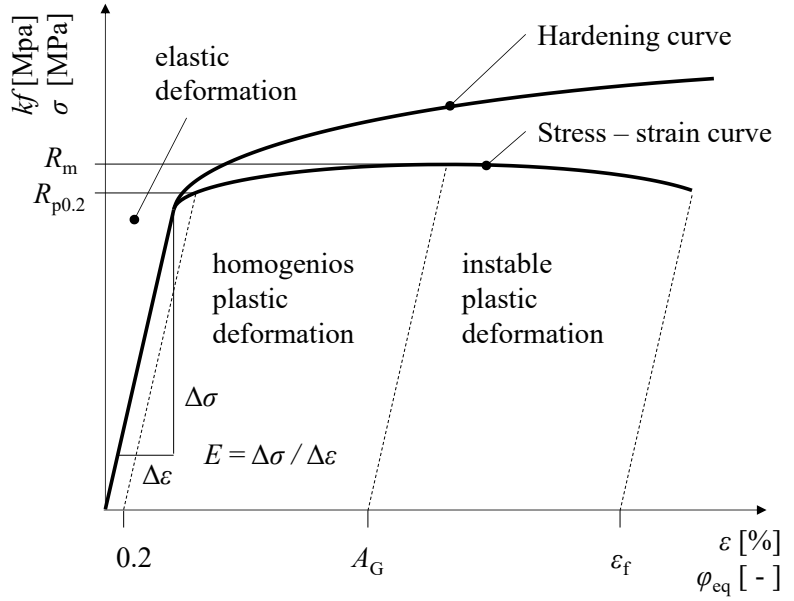

Figure 5: Stress - strain (σ - ε) curve, as measured from uniaxial tensile testing and relevant mechanical material parameters according to HOFFMANN, NEUGEBAUER, and SPUR (2012). Schematic indication of the corresponding hardening curve expressed as flow stress *kf* as a function of cross-sectional deformation over true equivalent strain φ_{eq}.

Within the area of elastic deformation, HOOKE's linear stress strain law applies for linear elastic materials, such as steel (Hooke 1678). The inclination delivers YOUNG's modulus of elasticity, E (Young 1845). Yield stress R_e is identified by a change from linear to non-linear behavior of stress over elongation. Since this spot is complicated to identify during a tensile test, a common convention is to allow at least 0.2 % of plastic strain, which is given by the yield stress parameter $R_{p0.2}$. In certain cases, low-alloyed and carbon rich materials tend to show a characteristic discontinuous and jagged trend in the area of yield stress, which is called LÜDERS strain. In this case, yield stress is parameterized by the highest local R_{eH} and lowest R_{eL} peak of the elastic – plastic transition. The maximum engineering stress delivers the parameter ultimate tensile strength R_m of the material.

Correspondingly, uniform tensile elongation A_G is obtained at this point (after release of force). During further tensile elongation, the material begins to localize strain and necking is observed in the parallel length of the test specimen. Because of the disproportional degradation of cross section, the process is generally assumed instable from the point of R_m/A_G. Eventually, material will fail due to cracking in a ductile or brittle form. Correspondingly, strain is given by the parameter of fracture strain ε_f.

The hardening curve is obtained by expressing engineering strain ε as true (logarithmic) strain φ (abscissa) and calculating flow stress kf (ordinate) from engineering stress σ by taking the actual cross section into account which results from transversal straining of material. This convention underlies the general assumption, that a constant uniform strain path with a strain ratio of ρ = - 0.5, defined by the ratio of minor strain over major strain, prevails throughout the tensile test and remains valid up to necking.

2.4.2 Dynamic determination of the elastic modulus *E*

Apart from evaluating the linear elastic area through tensile tests, YOUNG's modulus of elasticity E can also be determined in a dynamic way. According to the technical standard ASTM E 1876, the mechanical coefficients describing a material's elastic behavior (Young's Modulus E, Poisson ratio v and dynamic shear modulus G) relate to its resonant frequency. The specimens for the dynamic testing of E are cylinders or rectangular solids with the latter being suitable for testing sheet metal materials. During the test procedure, the specimen is either supported on polyurethane foam, rigid and isolated knife edges or by a wire suspension. An impulser with a steel ball at its tip excites the specimen's resonation, which is sensed by a transducer and processed by a signal amplifier with subsequent frequency analysis. From the frequency and the precise dimensions of the specimen, the elastic coefficients of the material are derived. The calculation for dynamic determination of E is given as:

$$E = 0.9465 \cdot \left(m_{plate} \cdot \frac{f_f^2}{h_0} \right) \cdot \frac{l_0^3}{s_0^3} \cdot T_1 \qquad \text{(eq. 5)}$$

with the mass m_{plate}, the fundamental resonant frequency f_f, the height of a sheet metal plate h_0, thickness s_0, length l_0 and the correction factor T_1. If the specimen fulfills the relation of $l_0 \geq 20\ s_0$, T_1 is given as:

$$T_1 = 1 + 6.585 \cdot \left(\frac{s_0}{l_0} \right)^2 . \qquad \text{(eq. 6)}$$

2.4.3 Work hardening modelling

In metal forming processes, several types of material hardening effects are considered namely dynamic, kinematic, thermal and strain hardening. Dynamic hardening is observed at elevated strain rates however it is negligible for quasi-static applications. It is usually tested and implemented on an experimental base, where a series of tensile tests are conducted with exponentially increasing strain rate and is interpolated during simulation (Klocke 2017). Kinematic hardening describes the material's hardening under back stresses. In addition, most materials would experience softening under elevated temperatures.

Strain hardening, a.k.a. work hardening, is caused by a number of different microstructural phenomena which relate to crystalline dislocations in metallic materials. The systematic shifting and interlocking effects of these dislocations during plastic deformation of metals cause the material to strengthen over strain. Typical lattice errors are linear (1D), planar (2D) and spatial (3D) defects out of which the linear types dislocate under stress along characteristic slipping planes of the microstructure and cause the material's plastic deformation (Hoffmann et al. 2012).

During plastic deformation of metallic materials an increasing stress over strain trend is observed, as schematically depicted for uniaxial tension in Figure 5. Hardening or flow curve models approximate this trend mathematically. Summarized by GRONOSTAJSKI (2000), a large number of models for work hardening of metallic materials is available in literature. In this thesis, three different work hardening laws are applied to the tested materials and are compared with respect to modelling compliance. In general, equivalent strain φ_{eq} needs to be considered when applying work hardening models because the individual strain ratio of a given forming process might diverge from uniaxial tension.

HOLLOMON and LUDWIK hardening laws

LUDWIK (1909) suggested an exponential hardening approach, which is characterized by a continuous mathematical function, that shows a passage through the coordinate origin and hence allows continuous material modelling. HOLLOMON (1945) extended the general exponential function by a constant stress coefficient C_H to describe the true stress – true strain relation as mentioned in the following equation:

$$k_f = C_H \cdot \left(\varphi_{eq}\right)^n . \qquad \text{(eq. 7)}$$

HOLLOMON's hardening law stress coefficient C_H is usually determined by empirical fitting.

STEINHEIMER (2005) developed a self-contained expression for C_H which allows to determine the coefficient based on mechanic material parameters obtained from tensile testing and is given as:

$$C_H = R_m \cdot \frac{e^n}{n^n} \quad \text{(eq. 8)}$$

with the EULER number as e.

SWIFT hardening law

SWIFT (1952) provided a hardening model for metals which adds the strain constant C_{S2} to the exponential approach. By mathematical means, hereby an ordinate intersection is hereby obtained so that SWIFT's work hardening model is applicable for plastic deformation. Hence, such hardening laws need to be combined with a function of elastic deformation. Usually, a linear approach is applied according to HOOKE (1678). By this formulation of work hardening, the plastic stress strain behavior is intended to be fitted more closely. SWIFT's equation with modelling coefficients C_{S1} (SWIFT stress parameter), strain parameter C_{S2} and hardening exponent C_{S3} is mentioned below:

$$k_f = C_{S1} \cdot \left(C_{S2} + \varphi_{eq}\right)^{C_{S3}} . \quad \text{(eq. 9)}$$

The coefficients of SWIFT's hardening law are usually determined by empirical fitting approaches. Like for the HOLLOMON/LUDWIK model, STEINHEIMER (2005) developed self-contained expressions to determine the coefficients C_{S1}, C_{S2} and C_{S3} based on mechanic material parameters:

$$C_{S1} = R_m \cdot \frac{e^n}{{C_{S3}}^{C_{S3}}} \quad \text{(eq. 10)}$$

$$C_{S2} = \frac{{R_e}^{\frac{1}{n}}}{R_m} \cdot \frac{n}{e} \quad \text{(eq. 11)}$$

with EULER's number as e and

$$C_{S3} = C_{S2} + n . \quad \text{(eq. 12)}$$

Bilinear work hardening model

Apart from exponential mathematical approaches, bilinear models are also applied to express the elastic-plastic stress-strain relationship associated with the deformation of metallic materials.

Subsequent to HOOKE's law of elasticity, a second linear function is applied to describe the area of plastic deformation within the stress-strain relationship. GERLACH (2010) suggested such a model and supported the linear function at two points, i.e. yield stress R_e and the value of flow stress corresponding to ultimate tensile stress kf (R_m). GERLACH's linear function of plasticity follows

$$k_f = m \cdot \varepsilon + R_e \cdot \left(1 - \frac{m}{E}\right) \qquad \text{(eq. 13)}$$

Here, inclination $m = \frac{R_m(1+A_G)-R_e}{A_G-\varepsilon_{el}}$. The elastic strain relation is given by $\varepsilon_{el} = \frac{\sigma}{E}$; where σ becomes R_e for uniaxial stress application. It is worth mentioning, that GERLACH build this relation based on engineering strain ε which must be considered during mathematical implementation of mechanical models.

2.4.4 Forming limit under plane stress

According to (Geiger et al. 2013), the forming limit curve (FLC) characterizes the plastic instability under plane stress conditions for a given material and is applied to determine failure in sheet metal forming. The curve is plotted in the plane of major φ_1 and minor true strain φ_2 and is denoted forming limit diagram (FLD). The FLC covers uniform biaxial strain ($\varphi_1 = \varphi_2$), e.g., stretch drawing, over plain strain ($\varphi_2 = 0$) and uniaxial tension ($\varphi_1 = -0.5\varphi_2$) until pure shear ($\varphi_1 = -\varphi_2$), e.g., deep drawing. Amongst a wide variety of testing methods for FLCs, testing procedure standardized in DIN EN ISO 12004-2 is the most commonly used procedure (Siegert 2015). Samples of varying taper width exhibit specific planar stress conditions when stretched over a hemisphere punch in a test assembly from NAKAZIMA, KIKUMA, and HASUKA (1968). During plastic straining, the tapered width of the specimens has a small effect on the strain and thus on the strain ratio ρ. Therefore, a variation of the width is chosen in such a way as to cover the FLC between the uniform biaxial strain and in the direction of pure shear. During the experiment, thorough lubrication between punch and specimen is crucial to reduce the influence of friction on the resulting instabilities. Different lubrication approaches are applied, e.g., oils and greases, as suggested by the technical standard, or polytetrafluorethylene (PTFE a.k.a. brand name TEFLON) films which have been used by KEELER (1961).

Modelling of the forming limit curve

In this thesis, the FLC is modeled (semi-) analytically according to the approaches of KEELER and STEINHEIMER. Numerical approximations are given by MARCINIAK and KUCZYŃSKI (1967) and HORA and TONG (2008). The most important models are summarized by JOCHAM (2018).

KEELER's semi – empirical formulations were developed on an experimental base of ductile deep drawing steels (R_e ranging from 217 up to 628 MPa) as well as aluminum, brass and copper alloys (Keeler 1961, 1966). In addition to empirical factorisations, the resulting model formulated by KEELER and BRAZIER (1977) takes into account the initial sheet thickness s0 and its hardening exponent n. The FLC is explained by the FLD_0 parameter, which is defined using metric (SI) units as defined by

$$FLD_0 = \ln\left[1 + \left((23.3 + 14.13s_0)\frac{n}{0.21}\right)/100\right]. \quad \text{(eq.14)}$$

KEELER's FLC equation is valid up to a sheet thickness of s_0 = 3.1 mm (Paul 2021). FLD_0 applies at plain strain conditions ($\varphi_2 = 0$). KEELER provided a case distinction for the curve according to the trend of the FLC in the first and second quadrants of the FLD according to

$$\varphi_1 = -\varphi_2 + FLD_0 \quad \text{(eq.15)}$$

for $\varphi_2 < 0$ and

$$\varphi_1 = 0.2 \cdot \varphi_2 + FLD_0 \quad \text{(eq.16)}$$

for $\varphi_2 > 0$.

STEINHEIMER pursued an approach to deliver a closed analytic solution for a worst-case scenario of FLC approximation and is hence known as "conservative FLC" (Steinheimer 2006). The conservative approach delivers an analytical solution for the FLC in the 2nd quadrant of the FLD. In the 1st quadrant it is extrapolated constantly by $\varphi_1 = n$, which represents the minimum formability the material should reveal under biaxial tension. By mathematical means, STEINHEIMER applied the hardening exponent at the knee of the FLC under plain strain. Similar to KEELER's FLC, the curve follows distinct formulations in the first and second quadrant of the FLD according to

$$\varphi_1 = -\varphi_2 + n \quad \text{(eq.17)}$$

for $\varphi_2 < 0$ and

$$\varphi_1 = n \quad \text{(eq.18)}$$

for $\varphi_2 > 0$.

2.4.5 Background on the herein used sheet metal materials

Incremental Swivel Bending is an incremental bending process which is particularly suitable for high, ultra-high-, and advanced high-strength steels due to the adaptability of the incremental procedure on the limited forming capabilities associated with these materials. Hence, for this thesis ultra-high and advanced high-strength grades of steel are considered. These materials are summarized in Table 1 and explained in detail in the following subsections. They are chosen in a way to cover a broad variety of mechanical properties, in particular strength and ductility.

Table 1: Materials tested and used in the present study. Material numbers according to DIN EN 10027-2.

material	**number**	**trade name**	**microstructure**	s_0	**coating**
	[-]	[-]	[-]	[mm]	[-]
HCT780X	1.0943	DP800	ferrite – martensite	1.0, 1.5, 2.0	zinc
22MnB5	1.5528	-	ferrite – pearlite	1.4	-
42SiCr	-	-	pearlite	2.0	tinder
S235JR	1.0038	St 37-2	ferrite	2.0	-
X30MnCrN16-14	1.4678	FORTA H800	austenite	1.0, 2.0	-

2.4.5.1 High-strength automotive steel DP800

HCT780X, No. 1.0943 according to DIN EN 10027-2 and commonly known as DP800, is a widely used high strength steel. Especially in automotive applications, dual-phase (DP) steels are used for structural parts like components for crash absorption and reinforcements in car bodies (beams and members). Due to their high strength, dual phase steels offer light-weight construction potential as they allow to reduce wall thickness and hence, the resulting light weight of components in comparison to softer streel grades. When comparing them to classic alloys, DP steels offer higher ductility in relation to strength; parts with higher complexity can be formed from these materials. In component design, this property potentially allows to integrate and substitute individual parts.

The predominant ferrite phase (70-95%) of the dual-phase “DP” microstructure plastically deforms reasonably well while enclosed islands of martensite phase (5-20%) deliver enhanced ultimate tensile strength. Due to the prevalent ferritic phase, DP800 is crystallized in a body-centered cubic structure. For the present study, DP800 has been obtained from the steel service center ESB (EUROPEAN STEEL BUSINESS) in three different thicknesses, 1.0, 1.5 and 2.0 mm, respectively. Each of these materials is hot-dip coated with zinc for corrosion inhibition. DP800 has been suggested by ENGEL et. al for first automotive implementation of ISB (Engel, Frohn, Hillebrecht, and André Knappe 2017).

2.4.5.2 Boron-alloyed heat treatable steel 22MnB5

For products of higher geometric complexity and ultra-high strength, hot forming a.k.a. press hardening is a common technique to utilize better formability of sheet metals at elevated temperatures (Neugebauer et al. 2012). As soon as the heated sheet metal plate comes in contact with the forming tools, quenching occurs depending on the surface pressure. The austenite phase transforms to martensite and hence, high strength is achieved. Looking at a large industrial scale, the most common hot forming sheet metal material is boron manganese steel grade 22MnB5 (Karbasian and Tekkaya 2010). Due to oxidation at elevated temperatures, heating for hot forming either has to be operated under inert nitrogen atmosphere or an oxidation inhibiting coat must be applied to the sheet metal beforehand. Commonly, 22MnB5 is coated by aluminum-silicon "AlSi", which diffuses into the sheet's skin and iron atoms diffuse into the coating during the heating process (Merklein, Lechler, and Stoehr 2008). Hence, a stable oxidation inhibition is achieved. Other process route strategies accept the surface oxidation during hot forming and treat the finished sheet metal parts by sand blasting.
Keeping in view in-plane bending in initially soft material structure, ISB is a promising technology to obtain pre-products for hot stamping and therefore, the corresponding material is included in this study. From SALZGITTER, uncoated blanks of 1.4 mm material were obtained. AlSi coated blanks have been excluded from this study because of their severe friction issues with aluminum during dry sliding friction. During preliminary dry friction tests, AlSi coating was abrasively corrupted, even at low applied pressures. Favorable tool coatings such as amorphous carbon coatings are encouraged for future studies if aluminum or aluminum-based sheet metal materials are to be subjected to ISB.

2.4.5.3 Carbon enriched, low-alloyed 42SiCr

In comparison to conventional quenching processes, Quenching and Partitioning (Q-P) is a relatively new hot forming technology which has been in focus since last two decades (Speer et al. 2003). In a Q-P process; after austenitization, the material is incompletely quenched well within the martensite transformation zone however it is still kept above finish temperature M_f. By subsequent heating, carbon is redistributed from the supersaturated martensite crystal to retain the remaining austenite.
42SiCr is a promising material which is still under research related discussion. According to JIRKOVÁ et al. (2014), the composition of 42SiCr is suitable for a Q-P process. JIRKOVA and KUCEROVA identified a carbon content of 0.42% which is sufficient to stabilize the austenite phase during partitioning (Jirkova and Kucerova 2016). After cooling to room temperature, not only ultra-high strength but a considerably elevated ductility is obtained compared to conventionally quenched steels. It happens due to the retained and fine-spread austenitic phase between the martensitic laths. The chromium content improves hardenability by lowering the temperature range of martensite formation but facilitates the emergence of carbides. Because silicon is known to suppress carbides, it is therefore

contained in the alloying composition of 42SiCr. JIRKOVÁ, KUČEROVÁ, and MAŠEK (2012) identified a significant improvement of ductility by adding Silicon to the alloy.

The initial carbon enriched pearlitic microstructure offers reasonable cold formability as a pre-step to hot forming or pure stamping. Hence, in case of 42SiCr, a combination of ISB and Q-P is suggested which may provide highly variable geometries whereby Q-P offers the possibility to achieve a wide range of material properties in its heat treated state (Frohn et al. 2017). For the investigations of the present thesis, material samples of 42SiCr were cast and rolled by the Czech steel research center COMTES. After hot rolling, thickness was reduced (until s_0 = 1.95 mm) by cold rolling with interstage annealing to achieve a pearlitic microstructure. The material reveals an uncoated surface with a thin layer of tinder resulting from the thermomechanical rolling process.

2.4.5.4 Standard industrial steel S235JR

In order to ascertain the applicability, application the theoretical results of this thesis are compared to a commonly used industrial steel known as E235 “ST 37-2” which is a widespread, soft and ductile steel. Tensile material tests have been conducted on 2.0 mm sheets.

2.4.5.5 Advanced high-strength steel OUTOKUMPU FORTA H800

Advanced high-strength steels (AHSS) offer enhanced straining behavior as compared to conventionally manufactured or quenched materials. As such an AHSS material, OUTOKUMPU FORTA H 800 offers a pronounced work hardening behavior during straining by phase transformation from ductile austenite to high-strength martensite. Due to this behavior, the material reveals sufficient cold forming capabilities by means of shaping complex geometries. Moreover, corrosion is restricted due to the initial austenitic microstructure. The H800 grade of OUTOKUMPU FORTA series has been pre-hardened by cold rolling to achieve a higher yield strength as compared to the base material. H800 has been suggested for structural car body applications by LINDNER (2016). In the present study, 1.0 and 2.0 mm blanks of H800 are investigated in the context of an ISB process.

The chemical composition OUTOKUMPU FORTA H800 is referred by OUTOKUMPU as a material number 1.4678 which corresponds to an alloy X30MnCrN16-14. However, since the material has been work hardened prior to its distribution therefore its chemical composition would be an indistinctive description and hence is referred to as “H800” in the remainder of this thesis. The material is crystallized in a cubic face centered microstructure. For dry friction at high contact pressure, austenitic microstructures are prone to adhesion, which might even initiate galling at tools. Thus, adequate tool coatings have been recommended by Hanson et al. (2008).

2.5 Tribology in metal forming

Tribology was defined as the theory of friction according to the Greek words “tribein” and “logos” by the work group of JOST (1966). The discipline includes the three fundamental scientific concepts of friction, lubrication and wear. These concepts also process substantial importance in technological and economical domains. In addition to the field of engineering, the interdisciplinary field of tribology also encompasses the academic fields of physics, biology, materials science, mathematics and chemistry. According to JOST (2006) tribology was neglected for a long time because only recent technical advances in each of these fields could only address the interdependence of these fields. According to KLOCKE (2017) every contact represents a tribological system, which essentially consists of both partners in contact with each other, an interface layer and an environment medium. With regards to metal forming, the physical conditions such as temperature, process forces and sliding velocity are referred to as collective load and are better understood as inputs to the system. The physical and chemical properties along with the topographic structures of surfaces of contact partners, given by the peaks and bottom values of their roughness, are of key importance for tribological behavior of the system (Hoffmann et al. 2012). The roughness of the bodies in interaction leads to micro contacts, which are significantly smaller, than the nominal contact surfaces given by the outer dimensions. Yet these micro contacts must transmit the normal and shear forces impinged on the system.

According to the classifications of CZICHOS and HABIG (2010), following four different forms of friction are defined related to the state of aggregation:

1) Friction of solids; any type of solid matter stays in direct contact with another solid partner.
2) Liquid friction, in particular where a lubricating interface layer is provided in between the solid bodies in contact influence friction and wear behavior of the tribological system. The category also applies, if both solid bodies are exclusively in contact to the liquid but not to each other.
3) Friction related to contact with gaseous matter, in particular if the gas acts as an interface layer.
4) Mixed types, usually a combination of solid and liquid friction.

With regards to the initially mentioned definition of tribology, the third scientific concept of wear results from friction, whether lubricated or unlubricated. Summarized by SIEGERT (2015), the surfaces of the bodies in contact experience alteration and material loss, which is commonly categorized as follows:

a) Adhesion, where material closure and splitting leads to material transfer and galling.
b) Abrasion, where micro cutting processes cause scratches and furrowing.

c) Surface cracks due to fatigue caused by alternating stress.

d) Tribo-chemical reactions.

Surface coating techniques

Apart from lubrication techniques, technical surface treatments can significantly reduce wear of the contact partners. In the domain of manufacturing engineering, tool surfaces are normally treated to prolong their endurance and time of operation as well as to improve surface quality of the product and to reduce process forces. Specifically, the tool resistance to wear can either be against abrasive effects, e.g., by dry lubricants (Hortig 2001), or by lowering the adhesion tendencies of the materials in contact, e.g., by stabilizing the lubricating interface layer or by amorphous carbon films (Nitzsche 2007). In order to provide a hard, wear resistant surface layer on production tooling, Hoffmann et al. (2012) differentiated between hardening the tools by heat treatment, overlay coating and reaction layers, cf. Figure 6.

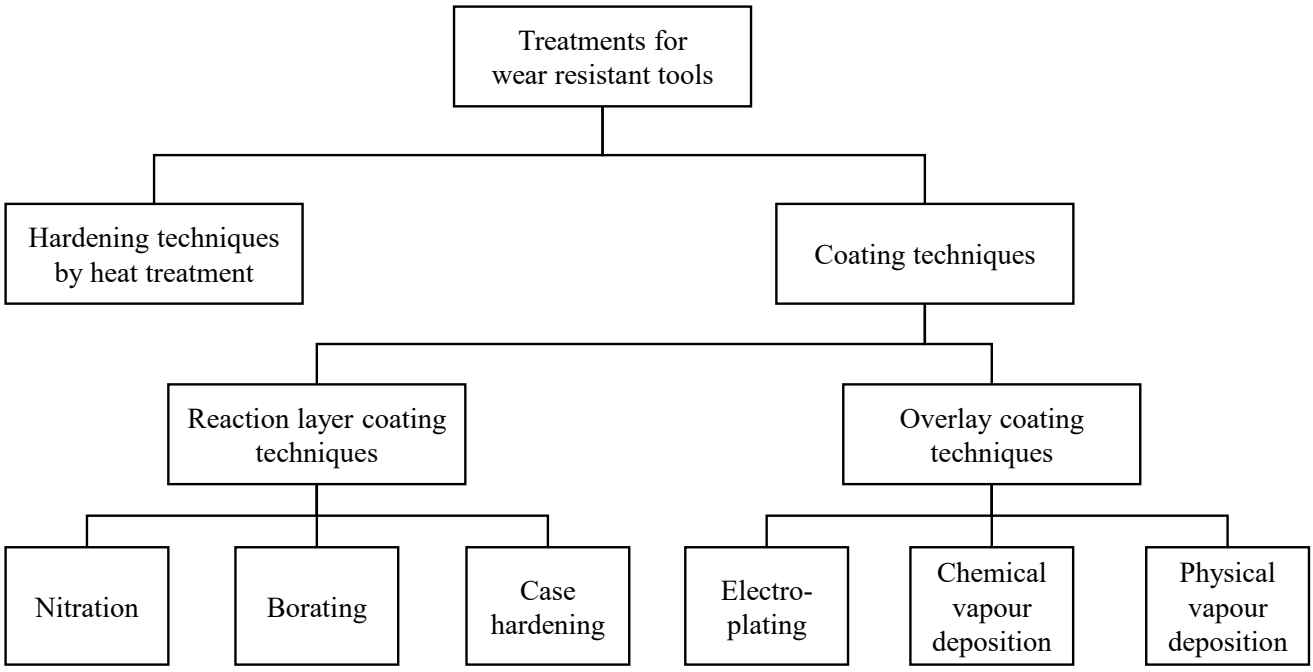

Figure 6: Groups of tool treatment techniques to provide a hard and wear resistant surface on forming tools following HOFFMANN et al. (2012).

In the latter group of reaction layer coatings, nitration (including gas, bath or plasma based techniques) represents the most common application and delivers a diffusion layer thickness of 10 - 30 µm (Liedtke et al. 2018; Macherauch and Zoch 2011). In overlay coating techniques, the chemical vapor deposition (CVD) and physical vapor deposition (PVD) processes are of particular interest in the context of sheet metal forming besides hard chrome electroplating (Bach et al. 2006). According to KLOCKE (2017), CVD techniques offer a higher bond strength making them suitable for heavy loads and abrasive wear demands. On the other hand, PVD coatings, such as diamond-like coating (DLC), can significantly improve adhesion tendencies, which are associated with processing

aluminum or austenitic steel sheets. Titanium nitride (TiN) coats offer a well-established industrial compromise to both adhesive and abrasive tool charges domains.

Surface topography characterization

On a microscopic scale, the topography of technical surfaces results from the combination of the material, the applied manufacturing methods and surface treatments. The surface appearance is governed by roughness, which is characterized by qualitative and quantitative means in a two- or three-dimensional way. Following DIN 4762, the surface roughness is divided into vertical and horizontal parts, of which the vertical parts are processed to obtain the outcomes. Based in two dimensional line samples, which are obtained by surface probing, the following evaluations are common according to WHITEHOUSE (2004):

- R_a, which is an arithmetical mean deviation of all peak and bottom values from the central line.
- R_z, which is an average over the tallest peak and the deepest bottom value within a line sample.

In order to determine the qualitative measures of the surface texture of a line sample, the bearing area curve (BAC) was suggested by ABBOTT and FIRESTONE (1933). The curve accumulates density over height values of the surface profile, thus representing the contact ratio of the tested surface. Three dimensional methods for characterization of surface topography have been summarized by WAGNER (1996, 1997).

2.5.1 Friction theory and modelling

For mechanical modelling of friction in forming processes, the relation of the applied normal force on two bodies in contact is of key interest to predict the resulting transverse force, which results from the conditions of the tribological system. According to KLOCKE (2017), two friction laws prevail in theory of plasticity namely the model of COULOMB and the friction factor model. These both models are summarized in the following paragraphs.

In fact, fundamental observations of friction date back to the times of LEONARDO DA VINCI in the 15th century however they were firstly described in a friction law by COULOMB (1821) as expressed in the following relation:

$$F_{fric} = F_N \cdot \mu \,. \qquad \text{(eq.19)}$$

Here, the applied normal force is F_N, the resulting transversal friction force is F_{fric} and the coefficient of friction is μ. Considering the collective load of the tribological system, the applied normal pressure σ_N is often considered in technical applications and significantly affects friction in dry or lubricated state. Decreasing friction coefficients are observed over increasing contact pressure, which is

explained by pressurized oil cushions, e.g., (Zöller 2016). Without lubrication, an increase of the friction coefficient over pressure is expected and is considered in detail in section 2.5.2. KLOCKE (2017) provides a formulation of COULOMB's friction law depending on the area of contact A_C, which follows as:

$$\frac{F_{fric}}{A_C} = \tau_{fric} = \sigma_N \cdot \mu = \frac{F_N}{A_C} \qquad \text{(eq.20)}$$

with the friction shear stress denoted as τ_{fric}.

In a tribological system, COULOMB's friction law is assumed valid if τ_{fric} stays well below shear strength k of the bodies in contact. Evidently, τ_{fric} cannot exceed k, as material would begin to undergo subsurface plastic shearing in the area of contact (Klocke 2017; Shaw, Ber, and Mamin 1960). $\tau_{fric,max}$ therefore denotes the maximum transferrable shear stress of the tribological system, which is applied in the friction factor model. The model is applied in the range where friction shear of the system approximates ultimate shear strength of the materials in contact and follows as:

$$\tau_{fric,max} = m_{ff} \cdot k \qquad \text{(eq.21)}$$

where m_{ff} represents an empirical factor. m_{ff} becomes 1 for static friction and lies in between 1 and zero for kinetic friction. m_{ff} = 0 represents a frictionless state. ECKSTEIN (2009) applies ring compression tests to determine m_{ff} for a given tribological combination. The method was found by MALE and COCKROFT (1964) and bases on the principle that under an axial compression, the inner diameter of a ring would directly relate to friction under plastic deformation and it was later validated by MALE and DEPIERRE (1970). If the materials in contact possess hardening properties, k increases proportionally to kf beyond the materials yielding. By incorporating V. MISES yield criterion, $k = kf / \sqrt{3}$, eq. (21) becomes

$$\tau_{fric,max} = m_{ff} \cdot \frac{kf}{\sqrt{3}}. \qquad \text{(eq.22)}$$

Mathematically, the friction factor model replaces COULOMB's model at the highest normal pressure applied to the tribological system. Two functions have to be combined leaving an unsteady intersection. Therefore, models have been developed, which aim to link both states of friction. SHAW (1963) provides a steady function for modelling both friction states according to

$$\frac{\tau_R}{k} = \sqrt[n_s]{\tanh\left(\frac{\mu \cdot \sigma_N}{k}\right)^{n_s}}. \qquad \text{(eq. 23)}$$

Here, the empirical coefficient n_s determines the smoothness of the transition of both friction states described above.

In addition to a normal pressure, the relative speed v_{rel} between both bodies in contact is an important variable which influences the tribological system. In lubricated state, μ declines significantly over increasing v_{rel} according to WAGNER (1999). It is commonly summarized by STRIBECK (1946) for hydrodynamic friction as a function of v_{rel} and the lubricant's viscosity. Generally, two states need to be differentiated, static friction, where v_{rel} becomes zero, and kinetic friction. According to COULOMB's postulations, most tribological combinations with lubricating interface layers possess a higher coefficient of friction for static conditions μ_0, than the kinetic friction coefficient: $\mu_0 \geq \mu$ (Elmer 1997). HUGHES (1977) suggest the ratio of both coefficients to characterize the adhesion risk of a tribological system, as a high ratio is generally associated with galling tendencies, e.g., it had been observed by GIBSON, HOBBS, and STEWART (1974) and specifically for aluminum, same had been observed by MÖSSLE (1983).

2.5.2 Dry friction

From a mechanical perspective, dry friction prevails in a tribological system in the absence of any lubricating interface layer. Due to the solid contact of both tribological partners, specific physical effects are required to be considered. First, an opposite effect of surface pressure on friction coefficients is observed as compared to lubricated systems. Due to flattening of the surface topographies of both partners, the effective area increases, and friction forces increase over surface pressure. In addition, VOLLERTSEN and SCHMIDT (2014) describe a drastic increase of wearing tendencies besides generally higher friction coefficients at rising surface pressure under dry friction conditions. Due to the nonlinear behavior of a dynamic dry friction system as postulated by ELMER (1997), a complex dependency of kinetic dry friction coefficient on the relative velocity has been observed (Heslot et al. 1994).

Dry metal forming was prominently addressed in the DFG priority program SPP 1676 as it opens up highly rewarding economic and ecologic benefits according to HÄFNER et al. (2018). In conventional forming processes, lubricants are used to reduce wear and process forces in addition to suppressing corrosion of products and tools (Schöler et al. 2018). On the other hand, these need to be applied before manufacturing, be removed after production and subsequently be recycled or disposed. VOLLERTSEN and SCHMIDT (2014) summarized three common strategies to execute dry metal forming, i.e., ceramic tools, self-lubricating surfaces and specific coating technologies. These approaches are necessary to withstand the high mechanical surface demands associated with dry friction.

Conventional tool materials often provide limited applicability to dry forming processes. For example, HETZNER et al. (2011) realized forming of high alloy steels with tool steel 1.2379 under dry conditions. For these conditions, specific surface treatments were developed. Diamond like carbon (DLC) coatings are reported to be suitable for forming stainless steels in dry condition by GHIOTTI and BRUSCHI (2011) and successfully applied to unlubricated forming of a variety of aluminum alloys by WEIHNACHT, BRÜCKNER, and BRÄUNLING (2008). In the group of DLC coatings, tetrahedral amorphous carbon (ta-C) coatings show promising potential to reduce wear and friction, as reported by MERKLEIN et al. (2015) for DC04 and aluminum AA5182. Moreover, according to VETTER (2014), hydrogen containing hard carbon coatings (a-C:H) provide a higher stability against adhesion than ta-C coatings and have been successfully applied in experimental investigation of dry friction of aluminum alloy 5083 by ABRAHAM et al. (2018). Other approaches of surface modifications suitable for dry friction follow the generation of α-Fe2O3 oxide layers on the tools surfaces in lubricant free processes (J. Glascott, Stott, and Wood 1985; J Glascott, Wood, and Stott 1985; Stott and Jordan 2001).

2.5.3 Experimental testing of friction

In order to evaluate the coefficients of friction, a number of test assemblies are established to apply the tribological system of a given process to a given material/tool combination under defined and measurable laboratory conditions. The testing assembly must not only feature the same materials of the regarded working piece and tool, but also apply the collective load in similarity to the considered process with respect to contact pressure, relative velocity and ambient influences such as temperature. Lubricants may be introduced to the test which are characterized by a number of methods summarized by KLOCKE (2017). According to LORENZ et al. (2015), friction tests in general are expected to reveal an elevated stochastic scattering. Therefore, an appropriate number of test repetitions is recommended. CZICHOS and HABIG (2010) systematically categorized tribological test assemblies into categories I-VI, as shown in Table 2. The higher the category, the higher the degree of abstraction. With the degree of abstraction, not only the effort would sink normally but the applicability to the real process would also be more limited.

Table 2: Categories of tribological testing technology according to Czichos and Habig 2010.

Category	Type of test		System structure	
I	Similar to operating tests	Field test	Original parts	Complete machine
II		Test bench experiment		Complete machine
III		Assembly on test bench		Complete assembly
IV		Experiment with unchanged component		Detached component
V	Tests with model systems	Experiment with similar loads on specimens		Parts with comparable load
VI		Model experiment with simple specimens	Model specimens	Simple specimens

For the tribological characterization of sheet metal forming with respect to friction and wear, the strip drawing test is an established model experiment according to FILZEK (2004) and is carried out on a flatbed in the standard setup. In principle, specimens from the sheet metal of interest are drawn through a clamping jaw of friction tools made from the identical material and surface treated the very same way as the considered forming tool (Häfner et al. 2018). The clamping jaw is pressed against the strip specimen by a defined force, which is measured by load cells or indirectly by the hydraulic pressure applied to the clamp. The tools need to be guided in a rigid way to ensure perpendicular application of the normal force F_N. The longitudinal drawing force F_D and travel l_{draw} of the strip material are tracked over the experiment. By the relation of F_N and F_D, μ is obtained depending on travel l_{draw}. The experimental procedure is usually applied by dedicated special purpose machines such as the fully automated unit capable to test whole coils described by NETSCH (1995). From the measured data of the strip drawing experiment, the distinct states of static and kinetic friction are evaluated according to ZÖLLER (2016).

Variations of the strip drawing experiment can be tailored to the conditions of a forming process. For a deep drawing process, c.f. (Colgan and Monaghan 2003; Hoffmann et al. 2012), NETSCH (1995) suggests four variations of the strip drawing experiment in relation to the process zones:

a) In flatbed representing the blankholder area near straight edges of the deep drawing process,
b) In a plane wedge arrangement representing the blankholder area near curved edges,
c) A redirected variant of the experiment running around a smooth edge of for instance 90 degrees angle instead of a flatbed to represent the drawing radius of deep drawing and
d) Strip drawing with beads in the friction jaw.

GROCHE, FILZEK, and NITZSCHE (2004) developed a cyclic strip drawing test for specifically testing wear over lot size. In their study, 15000 strokes were carried out to characterize distinct areas of a deep drawing tool.

2.6 Finite Elements Method background

The finite elements method (FEM) is used to describe the physical behavior of a system within enclosed outer boundaries. In particular, mechanical interactions are evaluated, such as between tool and working piece. In contrast to self-containing equations of continuum mechanics, the FEM pursues an approach of system discretization by breaking it down into uniform finite pieces. Within these elements, constant mechanical conditions are postulated, so that the interactions at the boundaries between elements are of interest. By solving the equations of these interactions, the stress-strain gradients are obtained, which are caused in the discretized material by the applied loads of the modeled system. For constant system conditions, usually an equilibrium needs to be calculated to which the model converges. If the system conditions, e.g., load, changes over time, the discrete time steps are calculated for the evaluation in post numerical processing.

In finite element (FE) - simulations of metal forming, the modelling setup usually begins with the computer generated design representation of the processes (Hoffmann et al. 2012). All relevant process boundaries, degrees of freedom, forces, pressures, etc. are formulated in cartesian or rotational kinematics. Contacts are defined according to the tested tribological coefficients (see section 2.5.1) between the deformable working piece and its enclosing tools. Tools can be simulated as deformable, however due to the large differences between tool and working piece in sheet metal forming, they are often represented by rigid bodies (Tekkaya 1998). Materials are implemented to the forming simulation with respect to their mechanical description according to GRONOSTAJSKI (2000) – e.g., density, elasticity, plasticity –, their outer dimensions and by a discretization into finite elements. Two major groups of element types are deployed for sheet metal forming simulations, reduced planar (2D) shell elements and spatial (3D) solid elements. The major difference in between both types is that plastic deformation by normal stress application in the direction of thickness can only be simulated in a valid way by solids. Shell elements, on the other hand only indirectly calculate the plastic chance of thickness by algorithms to simulate the deformation perpendicular to the shell's plane (Klocke 2017). On the other hand, solid finite elements possess a higher number of degrees of freedom, thus it needs a considerable higher numerical effort during solving. The continuous advances in computer technology is sooner going to allow a more common application of three dimensional elements (Wu, Tang, and Li 2000). The whole procedure of establishing and parameterizing the model is denoted as pre-processing. Afterwards, the simulation model is numerically processed by a computer, which solves the formulated model in an implicit or explicit

calculation method until either converging towards an equilibrium or reaching an abort criterion, e.g., a defined travel, time or contact respectively. The forming process simulation usually ends with an implicitly calculated springback step, where all process forces are released and the deformed product releases elastic stresses until an equilibrium of residual stresses within the material is reached and the simulation result converges (Rohleder 2002). Subsequently, the user begins evaluation within the post-processing step. From the deformed finite element mesh, dimensional properties such as change of thickness, stresses, strains and the resulting geometry of the simulated product can be examined.

2.7 Statistical methods background

For the statistic calculations of this thesis, the software MINITAB 17 by MINITAB Inc. is used. MINITAB offers calculation of statistic methods and moreover, to layout and analyze design of experiments (DoE). In particular, the software offers the possibility to derive a necessary amount of test specimens for a given experimental spread and a given tolerance (Back and Weigel 2014). In this context, the interval of confidence is often applied to describe a certain spread of experiments conducted in this thesis instead of providing the standard deviation. Figuratively, the interval of confidence tells the range in which the average mean of a certain value lies with a probability of 95%. For example, on a surface manufactured by grinding, a surface roughness of *Ra* of 0.32 ± 0.07 µm was tested. This means, that with 95% probability, the roughness of grinding lies in between 0.25 and 0.39 µm. When comparing two measurements, the t-test is used to identify that whether the mean values of two groups of samples vary from each other in a statistically significant way (Back and Weigel 2014).

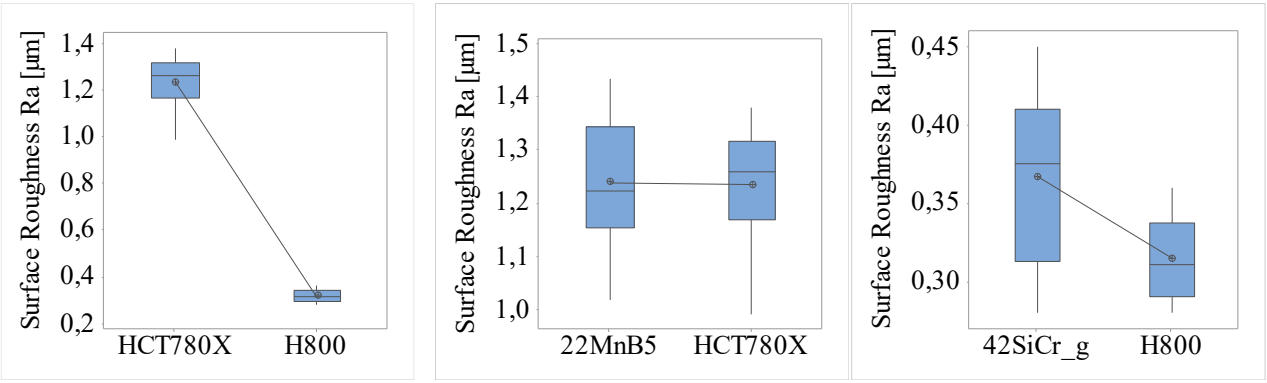

a) b) c)

Figure 7: Statistic test of significantly different mean values, illustrated by box plots.

The t-test is applied to determine in a comprehensible way whether a certain property differed between the tested, diverse materials or not. E.g., the significance in between the variation of tested surface roughness of materials considered in the present study is evaluated and illustrated in Figure 7 by box plots. In this example of tested surface roughness of various materials, the t-test delivers in case a) significant difference, b) no difference, c) significant difference despite overlapping spreads.

3 Objective

3.1 Motivation

Presently, due to higher demand of individualized production, an increased requirement of flexibility or reconfigurability in the manufacturing processes has been observed. Therefore, kinematic forming methods are becoming high in demand since they are able to define the shape of the product by the process parameters rather than by a fixed and inflexible tooling geometry (Hermes 2011). Incremental forming methods shape the product in sequences with generic sets of tools, which repeatedly move over the working piece and hence provide even more degrees of freedom – i.e., size and density of incremental steps (Scherer 2014). By adjusting these steps within the incremental sequence, the materials' straining is influenced. High production flexibility and a low demand of tools result from incremental methods yet the purposeful layout of these process parameters is crucial for shaping individual parts so that elaborate and material intense trial and error approaches are avoided. Incremental swivel bending (ISB) has been proven as flexible forming method for industry oriented demonstrators (Engel, Frohn, Hillebrecht, and Andre Knappe 2017). Before the research work conducted in this thesis, the state of development related to ISB was restricted to empiric experiments or simulations. Hence, a key research gap has been identified and is stated as: Even if ISB has shown high flexible forming potential, the method lacked a holistic layout to link the relation between an evolving bending geometry and the material and process parameters, which, up to now, has only been derived by using empirical approaches.

3.2 Aim and scope

The aim of this thesis is to provide a model for ISB, which, when considered along with material properties, determines the parameters necessary for bending a specific geometry according to the degrees of freedom given by the process. This model is intended to base exclusively on self-enclosing analytical relations in such a way that understandable model parameters are applicable in a universal way for changing process circumstances (e.g., material or geometry changes during production). Hence, empirical, self-learning or artificial intelligence based refinements of the herein established analytical models, e.g., grey box approaches (Vorkov et al. 2019), are out of the scope. With regard to the repeating incremental sequence, constant parameters are focused throughout a sequence. Because of the discontinuous forming method, ISB is expected to be suitable for high-strength steels, which are prone for failure in continuous processes (e.g., stretch bending). Consequently, a variation of ultra and advanced high-strength steels is considered. Because force is transmitted by traction, an unlubricated operation of ISB is favorable for the sake of elevated friction coefficients. Textured

surfaces, e.g., knurled (Hinkel 2013), are neglected. Finally, the findings of this thesis are kept limited to cold forming.

3.3 Process development approach

The process is developed based on plasto-mechanical considerations, which essentially represent ISB as an in-plane bending process under frictional engagement. These analytical models are validated by numerical simulations and practical experiments. The superposition of multiple increments is considered with respect to the discontinuous character of the forming method. A process window for ISB is derived from the analytical considerations.

In order to pursue a comprehensive process development, LANGE presented a systematic and holistic approach for substantial advancement in forming technology (Lange 2002). This methodology is applied to ISB to ensure the consideration of all technologically relevant fields. Following LANGE's development scheme, all aspects are applied to ISB in Figure 8 and explained in the following paragraphs.

1. Forming zone
   Plasticity theory of frictional bending
2. Product properties prior to forming
   Mechanical properties, forming limit, friction coefficients, surface
3. Product properties after forming
   Work hardening, failure, dimensions
4. Border area of contact, gap of effect
   Dry static friction
5. Forming tool
   In-plane and profile bending concepts
6. Surface reactions after forming
   Oxidation, gas absorption
7. Forming machine
   Press, bending or specialized machine
8. Operation, economic production, automation
   Use-case manufacture, semi-automated concept, Tolerances

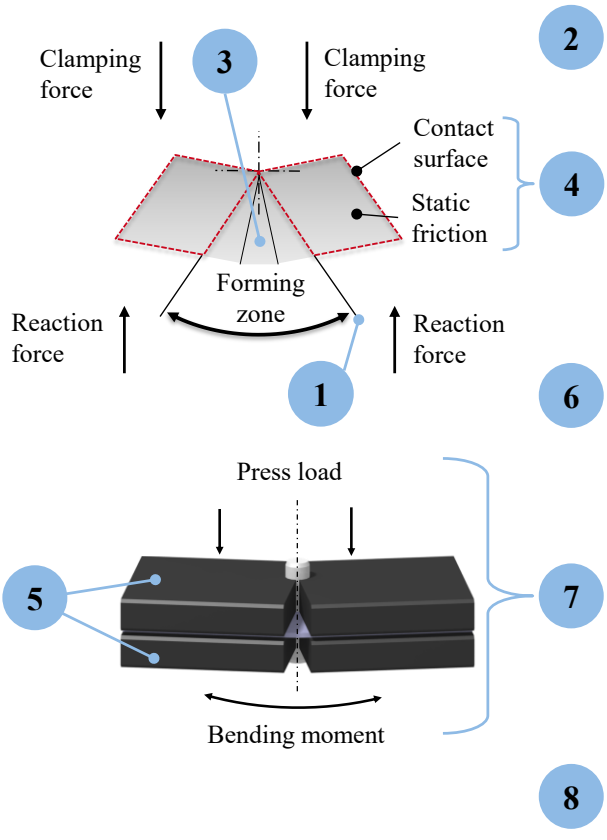

Figure 8: Systematical process development methodology according to LANGE (2002), applied to the ISB process within the scope of the present thesis. Mechanic representations of the ISB process in spatial (top right) and parallel side view (bottom right).

Forming zone

The ISB process is characterized by two clamping units, evenly loaded by a press. When these units form the material force-fittingly by rotating apart from each other, the forming zone emerges in between the tools. In essence, the material is partially drawn out from the clamped area. The border between firmly clamped material and strained material has been identified as yield sheath by STAEVES (1998). Developing a model to describe the sheaths' location allows to understand strain in the process development depending on tribology, the material under consideration and the process parameters. Additionally, the total area of deformation resulting from the overlapping forming zones of several bending increments is also considered.

Product properties prior to forming

The sheet metal materials considered herein are characterized in their pristine state. The elastic and plastic mechanical properties are obtained from tensile tests with additional dynamic tests of YOUNG's modulus of elasticity. Moreover, dry friction coefficients of the materials are evaluated in strip drawing experiments. For description of failure due to straining, forming limit curves are tested.

Product properties after forming

Work hardening represents the substantial change of material properties caused by the ISB process. For exemplary profiles, strain hardening is evaluated laterally over profile height by miniature tensile tests. In addition, a valid limit for failure due to cracking is investigated for the ISB process. Buckling tendencies and compensation strategies are considered in relation to the tool concepts. With regards to product dimensions, the curvature caused by the incremental bending method is of significant interest.

Border area of contact, gap of effect

In particular, the mechanical description of the position of yield sheath, which changes over progression, is the key aspect in understanding the process of bending under frictional engagement. The dry friction coefficients evaluated from the materials are applied to the contact area in between material and die faces, which changes significantly during plastic deformation.

Forming tool

Prior to this thesis, a prototype ISB tool was present, which is now reconstructed for the defined in-plane bending under laboratory conditions and advanced for bending various open profiles. In addition, an industrial scale, semi-automated ISB tool for bending a hat shaped profile in two planes is also developed which is related to the funded project ISB-ELEKTRO.

Surface reactions after forming

According to LANGE, surface reactions after forming encompass all physical or chemical reactions of the material, which are caused by the forming process, but happen during post-production, such as

oxidation or gas absorption. Due to focus on cold forming in the ISB technology, the aforementioned aspect has been neglected.

Forming machine

As suggested by the inventors SCHWARZ and ENGEL (2009), ISB is operated on a press. While a hydraulic try-out press is used during the laboratory-based experiments, a servo-mechanical press is utilized for the industrial scale application due to its superior kinematic capabilities. Apart from presses, bending and specialized machinery concepts are studied so as to adjust according to the requirements of an ISB process.

Operation, economical production, and automation

As industrial-scale, the manufacture of an electric car's longitudinal member is studied as a use-case of the ISB technology. Based on this application, a semi-automated concept of the ISB tool control is connected to the servo-mechanical forming press.

4 Analytical derivation of frictionally engaged forming

In the following chapters, a plasto-mechanical description of ISB is derived for the practical dimensioning of the process. In particular, the correlation in between process parameters, material properties and the required product dimensions is of key interest. According to the current state of research and existing technology, a direct relation between the process kinematics and the resulting geometry has not been established with regards to frictionally engaged forming processes and the corresponding product-unspecific tooling. Therefore, the key objective of this thesis is to identify and establish the aforementioned relationship. Apropos, this thesis is divided into three parts which are explained further in subsequent text; Firstly, a linear drawing process of plane material strips is analytically modelled under plasto-mechanical considerations. Tensile plastic deformation in longitudinal direction of strip drawing is applied by traction. After validation, these assumptions are applied to in-plane bending which resembles an elementary step of the ISB process. For this bending operation, a process window is derived which stretches out between the applied clamping force and the bending angle. In the last step, the incremental sequence of the ISB process is considered by means of the density at which the series of bending steps are formed. A schematic representation of the process development of an ISB process established in this thesis is shown in Figure 9.

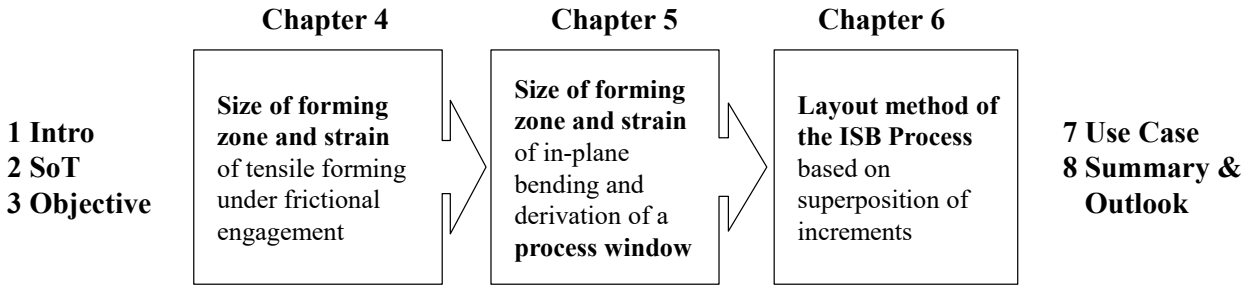

Figure 9: Scheme for analytical process development within the present thesis.

In the following part of this chapter, longitudinal tensile forming under traction is pursued as a first modelling approach towards understanding an ISB process.

4.1 Linear tensile forming under frictional engagement

An analytic model describing a tensile forming process of plane strip profiles is derived in this section under consideration of the fundamental mechanics of frictionally engaged forming processes. In contrast to bending, a constant stress distribution over the material's width h_0 can be assumed. Two distinct cases are considered in the following sections, i.e., elastic and plastic forming. In particular, the relation of clamping pressure, tool stroke and longitudinal strain is described.

4.1.1 Tensile elastic forming

In the simplest form, frictionally engaged tensile forming involves two clamping units moving apart from each other along a linear path. The symmetric process is illustrated in Figure 10 with the main parameters and variables as well as the elementary stress states in three distinct regions. Each of the clamping units is loaded by half the common press load F_N, which lasts perpendicular on the initial contact surface $A_{C,0}$ between die faces and the material. Hence, F_N causes a uniform distribution of the initial normal pressure $\sigma_{N,0}$ which is propagated over strip width h_0 and the initial contact length $l_{c,0}$ in between tool and strip material. $\sigma_{N,0}$ follows the relation

$$\sigma_{N,0} = \frac{F_N}{2h_0 \cdot l_{c,0}} \qquad \text{(eq. 24)}$$

under consideration of the opposed supporting force at the tool's base.

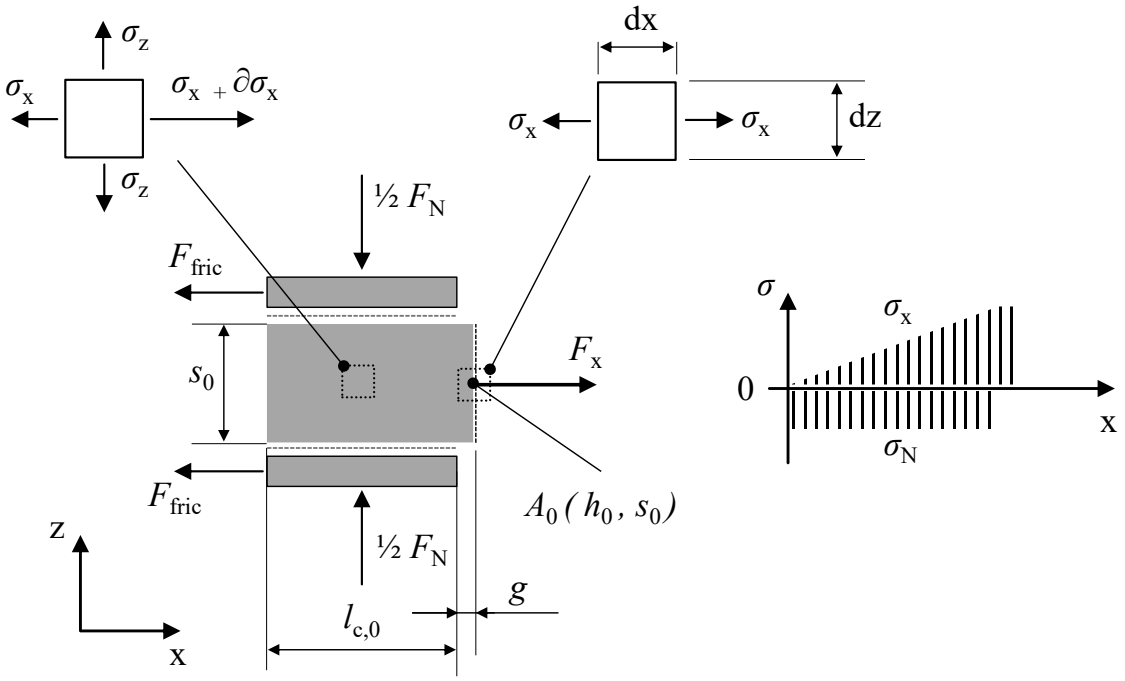

Figure 10: Mechanical representation of tensile elastic forming under frictional engagement. Annotations of dimensions and forces of the interaction of the strip material and the die faces of the clamping tools. Elementary stress states at three distinct regions. Longitudinal distribution of the multiaxial stress state (right).

The linear movement of the tools causes traction on the upper and lower material surfaces. Correspondingly, the friction forces F_{fric} result at the tools. Regarding the material's cross section A, the material deformation causes the longitudinal forming force F_x which is opposed to these friction forces. For mechanical equilibrium, the friction forces F_{fric} are kept equal to F_x. Within the area of traction, the friction shear stress τ_{fric} builds up longitudinally with a linear function causing longitudinal stress σ_x to follow a corresponding trend within the material. In multiaxial state, both

stresses, σ_N and σ_x, add up to equivalent stress. At a certain point, longitudinal drawing force would cause equivalent stress to reach the materials yield criterion at the foremost point of contact. Equivalent stress σ_{eq} is expressed according to v. MISES' principal plane stress relation (Mises 1913). In the case of elastic deformation, the forming zone is still under the influence of the clamping force, and F_x is obtained by propagating σ_{eq} over the initial cross section of the material A_0. F_x follows the relation

$$\begin{aligned} F_x = \sigma_{eq} \cdot A_0 &= \sqrt{\frac{1}{2}\left(\left(\sigma_x - \sigma_y\right)^2 + \left(\sigma_y - \sigma_z\right)^2 + (\sigma_x - \sigma_z)^2\right)} \cdot A_0 \\ &= \sqrt{\frac{1}{2}\left(2{\sigma_x}^2 + 2{\sigma_z}^2 - 2\sigma_x\sigma_z\right)} \cdot A_0 \\ &= \sqrt{\left({\sigma_x}^2 + {\sigma_z}^2 - \sigma_x\sigma_z\right)} \cdot A_0 \stackrel{!}{=} 2 \cdot F_{\text{fric}} = 2 \cdot \mu \cdot \frac{F_N}{2} \end{aligned} \qquad \text{(eq. 25)}$$

The yield criterion is reached, if σ_{eq} equals yield stress R_e. Thus, a lower drawing force F_x is required if a higher clamping Force F_N is applied. Note from Figure 10, that the yield criterion might be located eccentrically from the process symmetry plane if any gap g is in between the forming tools. It is assumed by the model, that any transversal elastic contractions of the initial cross section A_0 are negligible.

Elastic strain ε_{el} at material's yield criterion is expressed by

$$\varepsilon_{\text{el}} = \frac{\sigma_x}{E} \qquad \text{(eq. 26)}$$

taking YOUNG's Modulus of elasticity E into account.

4.1.2 Tensile plastic forming

The calculation of longitudinal strain φ_x is assumed by the ratio of tool stroke Δl to the length of lost clamping contact $l_{c,0} - l_{c,1}$, which represents the area of material that has been plastically deformed. For tensile forming, longitudinal true strain is expressed as

$$\varphi_x = \ln\left(\frac{\Delta l}{l_{c,0} - l_{c,1}} + 1\right). \qquad \text{(eq. 27)}$$

Equation (27) assumes a constant longitudinal strain distribution over the length of the clamping tools without any gradient. Hence longitudinal strain is averaged. Transversal strains in the directions of thickness and profile height are assumed to relate to uniaxial tension in the free length:

$$\varphi_y = \varphi_z = -\frac{1}{2}\varphi_x \,. \qquad \text{(eq. 28)}$$

Lateral strains cause the deformed cross section of the material A_1 which is expressed by thickness s_1 after plastic deformation and profile heigth h_1 after plastic deformation. During the advancing tool stroke, F_x causes equivalent stress to overcome the material's yield criterion and plastic flow sets in. Because of transversal plastic strain through thickness, i.e., thinning, contact to the clamping tools is lost within the forming zone because thinning draws material from the die faces, cf. Figure 11. If shear stress over the material thickness s_0 is neglected, uniaxial forming conditions are assumed within the forming zone.

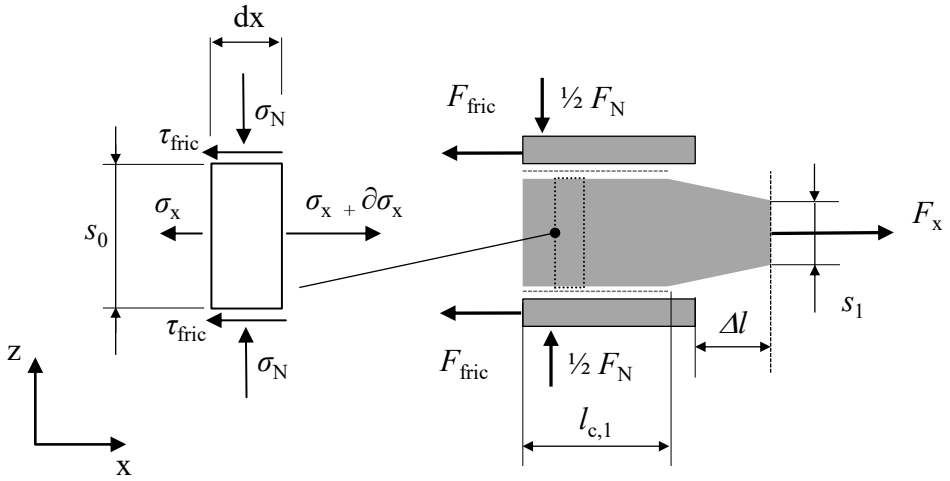

Figure 11: Mechanic process representation during plastic material flow. If yield criterion is exceeded, plastic tensile forming causes material being pulled out of the clamping and traction between tool and material is lost due to thinning.

Like in elastic tensile forming, the equilibrium of forces in longitudinal (x-) direction is valid during plastic deformation. Friction shear stress τ_{fric} is expressed by

$$\tau_{fric} = \mu_0 \cdot \sigma_{N,0} \qquad \text{(eq. 29)}$$

when applying Coulomb's friction law to stresses according to KÖNIG (2013) and using the static coefficient of friction μ_0 since material sliding under the clamping tools must be avoided for a well-defined operation of an ISB process. If large portions of material are pulled out of the clamping zones, severe normal pressure results which leads to very high friction shear stress τ_{fric}. If τ_{fric} exceeds

ultimate shear stress, Coulomb's friction law loses validity, cf. DOEGE and BEHRENS (2007). Therefore, the friction factor model limits τ_{fric} according to

$$\tau_{\mathrm{fric,max}} = m_{\mathrm{ff}} \cdot \frac{k_f}{\sqrt{3}}, \text{ for static friction } m_{\mathrm{ff}} = 1. \qquad \text{(eq. 30)}$$

During plastic material deformation, the forming resistance of the free cross section in between tools is expressed by work hardening stress k_{f} with the corresponding forming force F_{x}. In contrast to the elastic forming under multiaxial stress, the deformed cross section A_1 experiences uniaxial tensile deformation due to the loss of contact to the forming tools (see Figure 11). Unlike the elastic relation described in eq. (25) , F_{x} becomes

$$F_{\mathrm{x}} = k_{\mathrm{f}} \cdot A_1 = k_{\mathrm{f}} \cdot A_0 \cdot \mathrm{e}^{-\varphi_{\mathrm{x}}} . \qquad \text{(eq. 31)}$$

For a stable and defined process operation, traction should remain in the clamped area and the frictionally engaged process is hence assumed valid in this case. The clamped region is sharply distinguished from the area, where material thinning has led to free plastic deformation without any contact to tools. As no smooth transition is assumed, an unambiguous location in the form of a lateral line where material begins to plasticize is expected. This border is specifically subjected to the material yield criterion and agrees with the edge of the forming zone neglecting tool tilting and transverse elastic strain. During the advancing process, this line shifts through the clamped areas as material detaches from the die faces due to plastic thinning. This effect has been observed by previous studies on tensile stretching under contact pressure, cf. (Sengupta, Fogg, and Ghosh 1981; Staeves 1998), and is denoted as yield sheath in the remainder of this thesis. In the continuously shrinking clamping area, normal pressure $\sigma_{\mathrm{N,1}}$ rises proportionally to the reduction of clamping length $l_{\mathrm{c,1}}$, see Figure 12.

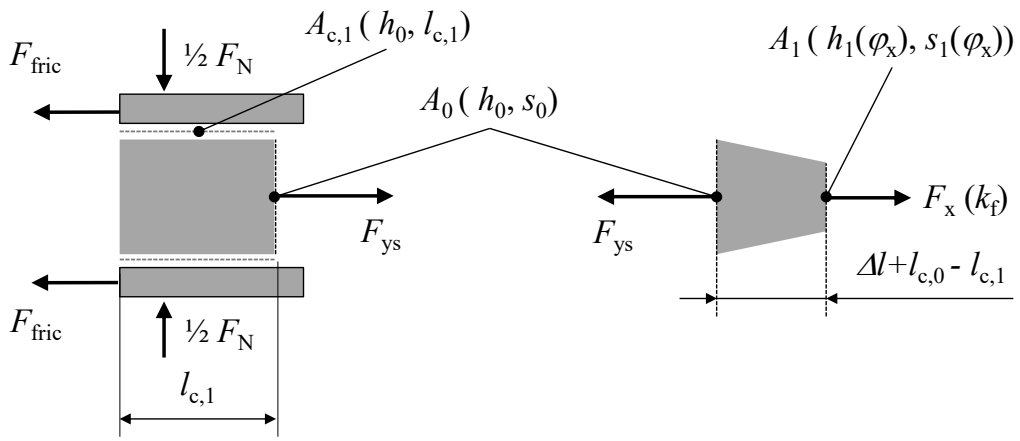

Figure 12: Mechanic representation of frictionally engaged tensile forming during plasticizing. Cut view through the location referred to as yield sheath where yield criterion applies, and which determines the boundary of the forming zone.

The friction shear stress τ_{fric} is transmitted by the die faces and increases in longitudinal direction up to the yield sheath. Throughout the process, equivalent stress σ_{eq} changes in the yield sheath because σ_N changes according to the actual clamping area $A_{c,1}$. Neglecting elastic deformation, the sheath is propagated on the initial cross section of the strip material A_0. The corresponding longitudinal force at the yield sheath F_{ys} is derived from longitudinal stress σ_x according to

$$\frac{F_{ys}}{A_0} = \sigma_x \qquad \text{(eq. 32)}$$

where σ_x is contained within the generalized formulation of v. MISES multiaxial stress relation. Equivalent stress σ_{eq} follows the relation

$$\sigma_{eq} = \sqrt{\frac{1}{2}\left(\left(\sigma_x - \sigma_y\right)^2 + \left(\sigma_y - \sigma_z\right)^2 + (\sigma_x - \sigma_z)^2\right) + 3\left(\sigma_{xy}{}^2 + \sigma_{yz}{}^2 + \sigma_{zx}{}^2\right)}. \qquad \text{(eq. 33)}$$

Applying the elementary stress relation from the cutaway view in Figure 11, the relation becomes

$$\sigma_{eq} = \sqrt{\frac{1}{2}\left(2\sigma_x{}^2 + 2\sigma_N{}^2 - 2\sigma_x\sigma_N\right) + 3 \cdot \tau_{fric}{}^2} = \sqrt{\sigma_x{}^2 + \sigma_N{}^2 - \sigma_x\sigma_N + 3 \cdot \tau_{fric}{}^2}\,. \qquad \text{(eq. 34)}$$

The contact normal force has two counteracting effects on the process, it would lower the required longitudinal stress within the yield criterion, so material starts easier to flow plastically. Conversely, it would cause higher transferrable friction shear stress (cf. eq. 29) so fewer material is drawn into

the forming zone. As the latter effect is assumed to be of higher relevance, the influence of σ_N on the yield criterion is neglected.

In this thesis, the following mathematical description of longitudinal stress σ_x in the yield sheath has proven sufficient for process modelling of frictionally engaged forming:

$$\sqrt{{R_e}^2 - 3 \cdot {\tau_{fric}}^2} = \sigma_x \,. \qquad \text{(eq. 35)}$$

The location of yield criterion corresponds to the remaining clamping length $l_{c,1}$ with regard to the clamping tools. Beyond the yield sheath, tensile stretching causes the material's transversal contractions over height and thickness, represented by the plastically deformed cross section A_1. In consequence of the mechanical representation according to Figure 12, equilibrium of all longitudinal forces is postulated:

$$\begin{aligned} F_x &\overset{!}{=} F_{YS} \overset{!}{=} 2F_{fric} \\ \Longrightarrow k_f \cdot A_0 \cdot e^{-\varphi_x} &= \sigma_x \cdot A_0 = 2F_{fric} \end{aligned} \qquad \text{(eq. 36)}$$

With $\tau_{fric} = \mu_0 \cdot \sigma_{N,1}$ and $\sigma_{N,1} = \frac{-F_N}{l_{c,1} \cdot h_0}$, eq. (36) becomes

$$k_f \cdot A_0 \cdot e^{-\varphi_x} = \sqrt{{R_e}^2 - 3\left(\mu_0 \cdot \frac{-F_N}{l_{c,1} \cdot h_0}\right)^2} \cdot A_0 = 2F_{fric} \,. \qquad \text{(eq. 37)}$$

The clamping force F_N is implemented with negative algebraic sign due to compression. Equation (36) connects the geometry and the mechanic parameters of the material to the process parameters to obtain true strain of frictionally engaged tensile forming. Analytically, according to eq. (27), strain needs to be solved by means of the unknown variable of remaining contact length, $l_{c,1}$.

Derivation of the mathematical model of the forming zone for linear plastic forming

Two simplifications are required to solve the equations for l_{c1}, which delivers the size of the forming zone and, in consequence, its longitudinal strain.

1) Due to the square rooted formulation, F_{YS} leads to equations of fourth order, which cannot be solved in a purely analytic approach. Hence, it is approximated according to

$$F_{\mathrm{ys}} = \sqrt{\left({R_{\mathrm{e}}}^2 - 3 \cdot {\tau_{\mathrm{fric}}}^2\right)} \cdot A_0 \approx \left(R_{\mathrm{e}} - \frac{\tau_{\mathrm{fric}}}{\sqrt{3}}\right) \cdot A_0 = \sigma_{eq} \cdot A_0 \qquad \text{(eq. 38)}$$

2) The bilinear hardening law is applied for k_{f} to be solved analytically.

The simplified equilibrium of longitudinal forces follows

$$F_{\mathrm{x}} \stackrel{!}{=} F_{\mathrm{YS}} \stackrel{!}{=} 2F_{fric}$$

$$\Longrightarrow \left(R_e + m \cdot \varepsilon_x - m \cdot \frac{R_e}{E}\right) \cdot A_0 \cdot \frac{1}{\varepsilon_x + 1} = R_{\mathrm{e}} - \frac{-\left(\frac{\mu_0 \cdot F_{\mathrm{N}}}{l_{\mathrm{c},1} \cdot h_0}\right)}{\sqrt{3}} \cdot A_0 = 2F_{fric} \qquad \text{(eq. 39)}$$

where $(\varepsilon_{\mathrm{x}} + 1)^{-1}$ expresses $\mathrm{e}^{-\varphi_{\mathrm{x}}}$.

$$\Longrightarrow \left(R_e + m \cdot \varepsilon_x - m \cdot \frac{R_e}{E}\right) \cdot \frac{1}{\varepsilon_x + 1} = R_{\mathrm{e}} + \frac{\left(\frac{\mu_0 \cdot F_{\mathrm{N}}}{l_{\mathrm{c},1} \cdot h_0}\right)}{\sqrt{3}}$$

$$\Leftrightarrow R_e + m \cdot \varepsilon_x - m \cdot \frac{R_e}{E} = \left(R_{\mathrm{e}} + \frac{\left(\frac{\mu_0 \cdot F_{\mathrm{N}}}{l_{\mathrm{c},1} \cdot h_0}\right)}{\sqrt{3}}\right)(\varepsilon_x + 1)$$

$$\Leftrightarrow R_e + m \cdot \varepsilon_x - m \cdot \frac{R_e}{E} = R_{\mathrm{e}} \cdot \varepsilon_x + R_{\mathrm{e}} + \frac{\left(\frac{\mu_0 \cdot F_{\mathrm{N}}}{l_{\mathrm{c},1} \cdot h_0}\right)}{\sqrt{3}} \varepsilon_x + \frac{\left(\frac{\mu_0 \cdot F_{\mathrm{N}}}{l_{\mathrm{c},1} \cdot h_0}\right)}{\sqrt{3}}$$

$$\Leftrightarrow \varepsilon_x \left(m - R_{\mathrm{e}} - \frac{\left(\frac{\mu_0 \cdot F_{\mathrm{N}}}{l_{\mathrm{c},1} \cdot h_0}\right)}{\sqrt{3}}\right) = m \cdot \frac{R_e}{E} + \frac{\left(\frac{\mu_0 \cdot F_{\mathrm{N}}}{l_{\mathrm{c},1} \cdot h_0}\right)}{\sqrt{3}}$$

with $\varepsilon_x = \frac{\Delta l}{l_{\mathrm{c},0} - l_{\mathrm{c},1}}$,

$$\frac{\Delta l}{l_{\mathrm{c},0} - l_{\mathrm{c},1}} \left(m - R_e - \frac{\mu_0 \cdot F_{\mathrm{N}}}{\sqrt{3} \cdot l_{\mathrm{c},1} \cdot h_0}\right) = m \cdot \frac{R_e}{E} + \frac{\mu_0 \cdot F_{\mathrm{N}}}{\sqrt{3} \cdot l_{\mathrm{c},1} \cdot h_0}$$

$$\frac{\Delta l}{l_{\mathrm{c},0} - l_{\mathrm{c},1}} \cdot m - \frac{\Delta l}{l_{\mathrm{c},0} - l_{\mathrm{c},1}} \cdot R_e - \frac{\Delta l}{l_{\mathrm{c},0} - l_{\mathrm{c},1}} \cdot \frac{\mu_0 \cdot F_{\mathrm{N}}}{\sqrt{3} \cdot l_{\mathrm{c},1} \cdot h_0} = m \cdot \frac{R_e}{E} + \frac{\mu_0 \cdot F_{\mathrm{N}}}{\sqrt{3} \cdot l_{\mathrm{c},1} \cdot h_0}$$

$$m - R_e - \frac{\mu_0 \cdot F_{\mathrm{N}}}{\sqrt{3} \cdot l_{\mathrm{c},1} \cdot h_0} = \left(l_{\mathrm{c},0} - l_{\mathrm{c},1}\right) \cdot \frac{m \cdot R_e}{\Delta l \cdot E} + \left(l_{\mathrm{c},0} - l_{\mathrm{c},1}\right) \cdot \frac{\mu_0 \cdot F_{\mathrm{N}}}{\sqrt{3} \cdot l_{\mathrm{c},1} \cdot h_0 \cdot \Delta l}$$

$$l_{\mathrm{c},1} \cdot \sqrt{3} \cdot h_0 \cdot (m - R_e) - \mu_0 \cdot F_{\mathrm{N}} = \left(l_{\mathrm{c},0} - l_{\mathrm{c},1}\right) \cdot l_{\mathrm{c},1} \cdot \frac{\sqrt{3} \cdot h_0 \cdot m \cdot R_e}{\Delta l \cdot E} + \left(l_{\mathrm{c},0} - l_{\mathrm{c},1}\right) \cdot \frac{\mu_0 \cdot F_{\mathrm{N}}}{\Delta l}$$

$$l_{c,1} \cdot \sqrt{3} \cdot h_0 \cdot (m - R_e) - (l_{c,0} - l_{c,1}) \cdot l_{c,1} \cdot \frac{\sqrt{3} \cdot h_0 \cdot m \cdot R_e}{\Delta l \cdot E} - (l_{c,0} - l_{c,1}) \cdot \frac{\mu_0 \cdot F_N}{\Delta l} = \mu_0 \cdot F_N$$

$$l_{c,1}{}^2 \cdot \frac{\sqrt{3} \cdot h_0 \cdot m \cdot R_e}{\Delta l \cdot E} + l_{c,1} \left(\sqrt{3} \cdot h_0 \cdot (m - R_e) + \frac{\mu_0 \cdot F_N}{\Delta l} - l_{c,0} \cdot \frac{\sqrt{3} \cdot h_0 \cdot m \cdot R_e}{\Delta l \cdot E} \right) = \mu_0 \cdot F_N \left(1 + \frac{l_{c,0}}{\Delta l} \right)$$

$$l_{c,1}{}^2 + l_{c,1} \left(\Delta l \cdot E \cdot \frac{(m + R_e)}{m \cdot R_e} - l_{c,0} + \frac{\mu_0 \cdot F_N \cdot E}{\sqrt{3} \cdot h_0 \cdot m \cdot R_e} \right) - \left(1 + \frac{l_{c,0}}{\Delta l} \right) \cdot \Delta l \cdot \frac{\mu_0 \cdot F_N \cdot E}{\sqrt{3} \cdot h_0 \cdot m \cdot R_e} = 0$$

$$\Rightarrow l_{c,1,1/2} = -\frac{\Delta l \cdot E \cdot \frac{(m + R_e)}{m \cdot R_e} - l_{c,0} + \frac{\mu_0 \cdot F_N \cdot E}{\sqrt{3} \cdot h_0 \cdot m \cdot R_e}}{2} \pm \sqrt{\left(\frac{\Delta l \cdot E \cdot \frac{(m + R_e)}{m \cdot R_e} - l_{c,0} + \frac{\mu_0 \cdot F_N \cdot E}{\sqrt{3} \cdot h_0 \cdot m \cdot R_e}}{2} \right)^2 + \left(1 + \frac{l_{c,0}}{\Delta l} \right) \cdot \Delta l \cdot \frac{\mu_0 \cdot F_N \cdot E}{\sqrt{3} \cdot h_0 \cdot m \cdot R_e}} \quad \text{(eq. 40)}$$

With regard to the forming process, reasonable results are obtained for $l_{c,1,1}$, i.e., positive algebraic sign in front of the square root of eq. (40). Under a given load F_N, the remaining clamping length $l_{c,1}$ is obtained depending on the stroke of tools. Strain is expressed by the strain assumption of eq. (27) by incorporating $l_{c,1}$. The above presented model determines the material portion being pulled-out in a tensile forming process under frictional engagement. For validation by numerical and practical experiments, the material properties used in the equations above need to be identified firstly.

4.2 Mechanical material characterization

The mechanical properties of the materials considered in this thesis, as presented in Table 1, section 2.4.5, are determined in the following subsections to allow their implementation in process models.

4.2.1 Tensile material properties

Uniaxial tensile tests were conducted according to DIN EN ISO 6892-1 on the institute's ZWICK/ROELL Z250 universal testing machine to mechanically characterize the sheet metal materials HCT780X, 22MnB5, 42SiCr, and FORTA H800. Flat dumbbell-shaped specimens with a gauge length of L_0 = 80 mm were manufactured by milling as defined in the technical standard DIN 50125 (specimen shape H). The machine is equipped with a type K load cell GTM GASSMANN THEISS MESSTECHNIK to capture force during the tensile test. The sensor features a nominal load capacity of 250 kN and an accuracy class of 0.02 %, which corresponds to a maximum measurement error of the

nominal load ≤ 50 N. Besides measuring displacement of the crossbeam, strain is captured by an optical extensometer provided by MESSPHYSIK MATERIAL TESTING. In order to exclude any stiffness or gap influenced by the machine's assembly, the extensometer measures strain locally at the specimen's gauge length.

Engineering stress σ is calculated from the force signal of the tensile tests set into relation to the initial cross section A_0 of the parallel length of the specimen so that stress-strain diagrams of the materials are obtained. The tensile mechanical parameters presented in Table 3 were evaluated from these curves, each for four tests repetitions. In the stress-strain relation, the maximum of the experimental force signal F_{max} determines both, ultimate tensile stress R_m as well as uniform tensile elongation A_G (i.e., strain without necking). Written as true, i.e., logarithmic, strain, A_G represents the material's hardening exponent n as long as the uniaxial stress relation remains valid. Furthermore, the approximation of an ideal linear behavior in the initial elastic part of the measured curves delivers Young's Modulus of elasticity E. Assuming linear elastic springback according to E allows to derive stress $R_{p0.2}$, which prevails at the elastic-plastic transition at 0.2 % of plastic strain.

Table 3: Mechanical material parameters (0.2% offset yield strength $R_{p0,2}$ or upper yield strength R_{eH} if materials revealed LÜDERS strain; ultimate tensile strength R_m; hardening exponent n; ultimate strain ε_f; Young's Modulus E) obtained from uniaxial tensile tests. From the repetitions of each value, the intervals of 95% confidence are calculated.

Material	s_0	$R_{p0,2}$	R_{eH}	R_m	n	ε_f	E
	[mm]	[MPa]	[MPa]	[MPa]	[-]	[%]	[GPa]
HCT780X	1.0	487 ± 7	-	774 ± 4	0.124 ± 0.002	19 ± 0.4	215.2 ± 0.3
22MnB5	1.4	-	339 ± 5	509 ± 7	0.113 ± 0.008	22 ± 0.3	207.3 ± 0.4
42SiCr	2.0	-	477 ± 10	664 ± 21	0.160 ± 0.004	27 ± 1	202.4 ± 0.1
S235JR	2.0	201 ± 1	-	319 ± 0.5	0.201 ± 0.002	38 ± 0.5	-
H800	2.0	734 ± 20	-	975 ± 1	0.262 ± 0.009	38 ± 2	195.9 ± 0.2

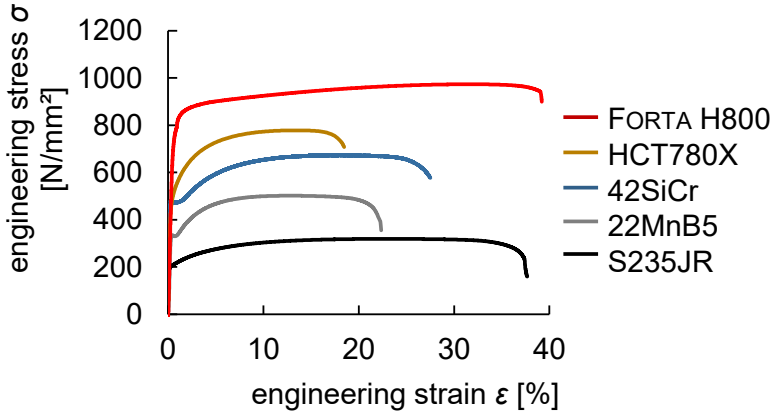

Figure 13: Stress-strain curves of the materials utilized in the present thesis.

Figure 13 shows the stress-strain curves of all materials, which have been selected to cover a diverse range of strength and ductility. In the case of the uniaxial tensile test, equivalent strain is equal to longitudinal strain due to the experiment's ratio of minor to major strain $\rho = -0.5$. According to GHOSH (1974) this assumption applies in the area of plastic elongation without necking. True stress *kf* is obtained when the measured force signal is referred to the effective cross section of the specimen, which is calculated from the law of volume constancy under assumption of a constant strain ratio ρ. Thus, the measured hardening curves are valid during uniform tensile elongation before necking.
When evaluated from the tensile tests according to DIN EN ISO 6892-1 appendix G, YOUNG's Modulus of elasticity shows a considerable scatter. Because E is implemented in the analytic models of this thesis as an important material parameter, it was determined by the method of dynamic excitation according to the technical standard ASTM E 1876. The experiments were conducted externally at the CHAIR OF METALFORMING AND CASTING (UTG) in Munich. S235JR is only used in analytical – numerical comparisons. Keeping aforementioned reason in view and also the fact that S235JR is the lowest alloyed material presented above, a standard modulus of elasticity of 210 GPa was considered.

4.2.2 Mechanical material approximation

For analytical and numerical material models, work hardening properties are described by mathematical relations for true stress over true equivalent strain. The uniaxial tensile tests of the materials considered in the present study are mechanically approximated by two common exponential approaches, namely LUDWIK / HOLLOMON (Hollomon 1945) and SWIFT (Swift 1952). The coefficients of these models are usually evaluated by empirical approaches, e.g., best fitting. Because this thesis aims for self-containing analytic expressions, the parameter determination methods according to STEINHEIMER (2005) are utilized. He derived equations to calculate the hardening curves based on the mechanic material parameters shown in Table 3. A (bi-)linear hardening law is employed alongside the models of LUDWIK / HOLLOMON and SWIFT because it allows mathematical integration. The bilinear model presented by GERLACH (2010) consists of a linear-elastic and a linear-plastic part. The first follows the incline of constant Young's Modulus E up to yield stress $R_{p0.2}$ or R_{eH}, while the second part reaches from yield stress to true stress k_f at uniform tensile elongation A_G. For all materials considered in the present thesis, the hardening curves resulting from uniaxial tensile tests are compared to the modelling approaches of LUDWIK / HOLLOMON, SWIFT and the bilinear approach in Figure 14.

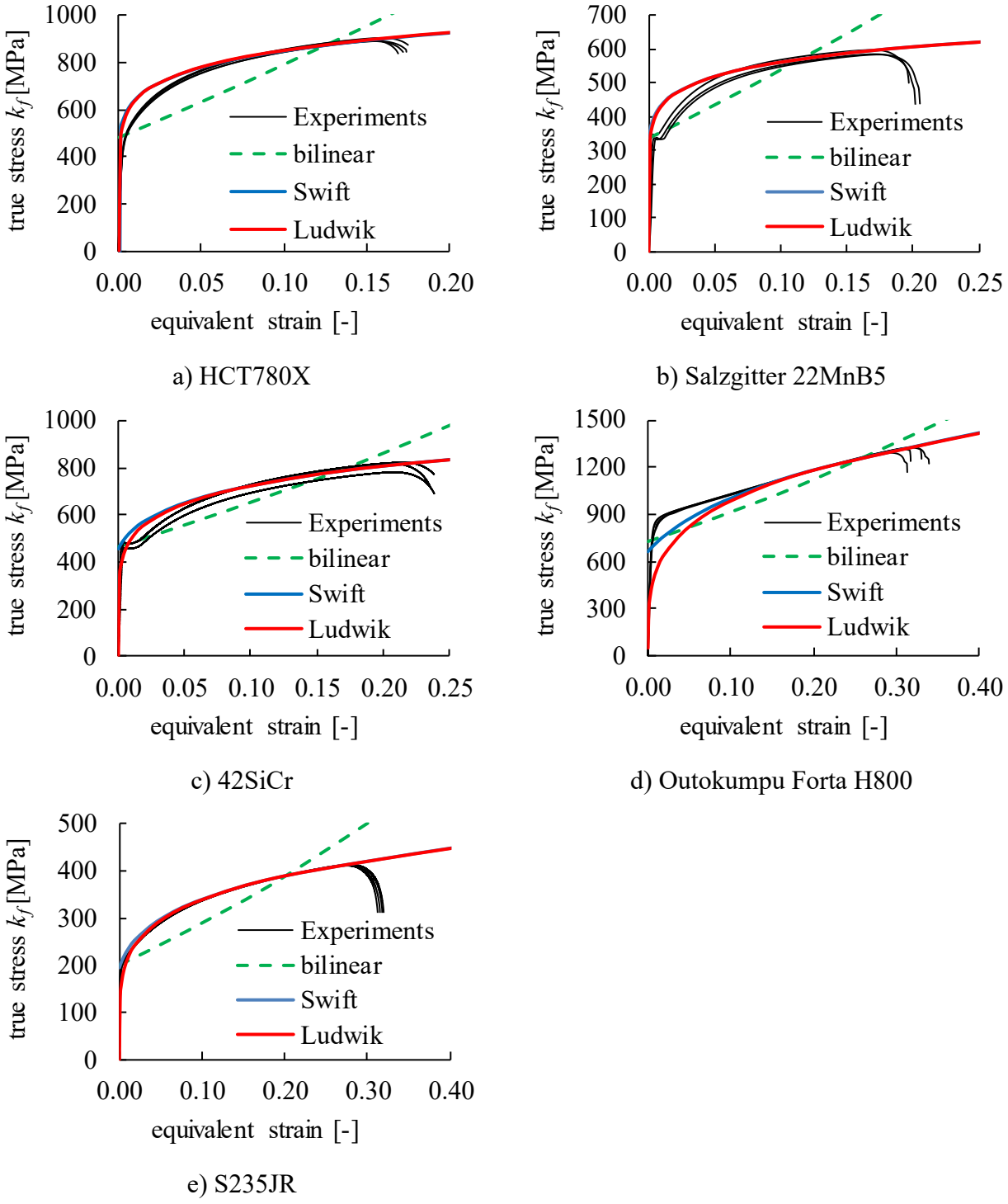

Figure 14: Experimentally determined hardening curves compared to bilinear, SWIFT's and LUDWIK / HOLLOMON's approximations for a) HCT780X, b) 22MnB5, c) 42SiCr, d) H800, e) S235JR. The coefficients utilized for the hardening curves are given in the Appendix, Table 27.

At uniform tensile elongation, the flow curve approximations predict the value of true stress precisely for all materials. Deviations are observed in particular for lower strain values. Evidently, the bilinear approach underestimates the hardening curves in this area because the linear mathematical equation cannot resemble any non-linear behavior of the experimental curves. Modelling accuracy and error hence strongly depend on the determination of the elastic-plastic transition at yield stress where the

first supporting point of the bilinear model is located. The exponential approaches achieve the best approximation in the case of S235JR. For 42SiCr and 22MnB5, deviations in the initial part of the hardening curves are caused by characteristic LÜDER's strain, which is not incorporated in the modelling approaches. Again, in the area of lower strain values, both exponential models overestimate the hardening curve in the case of HCT780X while they undersize FORTA H800. In between LUDWIK / HOLLOMON's and SWIFT, significant differences are only observed in the case of H800. The coarse elastic-plastic transition of the material results from preceding work hardening by cold rolling and cannot be captured by the equation of the LUDWIK / HOLLOMON law.

4.3 FE-simulations of frictionally engaged forming

A plane tensile stretching process represents the simplest form of force-fitted transmission of forming forces because it delivers a constant strain condition over width. In-plane bending, such as the ISB process, it adds up a lateral variation of strain and, thus, an angular forming zone. The analytical model suggested in 4.1 describes the evolution of the forming zone in such a stretching process with respect to tool stroke. A corresponding simulation model for tensile forming of plane strip materials under frictional engagement is introduced to validate the analytical model of section 4.1. The simulation is numerically calculated by the finite elements method (FEM) in the software PAM STAMP.

In order to provoke a constant tensile stress distribution within the rectangular cross section, two tool units move apart while they clamp the material under a constant load F_N. The material is discretized by solid finite elements with a material magnitude of 7 elements over thickness while the clamping tools are represented by rigid shells. According to Figure 15, the finite element (FE-) simulation is divided by two symmetry planes (lateral y-z plane; longitudinal x-z plane).

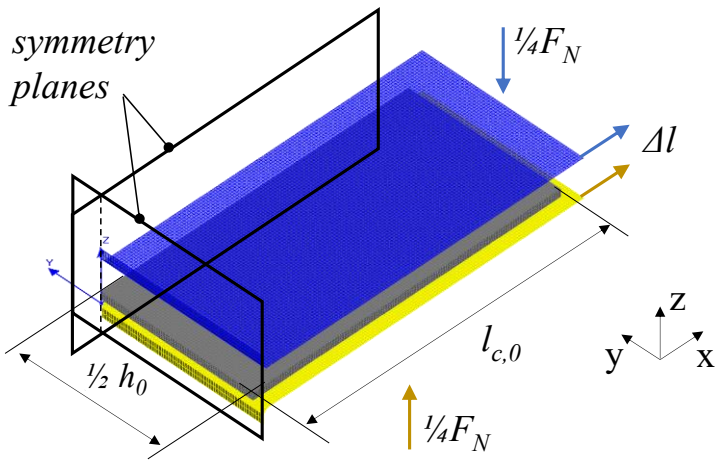

Figure 15: Finite element model of linear tensile forming. Evaluation of the relationship of the forming zone and the applied mechanical material parameters and process variables.

The process is represented by three explicit stages in the numerical model:

1) Initially, the tool is loaded by the clamping force ¼ F_N because of symmetry conditions.
2) Elastic forming is simulated with high state resolution to allow for the evaluation of yield criterion with respect to stroke Δl, drawing force F_{fric} and frictional shear stress τ_{fric}.
3) The third stage continues with stretching for evaluation of plastic deformation and ends by reaching a certain stroke Δl as stop criterion.

A variation of materials and clamping forces is implemented in the simulation to validate the analytic model with respect to process forces, as summarized in Table 4.

Table 4: Variation of materials and clamping force studied in the models (analytical, numerical) of frictionally engaged stretching. Indication of least necessary clamping force $F_{N,min}$ to prevent material slipping at uniform tensile elongation.

Material	$\boldsymbol{F_N}$ [kN]	$\boldsymbol{F_{N,min}}$ [kN]	case
S235JR	500; 1000; 3000	424	a), b), c)
HCT780X	900; 3000; 6000	774	d), e), f)
42SiCr	1500; 3000; 6000	885	g), h), i)
FORTA H800	1500; 3000; 6000	1373	j), k), l)

The simulations were parametrized with a uniform friction coefficient of $\mu = 0.12$ and material cross sections of 2 x 80 mm to test the model's sensitivity towards the influence of the mechanical material parameters and the clamping force. The material coefficients are assumed according to the material tests of this thesis. Derived from these specifications, Table 4 delivers the least necessary clamping force $F_{N,min}$ to transmit the forming force by the law of COULOMB, which is required for reaching uniform tensile elongation of each respective material according to

$$2\mu \cdot \frac{F_{N,min}}{2} = F_x \Leftrightarrow F_{N,min} = \frac{R_m \cdot A_0}{\mu}. \qquad \text{(eq. 41)}$$

The qualitative evolution of the forming zone is crucial for understanding the relation of strain in force-fitted forming processes. For this purpose, the material portion pulled out of the clamping is represented by $l_{c,1}$, i.e., the clamping length which remains in contact to tools. $l_{c,1}$ is studied as a function of tool stroke Δl in between the predictions of the analytic model and the results of the simulations. Each process configuration according to Table 4 is displayed in Figure 16.

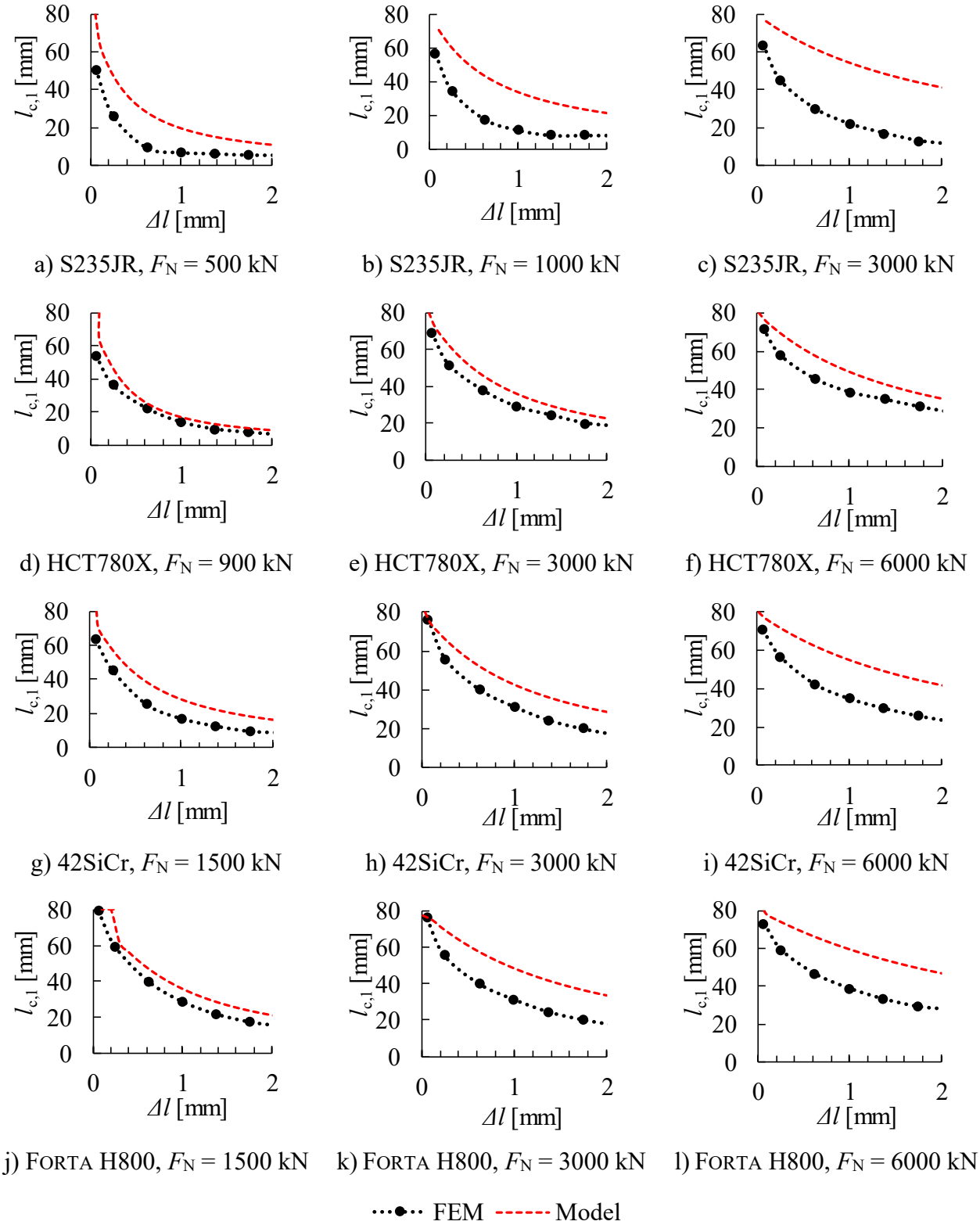

Figure 16: Longitudinal size of forming zone over tool stroke Δl of a linear tensile stretching process with force-fitted transmission of forming. For four different materials, the size of the clamping length $l_{c,1}$, which remains under surface contact, is evaluated for three different clamping load stages F_N.

Figure 16 shows the results of the parameter variation for a plane stretching process. The analytical predictions of the forming zone agree to the simulated trends under qualitative considerations: The

forming zone strongly decreases in the beginning while the loss of contact surface decelerates with higher values of tool stroke Δl. In addition, smaller forming zones are detected for higher clamping loads and for stronger materials, as in these cases less material is drawn out of the clamped area. Quantitatively, a better modelling compliance is achieved for the stronger materials (HCT780X, 42SiCr and H800) than for the very soft S235JR. In addition, very high clamping forces F_N, in relation to the least necessary load $F_{N,min}$, also lead to larger deviations between the analytical model and the simulations, which increase towards larger values of Δl. Both observed deviations are explained by the onset of bulk forming effects where contact pressure localizations begin to severely compress the material within the remaining clamped length $l_{c,1}$.

4.4 Characterization of relevant tribological zones

For the comparison of practical experiments with the herein developed processes models, the mechanisms of the surface interactions under friction are required since the forming force is transmitted under traction. Under tribological considerations, the characterization of the tool and material surfaces in contact is crucial to predict the effect on the material and its geometry in a comprehensible way. In an ISB process, dry friction without lubrication is preferred as the forming force can be transmitted in a more efficient way because of the process' underlying force-fitted principle. In the present study, tools and sheet metal materials are analyzed with respect to surfaces, coatings and topography, while their interaction in contact is quantified by friction coefficients. Particularly, static friction coefficients are required to describe ISB as no relative movements between tools and materials is postulated in the area of firm clamping. Moreover, the preceding simulations demonstrate that plastic deformation under traction requires high clamping forces F_N. Considerable normal pressure σ_N results in the contact area, and additionally rises drastically over progression because the initial contact surface is reduced continuously as material gets drawn out of the clamping. Depending on the combination of tool and material, σ_N changes drastically over progression and likely ranges up to 100 MPa, which must be considered when describing the surface interactions by friction coefficients. To evaluate the dry friction behavior of the investigated sheet metal materials, two test facilities have been utilized which differ by the type of tools used and thus provide diverse regions of applicable pressure. At UTS, planar rectangular tools are used for the characterization of friction at low pressure regions while at the CHAIR OF METAL FORMING AT THE MONTANUNIVERSITY LEOBEN short contact lengths allow testing friction at high contact pressures. Both test assemblies revealed distinct, legitimate areas of pressure application, which is why they are combined in this investigation to cover up the contact pressures which are observed in the ISB process.

4.4.1 Tool manufacture

Various friction tools were manufactured from specific tool steels according to the planned surface coating. Table 5 gives an overview of the herein utilized tools.

Table 5: Materials, manufacturing parameters and surface treatments of the friction tools used in this study.

steel	alloy	machining	heat treatment	hardness [HRC]	surface treatment	layer
1.2312	40CrMnMoS8-6	grinding			TENIFER (nitro carburizing)	oxide
1.2379	X155CrVMo12-1	polishing	case hardening	57	plasma nitriding	none
1.2379	X155CrVMo12-1	polishing	case hardening	57	PVD	AlTiN
1.2379	X155CrVMo12-1	fine grinding	case hardening	57.5	PACVD	TiN

Nitro-carburation is a widely spread surface treatment technique for forming tools (Kurz 1970). The friction jaws of this thesis were treated in the TENIFER process, where nitro-carburation is applied by a salt bath (Liedtke et al. 2018). This process is often combined with surface oxidation to achieve the growth of a stable, wear reducing coat of oxide at the treated surface (Marušić et al. 2006). Two pairs of friction tools were polished and plasma nitrided, also representing a standard procedure in forming, especially in deep-drawing processes. Additionally, one pair of these tools was duplex coated by aluminum titanium nitride by the method of physical vapor deposition (PVD-AlTiN). This coating method is well-known to reduce metallic adhesion tendencies in cold forming processes (Navinšek, Panjan, and Milošev 1997). Titanium nitride, TiN, is a coating system, that is especially suitable for dry friction (Stoiber et al. 2003; Vollertsen and Schmidt 2014). In the case of the friction jaws, which have been coated for this thesis, TiN was applied plasma assisted as a chemically deposited vapor (PACVD). For this purpose, these tools have been initially case hardened to a ROCKWELL hardness (HRC) of 57.5, based on a 1.2379 tool steel. All these coatings aim for wear resistance in dry friction under elevated contact pressure. Surfaces meant to specifically deliver higher friction coefficients, e.g., knurled as applied to clamping tools by HINKEL (2013) or tungsten carbide coatings, are promising to improve the efficiency of the ISB process with regard to the required clamping force to ensure traction. These are, however, out of scope of this thesis to keep the focus on dry friction with smooth, conventional surfaces, but will be addressed in future studies.

4.4.2 Evaluation of surface topography

In manufacturing regimes, the contact surfaces of the tools and the processed material belong to a tribological system. The topography of these surfaces can be characterized quantitatively with respect to roughness and qualitatively with respect to height distribution. The combination of the hardness and surfaces of both contact partners as well as the applied pressure would define the effective area of contact, which is in general fewer, than the geometrical surface (Müller 2013). Next to contactless tests, e.g., microscopy scans, a tactile surface profile gauge evaluates the surfaces by means of line samples. A needle is mounted at the tip of a sensing device and scratches over the specimen surface. During this procedure, the device records the profile of amplitude over displacement. In the present thesis, a Mitutoyo SURFTEST SJ210 was utilized to examine roughness profiles as well as the arithmetical roughness parameter *Ra*. Such profiles were sampled longitudinally (0°) and laterally (90°) on the tools and sheet metals with three repetitions each.

Characterization of the friction tool surfaces

The TENIFER treatment (nitro-carburation in salt bath) delivers a durable oxide layer, which has very high roughness in its initial state (1.24 ± 0.07 µm in average). In order to obtain stable results, the surface in pristine condition must run for a couple of times before conducting the relevant friction experiments. Therefore, the surface tests on TENIFER refer to used surfaces. Table 6 summarizes the results of the roughness tests of the friction tools.

Table 6: Arithmetic surface roughness *Ra* of the friction tools in longitudinal (i.e., direction of strip drawing) and lateral (90°) direction. For each parameter, the intervals of 95% confidence are calculated.

machining	**surface treatment**	$Ra_{0°}$ [µm]	$Ra_{90°}$ [µm]	***Ra*** [µm]
grinding	TENIFER	0.26 ± 0.03	0.38 ± 0.09	0.32 ± 0.07
polishing	plasma nitrided	0.05 ± 0.01	0.06 ± 0.01	0.06 ± 0.01
polishing	PVD-AlTiN	0.05 ± 0.01	0.06 ± 0.00	0.06 ± 0.00
fine grinding	PACVD-TiN	0.17 ± 0.10	0.16 ± 0.07	0.17 ± 0.05

The arithmetic roughness of the friction tools' contact surfaces varies significantly with the distinct types of surface finishing. Primarily, the last mechanical manufacturing technique (milling, grinding, polishing) before coating will affect roughness and its directionality. Secondly, the surface treatment may influence the roughness, as in the case of TENIFER by the growth of an oxide layer. The PVD-AlTiN treated jaws represent a forming tool coating that is widespread in lubricated forming techniques and, hence, as smooth as possible by polishing. The PACVD-TiN coated surfaces are optimized for dry friction with an intended, remaining roughness $Ra < 0.5$ to obtain a better cohesion

between tool and coating as well as to remain small areas of contact to the blank on the microscopic scale to lower the potential for adhesion (Persson et al. 2004). In addition, ABBOTT – FIRESTONE or bearing area curves (BAC) were evaluated from the surface tests in both longitudinal and lateral direction. The BAC is a graphical representation of the surface topology by means of a qualitative accumulation of roughness amplitudes over density, see Figure 17.

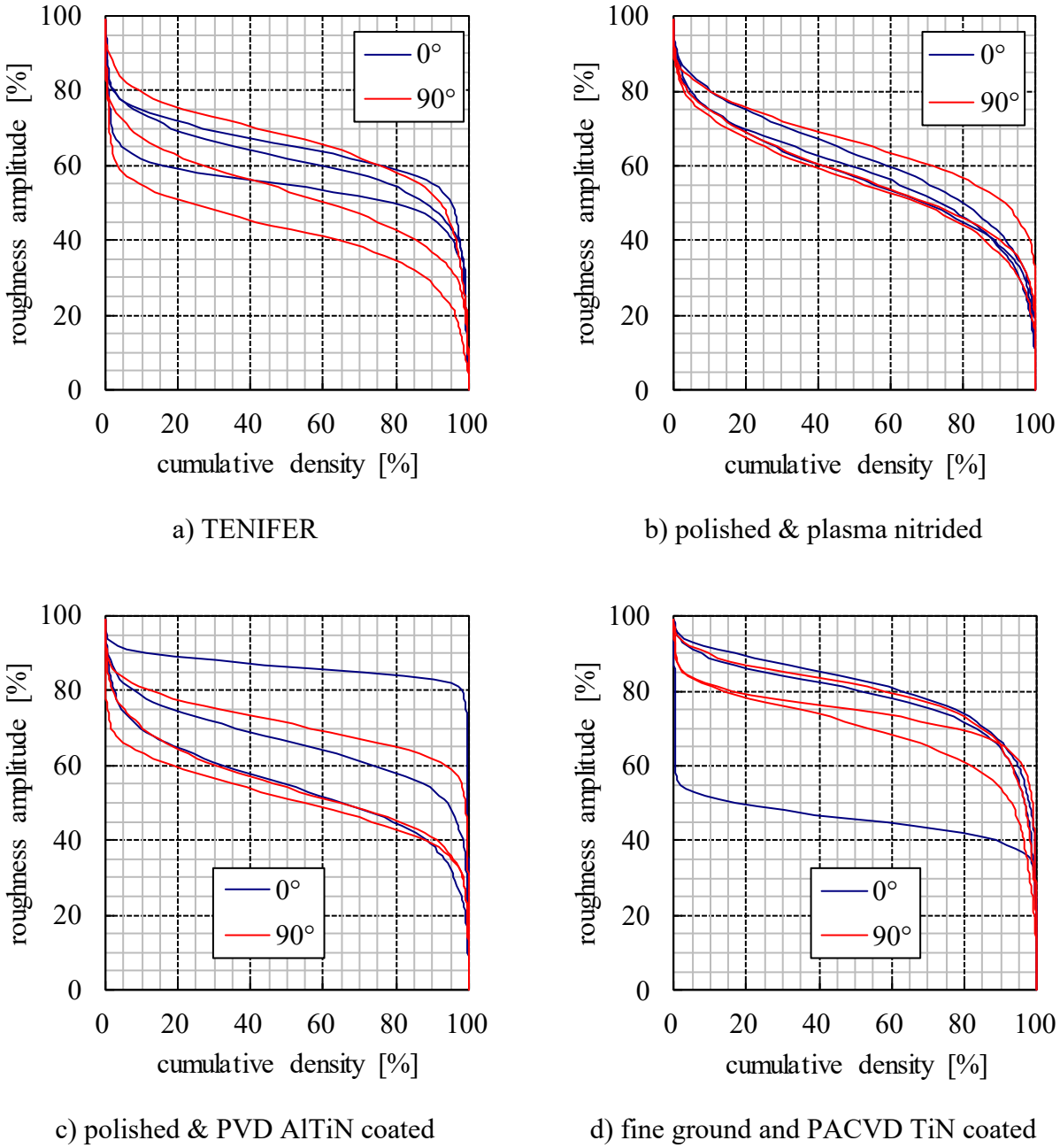

a) TENIFER

b) polished & plasma nitrided

c) polished & PVD AlTiN coated

d) fine ground and PACVD TiN coated

Figure 17: BAC or ABOTT curves of the friction tools' coatings in used conditions: a) TENIFER treated (nitro-carburation in salt bath), b) polished and plasma nitrided, c) polished, plasma nitrided and PVD-AlTiN coated, d) plasma assisted CVD-TiN coated.

While most of the surfaces show balanced trends of roughness amplitudes, or, figuratively speaking, an even distribution between peaks and valleys, the PACVD-TiN coated surface shows a high

accumulation of peaks, which could potentially lead to a raised ratio of microscopic to macroscopic (i.e., nominal) surface area.

Characterization of the sheet metal surfaces

The roughness of the materials was tested longitudinally (0°) and laterally (90°) in relation to the blanks' rolling direction, see Table 7. On the upper and lower blank surfaces, three repetitions were measured, and their average was considered. From thermomechanical rolling, 42SiCr was obtained with a thin layer of oxide. As a result of the experiments conducted in this thesis, the tinder crust cannot withstand strain values $\varepsilon > 0.05$ and would flake off, which is potentially not an issue for obtaining formed parts in reasonable quality. However, the gridded surface of specimen intended for optical strain measurement would be lost in the formed areas. Hence, tinder was removed from these profiles by sanding prior to the ISB process. Consequently, surface roughness was measured both with and without tinder.

Table 7: Roughness of the material blanks, relative to their rolling direction and mean value. For each parameter, the intervals of 95% confidence are calculated.

Material	$Ra_{0°}$ [µm]	$Ra_{90°}$ [µm]	Ra [µm]
HCT780X	1.14 ± 0.10	1.01 ± 0.16	1.07 ± 0.10
22MnB5	1.27 ± 0.10	1.28 ± 0.03	1.27 ± 0.05
42SiCr, tinder	0.33 ± 0.04	0.49 ± 0.18	0.41 ± 0.10
42SiCr, sanded	0.29 ± 0.03	0.34 ± 0.06	0.32 ± 0.03
H800	0.32 ± 0.05	0.31 ± 0.01	0.31 ± 0.02

As verified by the t-tests, two significantly diverse groups of material surface roughness can be denoted from these results; relatively rough materials are represented by HCT780X's and 22MnB5 while the other materials, 42SiCr and H800, represent a much smoother group of surfaces. In addition to the evaluation of arithmetical surface roughness, the BACs of the sheet metals are provided in Figure 18.

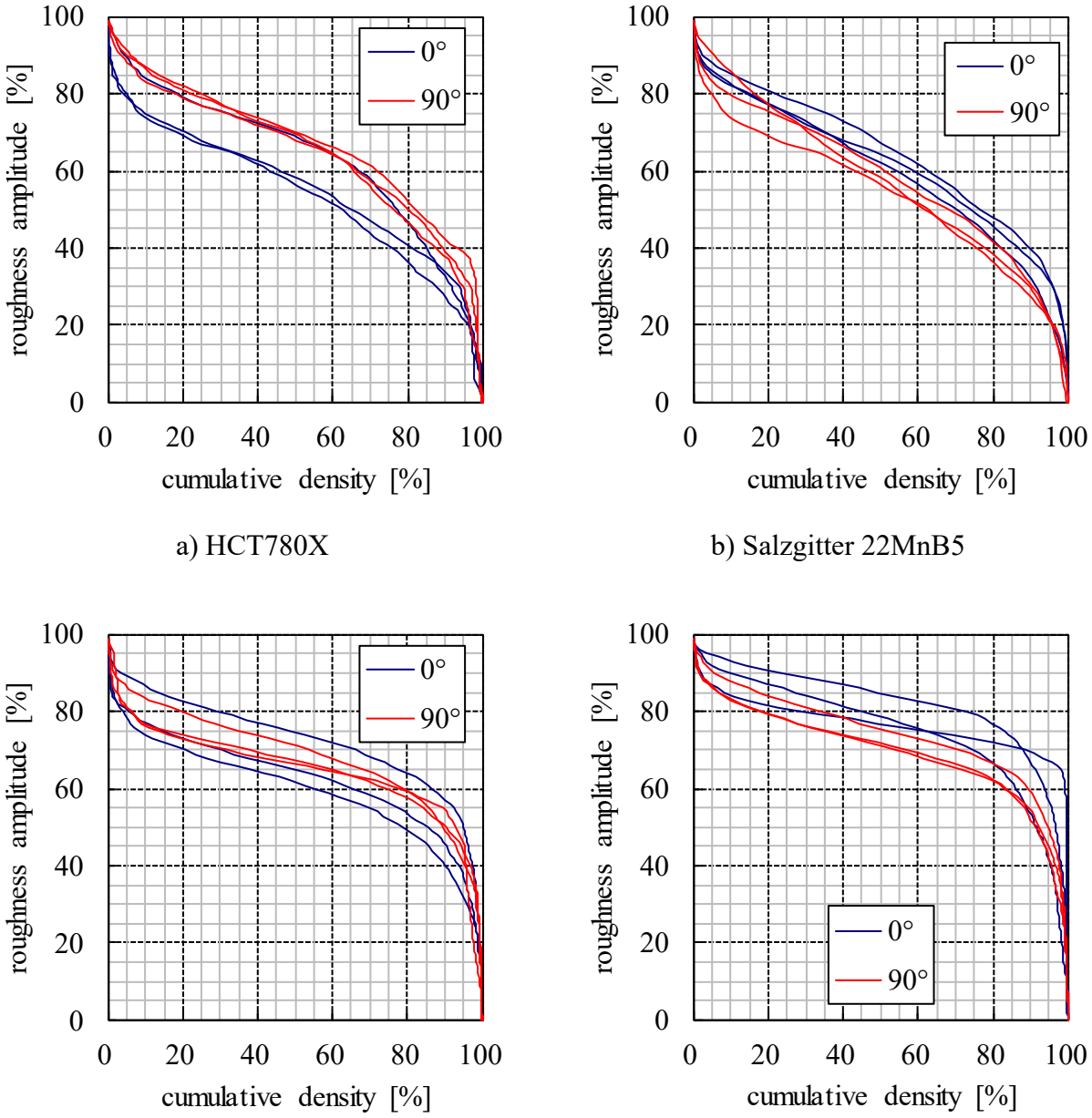

a) HCT780X

b) Salzgitter 22MnB5

c) 42SiCr (sanded)

d) Outokumpu FORTA H800

Figure 18: BAC for a) HCT780X, b) 22MnB5, c) 42SiCr and d) H800.

The BACs of the sheet metal materials indicate an enhanced ratio of effective contact surface in the case of 42SiCr in sanded condition (slightly) and FORTA H800 (significantly). HCT780X and 22MnB5 show balanced trends of roughness amplitude over density. For tinder coated 42SiCr, no curve is provided, because all specimens from this material treated in this thesis were sanded to be ready for optical strain measurement.

4.4.3 Strip drawing in a flatbed

Strip drawing experiments in a flatbed with particular regard to static friction coefficients were conducted without lubrication and within a range of pressure variation relevant for ISB. At UTS, the strip drawing experiment is directly adapted to the universal tensile testing machine ZWICK/ROELL Z250, see Figure 19.

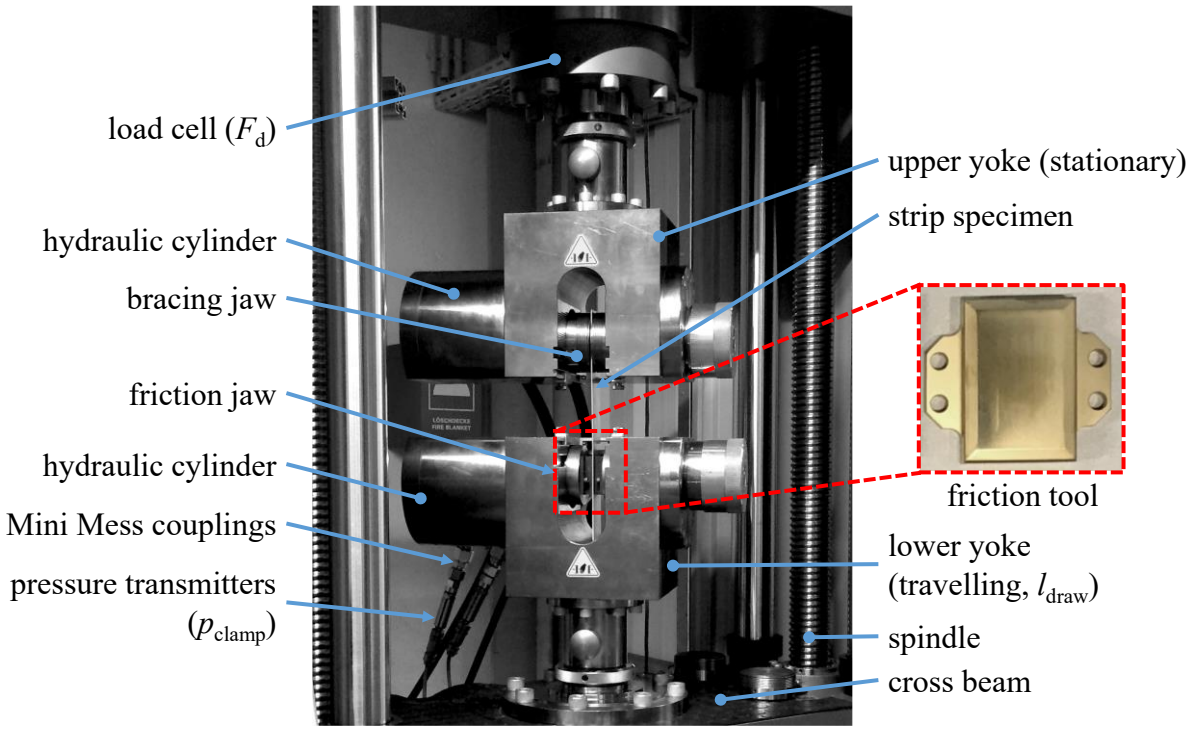

Figure 19: Flat-bed strip drawing experiment adapted to ZWICK/ROELL Z250 at UTS. The clamping force is applied by an external hydraulic power unit.

In the upper yoke, material strips are hydraulically clamped by the machine's internal hydraulic unit using a bracing yaw. At the lower yoke, two friction tools with a contact area of 25 x 41.5 mm (width x length) are fitted to the hydraulic piston. Throughout the friction experiment, these friction jaws apply the clamping force F_N to both surfaces of a sheet metal strip. In order to achieve variable surface pressures, the lower yoke is connected to an external hydraulic unit. The hydraulic clamping pressure p_{clamp} is picked off by MINI MESS couplings, each equipped with pressure transmitters PDRD E002 S14 C425 by BAUMER. The relation $F_N = p_{clamp} \cdot A_{piston}$ delivers the clamping force applied by the hydraulic piston taking its surface area A_{piston} into account. The pressure is monitored by the measurement unit DIADEM, which essentially encloses a digital analogue (DA) converter. During the friction experiments, DIADEM synchronously recorded the pressure sensor signals, and the testing machine´s channels drawing force F_d and the displacement as functions of time.

Under clamped conditions, the sheet metal strip is drawn longitudinally as the testing machine lowers its cross beam attached to the lower yoke. To evaluate the friction force F_{fric} as a function of experimental displacement l_{draw}, mathematically, the friction coefficient is mathematically given as:

$$\mu(l_{draw}) = \frac{F_{fric}(l_{draw})}{F_N} . \qquad \text{(eq.42)}$$

By its load cell, the testing machine directly measures the drawing force F_d which results from two friction forces F_f, each caused at the friction tools' surfaces, cf. Figure 20.

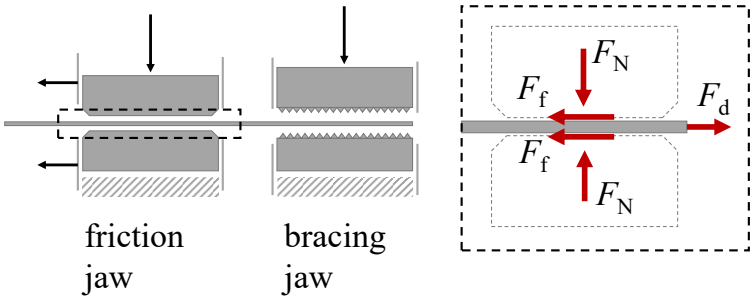

Figure 20: Mechanical representation of the strip drawing experiment.

Next to the combinations of sheet metal materials and friction tools, the clamping force F_N represents the essential parameter influencing the friction coefficient. In the scope of this thesis, the influence of the contact pressure σ_N on the friction coefficient μ is of key interest. In order to define σ_N, the macroscopic area of contact is measured by marking the friction jaws with engineer's blue, loading the test setup by F_N without drawing the strip and measuring the contact area with a caliper.

From each material, strips of 300 x 50 mm were cut by shearing. The width of 50 mm ensures, that the strip is wider, than the friction tools, so that the work hardened cut edges would not influence the experiment. As shown in Figure 19, the yokes of the ZWICK/ROELL Z250 only allow a maximum length of the strip until it touches their inner corner. Hence, the experimental travel l_{draw} is limited to 60 mm.

On UTS' strip drawing assembly, friction coefficients were evaluated in a range of σ_N = 1 up to 15 MPa.

Above, in a pressure range of σ_N = 30 to 100 MPa, the strip drawing assembly of UMFORMTECHNIK LEOBEN was utilized (shortly denoted LEOBEN in the remainder of this thesis). Their test setup is provided by the original equipment manufacturer ZWICK/ROELL and mounted to an identical uniaxial tensile testing machine as UTS´, cf. Figure 21.

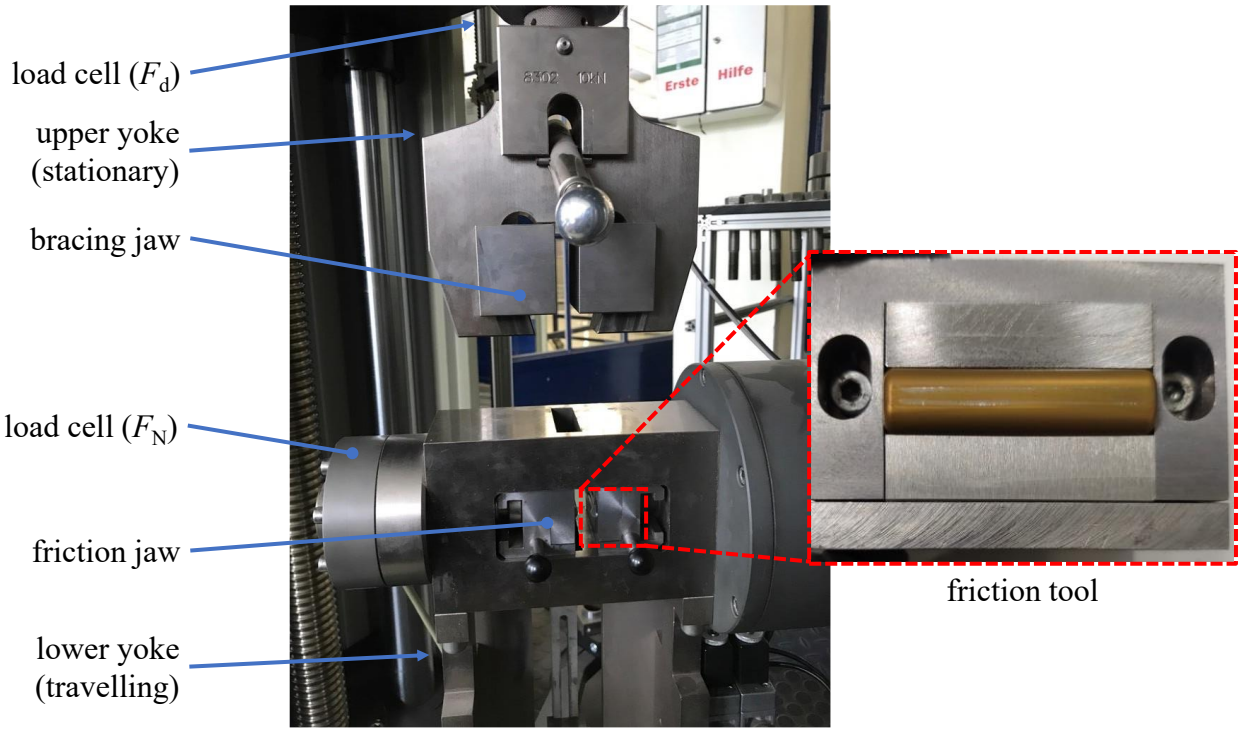

Figure 21: ZWICK/ROELL OEM strip drawing test setup equipped on LEOBEN's uniaxial tensile testing machine. Detail: Friction jaw.

In contrast to UTS´ strip drawing assembly, the friction tools used at LEOBEN are 37 mm wide but have a flat contact length of only 2.5 mm in drawing direction. Considering a comparable machine stiffness, thereby, considerably higher contact pressure ranges are feasible, than with the presented tooling of the UTS friction test assembly.

4.4.4 Evaluation of static and kinetic dry friction coefficients

By the load cell of the universal testing machine, the reaction force F_d from drawing the strip through the friction jaws is recorded as a function of travel l_{draw}. The experiment can be divided into three stages regarding l_{draw}, cf. Figure 22.

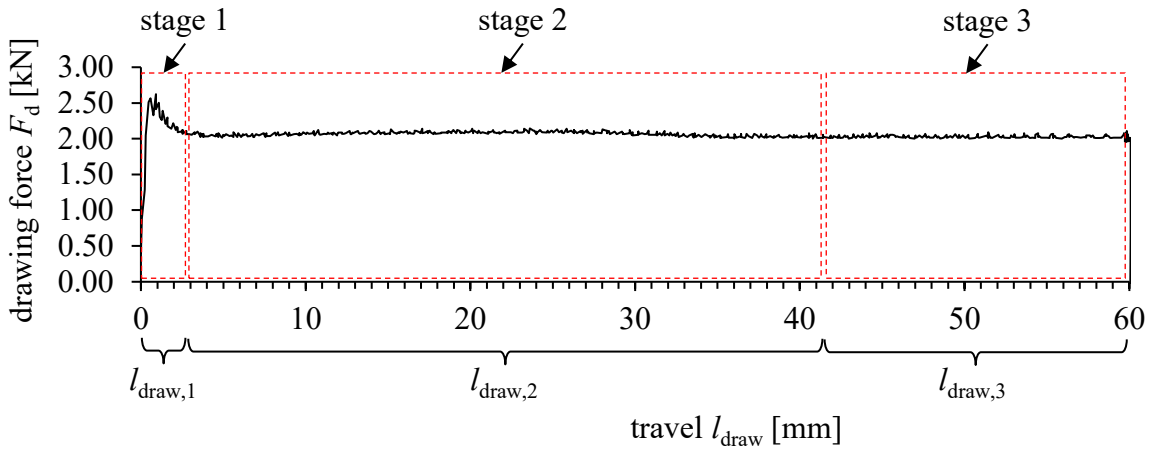

Figure 22: Evaluation stages of a strip drawing experiment, here: 22MnB5 at σ_N = 7.5 MPa.

1) The force to initialize slipping: During this phase, the friction force builds up until it overcomes the friction jaw's traction on the sheet metal surface. Elastic deformations of the specimen as well as the experimental assembly and machine determine travel during the first phase $l_{\mathrm{draw,1}}$, which is usually a very small interval of travel. Resulting from the maximum value of F_{d}, the static friction coefficient μ_0 is obtained:

$$\mu_0 = \frac{\max\left(F_{\mathrm{d}}(l_{\mathrm{draw,1}})\right)}{2F_{\mathrm{N}}} \qquad \text{(eq.43)}$$

This particular evaluation is of key importance for the layout of the frictionally engaged process as no slipping of material under the tools is stated as elementary prerequisite for a valid and stable operation of ISB.

2) Next, the clamping jaws slip over the metallic strip under kinetic friction. During this phase, the blanks surface which has been initially flattened during phase 1 is passed over. Potentially, the friction force F_{d} might hence vary over travel during phase 2 and may differ from its value obtained in phase 3. The friction jaws used in this thesis have a nominal contact length of 41.5 mm (UTS) or 2.5 mm (LEOBEN) respectively, which determines the interval of travel of phase 2 including phase 1.
3) During the remaining travel of the strip drawing experiment ($l_{\mathrm{draw}} \geq 41.5$ mm) the sheet metal in its pristine state is tested without any initial flattening. Therefore, F_{d} is expected constant over travel in the third phase of the experiment if intact tribological conditions prevail. The resulting coefficient of kinetic friction μ is obtained over $l_{\mathrm{draw,3}}$ according to

$$\mu = \frac{\overline{F_{\mathrm{d}}\left(l_{\mathrm{draw,3}}\right)}}{2F_{\mathrm{N}}}. \qquad \text{(eq.44)}$$

The absence of kinetic friction is a central assumption of the analytic model of the forming process under traction. The material is either firmly clamped under the tool faces or contact is lost due to transverse straining in the areas where material experiences plastic deformation. The third stage of the strip drawing experiments is therefore only considered to assess if an intact tribological system is present but must not indicate necessarily an unsuitable combination of tools and materials for the ISB process. In this context, insufficient tribological conditions might for example refer to adhesion, which leads to a strongly increasing force over travel signal. Abrasion is expected to reveal instable

and discontinuous signals. Because contamination, e.g., dirt or lubricants, potentially influence the experiments, the tools and specimens were cleaned with solvents before each experiment to obtain comprehensive and unbiased results. In the case of zinc coatings on sheet metals, citric acid was used for cleaning the tools after each test as it dissolves remaining zinc traces from previous experiments.

Dry friction experiments at low contact pressure

The sheet metals HCT780X (zinc coated), 22MnB5, 42SiCr (in sanded condition) and FORTA H800 were introduced to the strip drawing experiments. In general, at least four repetitions of each individual testing combination of tools and materials were conducted to assure reasonable statistical information. All experiments have been conducted without lubrication at a drawing speed of 10 mm/s, which lies well within the range of angular speed achieved in ISB. Firstly, on UTS testing assembly, all friction tools with various surface treatments shown in Table 5 were utilized in the strip drawing tests. From these tests, a number of combinations proved insufficient and were not pursued any further, as mentioned in the following details:

- The polished and plasma nitrided tools led to adhesion in combination with zinc coated HCT780X and austenitic FORTA H800. This tool treatment method is therefore abandoned for dry friction applications.
- The polished and AlTiN coated tools did not deliver significant static friction regimes leading to an absence of above described first stage of experiments. This observation is considered disadvantageous for the ISB process as an uncertain regime of traction could lead to material slipping within the clamping. Moreover, the repetitions of the individual tests show a very large scatter (see Appendix). Lastly, a constant trend of friction coefficient within the third experimental stage was rarely observed raising the question of a valid tribological system.

The other friction tool treatments were considered for further evaluation. Contact pressure was varied within a range of 1 up to 30 MPa. On UTS' strip drawing assembly, feasible results were achieved up to σ_N = 15 MPa while an applied pressure of 30 MPa often led to implausible results, which are suspected to relate to inferior stiffness of the assembly by means of tool tilting. In these cases, adhesion phenomena tended to occur locally at the run-in edge of the flatbed tools. Excluding the experiments at 30 MPa, Table 8 summarizes the static friction coefficients μ_0 evaluated from the first stage of each individual experiment while Table 9 shows the corresponding kinetic dry friction coefficients μ obtained from stage 3. The corresponding experimental plots of friction coefficient over machine travel are shown in the Appendix.

Table 8: Static friction coefficients μ_0 of the sheet metals, evaluated with respect to contact pressure. Intervals of 95% confidence are calculated from repetitions. Parentheses indicate $\mu_0 \leq \mu$, hence no static friction was observed with the respective material – tool coupling.

Material	Tool treatment	Surface	$\mu_{0,\sigma N1}$	$\mu_{0,\sigma N6}$	$\mu_{0,\sigma N15}$
HCT780X	TENIFER	oxides		0.15 ± 0.02	0.16 ± 0.01
HCT780X	PVD	AlTiN		0.20 ± 0.02	(0.18 ± 0.03)
HCT780X	PACVD	TiN	0.44 ± 0.05	0.27 ± 0.02	0.29 ± 0.01
22MnB5	PACVD	TiN	0.25 ± 0.01	0.18 ± 0.00	0.18 ± 0.01
42SiCr	TENIFER	oxides		(0.07 ± 0.01)	(0.10) [2]
42SiCr	PVD	AlTiN		(0.10 ± 0.01)	(0.07 ± 0.01)
42SiCr	PACVD	TiN		0.17 ± 0.03	0.16 ± 0.01
FORTA H800	TENIFER	oxides		0.15 [2]	
FORTA H800	PVD	AlTiN		(0.06 ± 0.00)	(0.08 ± 0.00)
FORTA H800	PACVD	TiN	0.28 ± 0.02	0.20 ± 0.01	0.19 ± 0.01

Table 9: Kinetic friction coefficients μ of the materials, evaluated with respect to contact pressure. Intervals of 95% confidence are calculated for four specimens each test setup.

Material	Tool treatment	Surface	$\mu_{\sigma N1}$	$\mu_{\sigma N6}$	$\mu_{\sigma N15}$
HCT780X	TENIFER	oxides		0.11 ± 0.00	0.15 ± 0.03
HCT780X	PVD	AlTiN		0.19 ± 0.07	0.20 ± 0.03
HCT780X	PACVD	TiN	0.30 ± 0.04	0.18 ± 0.01	0.24 ± 0.01
22MnB5	PACVD	TiN	0.19 ± 0.02	0.14 ± 0.01	0.14 ± 0.00
42SiCr	TENIFER	oxides		(adhesion)	(galling)
42SiCr	PVD	AlTiN		0.10 ± 0.02	0.17 ± 0.02
42SiCr	PACVD	TiN		0.13 ± 0.01	0.13 ± 0.00
FORTA H800	TENIFER	oxides		(galling)	
Forta H800	PVD	AlTiN		0.07 ± 0.01	0.13 ± 0.02
FORTA H800	PACVD	TiN	0.22 ± 0.01	0.16 ± 0.00	0.17 ± 0.00

Evidently, the PVD-AlTiN coating did not deliver valid static friction coefficients. The results obtained from the TENIFER treated tools show mostly distinct static friction regimes but led to severe tool damage in the later stages of kinetic friction. Thus, the externally conducted strip drawing experiments at LEOBEN were conducted with PACVD coated tools exclusively.

[2] No repetitions were conducted due to tool disruption by galling.

Dry friction experiments at higher contact pressure

At the testing facilities of LEOBEN, the friction coefficients of the considered sheet metals were measured at higher contact pressures in addition to the results obtained at the UTS institute. The tests were exclusively conduced in combination with PACVD-TiN coated tools, because the tests summarized in Table 8 and Table 9 suggest that only this coating delivers stable results for kinetic and static friction. The friction coefficients were evaluated in a range of 15 to 100 MPa. Some overlapping of the pressure range of both experimental series (UTS, LEOBEN) was planned to assure connectibility of the trends of friction over pressure. The resulting static friction coefficients μ_0 are summarized in Table 10 and the corresponding kinetic friction coefficients μ are shown Table 11. The experimental plots of μ over travel are shown in the Appendix.

Table 10: Static friction coefficients μ_0 for higher contact normal pressure values as measured on the test facility of LEOBEN. Intervals of 95% confidence are calculated for four specimens each test setup.

Material	Tool coat	treatment	$\mu_{0,\sigma N15}$	$\mu_{0,\sigma N30}$	$\mu_{0,\sigma N60}$	$\mu_{0,\sigma N100}$
HCT780X	TiN	PACVD	0.32 ± 0.05	0.36 ± 0.03	0.38 ± 0.05	0.43 ± 0.07
22MnB5	TiN	PACVD	0.26 ± 0.01	0.22± 0.01	0.26 ± 0.03	0.30 ± 0.01
42SiCr, sanded	TiN	PACVD		0.19 ± 0.02	0.23 ± 0.02	
Forta H800	TiN	PACVD	0.21 ± 0.01	0.20 ± 0.00	0.21 ± 0.02	0.25 ± 0.01

Table 11: Kinetic friction coefficients μ for higher contact normal pressure values as measured on the test facility of LEOBEN. Intervals of 95% confidence are calculated for four specimens each test setup.

Material	Tool coat	treatment	$\mu_{\sigma N15}$	$\mu_{\sigma N30}$	$\mu_{\sigma N60}$	$\mu_{\sigma N100}$
HCT780X	TiN	PACVD	0.16 ± 0.01	0.15 ± 0.02	0.15 ± 0.00	0.18 ± 0.02
22MnB5	TiN	PACVD	0.21 ± 0.02	0.16 ± 0.01	0.18 ± 0.02	0.24 ± 0.02
42SiCr, sanded	TiN	PACVD		0.15 ± 0.03	0.17 ± 0.03	
Forta H800	TiN	PACVD	0.18 ± 0.00	0.16 ± 0.01	0.17 ± 0.01	0.18 ± 0.02

All combinations revealed valid friction coefficients. HCT780X shows no significant influence of pressure on kinetic friction coefficients. For this material, exceptionally high static friction coefficients were obtained, which in turn significantly depend on pressure. This glaring feature is attributed to the zinc coating. In the case of 42SiCr only selected data points were evaluated due to scarce material availability.

4.4.5 Linear approximation of friction coefficients

Overarching both experimental assemblies (UTS, LEOBEN), the trends of static and kinetic friction coefficients over pressure are connected for the results on PACVD-TiN coated tools. In the cases, where overlapping pressure ranges were conducted, unusually high friction coefficients were noticed for small contact pressures in both cases of utilized tooling (41.5 - and 2.5 - mm contact length) and also for higher pressures applied on the larger tools, see Figure 23.

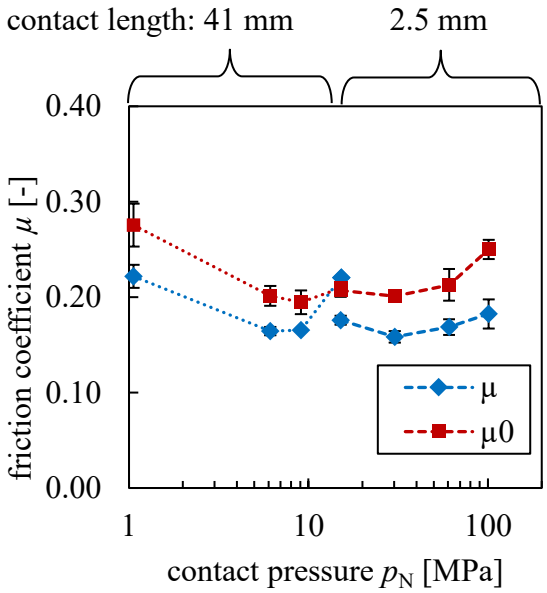

Figure 23: Combination of two friction testing series with variation of contact length, in this case FORTA H800.

With regards to the longer friction tools, the elevated friction coefficients relate to beginning (15 MPa) or pronounced (30 MPa) adhesion problems at higher pressure values. For the lower pressure ranges on both tool lengths, uneven contact marks were seen on the surfaces of the drawn strips. Hence, the unusually high friction coefficients observed in these cases are explained by poor compliance of tools to the sheet metal. Correspondingly, the normal force F_N of only 1 kN was applied in both cases of tools used, i.e., short tool and long tool. To conclude, distinct pressure ranges are recommended for each individual set of friction tools:

- For the long tools used at UTS (41.5 mm contact length): 5 – 15 MPa
- For the short tools used at LEOBEN (2.5 mm contact length): 30 – 100 MPa

The data points which were observed with excessively high friction coefficients were related to the explanation above and hence excluded from the linear interpolation. Figure 24 illustrates the approximated trends of static and kinetic friction over pressure for the investigated sheet metals.

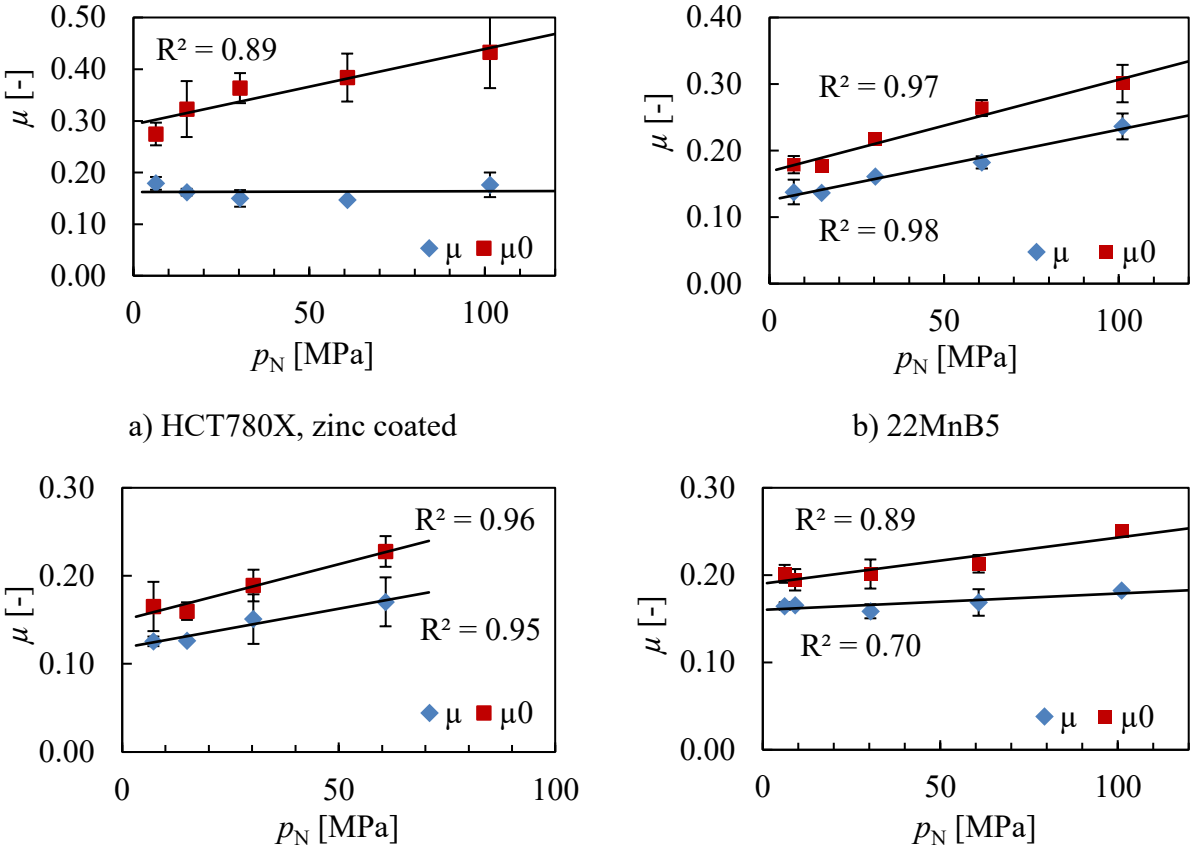

Figure 24: Linear regression of dry friction coefficients over contact pressure as evaluated from unlubricated contact with PACVD-TiN coated tools. Indication of coefficient of determination R² for each approximation.

In general, the interpolated trends of friction coefficients versus pressure follow the functions

$$\mu(p) = c \cdot p + \mu_{ini} \qquad \text{(eq.45)}$$

and

$$\mu_0(p) = c_0 \cdot p + \mu_{0,ini} \qquad \text{(eq.46)}$$

with the initial friction coefficients μ_{ini} and $\mu_{0,ini}$ and the inclination factors c and c_0, for kinetic and static friction, respectively. The values for these coefficients are given for the investigated sheet metals in Table 12.

Table 12: Linear regression coefficients for pressure dependent dry friction for selected sheet metal materials. Supporting experiments were conducted on PACVD-TiN coated tools.

	kinetic friction		static friction	
material	c	μ_{ini}	c_0	$\mu_{0,ini}$
HCT780X	0	0.162	$1.5 \cdot 10^{-3}$	0.293
22MnB5	$1.1 \cdot 10^{-3}$	0.125	$1.4 \cdot 10^{-3}$	0.169
42SiCr	$0.9 \cdot 10^{-3}$	0.118	$1.3 \cdot 10^{-3}$	0.149
Forta H800	$0.2 \cdot 10^{-3}$	0.160	$0.5 \cdot 10^{-3}$	0.190

The inclination coefficients c and c_0 demonstrate that the investigated sheet metals reveal diverse sensitivities of friction towards a variation of pressure. In all cases, a more pronounced increase of static friction was observed as compared to kinetic friction for continuously raising normal pressure. Interestingly, the zinc coated HCT780X shows no influence of pressure on kinetic friction. No coefficient of determination is obtained in this case because determination of a constant function is not defined mathematically.

4.5 Linear tensile forming experiments

Before applying the findings of the preceding sections to in-plane bending, the analytic model developed for tensile forming under frictional engagement needs to be validated. After mechanical and tribological material characterizations, all parameters for the analytical model are available to compare the model predictions with practical experiments. For this purpose, plane strip drawing is considered. However, in contrast to the experiment's application for evaluation of friction coefficients, clamping is more heavily loaded to provoke tensile plastic deformation of the strip material in the direction of strip drawing. The effect of a continuously dislocating yield sheath under the clamped surface is observed as a function of experimental displacement.

Due to the heavy clamping loads necessary to transfer the forming forces for plasticizing sheet metal under traction, the assembly designed by BORCHMANN (2021) for drawing tubular profiles was used for this experimental series and mounted on the universal testing machine ZWICK/ROELL Z250. Compared to the machine's clamping yokes, the assembly provides higher stiffness. Fundamentally, the assembly consists of interlocked steel plates that enclose the experiment and support the clamping force F_N provided by the hydraulic cylinder orientated lateral to the drawing direction l_{draw}. The setup was modified as explained in the proceeding text to allow for testing strips from sheet metal . The plane friction tools of the strip drawing experiments used for determination of friction coefficients were adapted to the assembly, in detail the PACVD-TiN coated tools. Two additional sensor systems are applied to track the experiment. Firstly, a video extensometer records longitudinal strain within

the free length of the strip, as used in conventional uniaxial tensile tests. Moreover, a planar pressure mapping sensor type TEKSCAN 5051 is positioned at the stationary friction tool to measure the distribution of contact pressure p. The stationary tool is located opposite of the hydraulic cylinder, see Figure 25.

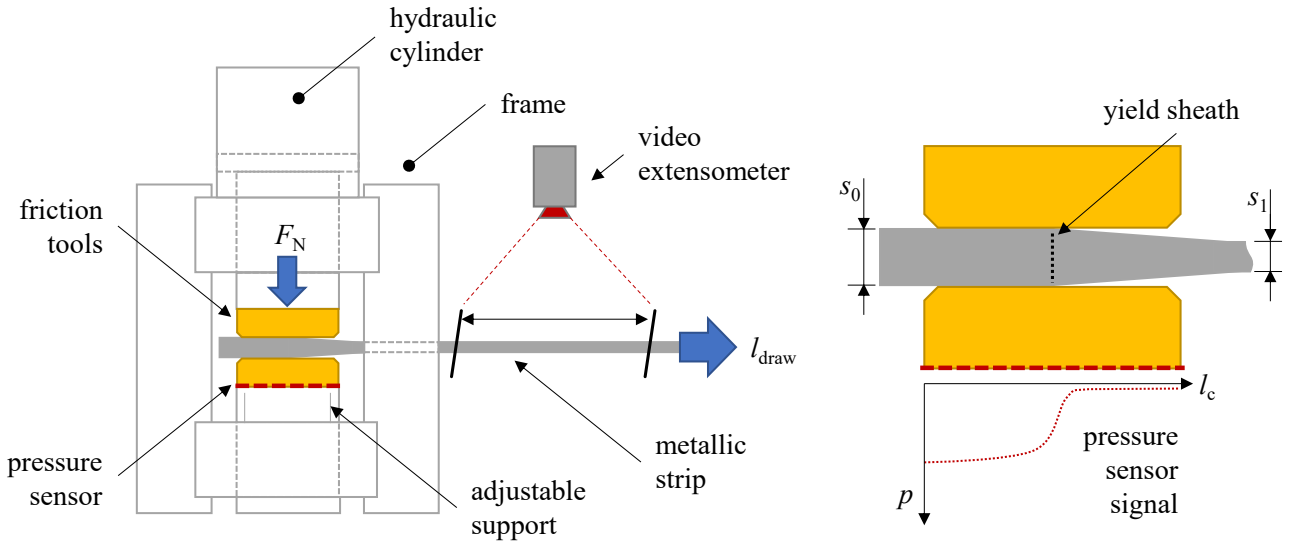

Figure 25: (left) Schematic illustration of the assembly of BORCHMANN (2021), modified for strip drawing under plastic tensile deformation. Main kinematics highlighted by blue arrows, active tools shown in yellow and relevant sensors in red. Location of yield sheath is determined by a drop in the signal of the pressure sensor (right).

The TEKSCAN 5051 sensor covers an area of 55.9 x 55.9 mm². A square matrix of pressure sensitive paths (piezoresistive principle) with an upper threshold of p = 172 MPa is arranged in 44 x 44 columns and rows, which hence deliver a resolution of 62 sensor cells / cm². The matrix arrangement is embedded in a 0.1 mm thick polymer film. The pressure mapping sensor is introduced to track the position of the yield sheath within the clamped surface during the experiment. It is placed at the mounting surface of the friction tool because it cannot bear any shear stress and, in addition, would change the tribological conditions when being directly placed in between tool and material. It is expected to measure a significant drop in the pressure signal over clamping length l_c at the location where the strip material reaches its yield point even at the backside of the friction tool's bulk. Corresponding to the established theoretical relationship mentioned in section 4.1, it is expected to observe an ongoing longitudinal displacement of the yield sheath in the opposite direction of strip drawing l_{draw}.

Three sheet metal materials, namely HCT780X, 22MnB5 and FORTA H800, were introduced to the strip drawing experiment with tensile plastic deformation. All strips were cut to a constant width of h_0 = 32 mm to exceed the size of the friction tools, whose lateral contact width measures 25 mm. Three repetitions of each individual experiment were conducted. The strips were drawn at a machine speed of 1.5 mm/s up to rupture or a maximum displacement of 165 mm (in the latter case 22MnB5),

see Appendix Figure 121. The clamping force F_N applied by the lateral hydraulic cylinder was kept constant throughout each individual experiment. F_N was initially laid out according to the experimental plan presented in Table 13 to assure firm stationary clamping conditions without material slipping. In detail, the precedingly determined pressure dependent static friction coefficients were applied according to COULOMB'S law so as to determine the minimum required clamping force $F_{N,min}$.

Table 13: Variation of strip materials studied in the experiment of strip drawing with tensile plastic deformation. Indication of least necessary clamping force $F_{N,min}$ to prevent material slipping at uniform tensile elongation.

Material	**cross section** $h_0 \times s_0$ [mm]	F_N [kN]	μ_0 (p) [-]	$F_{N,min}$ [kN]
HCT780X	32 × 1.0	59	0.389	32
22MnB5	32 × 1.4	61	0.262	44
FORTA H800	32 × 1.0	92	0.239	65

Resulting from these experiments, the experimental displacement l_{draw}, drawing force and longitudinal strain (which equals equivalent true strain φ_{eq} in the case of uniaxial tension) were obtained. Synchronously, the signal of the pressure mapping sensor was captured by the I-Scan system, which saves the local pressure values of each sensor cell in a matrix of 44 x 44 columns and rows at a rate of 10 Hz, cf. Figure 26. By this procedure, the pressure mapping information can be correlated to displacement l_{draw} or strain φ_{eq}.

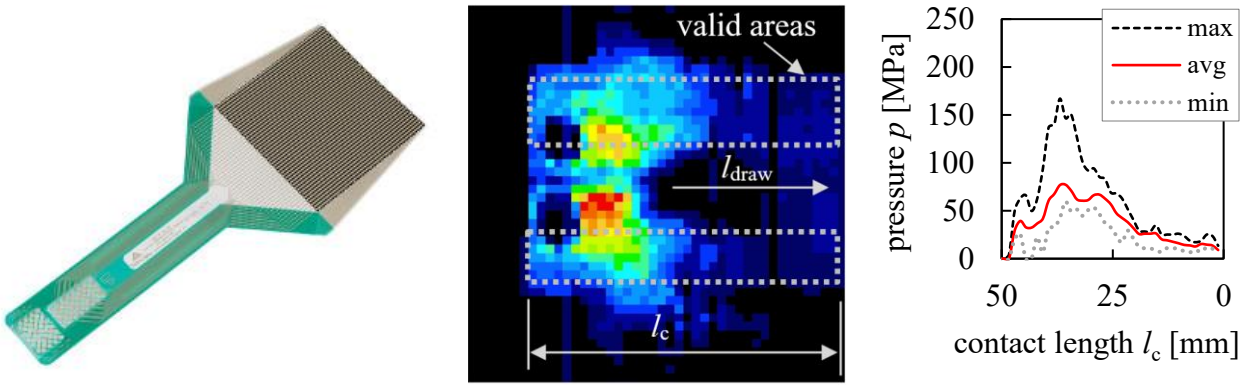

a) b) c)

Figure 26: Results from the TEKSCAN I-Scan system. a) Pressure mapping sensor 5051 and b) resulting pressure contour plot ranging from 0 (black) to 172 MPa (red) during strip drawing HCT780X. c) Resulting graphs for pressure over contact length.

As an example, a matrix measured by the TEKSCAN sensor is visualized in Figure 26 b) by false colors ranging from p = 0 (black) to 172 MPa (red). The longitudinal position of the sheet metal material's

yielding needs to be identified in relation to the friction tools clamping length l_c from these plots. From the analytic model, a constant lateral position of the yield sheath is expected. Therefore, the sensor's pressure values are compressed over width by calculating the lateral maximum, average or minimum for each frame. The average and minimum values are only calculated for uninterrupted paths as gaps in the measurements are caused by assembly holes, as seen from Figure 26 b). For each increment of time, graphs showing pressure over tool length result from this evaluation, namely maximum, average and minimum pressure, shown as an example in Figure 26 c). All graphs show a change of pressure at the location, where the yield sheath is suspected, however a stochastic scatter superposing these data remains. This scatter is observed least for the averaged values, which is why the average plots are favored henceforth. Moreover, the graphs do not drop to zero pressure where plastic deformation of the strip material is present. Two reasons might cause the latter behavior, i) the elastic flexibility of the friction tools leads to a compliant behavior at the materials change in thickness at the elastic-plastic transition and ii) since the sensor lies on the backside of the friction tool it experiences some lateral force even where the strip material underlies transverse plastic deformation. In Figure 27, the (width-) averaged pressure values of the experiment are visualized over the friction tool's longitudinal coordinate l_c and the experimental drawing length l_{draw} depending on time t.

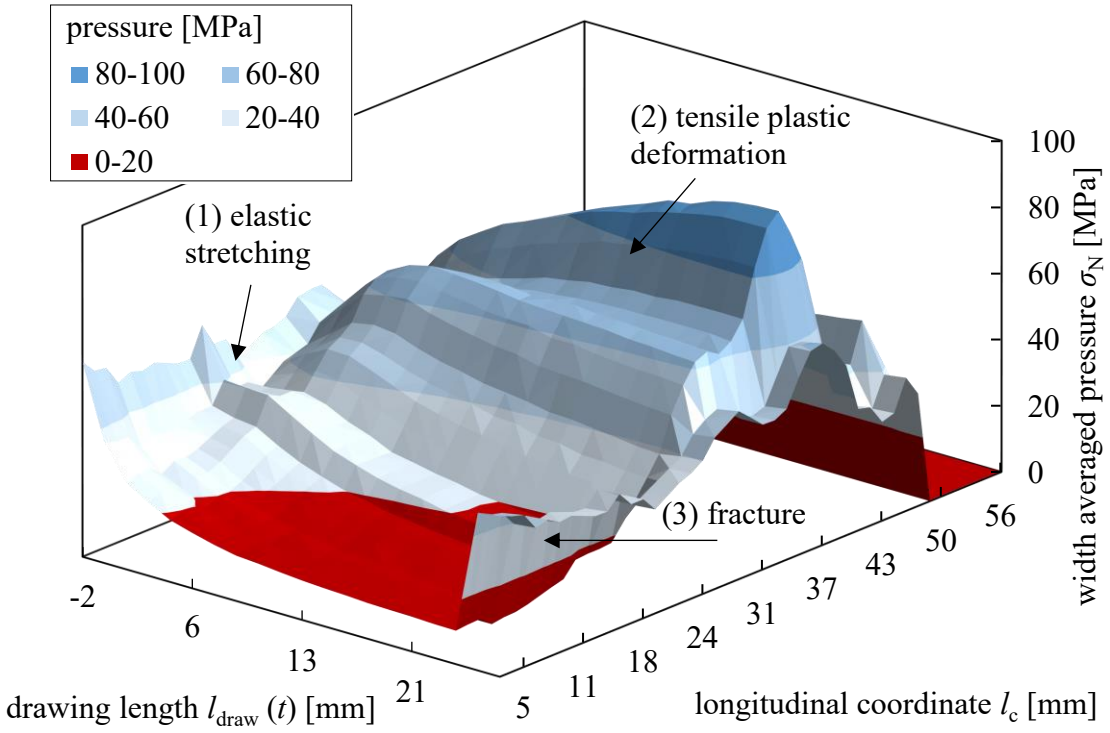

Figure 27: Visualization of the pressure mapping sensor signal for the first repetition of HCT780X strips. Width-averaged pressure values σ_N plotted over the longitudinal contact coordinate l_c and the experimental progress which is represented by drawing length l_{draw}. Red colors highlight the threshold were contact between tool and sheet metal is assumed to detach.

The experimental procedure is dived into three stages. It begins with an elastic tensile loading of the strip which stays in traction with the friction tools and the assembly (1). This initial stage follows a continuous plastic deformation where low pressure values occur at the foremost part of the friction tools' longitudinal coordinate (2). In the third stage of the experiment, the continuously increasing drawing length caused longitudinal strain to exceed the strip materials ductility resulting in fracture (3). Soon after, the elastic springback of the assembly is seen from the pressure signal in stage 3.

Evidently, the larger is the lost contact area between friction tool and strip material, the higher is the pressure rise in the remaining clamped surfaces. A threshold needs to be defined, which represents the region without static contact between tool and material in order to identify the longitudinal position of the yield sheath. This threshold is highlighted red for the experiment shown above and lies at 20 MPa. Reasonably, this margin is identical for experimental repetitions and set into relation to the applied clamping force F_N. For the present experiments, a threshold of ⅓ of the initial nominal clamping pressure $\sigma_{N,0} = F_N / A_{c,0}$ was applied to identify the position of the yield sheath from the width-averaged plots.

To compare these results to the predictions of the analytic model, the location of the yield sheath identified from the pressure maps is correlated to equivalent tensile strain ε_{eq} as measured from the universal testing machine's extensometer. In Figure 28, the location where the contact between tool and sheet metal detaches as identified from the thresholds is plotted over equivalent strain and compared to the calculation of the process model of eq. (40). Illustratively, the curves shown in Figure 28 represent the top view of the area highlighted in red in the spatial diagram shown in Figure 27.

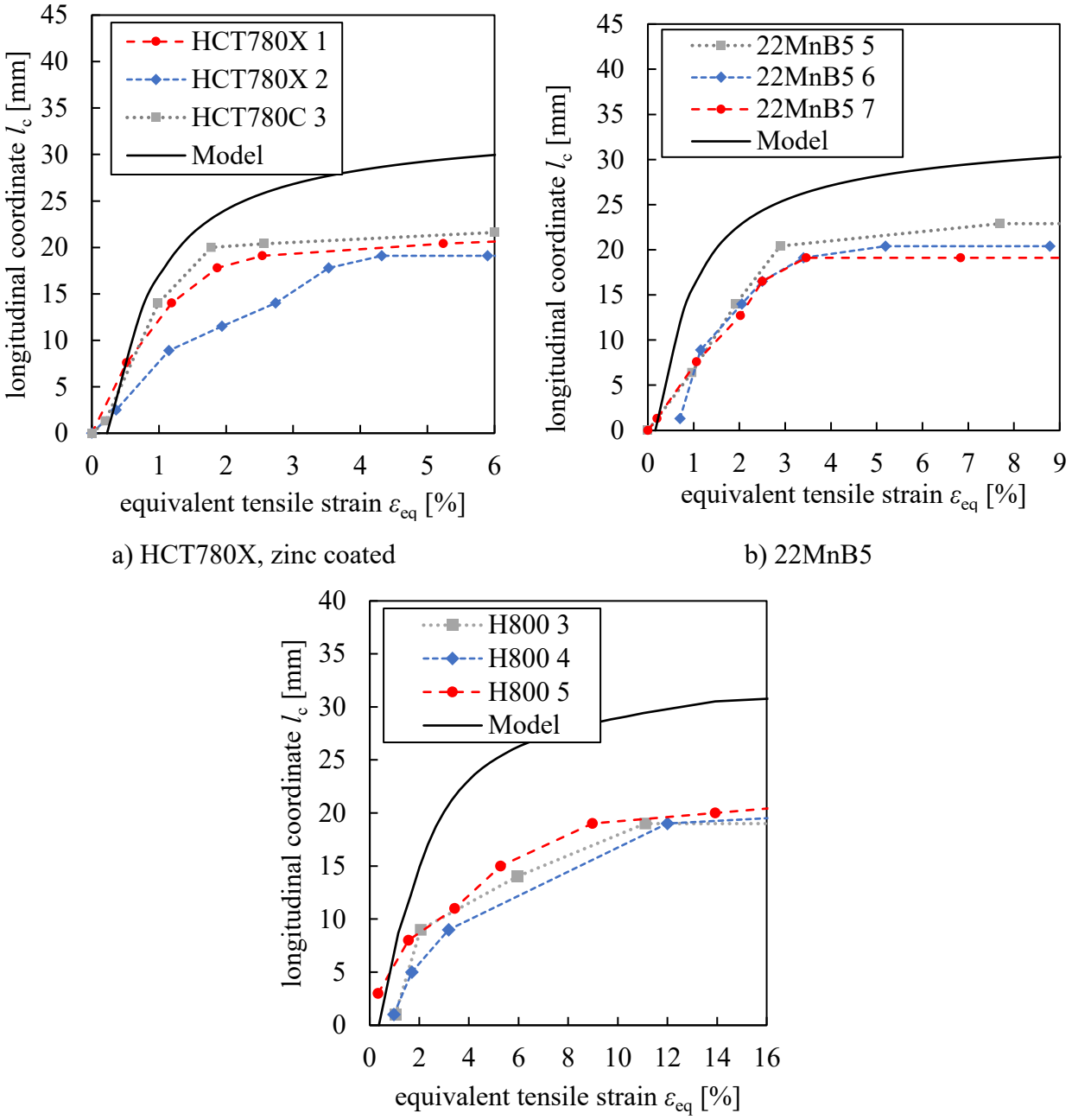

a) HCT780X, zinc coated

b) 22MnB5

c) FORTA H800

Figure 28: Location of the elastic-plastic transition of the strip material over longitudinal tensile strain for three repetitions on a) HCT780X, b) 22MnB5 and c) FORTA H800. From the experiments, the detaching contact between tool and sheet metal is identified where normal pressure values lies below a threshold of ⅓ $\sigma_{N,0}$.

By qualitative measures, the experimental curves obtained from the width-justified pressure values below threshold approximate the trend calculated from the analytical model. With an increasing longitudinal straining of the strip material, a large portion of the initial contact length is lost due to plastic transversal strain, i.e., thinning. By quantitative measures, a pronounced scatter is obtained for lower strain values considering the experimental repetitions. At higher strains, the repetitions lay

closer to each other and approximate a constant value beginning at l_c = 20 mm, while the model predicts a weak but further increase of l_c. Larger deviations between model and experiments are seen for strip drawing FORTA H800. Sporadic stick-slip effects were observed during these experiments.

4.6 Discussion and conclusions of chapter 4

The analytical model developed to describe a linear tensile process with a force transmission by traction predicts a continuously increasing loss of contact under clamping tools due to plastic thinning of the sheet metal material. Few assumptions are considered to keep the mathematical complexity within manageable limits. In detail, these are:

- During elastic stretching, a linear increase of longitudinal stress over the clamping length is assumed, reaching from beginning to end of the clamping tool,
- Considering no influence of elastic compression due to clamping load,
- Considering no influence of elastic transversal strain due to longitudinal strain within the material,
- Considering no influence of clamping load on the multiaxial stress state formulated at the location of yield sheath,
- Application of a bilinear hardening model to describe the plastic stress-strain relation,
- Unsteady decrease from initial cross section to deformed cross section and a constant plastic strain distribution in the forming zone.

Strip drawing of HCT780X is evaluated from the finite element model after the onset of plastic deformation for the discussion of the assumptions shown above. Over the length below the clamping tool, Figure 29 shows the trends of contact pressure as well as thinning, equivalent and plastic strain of the strip material.

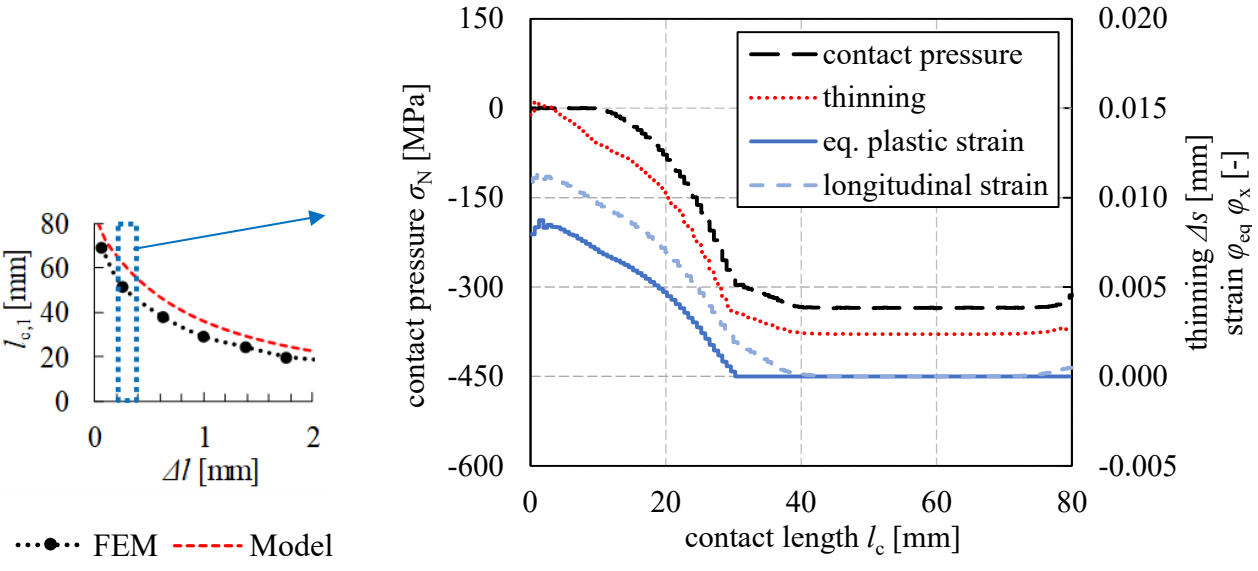

a) b)

Figure 29: Evaluation of strip drawing simulation using DP800 at a clamping force of F_N = 3000 kN and a drawing length of Δl = 0.25 mm under longitudinal load (no elastic springback). a) FE-simulation results compared to the analytical model, b) evaluation of contact pressure σ_N, thinning Δ_s, equivalent true strain φ_{eq} and longitudinal true strain φ_x over contact length l_c.

From the line plots, the elastic influence on the process description is seen in the difference between the location where plastic strain abruptly reaches zero at l_c = 30 mm while the other curves show a transition zone until l_c = 40 mm. On the one hand, these results show that longitudinal stress might not build up from the beginning of the clamping tool but on a distinctive length. On the other hand, pressure drops slightly at the location where elastic longitudinal strain and thinning begin. Still, a much steeper drop in pressure until zero is seen where plastic thinning of the material begins, so the predictions of the model aim for the more significant effect. In addition, from thinning the shape of transition from initial cross section to deformed is seen. A smoothly curved transition is obtained from simulation which reaches its minimum at the end of the forming tool while the analytical model predicts an abrupt change of cross section.

ISB is preferably operated without any lubrication owing to efficiency of force transmission. Dry friction experiments were conducted by strip drawing to determine friction coefficients as a function of contact pressure. Compared to standard friction coefficients for ferrous metals (μ = 0.12), the tested friction values significantly improve the modelling accuracy to predict the size of the forming zone and the resulting strain distribution. Overall, the materials reveal rising friction coefficients at higher pressure in dry conditions both for kinetic and static friction. As no lubrication has been imparted, the aforementioned observation agrees with the literature discussed in the preceding sections of this thesis, see section 2.5.2. The observation is explained by increasing the effective contact surface between both solid tribological partners by raising the applied contact

pressure since the topography of both surfaces is levelled in an elastic and plastic way. The friction tests demonstrate that smooth material combinations are prone to wearing (adhesion and galling), both regarding the surfaces of tools as well as sheet metals. Both polished tools, the plasma nitrided pair and the PVD AlTiN coated, did not provide valid static friction conditions. On the other hand, the TENIFER treated friction tools have revealed problems in dry sliding contact to the austenitic H800 material and the sanded surface of the pearlitic 42SiCr. Still, valid static friction was observed, and these combinations were applied in the later practical experiments. In the strip drawing experiments, severe sliding contact appears. In an ISB process, the material retracts from the tool surfaces once static friction is overcome at the yield sheath, thus avoiding wear phenomena associated with sliding contact. Plasma assisted chemical vapor deposition of titanium nitride (PACVD-TiN) delivered satisfying test conditions of the friction coefficients of all sheet metals throughout the tested range of pressure (Frohn-Sörensen, Cislo, et al. 2021).

Incorporating the dry static friction coefficients which were evaluated in this thesis, the analytic model is compared to practical experiments, where the strip drawing experiment is more heavily loaded to impart linear plastic deformation of the strip material under traction instead of slipping. The evaluation of the length under static contact in between tool and material, which continuously decreases over the experimental progression, underlies variations in between identical repetitions caused by side influences on the experiment, e.g., contaminations, alignment errors of strip and assembly, scatter within the sensor evaluation and spread generally associated with friction experiments, as seen from the friction curves in the Appendix. The experiments are intended to verify the analytical model if its predictions show similar qualitative trends. A remaining overestimation of the material portion losing contact is seen when comparing both model predictions and practical experiments. In addition, the experimental curves remain at an approximately constant drawn-out material portion after reaching half of the whole tool length, while the analytical model smoothly increases further with decreasing inclination. This observation is interpreted as the hydraulic cylinder of the experimental assembly attacks at the center of the friction tool, it thus potentially causes tilting after drawing out more than half of the contact due to eccentric loading conditions. The experiments on FORTA H800 show larger deviations towards the predictions of the model. Sporadic stick-slip effects occurred, judged by negative peaks (~ 4 peaks per experiment) in the force over displacement signals as well as a corresponding noise emission. Thus, the experiments fairly exhibit some delay in the function of longitudinal contact coordinate over strain.

5 Process description of frictionally engaged bending

In the previous chapter, a model to demonstrate tensile forming behavior of a plane strip under traction is developed and validated. Using this approach, the fundamental mechanisms depicting an ISB process are derived in the subsequent parts of this chapter by applying rotational kinematics to the model. For this purpose, in plane-bending of a single and continuous step is considered, before modelling the incremental procedure of the ISB process. Firstly, the clamping force, which is necessary throughout the forming process for firm fixation of the material is determined. In particular, the force layout must meet the process design requirement that the material does not slip in the clamping. In the tensile process of the previous chapter, COULOMB's law incorporating the tensile force maximum and the coefficient of friction delivers the necessary relation to dimension the clamping force. However, during bending operation the clamping force is related to a bending moment resulting from a lateral stress distribution over cross section. Since the process achieves highest bending moment when reaching uniform tensile elongation, the specific clamping force is investigated which corresponds to the required friction moment.

During bending of an arc increment, the forming zone will adjust to the multiaxial stress condition being applied by the processing parameters. In order to determine the strain distribution caused by a bending increment, the analytic description of the forming zone is of key interest for this investigation. For the ISB process it has been observed that the forming zone not only encloses the gap which opens in between the clamping tools, but moreover, reaches well into the clamped areas after the materials begins to plasticize. Similar to the tensile forming process under traction of the previous chapter, a sharp border, denoted as yield sheath, is identified to describe the edge of the forming zone, where the elastic-plastic transition is located. For in-plane bending, an analytical model is derived for the location of the yield sheath. As a result, the model is applicable to describe the size of the forming zone and the corresponding strain distribution. From the analytical descriptions, a process window is derived which spans the area of applicable clamping force over bending angle.

5.1 Mechanical representation of the ISB process

An ISB process is represented mechanically as frictionally engaged in-plane bending process under influence of a laterally shiftable bending axis. The forming process is subdivided by a repeated sequence to incrementally shape an arc, as illustrated in section 2.2.2, Figure 3 a):

- clamping,
- bending by the incremental angle δ,
- opening, resetting tools and
- feeding the distance Δf.

In order to transmit the bending moment M_Z by friction, the material is clamped by the stationary and rotatory clamping units of the ISB tool. The press commonly loads both units by the force F_N, which represents an elementary process parameter of ISB. Under load, the rotatory clamping unit pivots about the bending axis. In order to superimpose compressive or tensile strain to bending, the axis can be offset laterally, see section 2.2.2, Figure 3 b). The offset factor o represents the lateral shift of the pivot in relation to the width of the profiles in-plane, h_0 (Frohn, Engel, and Groth 2018). The pivot's neutral position in the center of the strip relates to zero. $o = -0.5$ represents a bending axis position at the extrados of an arc and hence results in pure compressive bending stresses. Vice versa, an exclusively tensile distribution is achieved by $o = 0.5$ and the bending axis is located at the intrados of the arc[3]. The elementary parameters are illustrated in the mechanical representation of the ISB process, see Figure 30.

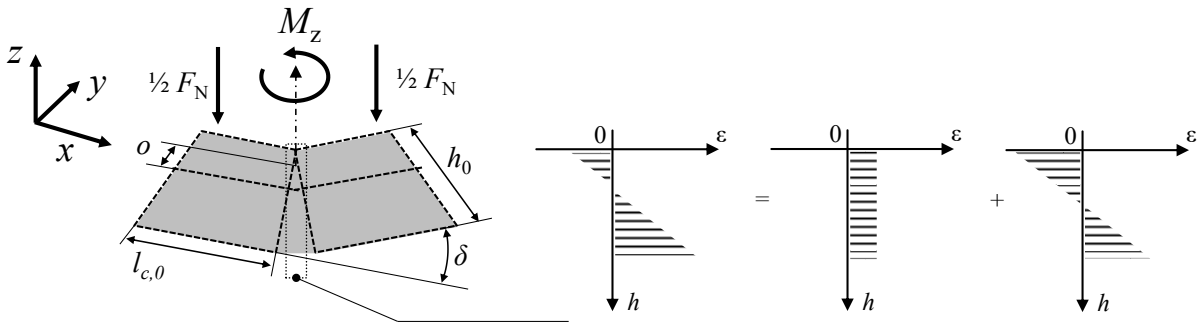

Figure 30: Mechanical representation of the ISB process: A profile of width h_0 is clamped by two clamping units of length $l_{c,0}$ under a common press load F_N to frictionally provoke the bending moment M_z in the bending pivot, which is laterally shifted by the factor o.

Similar to ENGEL and HASSAN (2014), the strain distribution in an ISB process consists of two elementary parts, bending strain and tension (or compression) strain. By superposition, both deliver the combined distribution schematically indicated in the right-hand image of Figure 30. ENGEL and HASSAN considered rotary draw bending in which the strain-neutral axis passively shifts towards the intrados of the arc. In an ISB process, the offset of the bending axis allows to actively influence the strain distribution and therefore to adjust the ratio of occurring compression and tension.

5.2 Clamping force for traction

The bending moment to incrementally bend an arc is transferred by frictional engagement in an ISB process. The clamping force required to bend a strip of sheet metal in-plane hence depends on friction and plasto-mechanical bending moment M_z of the material. In general, the moment is determined depending on the distribution of bending stress which is a function of strain and the material

[3] A similar factor k_{EBH} was suggested by ENGEL, BUHL, and HEFTRICH (2014) to describe neutral axis shifting in sandwich sheets. However, for practical reasons (positive values relate to tensile stress and vice versa; direct relation to absolute offset by factorization with h_0), o is used in ISB and can be related to previous work at UTS by $k_{EBH} = -2o$.

properties. M_z is propagated over the lateral dimension of the profile within the bending plane, h_0. Consequently, the derivation of the clamping force for an ISB process depends on two unknown variables:

i. The clamping force F_N, necessary to frictionally transfer the bending moment M_z
ii. Longitudinal strain $\varphi_x(y)$ as a function of the lateral coordinate y.

Calculation of strain has been done conventionally on the basis of the bending radius R_{cl} and its elongation caused at the arc lengths of the intrados or extrados. In an ISB process, the overall bending radius is represented by alternating kinks and linear sections in a polygon-shaped way. However, a radius definition for such a kink is not feasible so radius-based strain assumptions are not applicable and can only be used for the circular approximation of the whole, polygonised geometry. The maximum deformation forces occur when the material reaches uniform tensile elongation A_G. Hence, the least clamping force is investigated, which is sufficient to frictionally transfer the plasto-mechanically determined bending moment which corresponds to A_G.

Minimum and maximum bending moment

Based on the equations of ENGEL et al. (2014) for the description of the bending moment resulting from an offset bending axis, the following paragraphs derive the maximum bending moment of the ISB process at uniform tensile elongation. F_N is a crucial parameter of the ISB process layout because of the frictionally engaged transmission of bending moment.

In an ISB process, the shiftable bending axis influences the moment of inertia and hence, the transition between tensile and compressive stresses. According to eq. (4), the bending moment is generally described by

$$M_z = M_{z,\mathrm{ten}} + M_{z,\mathrm{comp}} = \int_{A,ten} \sigma(y) \cdot y \cdot dA \; + \int_{A,comp} -\sigma(y) \cdot y \cdot dA \qquad \text{(eq. 47)}$$

with the indices "*ten*" depicting tensile stress distribution and "*comp*" depicting compression, see Figure 31.

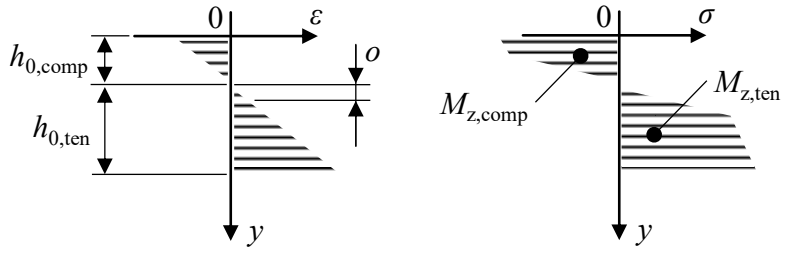

Figure 31: Bending strain and stress distribution, offset by factor *o* and separated into compressive and tensile shares.

The subdivision into tensile and compressive momenta requires corresponding boundaries reaching from the extrados to the bending axis and from the bending axis to the intrados of the to-be-bent arc. Within the bending plane, these boundaries are defined as profile height underlying tensile forming $h_{0,ten} = h_0 \cdot (½ + o)$ and height underlying compression $h_{0,comp} = h_0 \cdot (½ - o)$ in relation to the cross section's initial height h_0. Two states of bending moment are of interest: the minimum required bending moment $M_{z,\mathrm{yield}}$ to initiate plasticizing and the maximum bending moment $M_{z,\max}$ when uniform tensile elongation is achieved within the material. At this point, the clamping force necessary to ensure traction to transmit the bending moments at the materials yielding and for its plastic deformation until uniform tensile elongation at the extrados is investigated. For this purpose, the plasto-mechanical bending moment M_z of the material is assumed to be in the center of the process regardless of longitudinal stress distribution in the bending process. Transversal elastic contractions are neglected.

Initial plasticizing begins when the materials yield criterion is reached in the outer or inner fiber. Assuming a linear strain distribution over profile height h_0, yield stress R_e occurs at one or both edges. Under these assumptions, $M_{z,yield}$ described by

$$M_{z,\mathrm{yield}} = \begin{cases} \int_0^{h_{0,\mathrm{ten}}} \frac{R_e \cdot y}{h_{0,\mathrm{ten}}} \cdot y \cdot dy \cdot s_0 + \int_{h_{0,\mathrm{comp}}}^{0} -\frac{R_e \cdot y}{h_{0,\mathrm{ten}}} \cdot y \cdot dy \cdot s_0 & \text{if } o \geq 0 \\ \int_0^{h_{0,\mathrm{ten}}} \frac{R_e \cdot y}{h_{0,\mathrm{comp}}} \cdot y \cdot dy \cdot s_0 + \int_{h_{0,\mathrm{comp}}}^{0} -\frac{R_e \cdot y}{h_{0,\mathrm{comp}}} \cdot y \cdot dy \cdot s_0 & \text{if } o < 0 \end{cases} \qquad \text{(eq. 48)}$$

$M_{z,yield}$ is divided into tensile and compressive moments at the bending axis location which is offset by o. The linear stress distribution up to R_e is propagated over $h_{0,\mathrm{ten}}$ if equal or more tensile bending stress is achieved by an offset $o \geq 0$. Correspondingly, R_e is propagated over $h_{0,comp}$ if the bending stress distribution is dominated by compression ($o < 0$). The calculation of minimum bending moment disregards the influence of clamping force on the yield criterion, which would cause the criterion to decrease. However, because this section is intended to deliver the clamping force throughout the ISB process, worst case approaches are desirable. Analytically, the integrals of eq. (48) can be solved to

$$M_{z,\mathrm{yield}} = \begin{cases} \frac{R_e}{h_{0,\mathrm{ten}}} \cdot \frac{s_0}{3} \cdot \left({h_{0,\mathrm{ten}}}^3 + {h_{0,\mathrm{comp}}}^3 \right) & \text{if } o \geq 0 \\ \frac{R_e}{h_{0,\mathrm{comp}}} \cdot \frac{s_0}{3} \cdot \left({h_{0,\mathrm{ten}}}^3 + {h_{0,\mathrm{comp}}}^3 \right) & \text{if } o < 0 \end{cases} \qquad \text{(eq. 49)}$$

After yielding, the bending moment M_z would start to plastically deform the material. The stress distribution over the lateral profile coordinate y is determined by work hardening (see Figure 31 right), resulting from the assumption of a linear distribution of strain over y. In order to layout F_N for the entire process, the maximum bending moment $M_{z,max}$ is required. It is achieved at uniform tensile elongation and calculated by integrating the stress distribution over profile cross section. Applying SWIFT's hardening law and under neglect of transversal strain over thickness, $M_{z,max}$ follows

$$M_{z,\max} = \begin{cases} \int_0^{h_{1,\text{ten}}} C_{S1} \cdot \left(C_{S2} + n \cdot \frac{y}{h_{1,\text{ten}}} \right)^{C_{S3}} \cdot y \cdot dy \cdot s + \\ \int_{h_{1,\text{comp}}}^{0} -C_{S1} \cdot \left(C_{S2} + n \cdot \frac{y}{h_{1,\text{ten}}} \right)^{C_{S3}} \cdot y \cdot dy \cdot s \end{cases} \quad \text{if } o \geq 0$$

$$\begin{cases} \int_0^{h_{1,\text{ten}}} C_{S1} \cdot \left(C_{S2} + n \cdot \frac{y}{h_{1,\text{comp}}} \right)^{C_{S3}} \cdot y \cdot dy \cdot s + \\ \int_{h_{1,\text{comp}}}^{0} -C_{S1} \cdot \left(C_{S2} + n \cdot \frac{y}{h_{1,\text{comp}}} \right)^{C_{S3}} \cdot y \cdot dy \cdot s \end{cases} \quad \text{if } o < 0 \qquad \text{(eq. 50)}$$

with the case discrimination, if uniform tensile elongation is reached by tension at the extrados ($o \geq 0$), expressed by the term $n \cdot \frac{y}{h_{1,\text{ten}}}$, or, correspondingly, by compression at the intrados ($o < 0$). In the case of $M_{z,max}$, the integral reaches over the deformed profile height under the influence of the tensile and compressive stress distribution, $h_{1,ten}$ and $h_{1,comp}$ respectively. $M_{z,max}$ is formulated in uniaxial stress state because free deformation of the material is assumed in the gap which opens in between the forming tools. Elastic fractions of the bending moment near the neutral fiber of zero elongation are neglected because the maximum moment is calculated for uniform tensile elongation, hence a small fraction of A underlies elastic deformation.

Before analytical solution, equations (48) and (50) are solved numerically to evaluate the resulting bending moments. In Figure 32, the trends of bending moment M_z resulting from purely elastic deformation at yield stress and from work hardening under SWIFT's law are plotted over the offset factor for an arbitrary material.

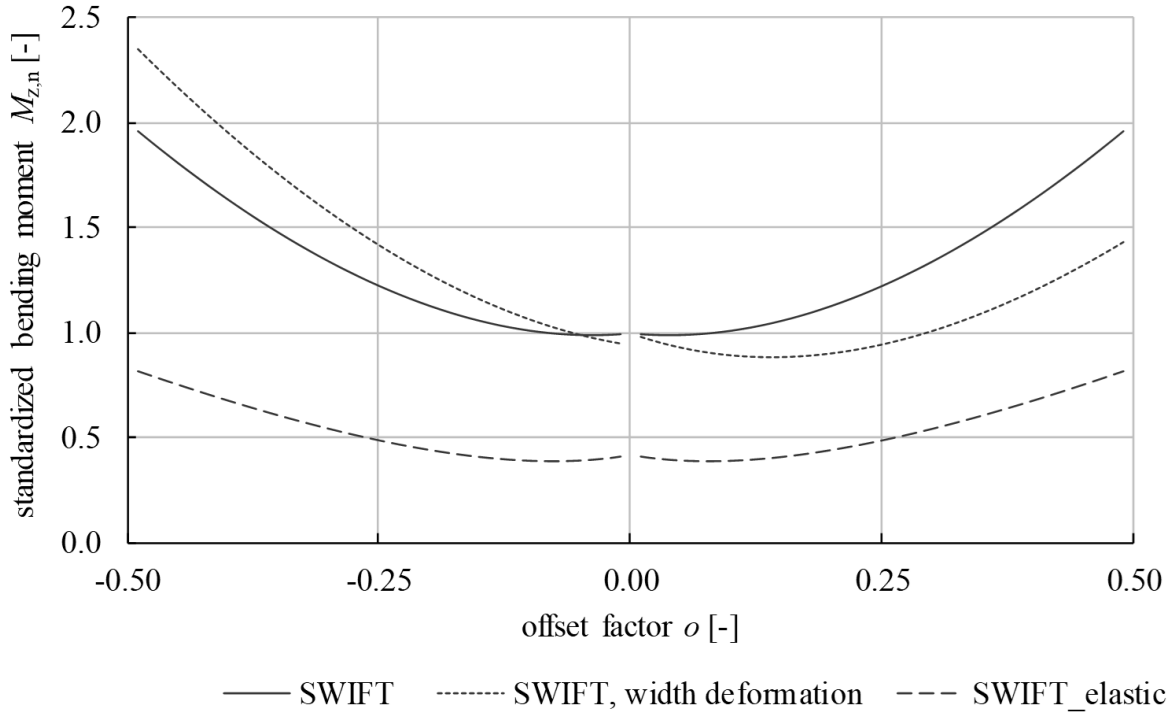

Figure 32: Bending moment $M_{z,n}$, standardized for $M_{z,max}$ and symmetric stress distribution (o = 0), plotted over offset factor o. Wide dashed lines indicate bending moment when plastic deformation sets on, $M_{z,yield}$, according to Equation 48). Bending moment at uniform tensile elongation $M_{z,max}$ is plotted with deformation of profile height h_0 (narrow dashed line, Equation 50)) and without (solid line).

The calculations take the influence of the bending axis offset on the stress distribution into account. Notably, a shifted bending axis delivers considerably higher bending momenta than the central position of axis because work hardening strongly increases towards the more severely strained edge. Equation 50) is constrained to uniform tensile elongation, expressed by the hardening exponent n. Depending on the position of the bending axis, R_e or n could either be reached at the intrados or at the extrados of a bent arc. Corresponding to these case discriminations, the functions shown in Figure 32 are composed of two curves.

Analytical determination of maximum bending moment

To solve equation (50) for maximum bending moment, the lateral stress distribution needs to be integrated over the cross section of the profile. To obtain analytically solvable equations, the bilinear hardening law is applied to the stress distribution. Consequently, the relation for the bending moment $M_{z,max}$ at uniform tensile elongation according to eq. 50) follows

$$M_{z,max} = \begin{cases} \int_{0}^{h_{1,\text{ten}}} \left(m \cdot \frac{A_G}{h_{0,\text{ten}}} \cdot y + R_e \cdot \left(1 - \frac{m}{E}\right) \right) \cdot y \cdot dy \cdot s + & \\ \int_{h_{1,\text{comp}}}^{0} -\left(m \cdot \frac{A_G}{h_{0,\text{ten}}} \cdot y + R_e \cdot \left(1 - \frac{m}{E}\right) \right) \cdot y \cdot dy \cdot s & \text{if } o \geq 0 \\ \int_{0}^{h_{1,\text{ten}}} \left(m \cdot \frac{A_G}{h_{0,\text{comp}}} \cdot y + R_e \cdot \left(1 - \frac{m}{E}\right) \right) \cdot y \cdot dy \cdot s + & \\ \int_{h_{1,\text{comp}}}^{0} -\left(m \cdot \frac{A_G}{h_{0,\text{comp}}} \cdot y + R_e \cdot \left(1 - \frac{m}{E}\right) \right) \cdot y \cdot dy \cdot s & \text{if } o < 0 \end{cases} \quad \text{(eq. 51)}$$

with the inclination factor m of the bilinear model $m = \frac{(1+A_G)\cdot R_m - R_e}{A_G}$. Solving the integrals leads to

$$M_{z,max} = \begin{cases} \left(m \cdot \frac{A_G}{3} + \frac{R_e}{2} \cdot \left(1 - \frac{m}{E}\right) \right) \cdot {h_{1,\text{ten}}}^2 \cdot s + & \\ \left(m \cdot \frac{A_G}{h_{1,\text{ten}}} \cdot \frac{h_{1,\text{comp}}}{3} + \frac{R_e}{2} \cdot \left(1 - \frac{m}{E}\right) \right) \cdot {h_{1,\text{comp}}}^2 \cdot s & \text{if } o \geq 0 \\ \left(m \cdot \frac{A_G}{3} + \frac{R_e}{2} \cdot \left(1 - \frac{m}{E}\right) \right) \cdot {h_{1,\text{comp}}}^2 \cdot s + & \\ \left(m \cdot \frac{A_G}{h_{1,\text{comp}}} \cdot \frac{h_{1,\text{ten}}}{3} + \frac{R_e}{2} \cdot \left(1 - \frac{m}{E}\right) \right) \cdot {h_{1,\text{ten}}}^2 \cdot s & \text{if } o < 0 \end{cases} \quad \text{(eq. 52)}$$

The integration of the deformed sheet thickness s is omitted to simplify the calculation. The approximation quality of the bilinear work hardening model implemented in the equation of maximum bending moment is compared to the implementation of SWIFT's law of equation (50). Figure 33 compares the maximum bending moment $M_{z,max}$ over pivot offset obtained from both hardening laws for an arbitrary material. Moreover, the influence of neglecting transversal strain σ_y over profile height h is indicated.

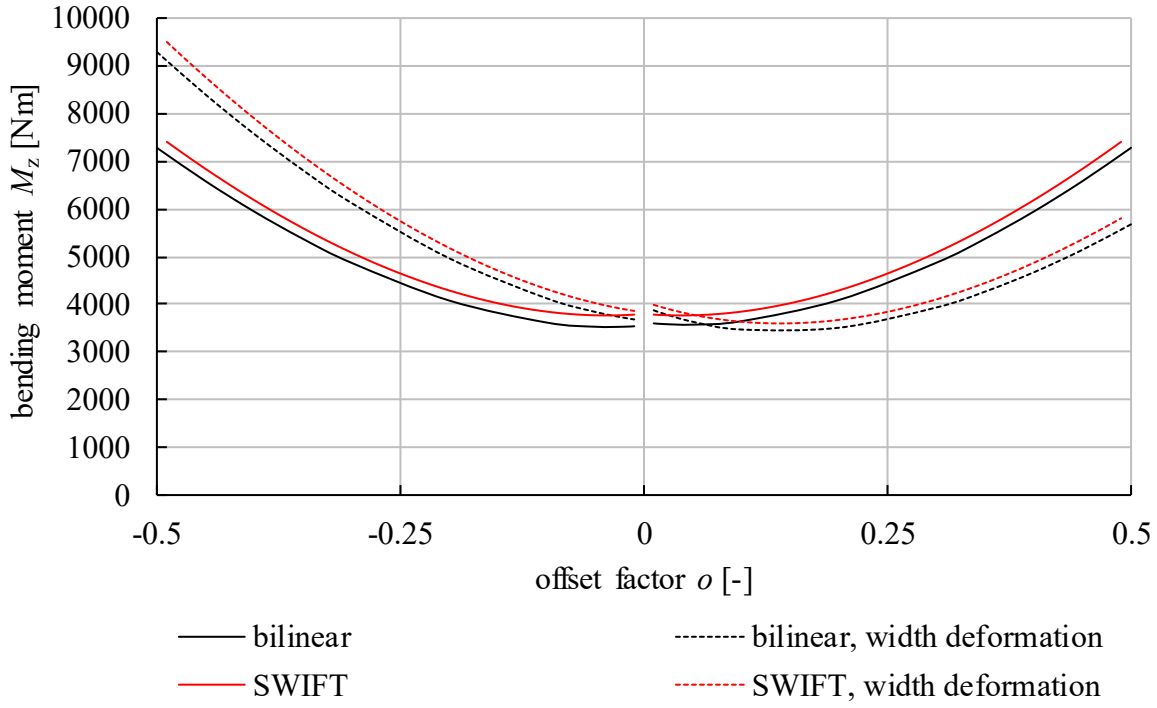

Figure 33: In-plane bending moment $M_{z,max}$ at uniform tensile elongation plotted over the lateral offset of bending axis. Comparison of the implemented hardening laws according to SWIFT and using a bilinear approach. Deformation of the initial strip height in compressive ($h_{1,comp}$) and tensile ($h_{1,ten}$) parts of the arc significantly influences the bending moment.

The analytical determination of bending moment based on the bilinear hardening law complies with the numerical solution of SWIFT's hardening law. Accordingly, the smallest deviations in between both hardening laws are expected at this point as the bilinear model uses true stress over uniform tensile elongation as supporting point. The deformation of profile height has a significant influence on the bending moment M_z which causes observed asymmetry of the trends of bending moment over offset.

Frictional transmission of bending moment

During ISB, bending moment is transferred force-fittingly by two clamping units. The upper and lower tools of each clamping unit fixate the profile by friction at the contact surfaces between material and die faces, as schematically illustrated in Figure 34 (a). Because the press load F_N is evenly separated on both units, and, under consideration of the resulting reaction force at the tool's base, ½ F_N is propagated on each of the four contact surfaces $A_{c,0} = h_0 \cdot l_{c,0}$ (Figure 34 (b)). Note, that the actual die face might be larger than the contact dimensions which result from the profile height h_0 in plane and the length of contact $l_{c,0}$.

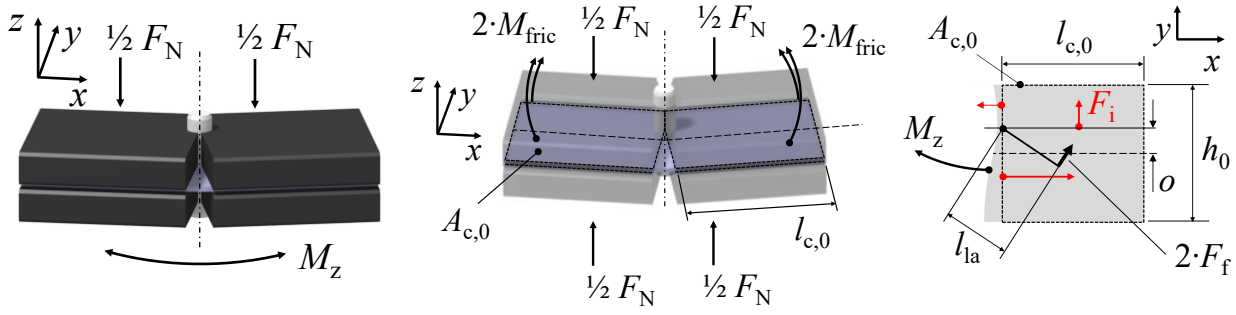

a) b) c)

Figure 34: Mechanic model of the transmission of bending moment in ISB. a) Clamping units of the ISB tool, each loaded by ½ F_N, b) transparent view showing the contact surfaces $A_{c,0}$ between tools and material, each with friction moment M_{fric}, c) cut view through an area of contact: Equivalent friction force F_{fric} and lever arm l_{la} corresponding to M_{fric} (M_z must be related to two areas of contact, therefore $2 \cdot F_{fric}$). Indication of tangential contact force vectors F_i (red).

COULOMB's friction law determines the maximum feasible friction force $F_{fric} = \mu \cdot ½ F_{N,min}$, which can be transmitted under traction. $F_{N,min}$ is the least necessary clamping force to allow bending a given material. According to the rotational kinematics of the bending procedure, the plasto-mechanical moment within the material, M_z, is transferred by four contact surfaces. Thus, for equilibrium of momenta at the cut section through the center of the material, M_z is equated to two friction momenta M_{fric}. At the tool surface, the sum of all tangential contact force vectors $\boldsymbol{F_i}$ causes M_{fric}. These vectors represent the resulting forces from friction on the surface and are assumed to act at the center of individual lever arms, which are oriented concentrical to the offset pivot, see Figure 34 c). Each lever reaches from the offset pivot towards the outer edges of the contact surface. Resultantly, the equivalent friction force F_{fric} acts at an equivalent lever arm l_{la} to represent M_{fric}. l_{la} is approximated by the relation

$$l_{la} = \frac{(l_{c,0} + h_0)}{8}. \qquad \text{(eq. 53)}$$

F_{fric} (as equivalent force expression) acts at the length of l_{la}. When laterally cutting through the center of the material, two friction momenta $2 \cdot M_{fric}$ equal the bending moment M_z due to the upper and lower die faces of the clamping units. By incorporating friction according to COULOMB's law, $F_{N,min}$ is related to M_z by the expression

$$M_z = 2 \cdot M_{fric} = 2 \cdot F_{fric} \cdot l_{la} = 2 \cdot \mu \cdot \frac{F_{N,min}}{2} \cdot l_{la} = \mu \cdot F_{N,min} \cdot \frac{(l_{c,0} + h_0)}{8}$$

$$\Leftrightarrow F_{N,min} = \frac{M_z}{\mu \cdot l_{la}} = 8 \cdot \frac{M_z}{\mu \cdot (l_{c,0} + h_0)}. \qquad \text{(eq. 54)}$$

Under consideration of the equations for $M_{z,yield}$ (49) and $M_{z,max}$ (52), eq. (54) allows to determine the least necessary clamping force $F_{N,min}$ for in-plane bending until specific straining of a profile is reached. The calculations of the bending momenta $M_{z,yield}$ and $M_{z,max}$ are based on both, profile cross section and mechanical material properties and represent yielding and uniform tensile elongation respectively.

5.3 In-plane bending under frictional engagement

In bending, a linear increase of strain is observed which begins from zero at the bending axis up to its maximum value at the extrados. The findings of section 4.1 for tensile forming are applied to the outer arc of a bending process. Corresponding to the equilibrium of longitudinal forces in the model for tensile forming, the momenta within the bending plane are equated. The mechanical representation is given in Figure 35.

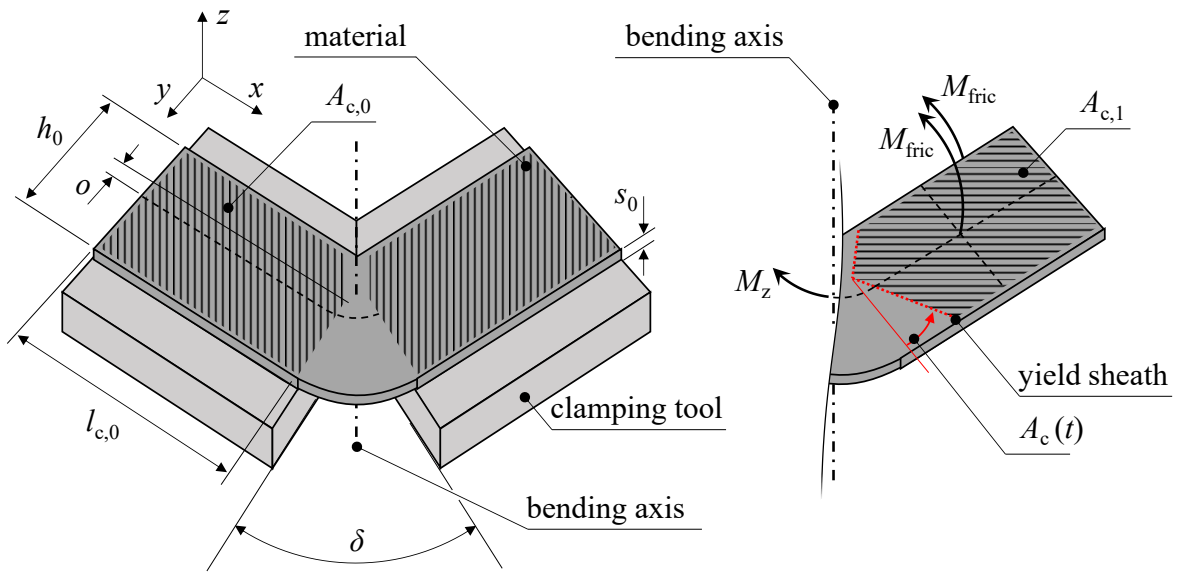

Figure 35: Mechanical representation of frictionally engaged bending. In the cut view (right), the equilibrium of momenta, caused by material deformation (M_z) and tangential friction shearing (M_{fric}), is applied in the bending plane.

During an ISB process sequence, both clamping units are loaded by a constant force F_N, which is determined according to section 5.1. Subsequently, one of the clamping units pivots about the bending axis, which can be offset by o, see chapter 6.1. For in-plane bending, the bending axis is located along the z-coordinate, i.e., normal to the bending plane. During initial tool rotation, purely elastic deformation is achieved until reaching the materials yield criterion at the inner and/or outer edge of the profile. Afterwards, plastic material deformation initiates. Strain follows a linear distribution from tensile forming at the outer fiber to compression at the intrados ($-0.5 < o < 0.5$). Work hardening and elastic deformation will cause a corresponding stress distribution over the profile width h. After

unloading, residual stresses would converge towards an equilibrium which causes angular springback geometrically.

5.3.1 In-plane bending under plastic material flow

The location, shape and size of the forming zone of frictionally engaged bending is of particular interest for the modelling approach of this thesis. Corresponding to the linear tensile process under frictional engagement, plastic strain builds up as a function of the material potion being stretched out from the firmly clamped area at the tool surfaces. A considerable influence of the clamping load F_N on the material drawn out of the clamping zone has been observed. Hence it determines the area of the forming zone. In conclusion, the remaining clamping area is required as a function of the bending angle and the clamping load applied by the clamping tools.

For the initial assumption of equilibrium of momenta according to Figure 35, each moment needs to be derived analytically. The plasto-mechanical bending moment M_z is caused by elastic deformations and the material's forming resistance related to work hardening. The lateral stress distribution over the y – coordinate, e.g., profile height, determines M_z. Hence, according to eq. (47), the general definition of M_z follows

$$M_z = \int_A \sigma(y) \cdot y \cdot dA = M_{z,\text{ten,pl}} + M_{z,\text{ten,el}} + M_{z,\text{comp,el}} + M_{z,\text{comp,pl}} \qquad \text{(eq. 55)}$$

where indices "*pl*" denote plastic forming and "*el*" represent elastic parts. The index "*ten*" indicates tensile amounts of the bending moments and "*comp*" indicates compressive elements, cf. Figure 36.

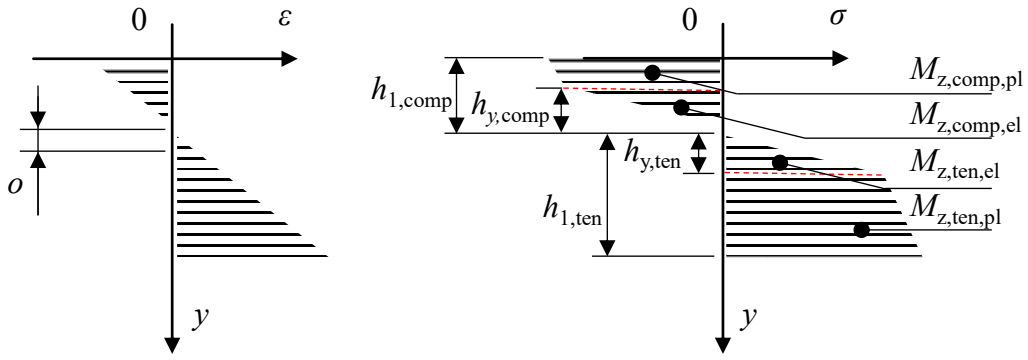

Figure 36: Lateral bending strain (left) and stress (right) distributions, offset by factor o and separated into compressive (*comp*) and tensile (*ten*) shares.

Corresponding to the offset bending axis and the lateral locations of yield criterion in the tensile and compressive areas, the profile's width h_0 is separated into four parts, which represent the integration limits. M_z is determined by

$$M_z = s(y) \cdot \int_{h_{y,ten}}^{h_{1,ten}} \sigma(y) \cdot y \cdot dy + s_0 \cdot \int_{h_{y,comp}}^{h_{y,ten}} \sigma(y) \cdot y \cdot dy + s(y) \cdot \int_{h_{1,comp}}^{h_{y,comp}} \sigma(y) \cdot y \cdot dy \quad \text{(eq. 56)}$$

with the lateral locations of yield criterion within the tensile $h_{y,ten}$ and the compressive $h_{y,comp}$ area. In the center of the forming zone close to the bending axis, in between $h_{y,ten}$ and $h_{y,comp}$, elastic bending prevails. In longitudinal direction, the elastic-plastic transition is associated to the yield sheath, corresponding to the tensile forming process. The yield sheath is introduced to frictionally engaged in-plane bending, according to Figure 37.

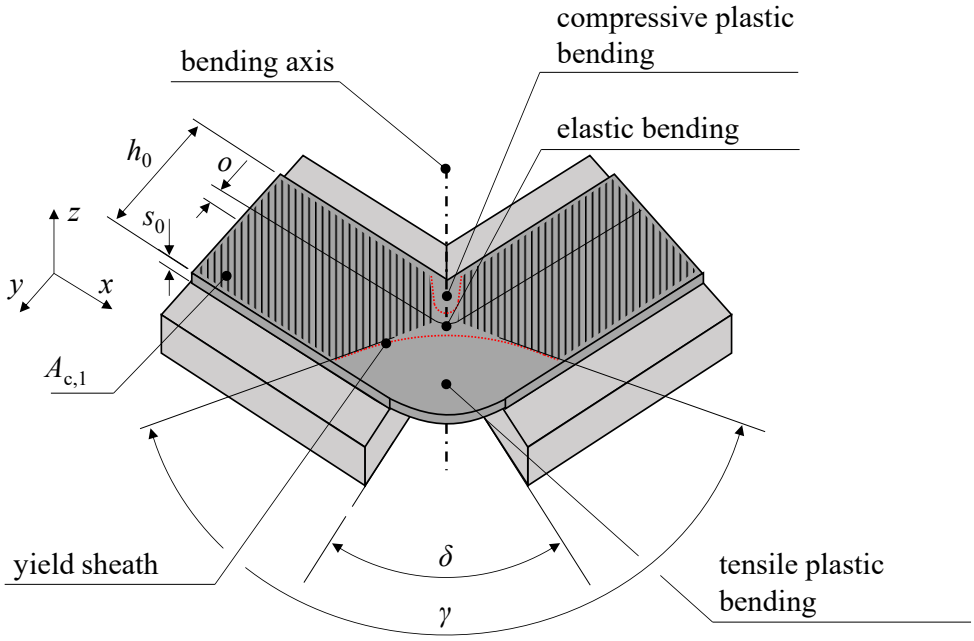

Figure 37: Illustration of the yield sheath during in-plane bending.

Evidently, the forming zone in between the borders of the yield sheath has an angular character and is measured by the forming zone angle γ. While free plastic bending deformation prevails within the forming zone, beyond the yield sheath the material is clamped under traction in the remaining contact areas $A_{c,1}$. At the yield sheath, no plastic deformation of cross section occurs and a constant distribution of equivalent strain σ_{eq} is propagated over profile height h_0 at the yield criterion. Under neglect of elastic bending moments, the bending moment at the yield sheath M_{ys} is expressed as

$$M_{ys} = s_0 \cdot \int_{h_{0,comp}}^{h_{0,ten}} \sigma_{eq} \cdot y \cdot dy = s_0 \cdot \frac{\sigma_{eq}}{2} \cdot {h_0}^2 . \quad \text{(eq. 57)}$$

M_{ys} is hence assumed independent of the bending axis offset and plastic strain within the forming zone. According to the assumption of eq. (38) for σ_{eq} in linear tensile forming, eq. (57) becomes

$$M_{ys} = s_0 \cdot {h_0}^2 \frac{R_e - \frac{\mu_0}{\sqrt{3}} \cdot \frac{-F_N}{2 \cdot A_{c,1}}}{2}. \quad \text{(eq. 58)}$$

σ_{eq} includes shearing applied to the multiaxial stress state but neglects the influence of normal pressure σ_N on the yield criterion. Note the negative algebraic sign for the implementation of F_N in eq. 58) due to compression.

Strain assumption for in-plane bending

During plastic deformation under increasing bending angle δ, work hardening successively raises the bending moment M_z required for material forming. According to COULOMB's law, the clamping force applied to the die surfaces corresponds to a maximum transmissible friction shear stress, which increases with the shrinking area of contact. In the yield sheath, a transition between the remaining firmly clamped material and the plastically formed material is observed which is characterized by the yield criterion of the multiaxial application of stresses. According to Figure 37, the yield sheath can be expressed by the zone angle γ, which spans significantly wider than the bending angle δ opened in between the clamping tools. With regard to the general formulation of strain, $\varepsilon = \Delta l / l_0$, the following conclusions are drawn in consequence

$$l_0 = (\gamma - \delta) \cdot \frac{\pi}{180} \cdot y \quad \text{(eq. 59)}$$

$$l_1 = \gamma \cdot \frac{\pi}{180} \cdot y \quad \text{(eq. 60)}$$

$$\Delta l = \delta \cdot \frac{\pi}{180} \cdot y \quad \text{(eq. 61)}$$

and longitudinal tensile strain at the extrados $\varepsilon_{x,ten,ecc}$ becomes

$$\varepsilon_{x,\mathrm{ten,ecc}} = \frac{\Delta l}{l_0} = \frac{\delta}{\gamma - \delta}. \quad \text{(eq. 62)}$$

Eq. (62) delivers a constant strain distribution over profile height. The definition is considered valid for straining of the extrados where material is stretched out from under the clamped surfaces. In order

to account for a linear strain distribution over profile height h, the distribution needs to be justified by the bending axis offset. If $o \neq 0.5$ is adjusted in the process, tensile strain at the extrados $\varepsilon_{x,\mathrm{ten}}$ follows

$$\varepsilon_{x,\mathrm{ten}} = \frac{\delta}{\gamma - \delta} \cdot (0.5 + o) \,. \qquad \text{(eq. 63)}$$

If the offset is chosen as $o < 0.5$, compressive strain will occur at the intrados. Here, material is not drawn out of the clamping in between the clamping tools as it underlies compression. Under the tool surfaces at the inner arc, material tends to thicken due to transversal strain but is severely hindered by the clamping pressure. Therefore, the effect of release of contact at the yield sheath is not observed at the intrados. For technical reasons, an angular gap λ in between both clamping tools is required at the intrados. Material will preferably plastically compress within this gap. Hence, compressive strain at the intrados must be expressed differently from the extrados and is assumed to be bound to the tool geometry. Compressive strain thus does not relate to the forming zone angle γ, as in the case of the tensile shares of bending strain. Consequently, compressive strain is formulated according to

$$\varepsilon_{x,\mathrm{comp,ecc}} = \frac{\Delta l}{l_0} = \frac{-\delta}{\lambda} \qquad \text{(eq. 64)}$$

which, like eq. (62), delivers no lateral dependency and is assumed valid for $o = -0.5$. For any other configuration, eq. (64) must be width justified by

$$\varepsilon_{x,\mathrm{comp}} = \frac{-\delta}{\lambda} \cdot (-o + 0.5) \,. \qquad \text{(eq. 65)}$$

When compressive strains are adjusted by o, buckling tendencies are observed and should be suppressed by tooling.

Derivation of the mathematical model for the forming zone of in-plane bending

The clamping force F_N is applied to the process to prevent material from slipping during bending. The previously presented dimensioning of F_N was based on the assumption, that maximum process forces appear at uniform tensile elongation regardless of the incremental bending angle δ. In contrast, the hereby developed model for the forming zone of in-plane bending is intended to describe strain as a function of δ besides the relation to the applied material and process parameters. The internal bending moment M_z is determined by the materials forming resistance against bending and underlies

free deformation where no tool contact applies, corresponding to Figure 35. From the lateral bending strain distribution according to Figure 36, the corresponding stress distribution is obtained within the areas of plastic material flow. Applying a bilinear hardening law, the internal bending moment M_z follows

$$M_z = M_{z,\text{ten,pl}} + M_{z,\text{ten,el}} + M_{z,\text{comp,el}} + M_{z,\text{comp,pl}} = M_{z,\text{ten,pl}} + M_{z,\text{el}} + M_{z,\text{comp,pl}}$$
$$= s(y) \cdot \int_{h_{\text{y,ten}}}^{h_{1,\text{ten}}} \left(m \cdot \frac{\varepsilon_{x,\text{ten}}}{h_{1,\text{ten}}} \cdot y + R_e \left(1 - \frac{m}{E}\right) \right) \cdot y \cdot dy + s_0 \cdot \int_{h_{\text{y,comp}}}^{h_{\text{y,ten}}} \frac{\sigma_M}{h_y} \cdot y \cdot y \cdot dy$$
$$+ s(y) \cdot \int_{h_{1,\text{comp}}}^{h_{\text{y,comp}}} - \left(m \cdot \frac{\varepsilon_{x,\text{comp}}}{h_{1,\text{comp}}} \cdot y + R_e \left(1 - \frac{m}{E}\right) \right) \cdot y \cdot dy$$

where σ_M/h_y becomes $\sigma_M/h_{\text{y,ten}}$ for $o \geq 0$ and $\sigma_M/h_{\text{y,comp}}$ for $o < 0$. Assuming an identical elastic modulus for compression and tension, the corresponding elastic bending moments are summarized in $M_{z,\text{el}}$. If transverse strain over thickness $\varepsilon_z(y)$ is neglected, the bending moment becomes

$$\frac{M_z}{s_0} = \left[\frac{m}{3} \cdot \frac{\varepsilon_{x,\text{ten}}}{h_{1,\text{ten}}} \cdot y^3 + \frac{R_e}{2} \left(1 - \frac{m}{E}\right) \cdot y^2 \right]_{h_{\text{y,ten}}}^{h_{1,\text{ten}}} + \left[-\frac{m}{3} \cdot \frac{\varepsilon_{x,\text{comp}}}{h_{1,\text{comp}}} \cdot y^3 - \frac{R_e}{2} \left(1 + \frac{m}{E}\right) \cdot y^2 \right]_{h_{1,\text{comp}}}^{h_{\text{y,comp}}}$$
$$+ \left[\frac{R_e}{3h_y} \cdot y^3 \right]_{h_{\text{y,comp}}}^{h_{\text{y,ten}}}$$

If elastic parts of the bending moment are excluded from the analytic derivation, the tensile and compressive bending moment integrals reach from zero to the outer edges of the profile height. $M_{z,\text{el}}$ contributes to the bending moment M_z only at small bending angles significantly and is therefore neglected. M_z/s_0 becomes

$$\frac{M_z}{s_0} = \left[\frac{m}{3} \cdot \frac{\varepsilon_{x,\text{ten}}}{h_{1,\text{ten}}} \cdot y^3 + \frac{R_e}{2} \left(1 - \frac{m}{E}\right) \cdot y^2 \right]_{0}^{h_{1,\text{ten}}} + \left[-\frac{m}{3} \cdot \frac{\varepsilon_{x,\text{comp}}}{h_{1,\text{comp}}} \cdot y^3 + \frac{R_e}{2} \left(1 - \frac{m}{E}\right) \cdot y^2 \right]_{h_{1,\text{comp}}}^{0}$$
$$= \frac{m}{3} \cdot \frac{\varepsilon_{x,\text{ten}}}{h_{1,\text{ten}}} \cdot {h_{1,\text{ten}}}^3 + \frac{R_e}{2} \left(1 - \frac{m}{E}\right) \cdot {h_{1,\text{ten}}}^2 - \left(-\frac{m}{3} \cdot \frac{\varepsilon_{x,\text{comp}}}{h_{1,\text{comp}}} \cdot {h_{1,\text{comp}}}^3 - \frac{R_e}{2} \left(1 + \frac{m}{E}\right) \cdot {h_{1,\text{comp}}}^2 \right)$$
$$= \frac{m}{3} \cdot \left(\varepsilon_{x,\text{ten}} \cdot {h_{1,\text{ten}}}^2 + \varepsilon_{x,\text{comp}} \cdot {h_{1,\text{comp}}}^2 \right) + \frac{R_e}{2} \left({h_{1,\text{ten}}}^2 \cdot \left(1 - \frac{m}{E}\right) + {h_{1,\text{comp}}}^2 \cdot \left(1 + \frac{m}{E}\right) \right)$$

Within the yield sheath, the bending moment M_{ys} is propagated over the undeformed cross section of the material A_0. The elastic deformations resulting from the surface-normal clamping pressure are neglected as well as transversal elastic contractions resulting from longitudinal elastic strain. Including the formulation of M_{ys} according to eq. (58), all moments within the bending plane are equated according to

$$M_z \stackrel{!}{=} M_{YS} \stackrel{!}{=} 2M_{fric}. \qquad \text{(eq. 66)}$$

and Figure 38.

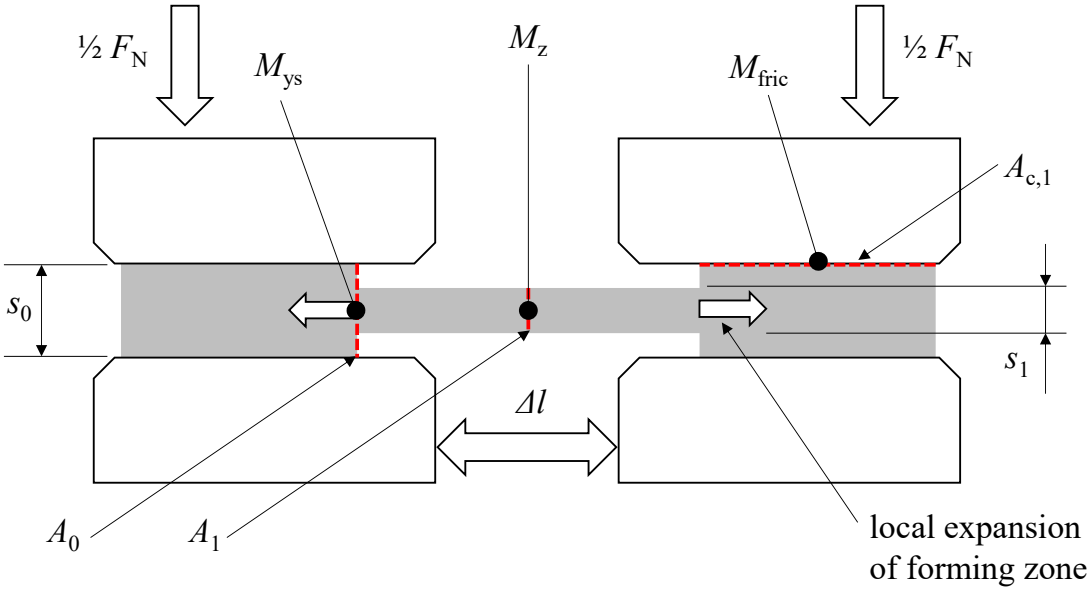

Figure 38: Illustration of the applied assumptions to describe the forming zone in frictionally engaged in-plane bending. The bending moment M_{ys} lasts at the yield sheath over the initial cross section of the material A_0. The model for the internal bending moment M_z is propagated over the cross section plastically deformed by transversal strains A_1. The friction moments M_{fric} are applied to the area of contact between tool faces and material $A_{c,1}$ which is continuously reduced by plastic thinning of the material.

Equation (66) becomes

$$\Rightarrow s_0 \left(\frac{m}{3} \cdot \left(\varepsilon_{x,ten} \cdot {h_{1,ten}}^2 + \varepsilon_{x,\mathrm{comp}} \cdot {h_{1,\mathrm{comp}}}^2 \right) + \frac{R_e}{2} \left({h_{1,ten}}^2 \cdot \left(1 - \frac{m}{E} \right) + {h_{1,\mathrm{comp}}}^2 \cdot \left(1 + \frac{m}{E} \right) \right) \right)$$

$$= s_0 \cdot {b_0}^2 \frac{R_e - \frac{\mu_0}{\sqrt{3}} \cdot \frac{-F_N}{2 \cdot A_{c,1}}}{2} = 2M_{fric}$$

$$\Leftrightarrow A_{c,1} \cdot \frac{m}{3} \cdot \left(\varepsilon_{x,ten} \cdot {h_{1,ten}}^2 + \varepsilon_{x,\mathrm{comp}} \cdot {h_{1,\mathrm{comp}}}^2\right)$$
$$+A_{c,1} \cdot \left(\frac{R_e}{2}\left({h_{1,\mathrm{ten}}}^2 \cdot \left(1 - \frac{m}{E}\right) + {h_{1,\mathrm{comp}}}^2 \cdot \left(1 + \frac{m}{E}\right)\right) - \frac{{h_0}^2 \cdot R_e}{2}\right) - \frac{\mu_0 \cdot {h_0}^2 \cdot F_N}{\sqrt{3} \cdot 4} = 0$$

The substitution $S_1 = \frac{\mu_0 \cdot {h_0}^2 \cdot F_N}{\sqrt{3} \cdot 4}$ is associated with the frictional transmission of force and delivers

$$0 = A_{c,1} \cdot \frac{m}{3} \cdot \left(\varepsilon_{x,\mathrm{ten}} \cdot {h_{1,\mathrm{ten}}}^2 + \varepsilon_{x,\mathrm{comp}} \cdot {h_{1,\mathrm{comp}}}^2\right)$$
$$+A_{c,1} \cdot \left(\frac{R_e}{2}\left({h_{1,\mathrm{ten}}}^2 \cdot \left(1 - \frac{m}{E}\right) + {h_{1,\mathrm{comp}}}^2 \cdot \left(1 + \frac{m}{E}\right)\right) - \frac{{h_0}^2 \cdot R_e}{2}\right) - S_1 \qquad \text{(eq. 67)}$$

If eq. (67) is solved for strain, equations to the power of five are obtained. To allow solving the equations in a purely analytical way, transversal strains over profile height and thickness are neglected: $\varepsilon_y(y) = \varepsilon_z(y) = 0$. Accordingly, eq. (67) is simplified by $h_1 = h_0$ and follows

$$0 = A_{c,1} \cdot \frac{m}{3} \cdot \left(\varepsilon_{x,\mathrm{ten}} \cdot {h_{0,\mathrm{ten}}}^2 + \varepsilon_{x,\mathrm{comp}} \cdot {h_{0,\mathrm{comp}}}^2\right)$$
$$+A_{c,1} \cdot \left(\frac{R_e}{2}\left({h_{0,\mathrm{ten}}}^2 \cdot \left(1 - \frac{m}{E}\right) + {h_{0,\mathrm{comp}}}^2 \cdot \left(1 + \frac{m}{E}\right)\right) - \frac{{h_0}^2 \cdot R_e}{2}\right) - S_1 \,. \qquad \text{(eq.68)}$$

Including the offset parts of the initial profile height according to $h_{0,\mathrm{ten}} = h_0 \cdot (½ + o)$ and $h_{0,\mathrm{comp}} = h_0 \cdot (½ - o)$, eq. (68) becomes

$$0 = A_{c,1} \cdot \frac{m}{3} \cdot \left(\varepsilon_{x,\mathrm{ten}} \cdot {h_0}^2 \cdot \left(\frac{1}{2} + o\right)^2 + \varepsilon_{x,\mathrm{comp}} \cdot {h_0}^2 \cdot \left(\frac{1}{2} - o\right)^2\right)$$
$$+A_{c,1} \cdot \left(\frac{R_e}{2} \cdot \left({h_0}^2 \cdot \left(\frac{1}{2} + o\right)^2 \cdot \left(1 - \frac{m}{E}\right) + {h_0}^2 \cdot \left(\frac{1}{2} - o\right)^2 \cdot \left(1 + \frac{m}{E}\right)\right) - \frac{{h_0}^2 \cdot R_e}{2}\right) - S_1$$
$$= A_{c,1} \cdot \frac{m}{3} \cdot {h_0}^2 \left(\varepsilon_{x,\mathrm{ten}} \cdot \left(\frac{1}{2} + o\right)^2 + \varepsilon_{x,\mathrm{comp}} \cdot \left(\frac{1}{2} - o\right)^2\right)$$
$$+A_{c,1} \cdot {h_0}^2 \cdot \frac{R_e}{2}\left(\left(\left(\frac{1}{2} + o\right)^2 \cdot \left(1 - \frac{m}{E}\right) + \left(\frac{1}{2} - o\right)^2 \cdot \left(1 + \frac{m}{E}\right)\right) - 1\right) - S_1$$

The substitution $S_2 = \left(\left(\left(\frac{1}{2}+o\right)^2 \cdot \left(1-\frac{m}{E}\right) + \left(\frac{1}{2}-o\right)^2 \cdot \left(1+\frac{m}{E}\right)\right) - 1\right)$ is related to stiffness and delivers

$$0 = A_{c,1} \cdot \frac{m}{3} \cdot {h_0}^2 \left(\varepsilon_{x,\text{ten}} \cdot \left(\frac{1}{2}+o\right)^2 + \varepsilon_{x,\text{comp}} \cdot \left(\frac{1}{2}-o\right)^2\right) + A_{c,1} \cdot {h_0}^2 \cdot \frac{R_e}{2} \cdot S_2 - S_1 \qquad \text{(eq. 69)}$$

The contact zone under plastic bending deformation of the clamped material $A_{c,1}$ is expressed by

$$A_{c,1} = h_0 \cdot \left(l_{c,0} - \frac{1}{2} \cdot h_0 \cdot 2 \cdot \frac{\gamma-\delta}{\pi}\right) \qquad \text{(eq. 70)}$$

with the mathematical approximation $\tan\left(\frac{\gamma-\delta}{2}\right) \approx 2\frac{\gamma-\delta}{\pi}$.

Together with the strain assumptions

- eq. (63), $\varepsilon_{x,\text{ten}} = \frac{\delta}{\gamma-\delta} \cdot \left(\frac{1}{2}+o\right)$,
- eq. (65), $\varepsilon_{x,\text{comp}} = \frac{-\delta}{\lambda} \cdot \left(-o+\frac{1}{2}\right)$,

eq. (69) becomes

$$\begin{aligned} 0 = {} & h_0 \cdot \left(l_{c,0} - \frac{1}{2} \cdot h_0 \cdot 2 \cdot \frac{\gamma-\delta}{\pi}\right) \cdot \frac{m}{3} \\ & \cdot {h_0}^2 \left(\frac{\delta}{\gamma-\delta} \cdot \left(\frac{1}{2}+o\right) \cdot \left(\frac{1}{2}+o\right)^2 + \frac{-\delta}{\lambda} \cdot \left(-o+\frac{1}{2}\right) \cdot \left(\frac{1}{2}-o\right)^2\right) + h_0 \\ & \cdot \left(l_{c,0} - \frac{1}{2} \cdot h_0 \cdot 2 \cdot \frac{\gamma-\delta}{\pi}\right) \cdot {h_0}^2 \cdot \frac{R_e}{2} \cdot S_2 - S_1 \\ = {} & \left(l_{c,0} - h_0 \cdot \frac{\gamma-\delta}{\pi}\right) \cdot \frac{m}{3} \cdot \left(\frac{\delta}{\gamma-\delta} \cdot \left(\frac{1}{2}+o\right)^3 + \frac{-\delta}{\lambda} \cdot \left(\frac{1}{2}-o\right)^3\right) + \left(l_{c,0} - h_0 \cdot \frac{\gamma-\delta}{\pi}\right) \cdot \frac{R_e}{2} \cdot S_2 \\ & - \frac{S_1}{{h_0}^3} \\ = {} & \left(l_{c,0} \cdot \frac{m}{3} - h_0 \cdot \frac{\gamma-\delta}{\pi} \cdot \frac{m}{3}\right) \cdot \left(\frac{\delta}{\gamma-\delta} \cdot \left(\frac{1}{2}+o\right)^3 - \delta \frac{\left(\frac{1}{2}-o\right)^3}{\lambda}\right) - \gamma \cdot \frac{h_0}{\pi} \cdot \frac{R_e \cdot S_2}{2} + \delta \cdot \frac{h_0}{\pi} \cdot \frac{R_e \cdot S_2}{2} \\ & + l_{c,0} \cdot \frac{R_e \cdot S_2}{2} - \frac{S_1}{{h_0}^3} \end{aligned}$$

$$= \frac{\delta}{\gamma-\delta}\cdot l_{c,0}\cdot\frac{m}{3}\cdot\left(\frac{1}{2}+o\right)^3-\delta\cdot\frac{m}{3}\cdot\left(\frac{h_0}{\pi}\cdot\left(\frac{1}{2}+o\right)^3+l_{c,0}\cdot\frac{\left(\frac{1}{2}-o\right)^3}{\lambda}\right)+(\gamma-\delta)\cdot\delta\cdot\frac{h_0}{\pi}\cdot\frac{m}{3}$$

$$\cdot\frac{\left(\frac{1}{2}-o\right)^3}{\lambda}-\gamma\cdot\frac{h_0}{\pi}\cdot\frac{R_e\cdot S_2}{2}+\delta\cdot\frac{h_0}{\pi}\cdot\frac{R_e\cdot S_2}{2}+l_{c,0}\cdot\frac{R_e\cdot S_2}{2}-\frac{S_1}{{h_0}^3}$$

$$= -(\gamma^2-\gamma\delta)\cdot\frac{h_0}{\pi}\cdot\frac{R_e\cdot S_2}{2}+(-\gamma\delta+\delta^2)$$

$$\cdot\left(\frac{m}{3}\cdot\left(\frac{h_0}{\pi}\cdot\left(\frac{1}{2}+o\right)^3+l_{c,0}\cdot\frac{\left(\frac{1}{2}-o\right)^3}{\lambda}\right)-\frac{h_0}{\pi}\cdot\frac{R_e\cdot S_2}{2}\right)+(\gamma\delta^2-2\gamma\delta^2+\delta^3)\cdot\frac{h_0}{\pi}$$

$$\cdot\frac{m}{3}\cdot\frac{\left(\frac{1}{2}-o\right)^3}{\lambda}+(\gamma-\delta)\cdot\left(l_{c,0}\cdot\frac{R_e\cdot S_2}{2}-\frac{S_1}{{h_0}^3}\right)+\delta\cdot l_{c,0}\cdot\frac{m}{3}\cdot\left(\frac{1}{2}+o\right)^3$$

Substituting the cubic offset terms for tension by

$$S_{3,\mathrm{t}} = \left(\frac{1}{2}+o\right)^3$$

and for compression by

$$S_{3,\mathrm{c}} = \left(\frac{1}{2}-o\right)^3$$

delivers

$$= -\gamma^2\cdot\frac{h_0}{\pi}\cdot\frac{R_e\cdot S_2}{2}+\gamma\delta\cdot\frac{h_0}{\pi}\cdot\frac{R_e\cdot S_2}{2}-\gamma\delta\cdot\left(\frac{m}{3}\cdot\left(\frac{h_0}{\pi}\cdot S_{3t}+l_{c,0}\cdot\frac{S_{3c}}{\lambda}\right)-\frac{h_0}{\pi}\cdot\frac{R_e\cdot S_2}{2}\right)+\delta^2$$

$$\cdot\left(\frac{m}{3}\cdot\left(\frac{h_0}{\pi}\cdot S_{3t}+l_{c,0}\cdot\frac{S_{3c}}{\lambda}\right)-\frac{h_0}{\pi}\cdot\frac{R_e\cdot S_2}{2}\right)+\delta^3\cdot\frac{h_0}{\pi}\cdot\frac{m}{3}\cdot\frac{S_{3c}}{\lambda}-\gamma\delta^2\cdot\frac{h_0}{\pi}\cdot\frac{m}{3}\cdot\frac{S_{3c}}{\lambda}+\gamma$$

$$\cdot\left(l_{c,0}\cdot\frac{R_e\cdot S_2}{2}-\frac{S_1}{{h_0}^3}\right)-\delta\cdot\left(l_{c,0}\cdot\frac{R_e\cdot S_2}{2}-\frac{S_1}{{h_0}^3}\right)+\delta\cdot l_{c,0}\cdot\frac{m}{3}\cdot S_{3t}$$

$$= -\gamma^2 \cdot \frac{h_0}{\pi} \cdot \frac{R_e \cdot S_2}{2} - \gamma \left(\delta^2 \cdot \frac{h_0}{\pi} \cdot \frac{m}{3} \cdot \frac{S_{3c}}{\lambda} - \delta \cdot \frac{h_0}{\pi} \cdot \frac{R_e \cdot S_2}{2} + \delta \cdot \left(\frac{m}{3} \cdot \left(\frac{h_0}{\pi} \cdot S_{3t} + l_{c,0} \cdot \frac{S_{3c}}{\lambda} \right) - \frac{h_0}{\pi} \cdot \frac{R_e \cdot S_2}{2} \right) - \left(l_{c,0} \cdot \frac{R_e \cdot S_2}{2} - \frac{S_1}{{h_0}^3} \right) \right) + \delta \left(\delta^2 \cdot \frac{h_0}{\pi} \cdot \frac{m}{3} \cdot \frac{S_{3c}}{\lambda} + \delta \cdot \left(\frac{m}{3} \cdot \left(\frac{h_0}{\pi} \cdot S_{3t} + l_{c,0} \cdot \frac{S_{3c}}{\lambda} \right) - \frac{h_0}{\pi} \cdot \frac{R_e \cdot S_2}{2} \right) - \left(l_{c,0} \cdot \frac{R_e \cdot S_2}{2} - \frac{S_1}{{h_0}^3} \right) + l_{c,0} \cdot \frac{m}{3} \cdot S_{3t} \right)$$

$$= \gamma^2 - \gamma \left(-\frac{2}{3} \cdot \delta^2 \cdot \frac{m}{R_e \cdot S_2} \cdot \frac{S_{3c}}{\lambda} + \delta - \delta \cdot \left(\frac{2}{3} \cdot \frac{m}{R_e \cdot S_2} \cdot \left(S_{3t} + \frac{\pi}{h_0} \cdot l_{c,0} \cdot \frac{S_{3c}}{\lambda} \right) - 1 \right) + \frac{\pi}{h_0} \cdot \left(l_{c,0} - \frac{S_1}{{h_0}^3} \cdot \frac{2}{R_e \cdot S_2} \right) \right) + \delta \left(-\frac{2}{3} \cdot \delta^2 \cdot \frac{m}{R_e \cdot S_2} \cdot \frac{S_{3c}}{\lambda} - \delta \cdot \left(\frac{2}{3} \cdot \frac{m}{R_e \cdot S_2} \cdot \left(S_{3t} + \frac{\pi}{h_0} \cdot l_{c,0} \cdot \frac{S_{3c}}{\lambda} \right) - 1 \right) + \frac{\pi}{h_0} \cdot \left(l_{c,0} - \frac{2}{R_e \cdot S_2} \cdot \frac{S_1}{{h_0}^3} \right) - \frac{\pi}{h_0} \cdot \frac{2}{R_e \cdot S_2} \cdot l_{c,0} \cdot \frac{m}{3} \cdot S_{3t} \right) \quad \text{(eq. 71)}$$

Eq. (71) delivers the universal formulation of the forming zone angle γ of in-plane bending under traction with

a) the transmission of force related substitution $S_1 = \frac{\mu \cdot {h_0}^2 \cdot F_N}{\sqrt{3} \cdot 4}$,

b) the stiffness term $S_2 = \left(\left(\left(\frac{1}{2} + o \right)^2 \cdot \left(1 - \frac{m}{E} \right) + \left(\frac{1}{2} - o \right)^2 \cdot \left(1 + \frac{m}{E} \right) \right) - 1 \right)$ and

c) the tension or compression related offset substitutions $S_{3t} = \left(\frac{1}{2} + o \right)^3$ and $S_{3c} = \left(\frac{1}{2} - o \right)^3$.

An eccentric bending axis with pure tensile bending values (o = 0.5) is often preferred in an ISB process to avoid wrinkles, in particular when bending hollow open profiles. For this offset, the substitutions deliver $S_2 = -m/E$, $S_{3t} = 1$ and $S_{3c} = 0$. Eq. (71) becomes

$$0 = \gamma^2 - \gamma\left(\frac{2}{3}\cdot\frac{E\cdot\delta}{R_e} + 2\delta + \pi\frac{l_{c,0}}{h_0} + \frac{\mu_0\cdot F_N\cdot E\cdot\pi}{\sqrt{3}\cdot 2R_e\cdot m\cdot {h_0}^2}\right) + \delta\left(\left(\frac{2}{3}\frac{E}{R_e}+1\right)\cdot\left(\delta + \frac{\pi\cdot l_{c,0}}{h_0}\right) + \frac{\mu_0\cdot F_N\cdot E\cdot\pi}{\sqrt{3}\cdot 2R_e\cdot m\cdot {h_0}^2}\right) \quad \text{(eq. 72)}$$

By substituting

$$q_1 = -\left(\frac{2}{3}\frac{E\cdot\delta}{R_e} + 2\delta + \pi\frac{l_{c,0}}{h_0} + \frac{\mu_0\cdot F_N\cdot E\cdot\pi}{\sqrt{3}\cdot 2R_e\cdot m\cdot {h_0}^2}\right)$$

and

$$q_2 = \delta\left(\left(\frac{2}{3}\frac{E}{R_e}+1\right)\cdot\left(\delta + \frac{\pi\cdot l_{c,0}}{h_0}\right) + \frac{\mu_0\cdot F_N\cdot E\cdot\pi}{\sqrt{3}\cdot 2R_e\cdot m\cdot {h_0}^2}\right),$$

eq. (72) is solved by the quadratic expression

$$\gamma_{1/2} = -\frac{q_1}{2} \pm \sqrt{\left(\frac{q_1}{2}\right)^2 - q_2} \quad \text{(eq. 73)}$$

Note: Throughout the derivation, all angles are expected in radiant units.

With regard to the bending process, reasonable results are obtained for γ_1, i.e., positive algebraic sign in front of the square root of eq. (72). Under a given load F_N and under consideration of the bending angle δ of the clamping tools, the size of the forming zone is obtained by means of the zone angle γ. If the forming zone is incorporated in a strain assumption such as eq. (62), strain is obtained in relation to the process and material parameters. For an in-plane bending process under frictional engagement such as ISB, the model presented above determines the material portion being drawn out of the contact area in between tools and material. The analytical model thus allows to determine strain within the forming zone. Besides mathematical approximations, specifically the following simplifications are specifically considered relevant:

- The elastic or plastic transversal strains are not accounted for in the internal bending moment M_z and also in the bending moment at the yield sheath M_{ys},
- Not considering elastic parts of M_z,
- Not considering normal pressure in the formulation of M_{ys},
- Application of a bilinear hardening law.

5.3.2 Sandglass-type strain assumption

In eq. (62), longitudinal strain is propagated with a constant distribution over the angular coordinate of the forming zone. Successive material flow associated with the continuous displacement of the yield sheath, however, will lead to longitudinal strain gradients with regard to beginning and ending of the forming zone. Regarding the discussion of the linear tensile process, the evaluation of a simulation result shows a transition of longitudinal strain and thickness, also see Figure 29, p. 74. Figure 39 schematically shows a longitudinal cut view through the forming zone to illustrate different strain assumptions. During plastic material flow, these assumptions underlie the law of volume constancy.

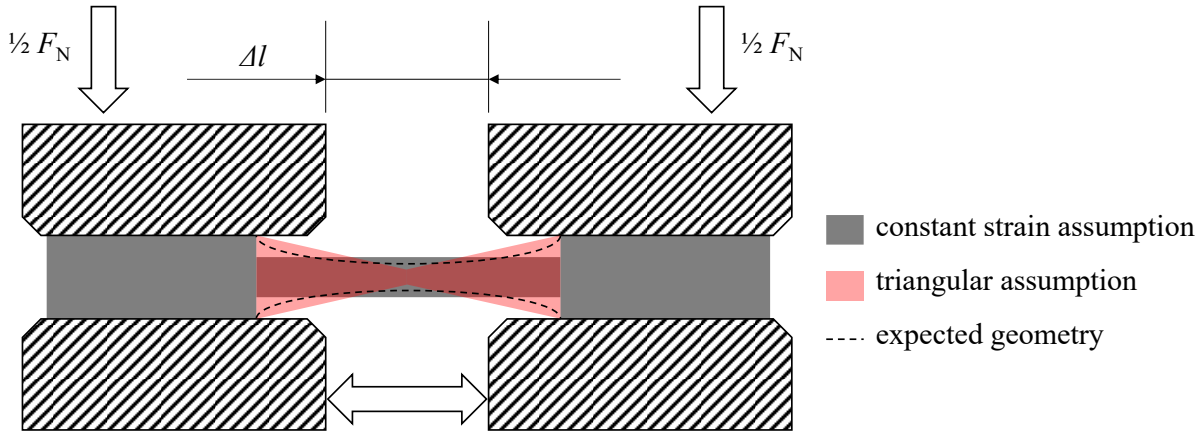

Figure 39: Longitudinal cross section of a metallic strip in the forming zone of frictionally engaged straining. Illustration of three different strain assumptions, i.e., constant or average strain, sandglass shaped approach and the expected realistic thickness distribution.

The strain hypothesis of eq. (62) propagates constant strain throughout the forming zone. Various experiments show however, that a transition of strain and accordingly, sheet metal thickness is obtained between the clamped area and the one freely stretched. To better agree to the expected transition, an sandglass or triangular shaped distribution is applied to the strain model. As illustrated in Figure 39, a sandglass assumption predicts higher material thinning in the central area of the forming zone and hence a higher strain maximum.

By geometric considerations, it can be shown that at the center of the sandglass shaped approach the longitudinal strain maximum $\varepsilon_{x,\Delta,max}$ is twice as high, as in the case of the linear approach:

$$\varepsilon_{x,\Delta,max} \approx 2 \cdot \varepsilon_x \qquad \text{(eq. 74)}$$

5.3.3 Springback

According to KHODAYARI (1993), the angle of springback results from the release of residual bending stresses. The plasto-mechanical bending moment M_z is opposed by a springback moment M_{SB} which results in the partial reversal of the formed angle. Hence, a reversing longitudinal strain $\varepsilon_{x,R}$ causes the incremental springback angle δ_{SB}. As strain is not related to any bending radius in the frictionally engaged bending process, the unloaded incremental bending angle δ_u is approximated as

$$\delta_u = \delta - \delta_{SB} \approx \delta(1 - 3 \cdot \frac{R_e}{E} \cdot \frac{1}{2\varepsilon_x}) \cdot \qquad \text{(eq. 75)}$$

in accordance to WITTEK, RICHTER, and LAZARZ (2011). For the remaining longitudinal strain $\varepsilon_{x,u}$ of the unloaded incremental bending angle, the relation

$$\varepsilon_{x,u} = \varepsilon - \varepsilon_{x,R} = \frac{\delta_u}{\gamma - \delta_u} \qquad \text{(eq. 76)}$$

is obtained.

5.4 Process window for frictionally engaged in-plane bending

With regards to practical use of the process model, it is desirable to provide a process window for the process variables. Considering the ISB process, the fundamental process variables are in detail are:

i. The clamping force F_N, by which the process is loaded,
ii. The bending angle δ, as imposed by the clamping tools,
iii. the offset o adjusted to the bending axis and
iv. feed Δf in between each bending increment.

In the preceding parts of this thesis, continuous bending of a single increment is considered. The key question addressed by the developed analytics is the prediction of strain and forming zone with respect to the process and material parameters. For bending by frictional engagement, the process window is developed by means of a diagram of clamping force plotted over bending angle. If a fully eccentric offset for tensile bending (o = 0.5) is adjusted, the simplified equation 72) is obtained. The corresponding process window is illustrated in Figure 40.

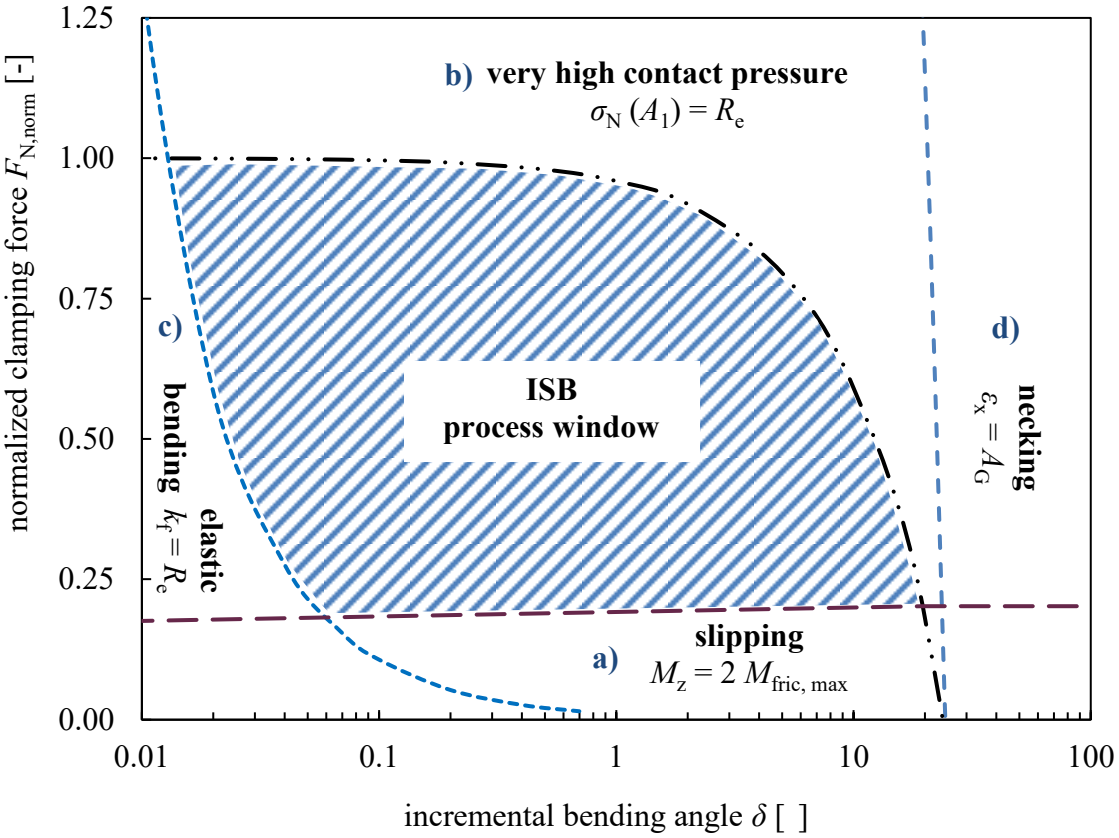

Figure 40: Process window for bending by frictional engagement plotted as normalized clamping force over bending angle. Four borders define the window, in detail a) if the clamping force is too low to transmit the forming forces, b) if the clamping force is so high, that material will be compressed over thickness, c) if the bending angle is too small for plasticizing or d) if the bending angle is so that it provokes material necking.

In the diagram, the clamping force F_N is normalized in a way that the initial clamping force $\sigma_{N,0}$ reaches the material's yield stress R_e. This normalized convention demonstrates the range of feasible process operation in comparison to the material's yielding. Under a uniaxial stress assumption, i.e., neglecting transversal compressive stresses due to friction at the tool surfaces, $F_{N,norm}$ is defined as

$$F_{N,norm} = \frac{F_N}{R_e \cdot 2A_{c,0}}. \qquad \text{(eq. 77)}$$

With regards to the process window, maximum and minimum process boundaries are obtained for the process variables F_N and δ:

a) F_N must be at least as high enough to allow traction at the tool surfaces to transmit the plasto-mechanical bending moment M_z. The maximum feasible friction moment a tool surface can transmit $M_{fric,max}$ is given by the law of COULOMB as a function of clamping force. Hence, the

friction moments must at least exceed the plasto-mechanical bending moment of the material: $2\,M_{fric,max} > M_z$.

b) A very high clamping force F_N could lead to plastic forming in the direction of sheet metal thickness by exceeding the material's yield stress ($F_{N,norm} = 1$). Under a uniaxial stress assumption, hence, normal pressure should be adjusted in a way $\sigma_N < R_e$. Since material is being pulled out of the clamping, the border will, in addition, drop significantly with increasing bending angle because of the reduction of contact surface. Exceeding this border could also lead to damaging the forming tools depending on the strength of the utilized tool steel. With regard to the process window, however, at small bending angles the critical clamping force is usually higher than any press intended for sheet metal forming could provide. Therefore, in practice, an additional upper border of the process window would be given by the forming machine (also see process windows in subchapters 0 and 7.3.2).

c) If the bending tool imposes an angle that is too small to provoke plasticizing, pure elastic bending will cause the angle to fully spring back to the original shape. Correspondingly, yield criterion is not exceeded at the extrados (or intrados). Hence, at the outer (or inner) edge, flow stress should at least exceed yield stress; $k_f > R_e$.

d) If high bending angles are adjusted, uniform tensile elongation might be exceeded at the intrados or extrados so material begins to neck. Thus, if necking is not intended, the bending angle must be chosen in a way to fulfill $\varepsilon_x \leq A_G$. In addition, the herein suggested design of an ISB tool would in only provide a limited bending angle due to the incremental forming nature of the process. Considering the relations of material formability and tool design, the maximum tool angle often limits the process windows right hand border by a constant bending angle, e.g., $\delta = 10°$ as in the case of the tools developed in this thesis.

Besides technological reasons (maximum press force and tool angle), the considered process boundaries a) – d) mathematically describe the borders of the process. They are defined by the following equations resulting from the aforementioned constraints. The least necessary clamping force $F_{N,min}$ to transmit the bending moment (case a) underlies the constraint $2M_{fric,max} = M_z$ which delivers

$$F_{N,min} = s_0 \cdot {h_0}^2 \cdot \left(\frac{m}{3} \cdot \varepsilon_x + \frac{R_e}{2} \cdot \left(1 - \frac{m}{E}\right)\right) \cdot \frac{8}{\mu_0 \cdot \left(l_{c,0} \cdot h_0\right)} \qquad \text{(eq. 78)}$$

Within the process window, eq. (78) is solved with a linear approach between $\varepsilon_x = 0$ and $\varepsilon_x = A_G$. As the forming forces and hence bending moment M_z would not increase after A_G, the lower border (a) of the process window is assumed constant after uniform tensile elongation.

For the highest feasible clamping force (case b), yield stress should not be exceeded in the actual clamping area $A_{c,1}$ to prevent bulk forming. Under assumption of uniaxial stress application, the corresponding critical normal pressure is expressed by

$$\sigma_N = R_e = \frac{F_N}{2A_{c,1}} = \frac{F_N}{2\left(h_0 \cdot \left(l_{c,0} - h_0 \cdot \frac{\gamma - \delta}{\pi}\right)\right)} \qquad \text{(eq. 79)}$$

under consideration of eq. (70). However, at the border of the process window, the forming zone angle γ is unknown. Therefore, the maximum feasible forming zone angle γ_{ult} which is related to the contact area is implemented in eq. 79). From observations, γ_{ult} is described by

$$\gamma_{ult} = \tan^{-1}\frac{l_{c,0}}{h_0}. \qquad \text{(eq. 80)}$$

Hence, γ_{ult} becomes 45° for a quadratic clamping ratio where $l_{c,0} = h_0$ applies.

If the bending angle δ is too small to exceed pure elastic deformation (case c), the material will spring back completely after release of clamping. For this border of the process window, the constraints $\varepsilon_x = \frac{R_e}{E}$ and $k_f = R_e$ are assumed at the extrados. Including any gap g between both clamping tools, for instance tool clearances and bevels, the equation for boundary (c) is derived from the elastic bending moment $M_{z,yield}$ in eq. (49) and follows

$$F_N = \frac{R_e \cdot s_0 \cdot A_{c,0}}{\mu_0 \cdot \left(\frac{\bar{\delta} \cdot E \cdot h_0}{R_e} - g\right)} \qquad \text{(eq. 81)}$$

To describe the border against necking as a function of bending angle and depending on clamping force, the equilibrium of moments in the bending plane according to eq. (66) can be solved for strain at uniform tensile elongation A_G delivering

$$F_N = \frac{\sqrt{3} \cdot m \cdot h_0}{\mu} \cdot \left(\frac{4}{3} A_G - \frac{2R_e}{E}\right) \cdot \left(l_{c,0} - \frac{h_0}{\pi} \cdot \delta \left(\frac{1}{A_G} - 1\right)\right) \qquad \text{(eq. 82)}$$

All equations to describe the boundaries of the process window of frictionally engaged bending, i.e., equations 78), 79), 81) and 82) underlie the simplifications and assumptions of the model developed in section 5.3.

5.5 FE-simulations of frictionally engaged bending

The analytical model for an in-plane bending process with a frictionally engaged transmission force is developed in a way to allow a self-containing mathematical solution. In addition, numerical methods are applied to complement the process modelling. For the dimensioning of clamping force, simulations based on planar shell elements are studied in an iterative way to review the layout of necessary clamping load application. In the second part of this section, a simulation model based on three-dimensional solid elements is established to analyze the forming zone in a qualitative and quantitative way. In general, the material modelling parameters are implemented according to the mechanical material tests conducted in chapter 4.2.1 and 4.2.2 using the work hardening law of SWIFT.

5.5.1 FE-Experiments on the clamping force during bending: Shell element simulations

The ISB process transmits the bending moment to the material under traction to shape a bending geometry in order to achieve high degree of flexibility because of an indistinct tooling. As a central claim of this thesis, the material must not slip under the firmly clamped surface for a defined and controlled process operation. To ensure this condition, the least necessary clamping force for stiction within the clamping is investigated by numerical simulations. A corresponding in-plane bending FE-model is implemented in the software PAM STAMP. The strip material is discretized by finite two-dimensional shell elements. Two square shaped clamping units are implemented by rigid bodies which act as active die faces. Under load, the pivoting unit rotates about the bending axis which is offsetable by the factor *o* while the stationary tool underlies fixed boundary conditions as shown in Figure 41.

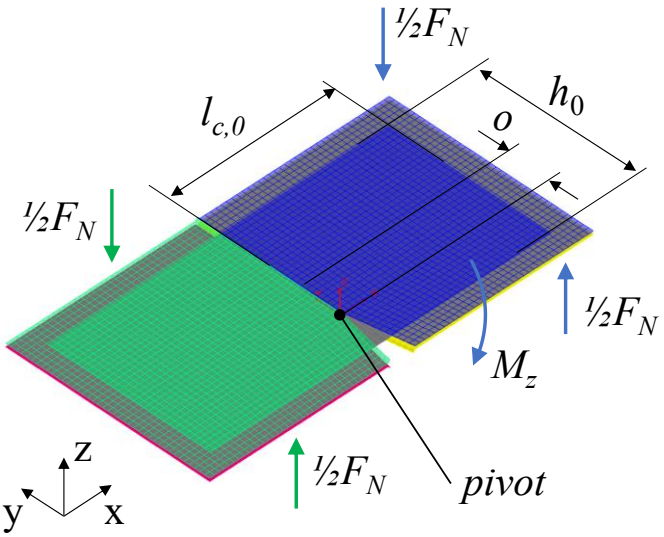

Figure 41: Visualization of the in-plane bending FE Model based on shell elements.

Corresponding to the physical ISB tools, the numerical tool models are angled at the inner arc, so thickening can freely adjust within the non-clamped area of the inner arc. If an offset with compressive bending stresses is adjusted ($o < 0.5$), wrinkles tend to appear at the inner arc. As instable buckling effects could influence the evaluation of bending moment, all finite elements of the blank are hindered from any displacement out of plane (translation along z coordinate). By monitoring the relative velocities between the elements of the material and the tools, a sufficient traction within the clamped surfaces is ensured. After the explicitly calculated bending stage, an additional implicit springback step is simulated.

Corresponding to the analytical model to determine the least necessary clamping force for firm fixation, two stages are of particular interest regarding material forming. Firstly, clamping must hold the material in place to allow the beginning of plastic deformation when the material overcomes yield stress. Secondly, the forming resistance would even rise until uniform tensile elongation is reached within the forming zone. For both stages, the clamping force can be determined by the analytical model. For validation, the corresponding FE-model is deployed to material strips from HCT780X, 42SiCr, FORTA H800 and S235JR, see Table 14. For each of these materials, the offset is varied within the discrete interval $o = \{-0.5, -0.25, 0, 0.25, 0.375, 0.5\}$. Constant friction coefficients were applied to the materials.

Table 14: Variation of materials and pivot offset implemented in the numerical model of in-plane bending. Evaluation of the least sufficient clamping force for frictional transmission of forming force.

Material	Bending axis offset	Cross section	Friction coefficient
	o	A_0	μ
	[-]	[mm²]	[-]
HCT780X	{-0.5, -0.25, 0, 0.25, 0.375, 0.5}	80 x 1.5	0.18
42SiCr			0.13
S235JR			0.12
FORTA H800			0.16

Regarding bending under offset conditions, the clamping force F_N is of particular interest as it represents a critical parameter for the process layout of the ISB process. The least necessary clamping force is evaluated from the FEM by raising F_N in an iterative approach until the inner or outer arc of the plane strip profile reaches i) yield stress or ii) uniform tensile elongation. From the results of the FE simulations, these states are assured by the criteria

i) Longitudinal true strain $\varphi_x = 0.002$, after calculation of springback.

ii) $\varphi_x = n$ at the inner or outer arc.

Firm fixation without the profile slipping under the tool surfaces was assured with respect to the relative velocity of tool and material. The necessary clamping forces, as predicted by the analytic model, are set in relation to the simulated F_N as a function of bending axis offset in Figure 42 for all considered sheet metals. Note that depending on the position of the bending axis, R_e or n could either be reached at the intrados or at the extrados of a bent arc. Given by these two cases, the graphs from the analytical models are composed of two curves, corresponding to these case discriminations.

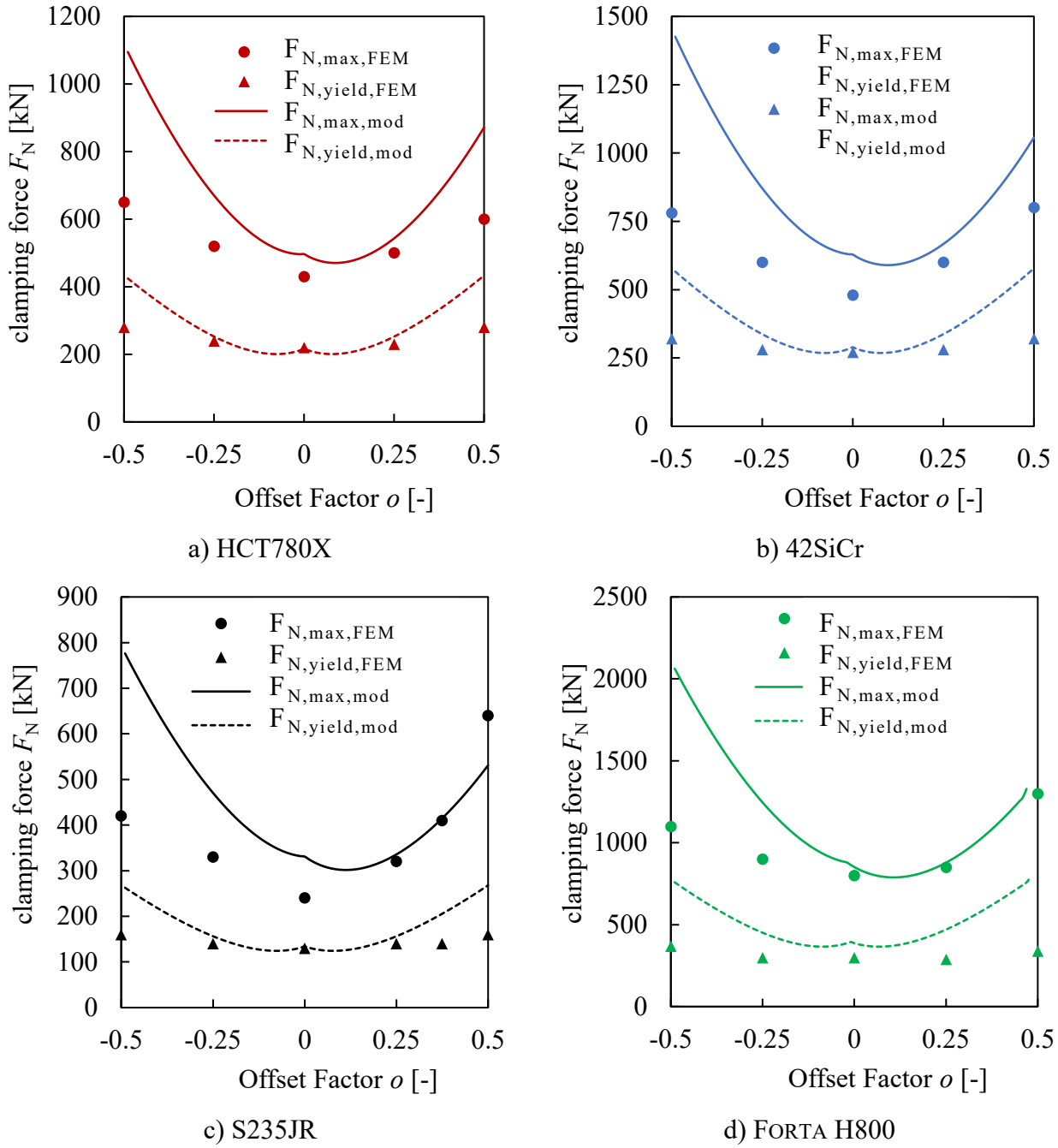

Figure 42: Clamping force F_N, necessary for bending until reaching yield stress or uniform tensile elongation, each plotted over bending pivot offset o, respectively. Comparison of the analytical model with the numerical simulations of in-plane bending. At $o = 0$, the analytical curves show an unsteady because two distinct functions are utilized to describe reaching yield stress or uniform tensile elongation at the extrados ($o \geq 0$) or intrados ($o < 0$), respectively.

When comparing the forces evaluated from the simulations with the predictions of the analytical model, it is observed at the materials' yield stress that any influence of the lateral bending axis shift on the necessary clamping force F_N is negligible in case of FE simulated results. The model calculations deliver reasonable correspondence for $F_{N,yield}$ at a centric axis positions. Well within the range of plastic deformation and at uniform tensile elongation, a more pronounced influence of the bending axis offset is observed from both models, the FE-simulations as well as the analytic

calculations. At eccentric positions of the bending axis, F_N increases strongly. With positive offsets $o > 0$, the bending process experiences a larger portion of tension than compression. On this side of the diagrams, the analytical predictions slightly overestimate the simulated clamping forces which gives a reasonable backup for process layout, considering the necessary yet idealized assumptions of the models. This safety could compensate for expected differences between the models and practical bending conditions, e.g., non-ideal dry friction due to contaminations. An exception is seen for the very soft S235JR which shows an extraordinarily high F_N for offsets $o \geq 0.375$ in simulation. Compared to the mechanical behavior of the other materials, the observation is explained by the very low yield strength of S235JR.

Compressive longitudinal strain is present at the intrados if an offset of $o < 0.5$ is adjusted. Within this range of the diagrams, larger deviations are observed in between the analytic model and the simulations. Due to the pre-defined tool gap, uniform tensile elongation was reached already at very small angles at the intrados of the simulated data points, see Figure 43.

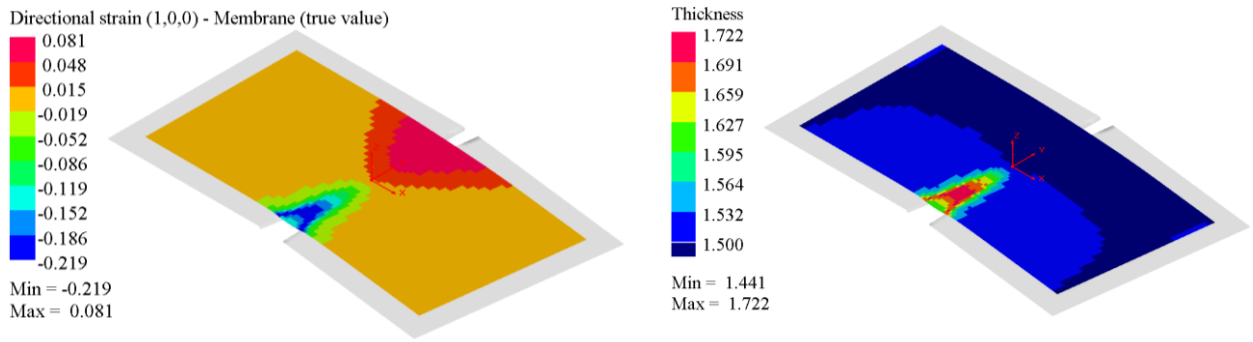

a) b)

Figure 43: In-plane bending with centric bending axis. a) Uniform tensile elongation is reached at the intrados earlier than at the extrados due to the different forming mechanisms. While material is stretched out from the clamping under tensile forming, thickening almost exclusively appears within the gap at the intrados, as seen from the material thickness distribution in b).

In contrast to the forming mechanism at the extrados, where the material is stretched out of the clamping (equilibrium at the yield sheath), the clamping force largely restricts material from thickening within the contact area at the inner side of the bending axis. In addition, any out-of-plane displacement of the finite elements was locked to prevent buckling at the intrados and hence avoid instable forming conditions.

5.5.2 Extended Fe-simulation model for in-plane bending

In addition to the previous simulation model, the frictionally engaged in-plane bending process is implemented in a numerical process model based on solid (3D) finite elements for the evaluation of pressure gradients on the material surface. The model is designed and numerically solved in the

simulation software ABAQUS 6.14 by DASSAULT SYSTÈMES. The clamping tools are represented by elastically deformable volumes (E = 210 GPa, POISSON ratio ν = 0.3) of identical thickness as the dies used in the ISB research tool. The clamping force and the rotational kinematics are applied to these model instances. The strip material is represented by a cubic mesh (edge size 1 mm) of fully integrated hex elements (type C3D8) with seven layers over thickness. Analogous to the analytically modelled process, each clamping unit loads the strip by half of the nominal clamping force, ½ F_N. Under load, the swivel unit pivots about the bending axis, see Figure 44 a). The simulation is based on an explicit calculation method.

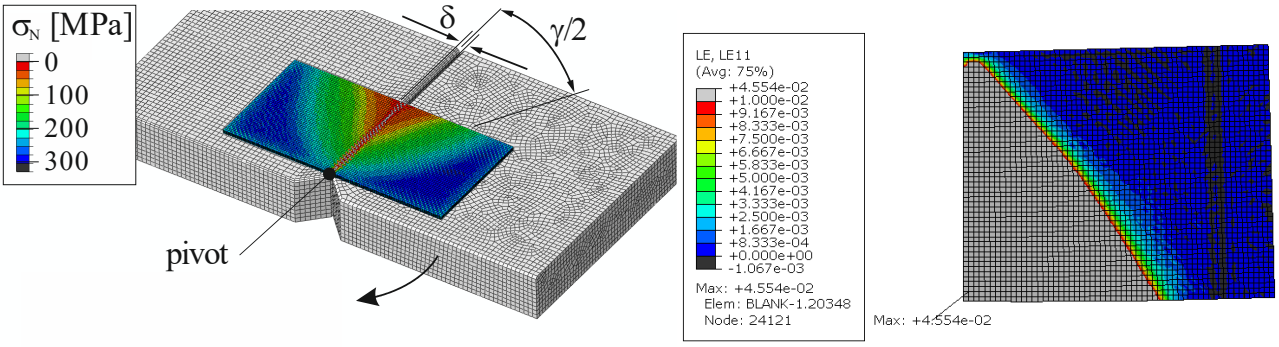

a) b)

Figure 44: a) Finite element model of a frictionally engaged in-plane bending process (hidden upper clamping tools). b) Evaluation of the forming zone angle and strain maximum from the simulation of in-plane bent material strips.

From these FE-simulations the longitudinal strain maximum $\varphi_{x,ex}$ at the extrados and the angle of forming zone γ are evaluated at every 0.1 degrees of bending angle. To evaluate γ in a consistent way, the limits of longitudinal strain are fixed at $0 \leq \varphi_x \leq 0.01$ (Figure 44 b) to ensure comparability to the strain evaluations from practical experiments.

5.6 Practical experiments

Considering the so-far progress, at the present state of this thesis, the process development for an ISB process allows to describe the forming zone in a continuously bent arc. Before modelling the mechanisms of the incremental sequence with respect to overlapping forming zones, the models developed in this chapter are validated by practical experiments. Initially, the laboratory tool and the utilized press facility are presented.

5.6.1 ISB laboratory scale tool for in-plane bending

An early state of the ISB research tool was already present at UTS, see chapter 2.2.2. The original design was developed by DUBRATZ (2006), patented by SCHWARZ and ENGEL (2009) and operated by MATHES (2007) for first investigations on bending profiles with flat cross sections from mild steels (width of floor > depth of walls). However, for validation of the development of the ISB process,

modifications of the research tool were required because it must agree closely to the ISB process with respect to kinematic and mechanic properties. Most importantly, the bending axis was relocated to a centric orientation in between both clamping units, see Figure 45 a). In its initial stage, the bending axis had a longitudinal and lateral offset. By the modification, a pure bending process is obtained free of radial stresses, as it is described by ADELHOF (1992); CHATTI (1998) according to DIN8586 and VDI3430. For pivoting the rotatory clamping unit, self-lubricated sliding plates from brass were placed under and over the unit to reduce friction and wear within the tool. The interlocking between upper and lower tool was designed as stiff as possible by minimizing the free length of pillars in closed tool condition, see Figure 45 (b).

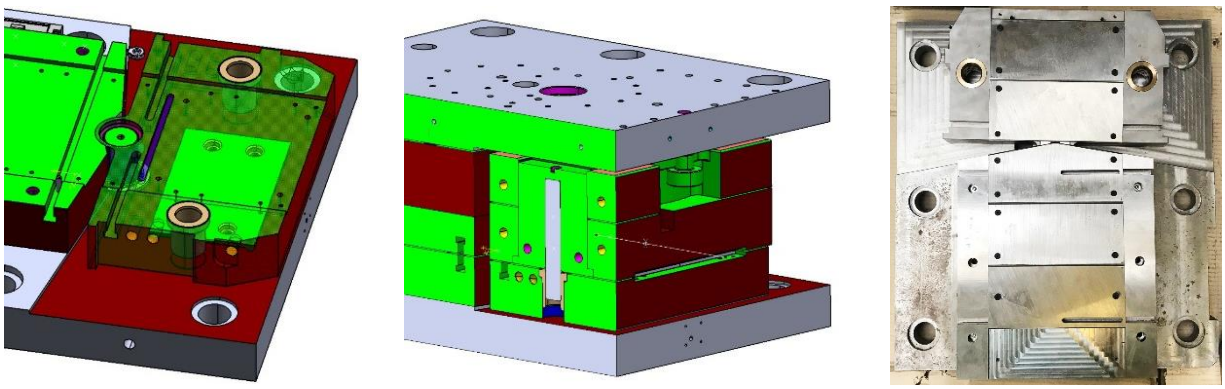

a) b) c)

Figure 45: ISB tool modification for in-plane bending of plane sheets. a) Transparent CAD view of the pivoted unit's lower tool to illustrate centric bending axis and sliding plates, b) cut CAD view of the interlocked clamping unit, c) top view of the lower part of the physical tool with segmented tool inserts which allow to stepwise modify the clamping length.

For the in-plane bending of plane sheets, the clamping tools were represented by flat plates which are arranged in segments as shown in Figure 45 (c) to allow bending with a variation of contact length $l_{c,0}$ in between 50, 100 and 200 mm. The die faces of the ISB clamping tools were finished by fine milling and subsequently coated by the TENIFER treatment (nitro carburation and oxidization in salt bath). The surfaces roughness was tested longitudinally (0°) and laterally (90°) in relation to the x and y – coordinates of the process model. The results are documented in Table 15.

Table 15: Roughness of the contact surfaces of the ISB tool in longitudinal and lateral direction. For each parameter, the intervals of 95% confidence are given from five repetitions.

ISB tool	**Condition**	$Ra_{0°}$ [µm]	$Ra_{90°}$ [µm]
Research tool for in-plane bending	before run-in	2.06 ± 0.52	1.68 ± 0.09
	used	0.78 ± 0.22	1.79 ± 0.12

The first "run-in" operation of the TENIFER treated tools significantly decreases roughness which is explained by an initial flattening of the surface oxides. Therefore, prior to relevant experiments, the forming tools were run in with spare sheet metal material. Subsequently, the parallel alignment of the tool and an even load application was verified by the TEKSCAN pressure sensor system which is presented earlier in the experiments on strip drawing, see subchapter 4.5. The resulting pressure distribution in the ISB tool is shown in the Appendix, Figure 104.

5.6.2 Forming machinery

The ISB research tool was designed for operation on a 1MN hydraulic press type WALTER WUP which is a part of UTS shop floor. The press is utilized by UTS for research try-out experiments. Essentially, the WALTER press is constructed as an O-frame to guarantee stiffness and parallel elastic deflections. The press offers no option to operate supplementary axes. Therefore, the bending axis of the ISB research tool is operated by the independent hydraulic unit WOODTLI, see Figure 46.

Figure 46: WALTER WUP press with independent hydraulic unit attached to the ISB research tool.

The hydraulic unit is equipped with a valve block to operate several hydraulic channels. One of these channels connects the bending axis of the research tool and a hydraulic feed unit will be introduced in the use case, chapter 7, for semi-automatic operation of the incremental sequence. A third channel is required for idle circulation of the power unit. The unit is driven by a custom-made machine control based on the digital / analogue (DA) converter LABJACK UE9 and is programmed in the software PROFILAB-EXPERT 4.0, see Appendix, Figure 103. The ISB tool is equipped with a linear potentiometric displacement sensor to measure the angle at the bending axis which is driven by a hydraulic bending cylinder attached to the unit. The sensor signal is connected to the analogue inputs of the DA converter while its outputs actuate the hydraulic valves of the WOODTLI power unit.

5.6.3 In-plane bending experiments

Experimental design

Compared to stretching of plane strips, in-plane bending adds up a lateral stress distribution over the material – i.e., over profile height h_0. While the forming resistance resulting from work hardening has to be transmitted force-fittingly by the clamping tools in stretching, the internal moment M_z results from bending and needs to be transmitted by the clamping tools' traction. The analytics for the in-plane bending process are established in subchapter 5.3 and result in the definition of a process window. For validation, practical experiments are conducted according to the parametrical variation summarized in Table 16. The evaluation of these experiments is compared to the predictions of the analytical model and numerical in-plane bending simulations according to subchapter 5.5.2.

Table 16: Variation of materials and clamping force applied to the model of force-fitted in-plane bending. Least necessary clamping force $F_{N,min}$ is required to prevent slipping at the material's uniform tensile elongation.

Material	s_0 [mm]	h_0 [mm]	$l_{c,0}$ [mm]	F_N [kN]	$F_{N,min}$ [kN]	case
22MnB5	1.4	50	50	500	342.5	a)
		80	100	816	548.0	b)
HCT780X	1.5	50	50	700	314.5	c)
			100	816		d)
42SiCr	1.95	50	50	816	694.3	e)
FORTA H800	1.0	50	50	500	384.7	f)
				900		g)

All experiments are designed with a bending axis offset towards the intrados ($o = 0.5$) to exclusively cause tensile stresses in the bending stress distribution. The intention is to focus the results on validating the description of the forming zone which reaches well under the clamping surfaces in tension. Compressive stresses would cause interlocking of the material with the edges of the clamping tools due to the thickening. The least necessary clamping force $F_{N,min}$ was initially laid out for each process setup according to the model for dimensioning the clamping force (subchapter 5.2). With respect to strength and available thickness, the experimental setups provide a broad variation for validation. In addition, two stages of clamping force are suggested; on H800 exclusively, while on HCT780X and 22MnB5 connected to other parameter variations. From each material, 50 mm wide strips are introduced to in-plane bending. For 22MnB5, additional strips with a profile height $h_0 = 80$ mm are subjected to the process. The clamping length $l_{c,o}$ is adjusted by the segmentation of the active die faces of the ISB research tool and varied in discrete steps of 50 and 100 mm (cf. Figure 45 c). As

dry friction conditions are desirable for the ISB process, the die faces and material strips are cleaned by solvents prior to each experiment, so the tested friction coefficients μ and μ_0 can be utilized in the models.

The process window of an ISB process is an important tool for the design of experiments as well as to plan the process setup by means of kinematic parameters for a desired geometry. The window is a result of the individual combination of sheet metal material, tool and machine. The experiments suggested in Table 16 are located in relation to the resulting ISB process windows in Figure 47.

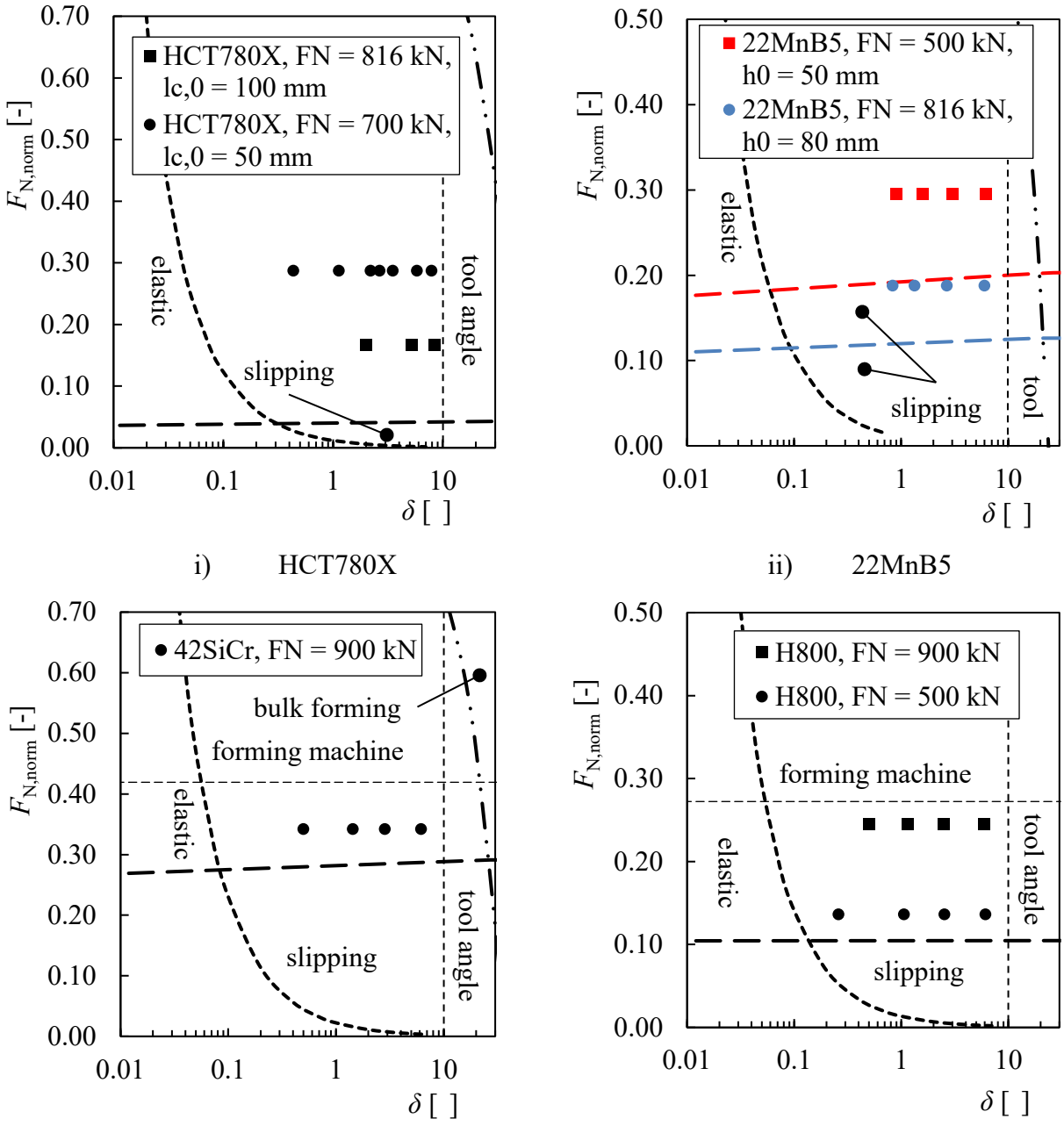

i) HCT780X ii) 22MnB5

iii) 42SiCr iv) FORTA H800

Figure 47: Location of the experiments in the ISB process windows.

The lower margin of the process window is determined by the minimum required press force to transmit the bending moment by traction. While large process windows are given for the materials

HCT780X and FORTA H800, the window gets considerably narrow if a comparably high sheet metal thickness is introduced to the process as in the case of 42SiCr. For the variations on 22MnB5, two borders against slipping must be considered: Because of the larger contact surface of the wider variant (h_0 = 80 mm), higher friction moments are transferrable thus reducing the lower border. Similarly, the lower border of HCT780X lies comparably low because of the high friction coefficients of this material which allow for an efficient transmission of bending moment.

The upper border of the window indicates a theoretical risk of bulk sheet metal forming which in all cases, requires far higher press loads than applicable by the try out facility WALTER WUP. If identical contact areas are used within variations on a specific material, the upper border given by the press is indicated in the process window (i.e., 42SiCr and H800). If the press load is applied onto different contact areas, as for the parameter variations of HCT780X and 22MnB5, the press-related border is different for the variations and hence excluded from the diagrams for the sake of clarity.

For the processed materials, the border against necking (right hand border of the diagrams) is unlikely to be reached within a single bending increment. The ISB research tool is designed to bend the materials in an incremental process, thus providing only bending angles up to 10 degrees. Moreover, at higher incremental forming angles, necking often lies beyond beginning bulk forming aspects, which can be seen at the upper right edge of the process window for 42SiCr. In this case, however, the border still lies well beyond the mechanical borders given by the combination of press and tool.

At the left-hand border of the process windows, the clamping force dependent on minimum bending angles are indicated. Below, the material is only formed elastically and springs back completely after release of force. Due to the stochastic scatter of strain and bending angle observed close to the elastic-plastic transition, in consequence, this boundary of the process window cannot be validated sufficiently by practical experiments but estimated from the numerical simulations.

Evaluation methods

From the surface of the sheet metal materials subjected to in-plane bending, strain gradient maps are evaluated by the method of optical strain measurement (OSM) as described by KEELER (1968). Initially, the surfaces were electrolytically marked with a quadratic grid pattern. After gridding, the specimens were subjected to the forming process and the surface grids were deformed due to plane straining. Next, the residual plastic deformation was captured by a 3D camera system from the grid by referring the points of intersection of the distorted grid to its nominal size. For the evaluation and processing of strain maps, the AUTOGRID System by the company VIALUX was used. False color representations visualize the strain maps captured from surfaces of the bending specimens. The resulting bending angles from the practical experiments were measured by the angle gauge TUBOCONTROL. On a solid measuring table, a rotatable beam pivots against a fixed beam to digitally

evaluate the bending angle of the profiles. The resulting angle is obtained with an accuracy of 0.1° from the device.

Experimental procedure

In the practical experiments, individual specimens were bent with increasing bending angles. In order to obtain a higher resolution of results in the region of small bending angles, the evaluation interval was arranged in an exponential spacing, i.e., $\delta = \{0.75; 1.5; 3; 6\}$ degrees. Strain and forming zone angle were measured from the major strain maps obtained by OSM, see Figure 48. Before the evaluation, it was ensured that major true strain φ_l follows the longitudinal direction x of the sheet metal strips according to the coordinates used in the analytical and numerical models.

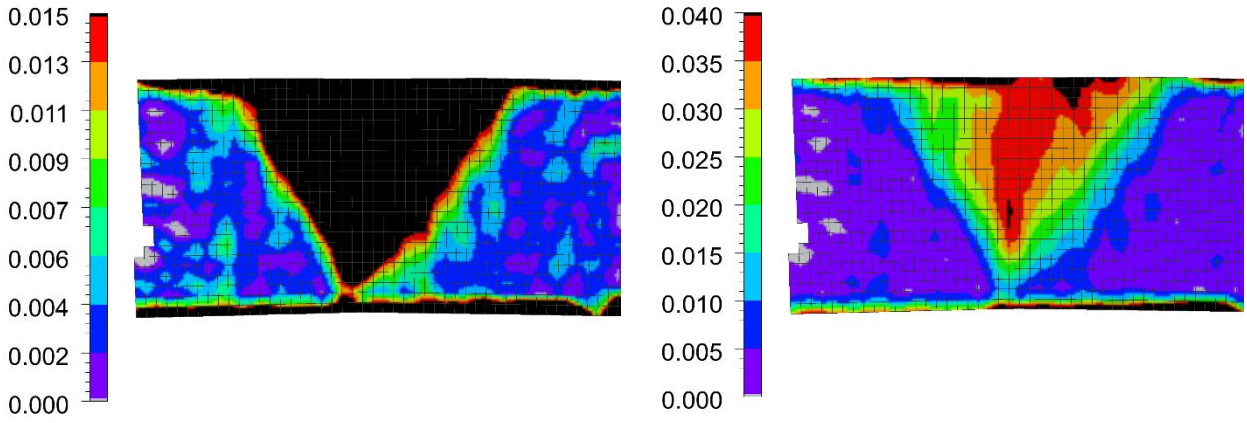

Figure 48: Major strain maps, as captured from the surfaces of the bending experiments. Visualization of the forming zone of case g), FORTA H800 at 900 kN press force at a bending angle of 2.49 degrees (note: after elastic springback). a) Strain map in between $0 \leq \varphi_l \leq 0.01$ for the evaluation of forming zone angle (here: $\gamma = 65°$) and b) strain map in between $0 \leq \varphi_l \leq 0.04$ for the evaluation of strain maximum at extrados (here: $\varphi_{x,ex} = 0.375$).

A minimum of three repetitions of each bending angle were conducted in the experiments. For the very small bending angles of 1.5 and 0.75 degrees, five repetitions were necessary for achieving statistical confidence due to the prominent scatter obtained at minor forming zone angles. The springback angle δ_{SB} is obtained by measuring with the angle gauge TUBOCONTROL and averaged over the repetitions of each experiment. Because the individual repetitions were conducted on the same metal strip, the resulting total or accumulated bending angle α is divided by the number of repetitions to obtain the average of the unloaded bending angle $\delta_u = \delta - \delta_{SB}$.

In following pages, Figure 49 shows the zone angles γ and strain maxima at the extradoses $\varphi_{x,ex}$ being evaluated by OSM from the practical experiments according to the parameter variation of Table 16. In addition, the springback angles δ_{SB} after bending are presented for each individual experimental setting. The results from the simulation model were evaluated correspondingly. These results are compared to the predictions of the analytical process model.

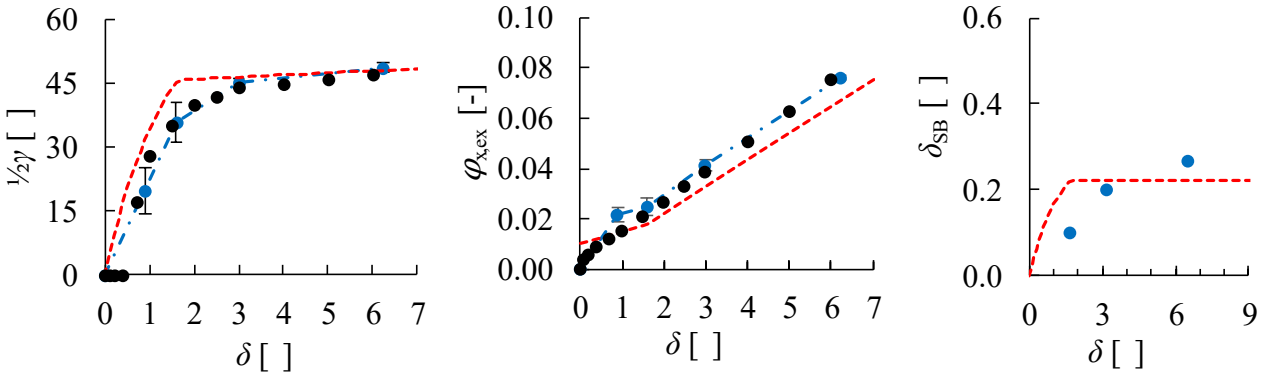

a) 22MnB5, F_N = 500 kN, h_0 = 50 mm

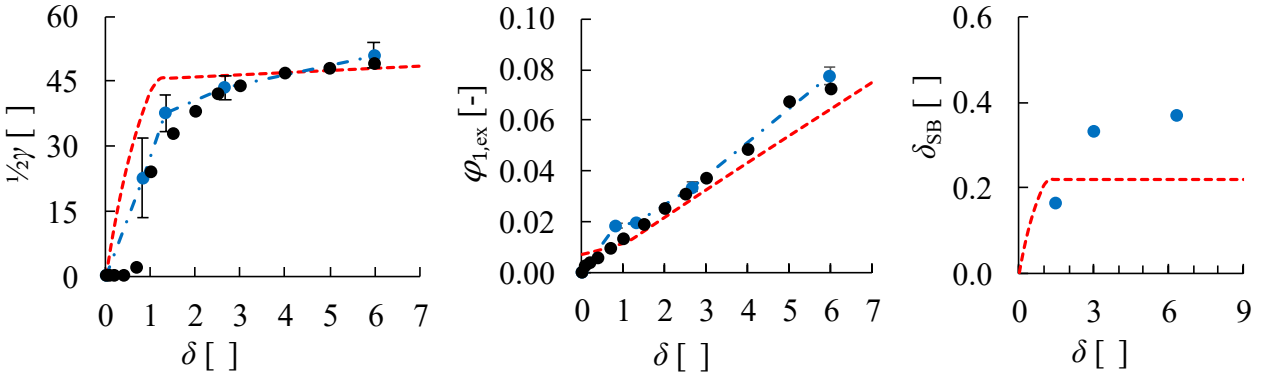

b) 22MnB5, F_N = 816 kN, h_0 = 80 mm, $l_{c,0}$ = 100 mm

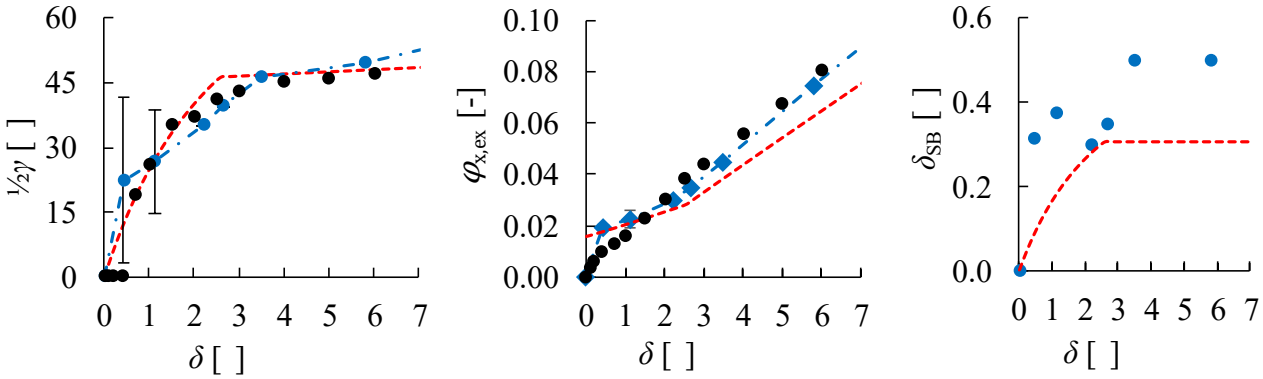

c) HCT780X, F_N = 700 kN, $l_{c,0}$ = 50 mm

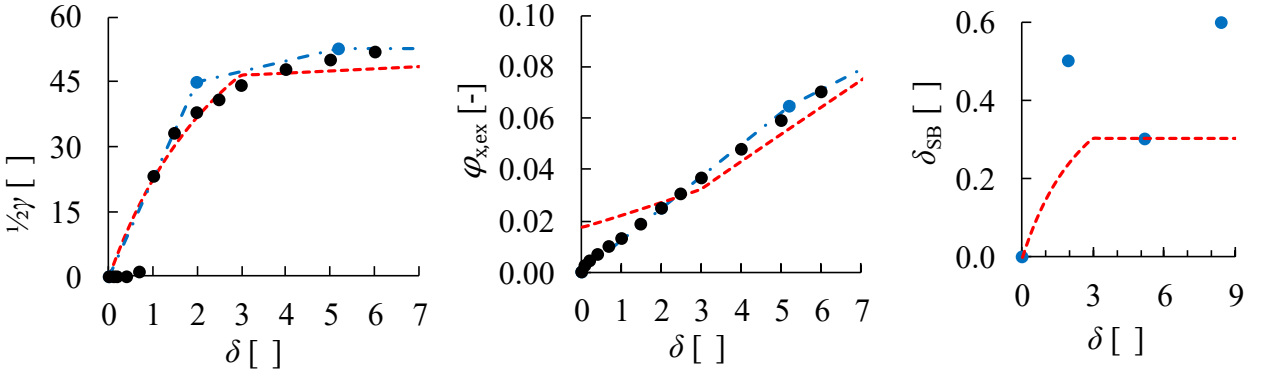

d) HCT780X, F_N = 816 kN, $l_{c,0}$ = 100 mm

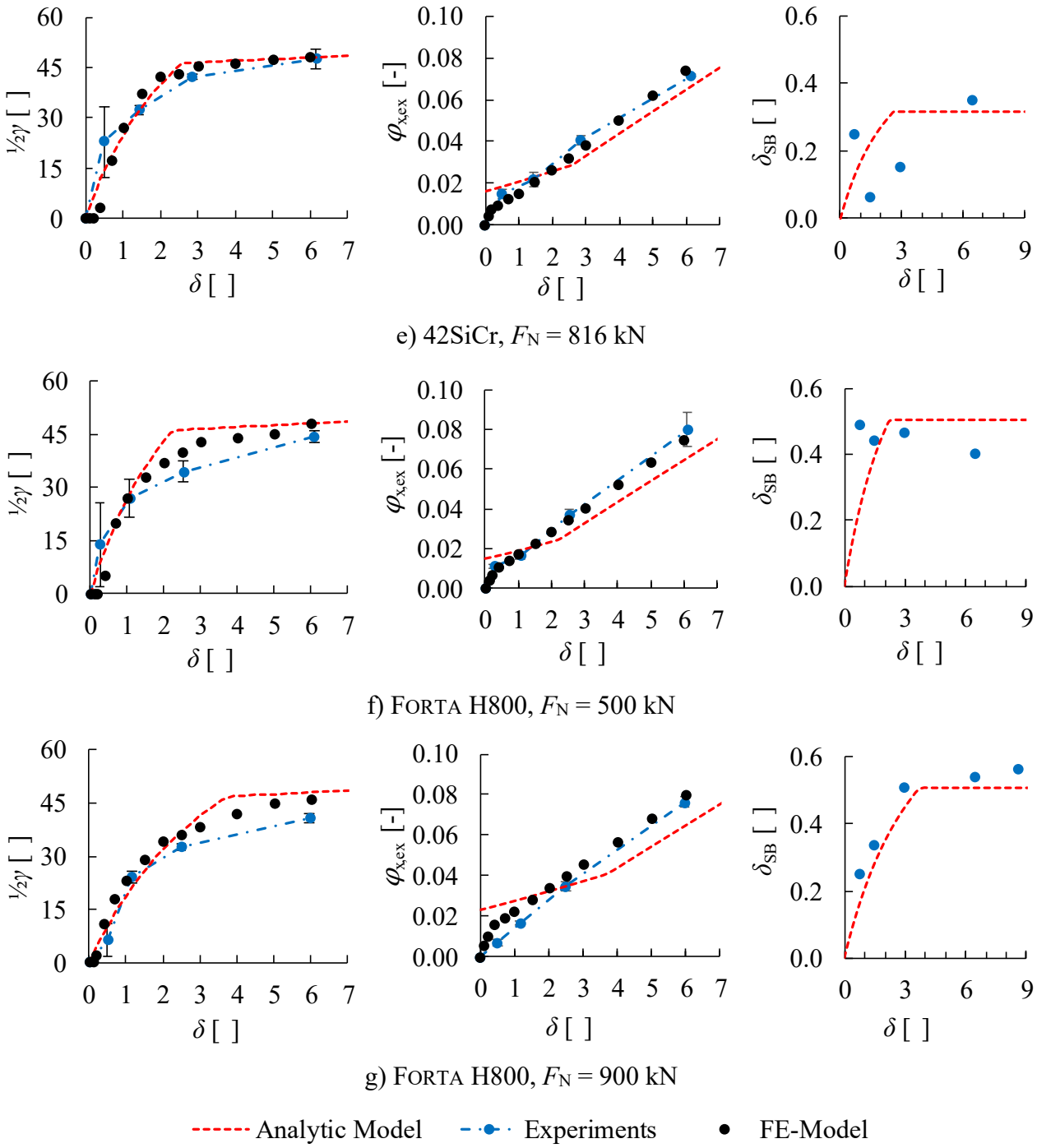

Figure 49: Comparison of practical experiments conducted on the ISB research tool to the predictions of the analytical model for force-fitted in-plane bending and FE-simulations. The angle γ of the resulting forming zones, the longitudinal strain maxima at the extradoses $\varphi_{x,ex}$ and the springback angles δ_{SB} are evaluated over increasing incremental bending angles δ. Within the parameter variation, four different materials are studied. Different clamping forces, tool lengths, strip widths and material thicknesses are covered by the experiments.

To a lesser extent than sensitivity analysis, the parametric study aims to validate the analytical and numerical models by means of selected, preferably diverse process setups with regard to the ISB process window. The experiments include all materials used in this thesis and the mechanical possibilities provided by the technological equipment with regards to the ISB tool and the try-out

press are explored. The experimental observations confirm the predicted forming zones and corresponding strain maxima of the analytical and numerical models. The following conclusions are drawn from these results:

1. The implementation of the static friction coefficients evaluated from the strip drawing experiments significantly helped to improve the quality of model prediction.
2. From the variation of materials, substantially different forming zones are observed. Stronger materials reveal forming zones with smaller zone angles, e.g., cases a) vs. f): The austenitic material exhibits a considerably tighter forming zone than the boron manganese steel which points out the influence of the mechanical material properties. This aspect agrees to the observations from the linear stretching process.
3. An increase of clamping force restricts the forming zone, e.g., f) vs. g). Higher contact pressure allows for higher frictional shear stress at the contact surfaces, thus more material is prevented from being plastically stretched within the forming zone. Again, this conclusion agrees to the observations from the linear tensile process under frictional engagement.

The springback angle δ_{SB} is exclusively compared in between the experiments and the analytical model. From the experiments, a pronounced stochastic scatter can be seen in the results which is traced back to the limited accuracy of the measurement apparatus. The results of the springback angle δ_{SB} and its trend over δ still confirm the applied springback model of WITTEK et al. (2011).

For both models, several premises led to the presented compliance of results and model predictions. As for the analytical model, the following constraints were applied:

a) The opening angle of the forming zone increases strongly over the very first few degrees of bending angle. Looking at the results from the practical experiments, γ would asymptotically reach a certain threshold γ_{ult} with increasing δ. If a square ratio between profile height h_0 and tool clamping length $l_{c,0}$ is introduced to the process, γ_{ult} becomes $90° + \delta$, as in cases a), c), e) – g). Even if the other cases where longer tool contacts are used than the profile height, the forming zone angle hardly exceeds this limit. Therefore, the analytical model to describe the size of the forming zone of in-plane bending is complemented by a case distinction as soon as γ reaches γ_{ult}:

$$\gamma_{\mathrm{ult}} = 2 \cdot \tan^{-1}\left(\frac{l_{c,0}}{h_0}\right) + \delta \; ; \; \gamma_{\mathrm{ult}} \leq 90° + \delta \qquad \text{(eq. 83)}$$

b) The constant strain hypothesis (section 5.3.2) slightly underestimates the observed strain maxima and is explained due to the unsteady transition in between firmly clamped and freely stretched material. The sandglass strain assumption, in turn, delivers overshooting strain

values as a function of bending angle. Both are compared exemplarily in Figure 50 for FORTA H800 at 900kN press load where a better strain prediction by the constant hypothesis is evident.

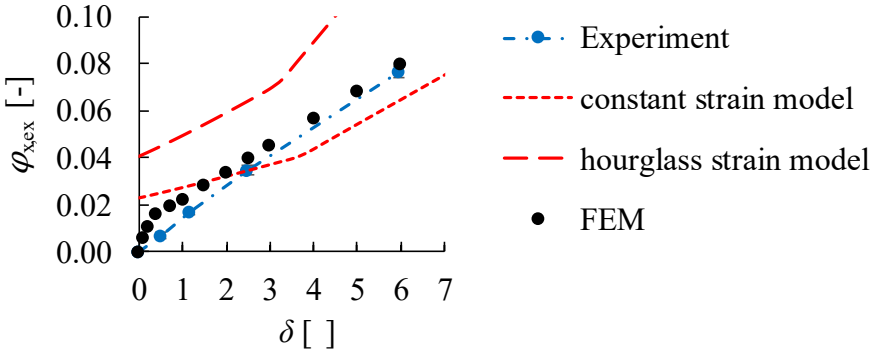

Figure 50: Comparison of the constant and hourglass-type strain hypotheses for case g).

Note that the trends of the analytical models do not begin at the coordinate origin. This offset is obtained due to the fact of neglecting elastic bending moments.

The FE-simulations are utilized to validate the analytic modelling approach based on the material portion pulled out of the clamping zone. For this purpose, the FE simulation model has been applied to cases a) – g) with the following premises:

a) Consistent results regarding the size of the forming zone as a function of bending angle were obtained by using deformable tool surfaces.

b) As for the analytical model, the implementation of the tested pressure dependent static dry friction coefficients reveal a better consistency between simulated and practically obtained results.

5.7 Discussion and conclusions of chapter 5

For the layout of the ISB process the clamping force is initially determined on the basis of the processed material. F_N is kept constant in the context of this thesis and delivers a constraint for the calculations. In the preceding chapter, the forming zone of a tensile process is considered because it provides a constant strain distribution over profile width. The equilibrium between drawing force at tools, forming force caused by work hardening and the force present within the cross section at the yield sheath is the central hypothesis of the analytical considerations. Correspondingly, the moments are calculated at these locations for an in-plane bending process to determine the forming zone as a function of incremental bending angle and strain.

Mathematically, modelling the bending process by purely analytical equations requires several approximations in order to obtain solvable equations. For the calculation of the forming zone, elastic parts of the bending moment are not considered. With a pure plastic bending moment, consequently,

strain generated in the first tenths of a degree of the bending angle δ is overestimated. For selected cases of the experiments, Figure 51 shows details for small values of δ.

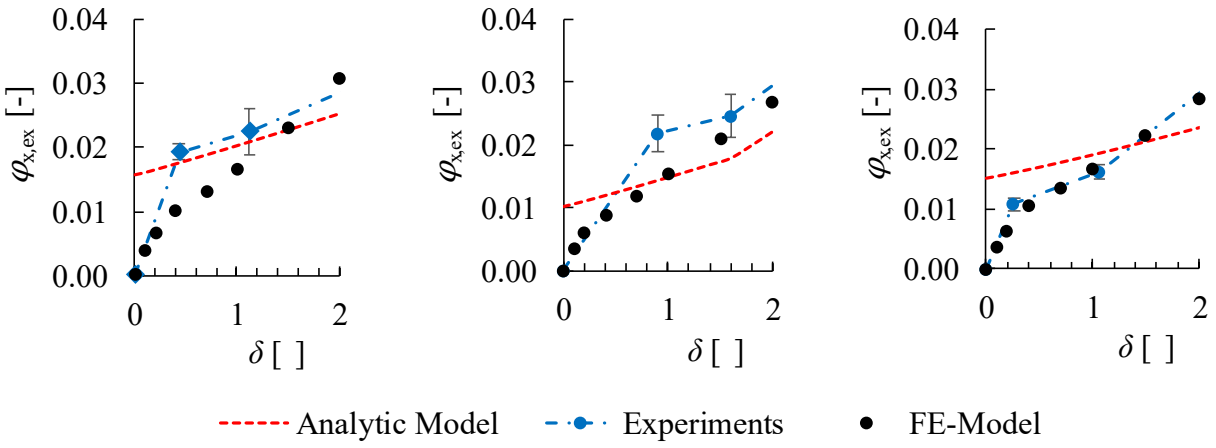

a) HC780X, F_N = 700 kN b) 22MnB5, F_N = 500 kN c) FORTA H800, F_N = 500 kN

Figure 51: Development of the strain maximum during bending the first degrees of incremental bending angle δ under consideration of three exemplary sheet metal strips. While strain over bending angle shows a linear trend during higher values of δ, at lower values a flatter inclination of all trends is observed in the analytical and numerical models as well as from the experiments. Considering the first tenths of degrees bending angle, the numerical and practical experiments reach from the coordinate origin while the graphs of the analytical model show ordinate intersections due to the lack of elastic bending moments.

From the examples, the effect of the modelling deviation due to neglecting elastic bending moments can be discerned at the first tenths of degrees bending angle. Hence, strain could be overestimated when bending only very small bending increments. It is moreover observed from the experiments that a higher scatter is obtained in the resulting geometries when operating the bending process with very small bending angles. In addition, the risk of out of plane buckling increases considerably when bending with very small increments. In conclusion, it is generally discouraged to operate the process with very small bending increments from a practical point of view.

Further simplifications of the analytical model may explain the residual deviations observed in comparison to the experiments (Figure 49). In order of decreasing estimated significance, these are:

1) The constant strain assumption underestimates the central strain maximum in the middle by averaging the whole forming zone. Hence, strain is slightly underestimated by the model. No longitudinal strain transitions are modeled at the beginnings and endings of a bending increment.
2) The exclusion of deformation over thickness and profile height assumes the tensile part of the bending moment to be too high due to no cross-sectional deformation.
3) A bilinear hardening law was deployed within the analytical modelling approach. In particular, for strain values close to uniform tensile elongation, this law delivers reliable

material predictions while deviations are expected for low strain values, also see comparison of hardening curves in subsection 4.2.2.

4) The assumptions discussed in chapter 4.
   a. Linear increase of longitudinal stress over the clamping length, applied from beginning to end of the clamping tool,
   b. Not considering the elastic compression due to clamping load,
   c. Not considering the elastic transverse strain due to longitudinal strain within the material and
   d. Not considering the clamping load on the multiaxial stress state formulated at the location of yield sheath.

The presented analytical model is provided to study the major influencing parameters on the forming zone which develops within the area where clamping tools force fittingly apply the bending moment. For the springback angles measured from the experiments with successively increasing incremental bending angle, a large stochastic scatter is obtained even if individual angles were bent multiple times (without superposition) and then divided by the total bending angle. The spread of these results is related to the limited accuracy of the digital gauge TUBOCONTROL and, by fewer parts, to the bending angle of the ISB tool. Nevertheless, the modelling approach of WITTEK delivers a reasonable prediction of the experimental results if interpolated.

The soft construction steel S235JR is exclusively considered in the numerical studies of the layout method for the required clamping force for sufficient bending (subsection 5.5.1). This material diverges more from the modelled trends which is traced back to larger portions of bulk forming effects. Correspondingly, the high-strength materials show similar deviations to the model if excessive clamping loads are applied (subsection 4.3).

The verification of the clamping force model is conducted with constant friction coefficients. This approach was chosen because both models, the finite element-based simulation and the analytical calculation, offer the opportunity to implement identical friction laws. Parameterization of the models with contact pressure-dependent friction values only takes on relevance when they are compared with the practical experiments.

6 Layout method for the ISB process

In the preceding chapters, a fundamental mechanical model of an ISB process is established. In the first step, the analytical description of the forming zone which emerges during frictionally engaged forming under tension is derived. For bending, a lateral strain distribution is propagated over the material cross section. Based on the validated analytical model, the incremental forming sequence of the ISB process is applied in the next step. Four fundamental process parameters determine the ISB method:

1) The clamping force $\boldsymbol{F_N}$ which is applied constantly throughout the process.
2) The incremental bending angle $\boldsymbol{\delta}$ which applies strain within a bending increment. From the total bending angle α required by the bending product, the number of increments n_{ISB} is determined.
3) The bending axis offset $\boldsymbol{o}$ which allows to influence the lateral bending strain distribution by superposed longitudinal tension or compression.
4) The density of the incremental bending steps which is adjusted by the incremental feeding distance $\boldsymbol{\Delta f}$. For a fixed bending radius required by a product, the incremental density will in turn influence the number of increments.

The dimensioning of clamping force and the influence of the bending angle are discussed in the preceding sections of this thesis. In this chapter, the bending axis offset and the incremental feeding distance are laid out to dimension the ISB process.

6.1 Bending axis offset and ISB strain diagram

For a given bending geometry and cross section, the strain distribution is obtained from the elementary bending theory. Under consideration of the bending factor B, the distribution of true strain in a bent arc is defined as a function of the profile height within the bending plane h_0. For this purpose, GERLACH (2010) introduced the lateral coordinate y, which represents the radial distance to the location of zero elongation in the bent arc. Together with the theoretical bending radius R_{th} at the strain-neutral axis, the strain distribution over h_0 can be expressed as

$$\varphi(y) = \ln\left(\frac{\Delta l}{l_0} + 1\right) = \ln\left(\frac{y}{R_{\mathrm{th}}} + 1\right). \qquad \text{(eq. 84)}$$

In the case of an unshifted neutral axis in the centerline of a profile ($R_{th} = R_{cl}$), symmetrical bending strain distribution is propagated. The lateral coordinate y reaches up to half of the profile width h_0 at the inner and outer arc.

For the outer edges of an arc, eq. (84) can hence be expressed as

$$\varphi = \begin{cases} \ln\left(\frac{0.5\ h_0}{R_{\mathrm{th}}} + 1\right) = \ln\left(\frac{1}{2B} + 1\right) & \text{for the extrados} \\ \ln\left(\frac{-0.5\ h_0}{R_{\mathrm{th}}} + 1\right) = \ln\left(\frac{1}{-2B} + 1\right) & \text{for the intrados .} \end{cases} \qquad \text{(eq. 85)}$$

In an ISB process, the neutral axis might be shifted by the pivot offset o and therefore the relation between radius at the neutral axis and at the centerline of the profile follows $R_{\mathrm{th}} = R_{\mathrm{cl}} - o \cdot h_0$. Consequently, eq. (85) is modified by taking the profile's centerline radius R_{cl} and the offset o into account. Hence, strain is expressed by

$$\varphi(y) = \ln\left(\frac{y}{R_{\mathrm{th}}} + 1\right) = \ln\left(\frac{y}{R_{\mathrm{cl}} - o \cdot h_0} + 1\right) \qquad \text{(eq. 86)}$$

The maximum of longitudinal strain $\varphi_{\mathrm{x,ex}}$ occurs at the radius at the extrados of an arc, R_{ex}. Correspondingly, the radius at the intrados is denoted R_{in}. Including the equations above, strain is expressed as a function of offset and bending factor.

$$\begin{aligned} \varphi_{\mathrm{x,ex}} &= \ln\left(\frac{R_{\mathrm{ex}} - R_{\mathrm{th}}}{R_{\mathrm{th}}} + 1\right) = \ln\left(\frac{h_0 \cdot (0.5 + o)}{R_{\mathrm{cl}} - o \cdot h_0} + 1\right) \\ &= \ln\left(\frac{0.5 + o}{B} + 1\right) \end{aligned} \qquad \text{(eq. 87)}$$

Figure 52 delivers the graphic interpretation of eq. (87). Major strain at the extrados increases logarithmically towards smaller bending factors (i.e., tighter arcs). The function is shifted by the offset factor towards larger strain values if the bending axis is located closer to the intrados of the arc which results in tensile strain superposing the lateral bending strain distribution. In turn, if the axis is positioned closer to the extrados, the strain maximum at the extrados is reduced due to superposed compression. Offset values larger than 0.5 and lower than -0.5 are feasible during an ISB operation but have an insignificant practical relevance due to excessive straining.

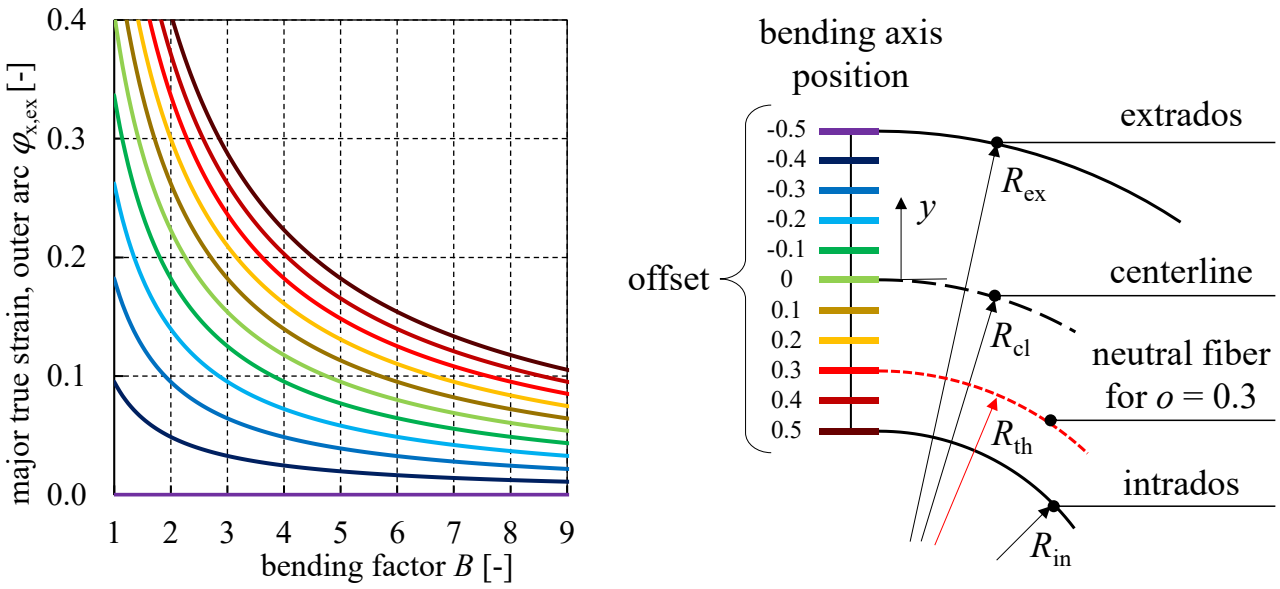

Figure 52: ISB strain diagram. a) Maximum longitudinal strain at the extrados plotted over bending factor as a function of the bending axis offset factor. b) Position of bending axis associated with these offset factors. Indication of lateral coordinate y, relevant radii at an arc and theoretical location of the neutral fiber and its corresponding radius R_{th} for an offset of 0.3 as example.

For a variation of the offset factor, the diagram shows iso-lines for the function of major (longitudinal) strain at the extrados $\varphi_{x,ex}$ over bending factor B. Due to the dimensionless calculation of B, the depiction is independent of the material and applicable in a general way. With reference to OEHLER and KAISER (2013), the technical guideline VDI 3430 summarizes three bending failure characteristics. Tensile longitudinal strain at the extrados leads to cracking and deformation of the profile's cross section. While the latter failure can be prevented by a mandrel to support the profile during the ISB process, as applied by MATHES (2007), cracking is bound to the materials ductility but might be influenced by compressive strain superposition such as by bending axis offset. In addition, VDI 3430 lists the formation of wrinkles as characteristic bending defect at the intrados which occurs because compressive longitudinal strain causes the profile to buckle (Oehler 1963). Wrinkles are hence bound to the cross section's stiffness (Borchmann 2021; Schapitz and Levin 1963) and must be compensated by tooling or longitudinal tensile strain superposition. During profile bending, once again, the mandrel is a crucial supporting part but it must act opposite to the profile's outer surface which is applied with a force by a wiper die in conventional bending processes (Franz 1961).

However, due to the kinematic forming nature of an ISB process, its tools are laid out independently from any bending geometry, so only limited wrinkling support can be provided within the process and must be compensated by superposition of strain. In this context, specific offset factors cause different strain distributions. Figure 52 is utilized to dimension the offset parameter o for the ISB

process as follows. A given product geometry, which is intended to be manufactured by an ISB process, is determined by its bending factor B. The following approach is feasible to layout the bending axis' shifting:

1. To avoid any wrinkling, superposition of tensile strain has proven sufficient according to CLAUSEN, HOPPERSTAD, and LANGSETH (2000); SELTER (2017). Hence, the bending axis is shifted towards the intrados, corresponding to an offset factor of $o > 0$. However, high major strain values would result and bending is prone to cracking. Therefore, a material related failure criterion needs to be included in the diagram to assess the geometry's feasibility.
2. Depending on the cross section, compressive strains might be tolerable without buckling in the ISB process. Especially the clamped areas of the profile are well supported. Thus, plane sheets and profiles that have no folding at the inner arc, such as Z-profiles, can be bent in-plane with the offset factors $o < 0.5$ as demonstrated by Frohn-Sörensen, Mašek, et al. (2020). Cross sections with edges at the intrados such as hat- shaped- and U-profiles, are processible by ISB but wrinkles must be prevented preferably by a bending axis position at the intrados ($o = 0.5$). For offsets $o < 0.5$, the desired bending factor and the shape of tooling will strongly influence the profile's support against buckling. Moreover, buckling depends on the wall thickness. If any compressive strains are introduced to bending including ISB, the risk for wrinkles is expected to rise with increasing wall thickness factor, defined as $W = h_0 / s_0$.

Example: A Z-profile is made from a material whose ductility limits longitudinal strain in bending to $\varphi_{x,max} = 0.2$. For a given bending product, an arc with bending factor of $B = 3$ should be manufactured in an ISB process. If o was set to 0.5, best wrinkle compensation would be achieved but $B = 4.5$ represents the tightest arc, that can be manufactured considering the material's ductility. Hence, the offset is reduced to 0.1 to reach the planned bending factor without excessive straining. Major longitudinal strain is estimated to be $\varphi_{x,ex} = 0.18$.

6.2 Failure criterion against rupture

The material specific forming limit curve (FLC) is a well-established tool in research and development to describe failure due to onset of necking in sheet metal forming. The strain ratio or strain path corresponding to the sheet metal forming process is evaluated against the FLC. For bending, longitudinal strain is assumed to increase linearly over profile height along the coordinate y according to eq. (84). A characteristic bending strain distribution would appear in the forming limit diagram (FLD) which is increasing linearly towards the arc's extrados. Figure 53 shows the FLD of a plane bending specimen from HCT780X which was formed close to failure. For the extrados of an ISB processed plane sheet, a strain ratio of approximately $\rho = \varphi_2 / \varphi_1 = -0.5$ is evaluated. Beginning from the onset of necking, ρ reveals steeper inclinations until failure.

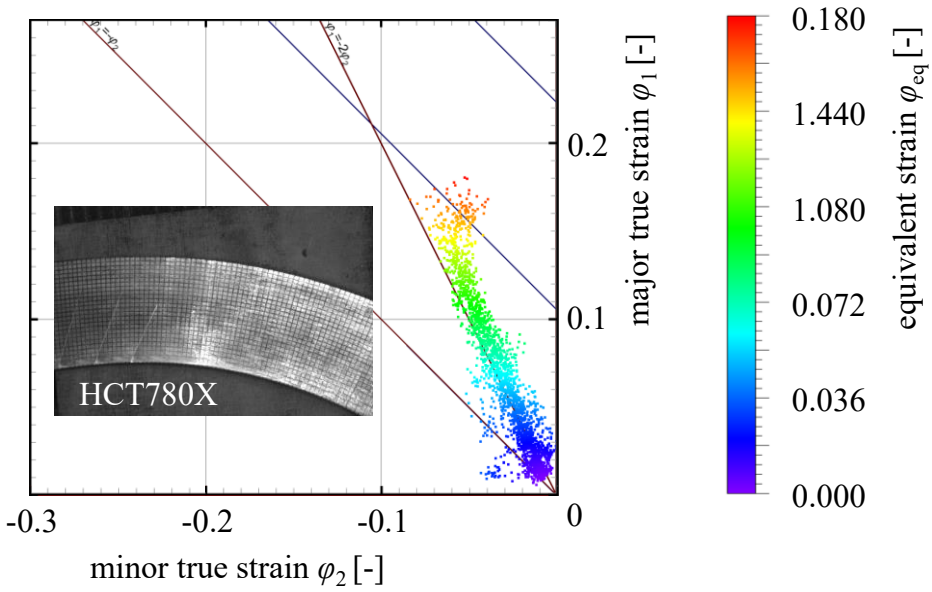

Figure 53: Datapoints obtained by optical strain measurement from a plane HCT780X bending specimen (o = 0.5), plotted as major over minor strain cloud in the FLD. Strain path follows ρ = -0.5 during stable forming and gets considerably steeper with the onset of necking.

FLC models

Two modelling approaches for the FLC are considered in this thesis and these are parameterized by the mechanical material properties evaluated in tensile tests (see 4.2.1, Table 3). KEELER (1965) developed semi – empirical formulations which were statistically derived from experiments. The KEELER FLC is parameterized by initial sheet metal thickness s_0 as well as the hardening exponent n. STEINHEIMER (2006) presented a model, which delivers a worst-case FLC approximation and is therefore denoted “conservative FLC”. Likewise, the hardening exponent is implemented. Both FLC models are graphically compared in Figure 54 for HCT780X in various sheet thickness.

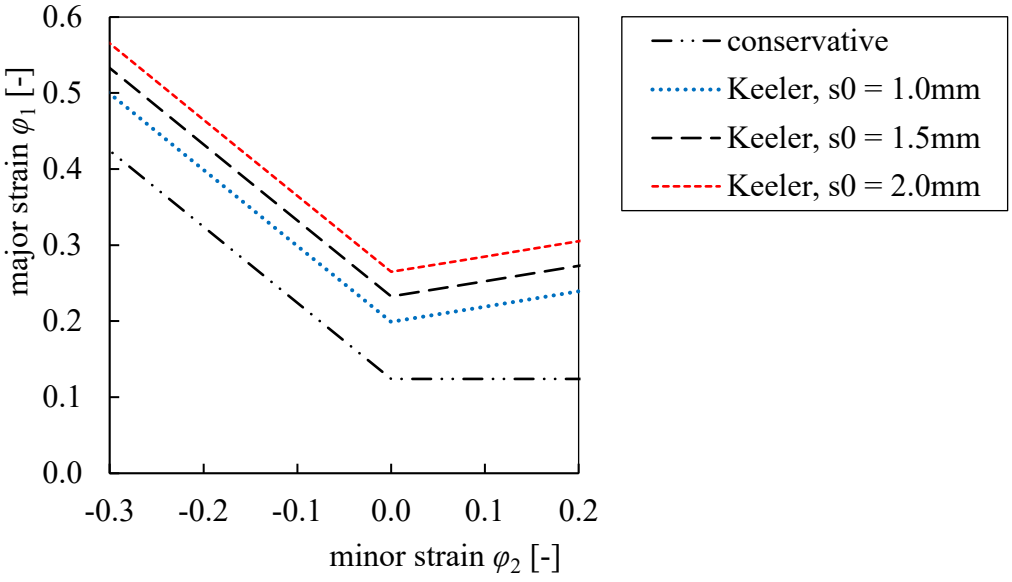

Figure 54: FLC models of KEELER and STEINHEIMER for HCT780X.

Both FLC approximations model the knee of the curve at plane strain ($\varphi_2 = 0$) which evidently represents the materials' highest sensitivity against forming under plane stress conditions. At this point, the conservative FLC equals *n*, while KEELER's FLC supports on *FLD0*. The conservative FLC lies well below KEELER's approach. Both mathematical models assume an inclination of $\rho = -1$ for the FLCs in the second quadrant of the FLD. In the first quadrant, the conservative FLC stays constant on *n*, while KEELER's FLC assumes a material specific, positive inclination. Moreover, KEELER's FLC takes sensitivity towards varying sheet metal thickness s_0 into account.

Failure criterion hypotheses

In the ISB process, it is observed, that major strain is given by the longitudinal strain component at the extrados. From the ISB strain path and the considered FLC models, several hypotheses are developed for the limiting longitudinal failure strain $\varphi_{x,max}$ in an ISB process with regard to geometrical assessment:

I. The ISB strain maximum is given by the mechanical material parameter Fracture strain ε_f. This approach has been pursued in the early stages of ISB process development due to the similarity of the strain path of ISB and the uniaxial tensile test (Frohn et al. 2017). However, ε_f only evaluates strain globally while local strain gradients dominate during necking (Marciniak and Kuczyński 1967). Therefore, hypothesis I is considered as a rough estimation, in particular for ductile materials, and is given as follows

$$\varphi_{x,max} = \ln(\varepsilon_f + 1)\,. \qquad \text{(eq. 88)}$$

II. The strain ratio $\rho = -0.5$ is compared to a FLC experiment or model. Changes of strain ratio ρ associated with necking such as described by GHOSH (1974) are neglected in this approach which, hence, might be prone to overestimate feasible longitudinal strain $\varphi_{x,max}$ in bending. Depending on the applied FLC model or experiment, also see State of Research and Technology subsection 2.4.4, hypothesis II leads

   i. for the conservative FLC approach

$$\varphi_{x,max} = 2n \qquad \text{(eq. 89)}$$

   ii. for KELLER ´s FLC model

$$\varphi_{x,max} = 2FLD_0 \qquad \text{(eq. 90)}$$

iii. a graphical derivation of $\varphi_{x,max}$ based on an experimental FLC.

For hypothesis II i) – iii), Figure 55 shows a graphical interpretation.

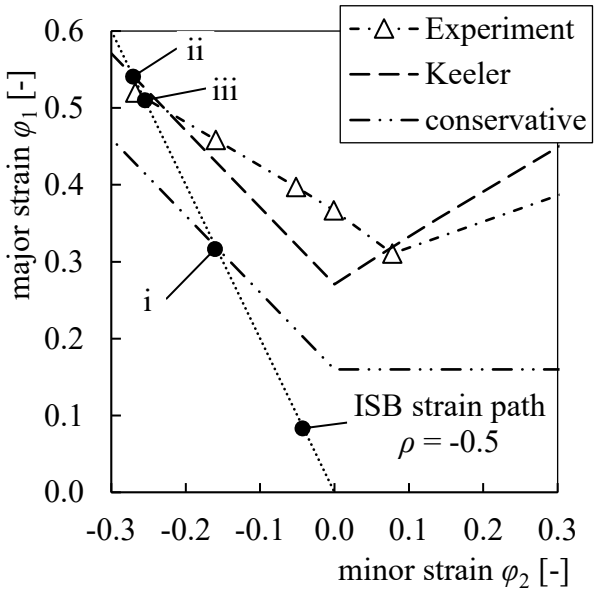

Figure 55: Graphic interpretation of the hypotheses for maximum major strain in ISB for an exemplary material. Diverse FLCs (see legend) are compared to a constant strain ratio of ρ = -0.5 which is assumed for ISB. Cases i) – iii) deliver wide-ranging maxima for major strain.

The FLCs of cases i) – iii) are correlated to the assumed strain path of ISB. Diverse results are obtained for $\varphi_{x,max}$. For the materials considered in this thesis, the respective cases are presented in Table 17. The so-called limit strain parameter *FLD0* is listed for reference to KEELER's FLC model.

Table 17: Maximum longitudinal strain limits $\varphi_{x,max}$ for ISB applied to the materials objected in this thesis as given by different FLC hypotheses.

Hypothesis		**HCT780X**	**22MnB5**	**42SiCr**	**H800**
	FLD0	0.199	0.210	0.327	0.495
I	*fracture strain* ε_f	0.174	0.199	0.240	0.322
II - i)	*strain ratio - conservative FLC*	0.248	0.226	0.320	0.524
II - ii)	*strain ratio - KEELER FLC*	0.398	0.420	0.654	0.990

Large differences are obtained for the resulting failure strain $\varphi_{x,max}$ maxima as derived from the individual hypotheses. The maxima will be compared to the experimental part of this chapter. Besides these FLC approaches, major strain corresponding to an ISB failure criterion could be determined directly by in-plane bending experiments.

6.3 Layout of the incremental sequence/density

Incremental Swivel Bending is operated in a sequence of alternating bending and feeding steps. When considering the incremental feeding distance Δf introduced in between the bending increments, the process can be discretized by the number of superposed forming zones, quantified by the factor SP. Therefore, SP represents the density of formed increments within a sequence. The analytic process model of chapter 5 delivers an approximation for the size of the forming zone regarding its opening angle γ. Applied on the profile height h_0, the longitudinal extension of the forming zone is obtained. Therefore, discrete intervals of Δf can be related to a specific number SP of superposed forming zones:

$$\frac{2}{SP+1} \cdot h_0 \cdot \tan\frac{\gamma}{2} > \Delta f \geq \frac{2}{SP} \cdot h_0 \cdot \tan\frac{\gamma}{2} \qquad \text{(eq. 91)}$$

Figure 56 graphically elucidates the superposition of incremental forming zones up to $SP = 3$.

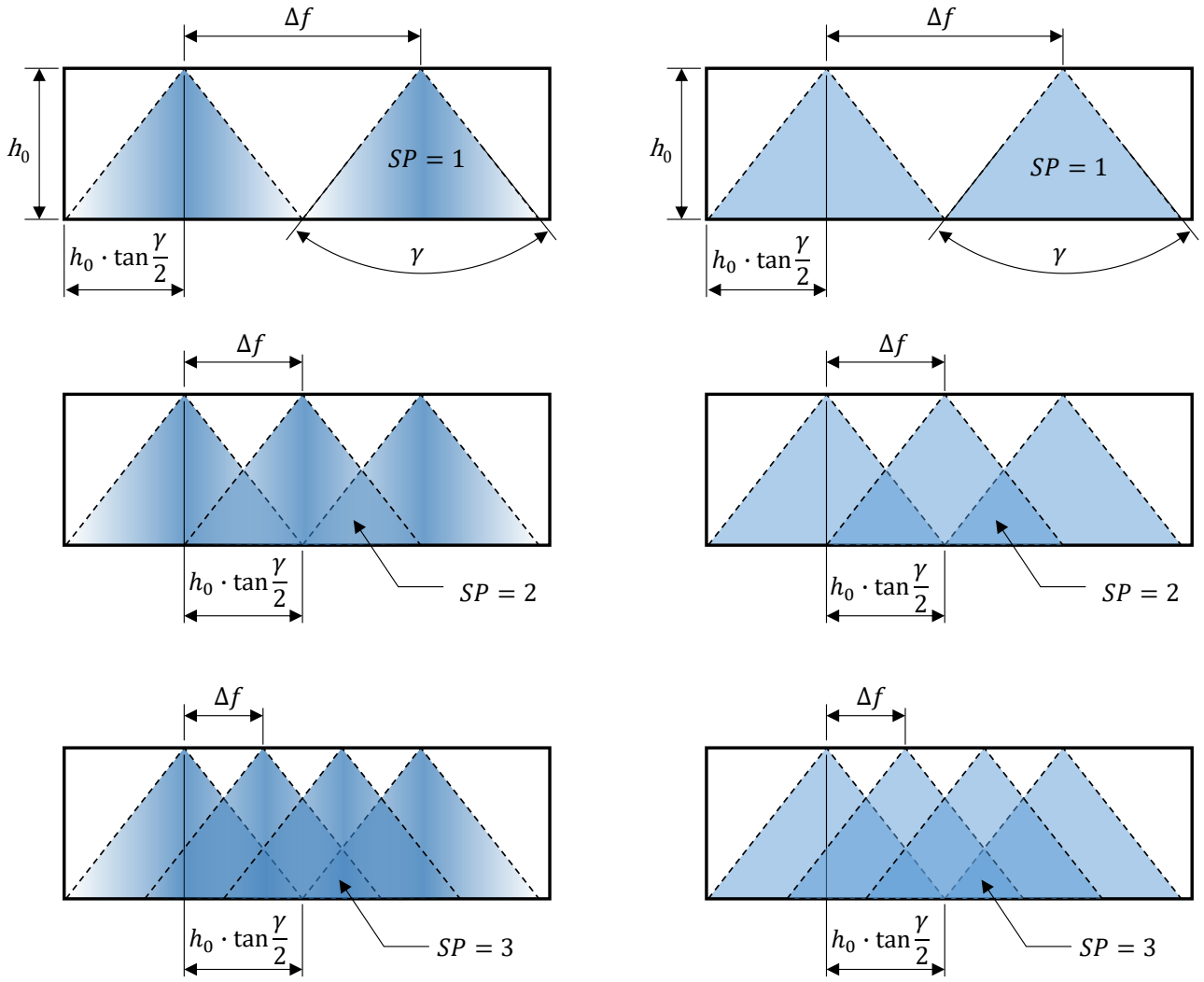

Figure 56: Schematic illustration of one- to threefold superposition of incremental forming zones. Color hues indicate strain intensity for longitudinal gradients (left) and constant distributions (right) within each forming zone.

According to section 5.3.2, longitudinal strain gradients are expected within the forming zone. From Figure 56 it is evident that superposed forming zones, when described by constant strain distributions, might lead to exaggerated strain in the overlapping areas, in particular for $SP = 2$. However, as SP increases, the difference between a gradient based and constant description decreases. Therefore, constant gradients are expected to describe the ISB process quite accurately in case of a superposition $SP > 3$. In order to layout the strain maximum resulting from the superposing forming zones, strain is assumed constantly throughout the forming zone and can be multiplied by SP. This hypothesis is graphically represented by the right-hand side of Figure 56, illustrated by the intensity of color hues. According to eq. (91), Δf is chosen corresponding to a certain degree of superposition. In a plain linear assumption, the accumulated maximum longitudinal strain of the incremental sequence $\varphi_{x,s}$ is described by

$$\varphi_{x,s} = \varphi_x \cdot SP = \ln\left(\frac{\delta_u}{\gamma - \delta_u} + 1\right) \cdot \frac{2}{\Delta f} \cdot h_0 \cdot \tan\frac{\gamma}{2} \qquad \text{(eq. 92)}$$

where γ is determined by the analytics of chapter 5. Strain is denoted in the form of longitudinal true strain φ_x to allow summing up the values sequentially. However, eq. (92) does not take work hardening into account. If the forming zones of the incremental steps overlap, work hardening stress $k_{f,i}$ is raised successively and varies from increment to increment according to the incremental index variable i. First of all, traction withing the fixation by the clamping tools must be assured. Additionally, the forming zone angle γ is expected constant throughout the process sequence as derived for a single bending increment. The unloaded bending angle δ_u highly depends on work hardening because stress determines reversing strain during elastic springback. Therefore, the constant assumption of eq. (92) is modified by a variable formulation of longitudinal strain $\varphi_{x,i}$ which is dependent on individual springback angles $\delta_{u,i}$ according to the incremental index i. In this case, strain for the incremental sequence is described by

$$\varphi_{x,s} = \sum_{i=1}^{SP} \varphi_{x,i} = \sum_{i=0}^{SP} \ln\left(\frac{\delta_{u,i}}{\gamma - \delta_{u,i}} + 1\right) \qquad \text{(eq. 93)}$$

with $\delta_{u,i} = \delta - \delta_{SB,i}$ and $\delta_{SB,i} = 3 \cdot \frac{k_{f,i-1}}{E} \cdot \frac{1}{2 \cdot \varepsilon_x} \cdot \delta$ according to the springback assumption of WITTEK, RICHTER, and LAZARZ (2011), eq. (75). Eq. (93) becomes

$$\varphi_{x,s} = \sum_{i=1}^{SP} \ln\left(\frac{\delta \cdot \left(1 - 3 \cdot \frac{k_{f,i-1}(\varphi_{x,i-1})}{E} \cdot \frac{1}{2 \cdot \varepsilon_x}\right)}{\gamma - \delta \cdot \left(1 - 3 \cdot \frac{k_{f,i-1}(\varphi_{x,i-1})}{E} \cdot \frac{1}{2 \cdot \varepsilon_x}\right)} + 1\right) \quad \text{(eq. 94)}$$

where $k_{f,i-1}$ is a function of $\varphi_{x,i-1}$ and determined according to a hardening law. For successive forming within an incremental sequence, k_{fi-1} replaces yield stress in the general formulation of springback of eq. (75). With known average incremental bending angles $\delta_{u,s}$ after release of force and the incremental feeding distance Δf, curvature κ can be derived from trigonometrical considerations. These are assumed according to the curvature models developed for the sequential operation of swivel bending machines for bending of cylindrical or conical shapes (Frohn-Sörensen, Hochstrate, et al. 2020):

$$\kappa_{\mathrm{NF}} = \frac{4}{\Delta f \cdot \left(\frac{1}{\sin\frac{\delta_{u,s}}{2}} + \frac{1}{\tan\frac{\delta_{u,s}}{2}}\right)}. \quad \text{(eq. 95)}$$

κ_{NF} refers to curvature at the strain-neutral fiber of the incrementally bent arc. The circular interpolation of a polygonised shape, which consists of edges and straight parts, does not take the profile height h_0 into account. In order to calculate the curvature at the intrados κ_{in} and curvature at the extrados κ_{ex} of the arc, eq. 95) must incorporate the offset factor o according to

$$\kappa_{\mathrm{ex/in}} = \frac{4}{\Delta f \cdot \left(\frac{1}{\sin\frac{\delta_{u,s}}{2} \pm (o \cdot h_0)} + \frac{1}{\tan\frac{\delta_{u,s}}{2} \pm (o \cdot h_0)}\right)}. \quad \text{(eq. 96)}$$

6.4 Practical validation of the ISB process layout method

The layout method for the incremental sequence of ISB presented in theoretical approaches in the preceding subchapters is applied to practical bending experiments. For these investigations, the ISB laboratory tool is upgraded for profile bending to not only conduct the experiments on flat sheets but also to demonstrate the application of the process layout method on the basis of profiles.

6.4.1 ISB laboratory scale tool for profile bending

The research tool was upgraded to allow bending open hollow cross sections such as L-, U-, Z- and hat-shaped profiles while maintaining the possibility to shift the bending axis along the lateral direction. A maximum incremental bending angle of $\delta_M = 10$ degrees as well as a minimum bending factor of $B = 1.5$ were the requirements for this stage of tool development. A mandrel according to the cavity of the cross section is introduced to the tool setup. In the stationary part, the mandrel shaft is a plain tool core, see Figure 57 (3). In order to allow adjusting the bending axis, the mandrel cannot be connected from stationary tool part to the pivoting unit from a constructive point of view. Instead, the pivoting part of the mandrel is an autonomous segmented chain (4), linked by hinge joints which allow the segments to move within the bending plane. The first segment is fixed and locked to the movement of the pivoting unit. The last optional segment of the mandrel is a solid core for additional profile support against twisting. In both tool units, i.e., stationary unit and pivoting unit, the mandrel sits on lateral rails to offset the bending axis.

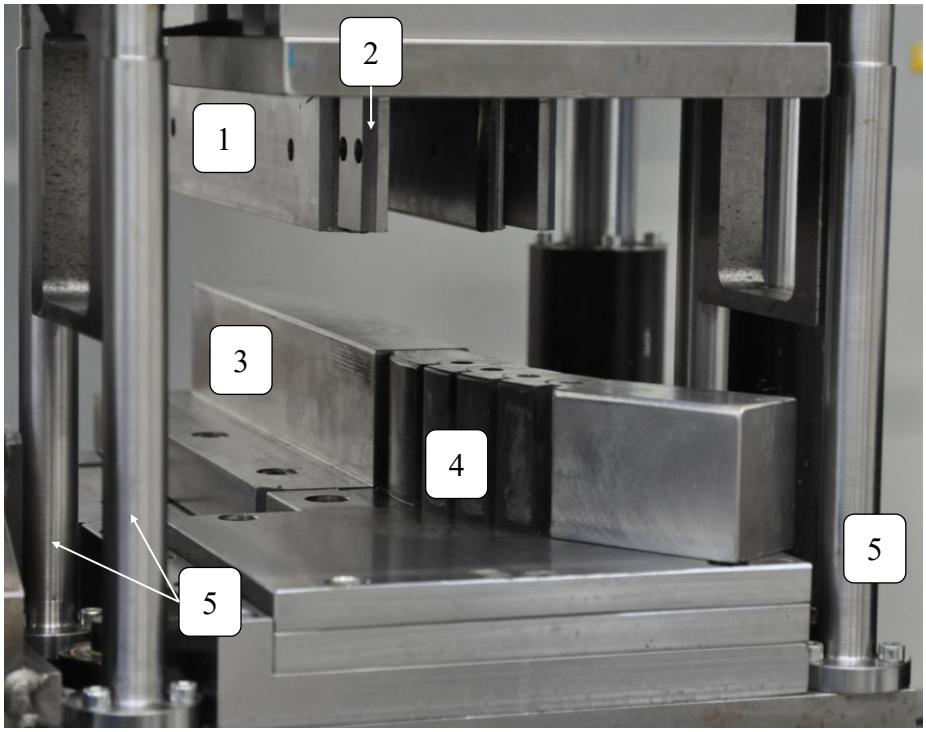

1) Upper stationary tool, flange holder
2) Upper pivoted tool, flange holder
3) Lower stationary tool, mandrel
4) Lower pivoted tool, segmented mandrel
5) Interlocking pillars between upper and lower pivoted tools

Figure 57: ISB research tool modifications for profile bending of hat-shaped cross sections about their symmetry axis.

At the upper parts of the clamping units (stationary and pivoting unit), flange holders are introduced to clamp the outer edges of the profile. These holders are internally loaded by gas springs or sit on solid filling pieces which are adjusted by shims, see Figure 57 (1, 2 respectively). In addition to clamping the flanges for force transmission during bending, the holders also support the inner wall of the profile from buckling. All effective die faces of the tooling were treated by the TENIFER process, which is described in section 4.4.1. After initial run-in trials, the roughness of the tool surfaces was tested longitudinally (0°) and laterally (90°) in relation to profile orientation. The results are documented in Table 15.

Table 18: Roughness of the contact surfaces of the ISB tool in longitudinal and lateral direction. For each parameter, the intervals of 95% confidence are given from five repetitions.

ISB tool	**Condition**	$Ra_{0°}$ [µm]	$Ra_{90°}$ [µm]
Research tool for profile bending	used	0.71 ± 0.14	1.02 ± 0.16

Running in the TENIFER treated surfaces significantly decreases roughness which is explained by an initial flattening of surface oxides. Therefore, the *Ra* values are given in used tool condition. The ISB research tool is mounted in a standard die set with six outer pillars for vertical guiding. Within this frame, the pivoted unit is constrained to rotate about the bending axis by shafts in the upper and lower part of the tool. The hydraulic bending cylinder is attached to the lower frame of the die set and the lower tool of the pivoted clamping unit. Because the upper part needs follow the rotational kinematic of the lower part, the additional inner pillars (5) interlock the upper and lower part of the pivoting clamping unit when closing the ISB tool.

6.4.2 Process scatter and accuracy evaluation

On the ISB research tool equipped for profile bending, two small series of hat shaped profile cross sections were bent to predict the process tolerances in serial operation. For this purpose, cross sections with 10 mm flanges, 60 mm tall walls and an inner bottom width of 43 mm were manufactured from HCT780X in 1.0 mm sheet metal thickness, Figure 58. The feed and bending steps of the ISB sequence were operated manually. In detail, the profile was positioned at evenly spaced marks for feeding and the pivoting unit was rotated towards a fixed mark during bending. With this approach, five samples of the parametrical study shown in Table 19 were bent. In both variants, the bending axis was offset towards the inner profile wall, so compression resulting from bending was only applied at the inner flange. A clamping force of 942 kN was found sufficient for bending these profiles without any slipping effects in the clamping units. The first series was formed with larger bending increments but a fewer number of incremental steps. In the second series, a smoother curvature was

intended by using a higher number of small bending angles. All parameters were adjusted so that two comparable bending series resulted with respect to their geometrical features.

Table 19: ISB processing parameters of bending series.

Series [No.]	**Repetitions**	***o*** [-]	F_N [kN]	n_{ISB} [-]	***δ*** [°]	***Δf*** [mm]
1	5	0.5	942	6	9	15
2	5	0.5	942	9	5	10

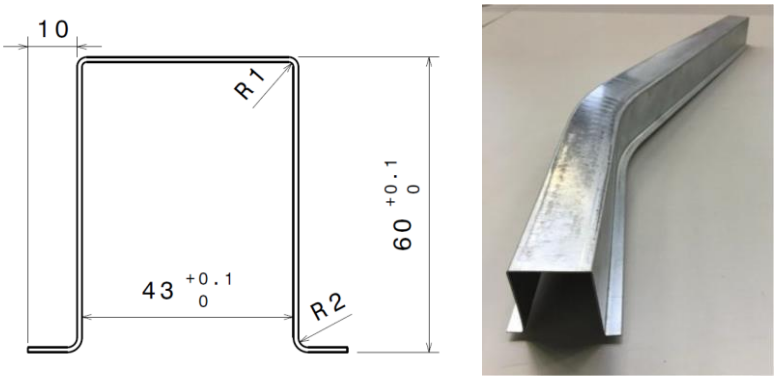

a) b)

Figure 58: Hat shaped profiles, manufactured for serial bending experiments.

After bending, the resulting bending radii and angles of these profiles were measured at six distinct regions by the FARO ARM coordinate sampler. The data were measured at the inner and outer flanges of the hat-shaped profile, *fi* and *fo* respectively, at the inner and outer walls, *wi* and *wo* respectively, and at the inner and outer edge of the bottom, *bi* and *bo* respectively. The obtained geometrical features are presented in the diagrams of Figure 59. The first series resulted in tighter profile bending radii with a higher total bending angle.

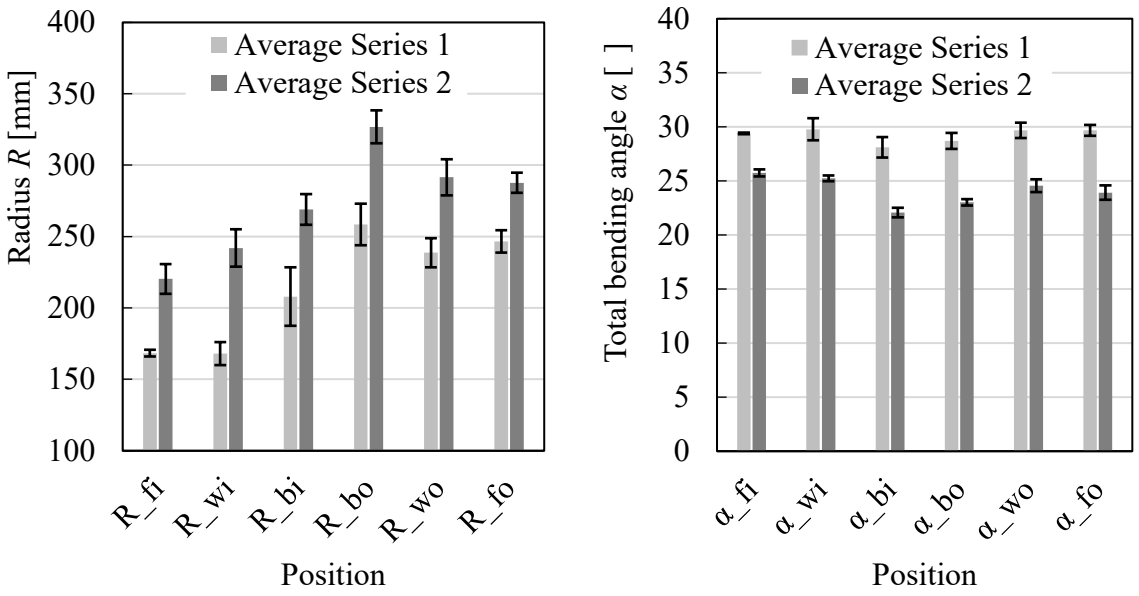

Figure 59: Incremental bending series based on hat shaped profiles. Investigation of process scatter with respect to bending radius and bending angle.

From these data, total average standard deviations of 10.6 mm and 9.8 mm for the radii of the first and second series are obtained respectively. An angular standard deviation of 0.65 degrees is obtained from the first series, while the angles of the second series spread by 0.43 degrees.

6.4.3 Validation of the bending axis offset

A bending geometry is represented by the bending factor B which is the quotient of profile height and bending radius. From a demanded target geometry, the average longitudinal strain distribution is essentially derived on the basis of the elementary bending theory under neglect of the incremental forming nature of an ISB process. Using this theory, the ISB strain diagram displays longitudinal strain at the extrados over bending factor as a function of bending axis offset and therefore facilitates to layout the lateral position of the axis based on the material's ductility. Based on the cross section of the profile and the ductility of the material, the feasibility of the demanded target geometry as well as suitable positions of the bending axis are assessed. If an arc is formed with a smooth incremental subdivision without the onset of necking effects, this assumption is expected to deliver sufficient approximation which allows to initially lay out the lateral shift of the bending axis. To validate this layout procedure, a series of profiles was bent on the ISB research tool equipped for profile bending. Parallel sheets from 42SiCr steel were prepared for profiling with a length of 800 mm and a nominal thickness of 2 mm. For optical strain evaluation, a square grid (mesh size 1 mm) was electrolytically applied on the surface of the plane sheet metal material. Subsequently, U-, L- and Z-shaped profiles were bent in a press brake. The cross sections' dimensions are shown schematically in Figure 60.

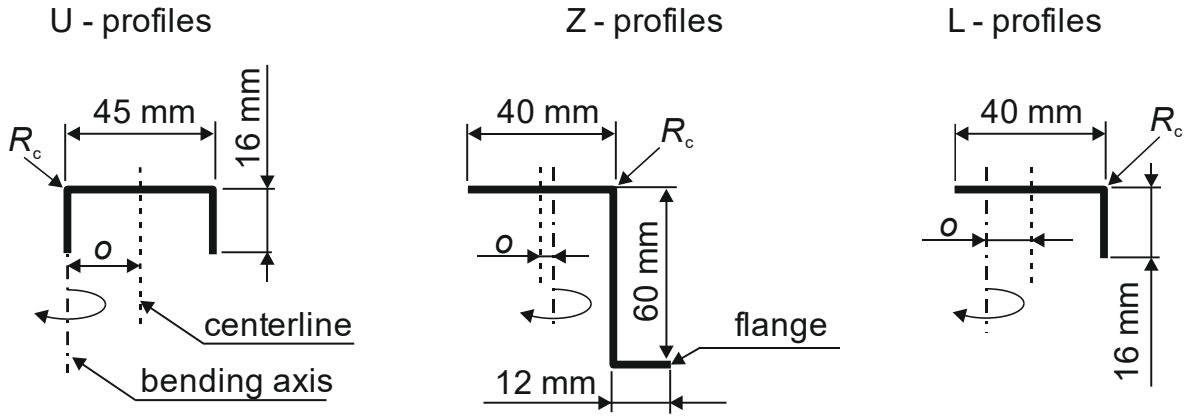

Figure 60: Cross sections manufactured from 42SiCr blanks. Offset *o* indicates the position of the bending axis during ISB.

From bending on the press brake, an outer edge radius of R_c = 4.0 mm resulted at the profiles. Next, these profiles were incrementally swivel bent with a variation of the following ISB process parameters: i) incremental feeding distance Δf, ii) number of increments n_{ISB} and iii) the offset factor *o*. The resulting geometrical variation of the bent profiles demonstrates the forming flexibility of the ISB process, both by means of processible cross sections as well as manufacturable arcs, see Figure 61.

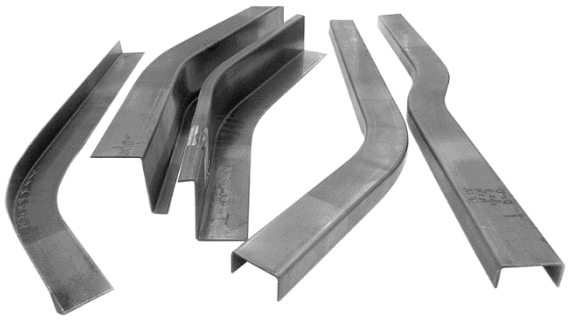

Figure 61: Practical demonstration of the flexibility of the ISB process: L, Z and U-Profiles (left to right) were incrementally bent using the same tool configuration.

The forming process parameters used for these specimens were chosen in a way to obtain tight bending radii at high strain values. Table 20 summarizes the parameters for the different ISB process setups along with specimen numbers for the individual profiles. All bending sequences have been bent with a constant incremental bending angle δ of 9°.

Table 20: ISB process parameters for bending profiles from 42SiCr, see Figure 61.

Cross section	Profile specimen ***no.***	Number of sequences n_{ISB} [-]	Incremental feed Δf [mm]	Pivot offset o [-]
U	3	7	15	0.5
U	5	5	12	0.5
U	6a	4	15	0.5
U	6b	4	15	0.5
L	7	7	13	0.35
L	8	7	13	0.35
Z	10	6	15	-0.1
Z	11	6	15	-0.1

In the case of U-profiles, the bending axis was positioned at the intrados to avoid wrinkling of the inner profile wall according to Figure 60. This offset causes a tensile strain to superpose the bending strain distribution and corresponds to a factor of $o = 0.5$. For the L-profiles the offset was set to $o = 0.35$ to allow some compression at the inner arc. In the case of Z-profiles, an offset of $o = -0.1$ was adjusted to cause even more compressive than tensile forming within the bending strain distribution. By the reduction of incremental feed, U-profile no. 5 was bent by a very tight radius. As it exceeded the material's ductility, this experiment resulted in a crack at the outer arc. U-profile no. 6 was bent twice in alternating directions to demonstrate an S-shaped arc (right hand profile shown in Figure 61). Both arcs of no.6 were evaluated individually, referred to as 6a and 6b in Table 20. The electrolytically applied grid marks on the profiles were evaluated by optical strain measurement (OSM) posterior to forming, see Figure 62 a).

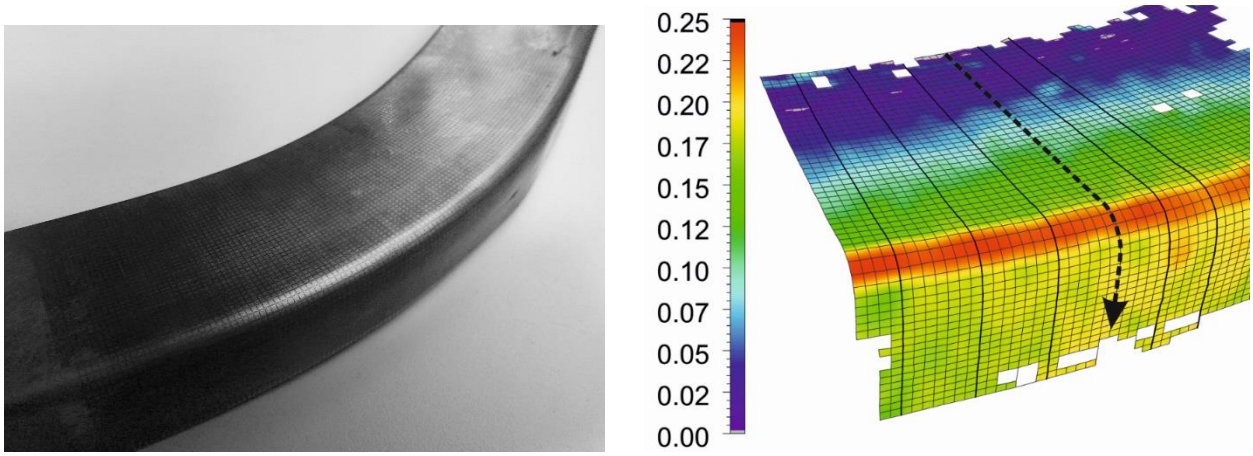

a) b)

Figure 62: a) Arc of L-profile no. 8, 1 mm square grid marked for optical strain examination and b) corresponding distribution of major true strain $\varphi_{1,opt}$ which exhibits a radial increase with maximum values at the extrados. Indication of lateral line section evaluations (arrow).

The specimens of this experimental series were evaluated by the OSM system AUTOGRID by the company VIALUX. As an example, Figure 62 b) shows the major true strain distribution within the arc of L-profile no. 8. Due to the short feeding distances Δf introduced to the forming sequence of these profiles, the incremental steps overlap multiple times. Hence, by qualitative means individual increments are barely discernable from the strain map. The continuous modelling approach of this section is therefore assumed applicable.

From the information gathered within the strain maps of the evaluated profiles, qualitative trends and the quantification of corresponding maxima are of key interest. Therefore, several lateral line plots were evaluated in the bent arcs. A corresponding path is indicated in Figure 62 b) by an arrow across the bent arc. Qualitatively, major true strain starts from zero near the inner arc and shows a radial increase over the profile height (in the bending plane). Maximum values are observed at the specimen's outer edge where the cross section's radius R_c and the radius at the extrados R_{ex} of the ISB-manufactured arc overlap because the profiles were gridded prior to bending the cross sections on the press brake. Continuing along the cross section's circumference, constant values are observed in the profile wall. Strain decreases in longitudinal direction towards the arc's beginning and end.

Curvature distribution

A tactile coordinate sampler was used to evaluate the radii of the incrementally swivel bent profiles. The gauge arm FAROARM EDGE spatially measures the position of its tip with an accuracy of 0.024 mm. For the present evaluation, polylines were sampled in the software POLYWORKS 2016 by equidistant time or displacement intervals. The ISB bending radii of the profiles were evaluated by this sampling method with a step size of 1 mm, see Figure 63 a).

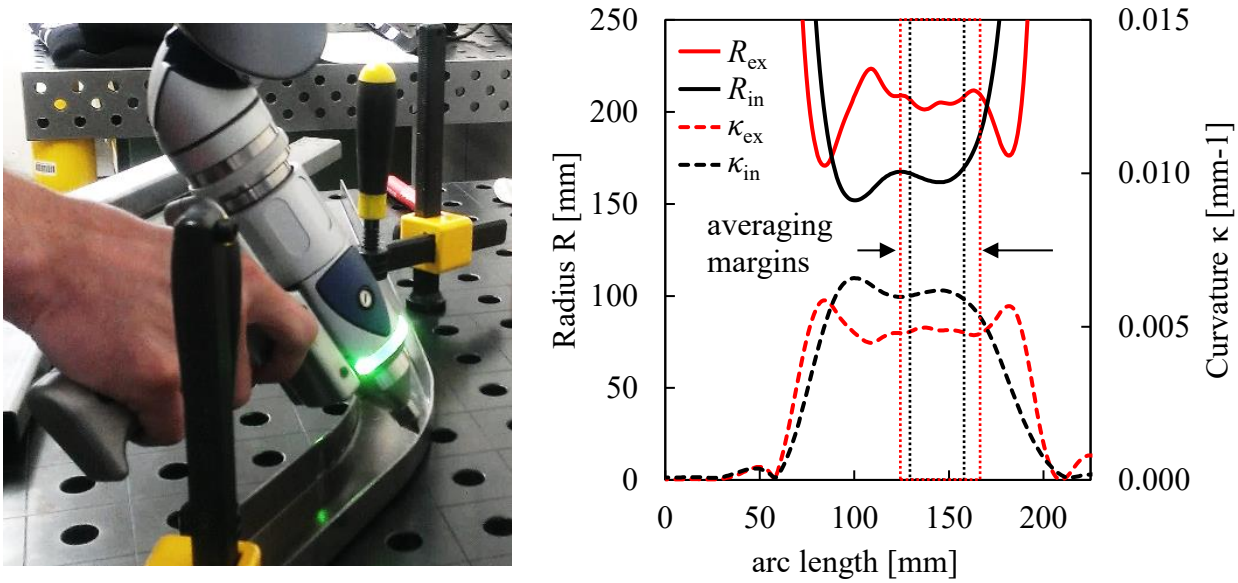

a) b)

Figure 63: Spatial coordinate sampling for the evaluation of geometric features. a) FAROARM Edge device sampling continuous coordinates alongside the inner radius of an ISB formed U-profile. b) Longitudinal curvature distributions of the intrados and extrados of an ISB formed arc.

The curvature distributions of the ISB profiles were evaluated corresponding to the method of VATTER and PLETTKE (2013) who utilized the FRENET-SERRET formulae to obtain curvature over length plots. Figure 63 b) shows an example for the local curvature distributions over the arc length of a bent ISB profile. The trends increase at the beginning of the formed arc at the intrados (κ_{in}) and the extrados (κ_{ex}). Both values show overshooting peaks before reaching nominal curvatures where approximately constant values are seen. This nearly constant area is averaged for evaluation of nominal inner and outer bending radii. In between, each specimen's central bending radius was calculated as mean value:

$$R_{cl} = \frac{\overline{R_{ex}}+\overline{R_{in}}}{2} = \left(\frac{\overline{\kappa_{ex}}+\overline{\kappa_{in}}}{2}\right)^{-1} \quad \text{(eq.97)}$$

For all ISB specimens, distinct areas of beginning and ending slopes were observed in their curvature distributions, similar as reported by GROTH (2020).

Miniature tensile tests

For bending geometries manufactured by an ISB process, a linear function of the lateral strain distribution is assumed over profile width *h*. According to the ISB strain diagram of chapter 6.1, this bending strain distribution is expected to be superposed by a constant compressive or tensile strain distribution by means of the bending axis offset *o*. Correspondingly, stress is expected to follow a lateral distribution given by the work hardening law. For layout of an ISB bending product, it is crucial to be aware of exploiting the material's ductility, in particular for forming very tight arcs. For

this reason, miniature tensile test samples were extracted from ISB profiles. Miniature tensile tests provide the opportunity to locally analyze the mechanical material properties. Such miniature tensile tests require a gauge length of L_0 = 5mm and outer dimensions of 20 x 5 mm^2. From two exemplary profiles (U-profile No.3 and L-profile No.8), test specimens were extracted by wire erosion, see Figure 64. While each specimen was oriented in longitudinal profile orientation, lateral series were taken over the cross section's circumference of the profiles.

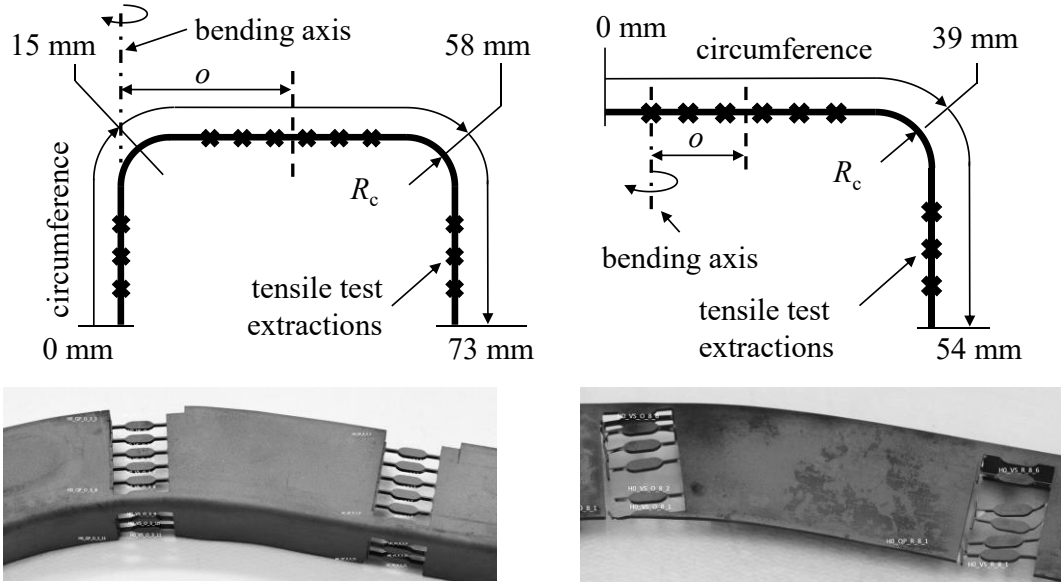

Figure 64: Extraction of miniature tensile test samples in the straight and incrementally bent areas of ISB profiles. Circumferential evaluation coordinates (top) and corresponding profiles after extraction (bottom). Left: U-profile no.3; right: L-profile no. 8.

The samples were subjected to quasi-static tensile testing to investigate local material properties. For referencing the miniaturized test specimens, the material properties were examined in the straight profile areas as well as in the bent areas of the herein manufactured profiles.

The correlation of both examination methods, OSM and miniature tensile tests, delivers the influence of the bending process on the material's ductility which results from longitudinal straining. For both profiles, Figure 65 compares five lateral line plots of optically captured major true strain $\varphi_{1,opt}$ with the corresponding uniform tensile elongation values as obtained from the mini tensile tests. Evidently, a linear increase over profile height is identified.

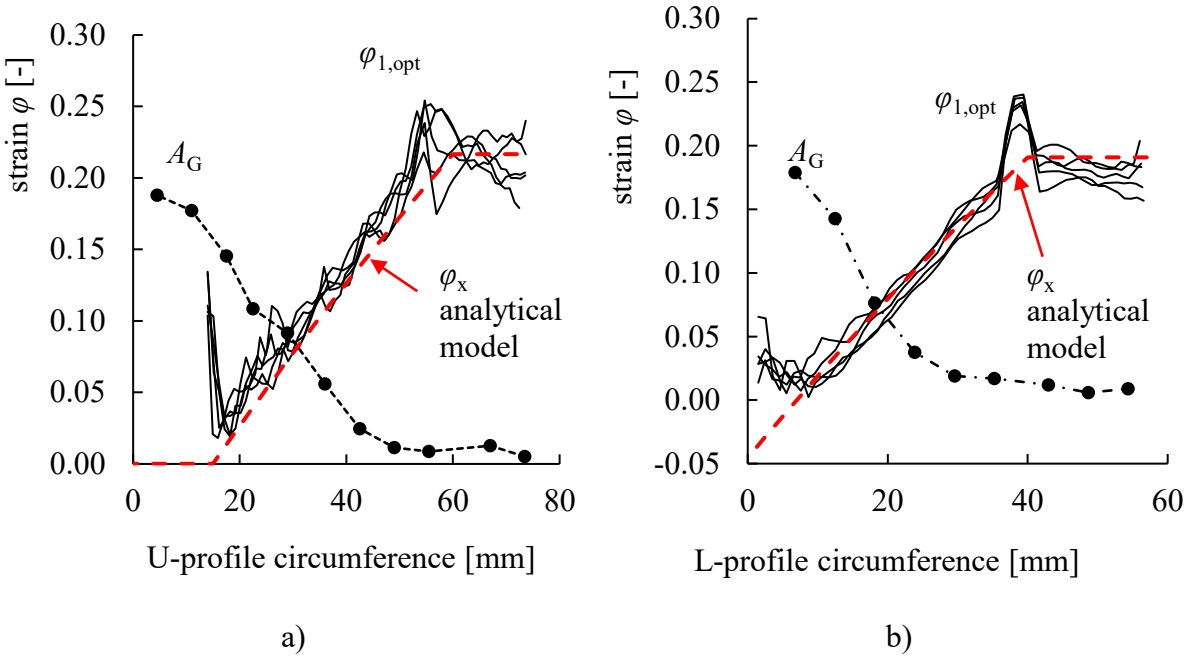

Figure 65: Major true strain $\varphi_{1,opt}$ and locally tested uniform tensile elongation A_G (in logarithmical form as true strain), both laterally evaluated from ISB processed profiles. The comparison indicates the utilization of the material's ductility for the forming process. a) U-profile No.3; b) L-profile No.8. The predictions of the analytical model associated with the ISB strain diagram well agree with the strain values measured by OSM

At the circumferential positions of the bending axis, a) 15 mm; b) 7 mm, major true strain $\varphi_{1,opt}$ begins to increase linearly from zero up to the extradoses of the evaluated profiles. Peaks caused by the outer edge radius R_c are observed at a) 58 mm and b) 39 mm. At the profiles' outer walls, longitudinal strain remains constant. In contrast, inverse trends of the material's residual ductility over profile height are obtained from the tensile tests (judged on uniform tensile elongation). In addition, the analytical model behind the ISB strain diagram is utilized to predict longitudinal strain φ_x as a function of the lateral profile coordinate y. Compared to major strain obtained by optical strain measurement, the analytical predictions of eq. (87) well agree to the measured surface strains from the profiles.

In conclusion, strain increases linear over the height of the profile within an arc similar to continuous bending processes. The strain maximum is located at the extrados and is shifted laterally corresponding to the bending axis offset. To quantify tensile strain reached at the outer arcs of all profiles, major (longitudinal, $\varphi_{1,opt}$) and minor (radial, $\varphi_{2,opt}$) true strain maxima are examined from the strain maps. Especially in the case of necking or cracking, optically measured strain distributions exhibit coarse and steep trends at their extrema. The technical standard DIN EN ISO 12004-2 (2008), intended for the approximation of forming limit curves (FLC) suggests a method for evaluating strain maxima in a repeatable way. The supporting points for an inverse parabolic mathematical trend are fixed at the zeroes of the major strain distribution´s second derivation, while the crest of the parabola

represents the strain maximum. This method is applied to the line plots evaluated from the strain maps to quantify $\varphi_{1,opt}$ and $\varphi_{2,opt}$.

Resulting from the bending factor of an ISB profile and the offset, the analytical model associated to the strain diagram of section 6.1 is utilized to calculate the corresponding longitudinal strain maximum at the extrados $\varphi_{x,ex}$. Based on the specimens of this experimental series, Table 21 compares the bending factors and optically evaluated strain extrema $\varphi_{1,opt}$ and $\varphi_{2,opt}$ with the calculated values.

Table 21: Results from the ISB profile bending experiments. Examination of the bending factor B and minor $\varphi_{2,opt}$ and major $\varphi_{1,opt}$ strain components which result from the process parameters of Table 20. The comparison to the analytic strain model $\varphi_{x,ex}$ agrees well with the optically measured values $\varphi_{1,opt}$.

Cross section	Profile specimen **no.**	Pivot offset o [-]	Bending radius R_{cl} [mm]	Bending factor B [mm]	Major strain $\varphi_{1,opt}$ [-]	Minor strain $\varphi_{2,opt}$ [-]	Strain ratio ρ [-]	Calculated max. strain $\varphi_{x,ex}$ [-]
U	3	0.5	186	3.6	0.231	-0.120	-0.52	0.24
U	5	0.5	155	2.9	0.280	-0.070	-0.26	0.29
U	6a	0.5	165	3.2	0.225	-0.105	-0.47	0.27
U	6b	0.5	172	3.3	0.210	-0.120	-0.57	0.26
L	7	0.35	143	3.2	0.230	-0.115	-0.51	0.24
L	8	0.35	170	3.9	0.194	-0.102	-0.53	0.20
Z	10	-0.1	185	4.5	0.076	-0.040	-0.53	0.09
Z	11	-0.1	211	5.1	0.065	-0.032	-0.49	0.08

Evidently, the experiments on U-profiles indicate that a decreasing feed results in tighter arcs with higher strain values. The experiments on L-profiles show that shifting the bending axis towards the outer arc results in reduced true strain values. Hence, an even tighter arc than U-profile no. 5, which failed due to cracking, could be bent successfully in the case of L- profile no. 7 by shifting the bending axis from the intrados towards the center line of the profile. The corresponding major strain maxima of these experiments are plotted over bending factor within the ISB strain diagram as a function of the bending axis offset in Figure 66.

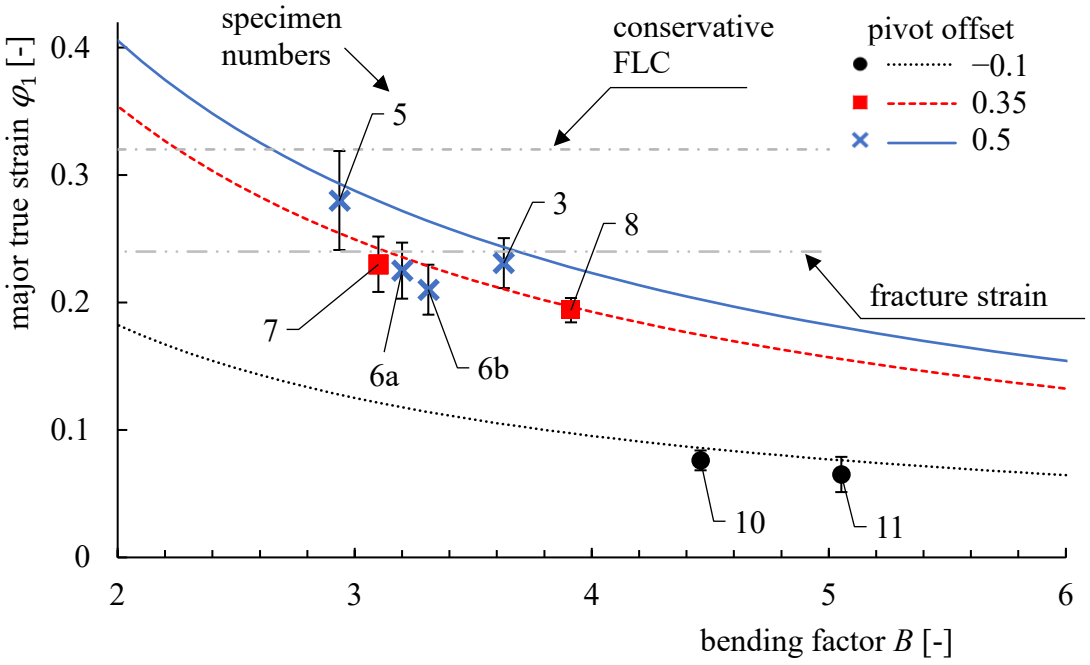

Figure 66: ISB strain diagram for the profile bending experiments. Comparison of the experimentally obtained major true strain maxima $\varphi_{1,opt}$ with the analytically calculated strain at the extrados $\varphi_{x,ex}$, both as a function of bending factor B and bending axis offset o.

The optically captured strain maxima of most specimens are approximated in accordance with the theoretical assumptions of the strain diagram. Both arcs of profile no.6 (6a, 6b) show somewhat lower strain maxima than calculated by the model because by only four incremental steps n_{ISB} each, a lower incremental density was present within the deformation zones of these sequences. This relation will be explained in the following subchapter. The cracked profile no. 5 is compared to two of the presented failure hypotheses, i.e., fracture strain and the maximum tolerable value for major strain when matching the assumed ISB strain ratio with the conservative FLC. Interestingly, both hypotheses lie just at the border of the spread of the experimentally observed strain for this bending ratio, as indicated by the error bars. The ISB failure criterion has been investigated experimentally in detail and is presented in section 6.4.5.

6.4.4 Validation of the deformation zone of ISB sequences

From a systematic point of view, the incremental process sequence of ISB is characterized by the density of incremental steps which is expressed as the amount of superposed forming zones *SP* in this thesis. It is expected that the incremental density influences strain, curvature and springback of an incrementally formed arc. The analytic model for a single bending increment (chapter 0) delivers an approach to estimate the size of the triangular forming zone which in combination with the feeding distance Δf (in between two bending steps) determines *SP*. In turn, distinct feeding intervals are associated with *SP*. Moreover, the model for a single bending increment delivers longitudinal strain

at the extrados which is either averaged over the whole forming zone by the constant strain hypothesis or represented by an sandglass shaped approach. From simulations, a sudden increase of strain is seen at the location of yield sheath which smoothly approximates the maximum in the process center, see Figure 29, page 74.

From OSM, strain is observed to longitudinally decrease towards the beginning and ending of the forming zone, see Figure 48 b) on page 114. Even so, multiple superposed increments are assumed to directly accumulate by the factor *SP* in a first approach which is denoted as "cumulated strain" hypothesis in the following paragraphs. Judged on the graphical interpretation of superposed forming zones illustrated in Figure 56, the constant strain hypothesis is assumed valid in between $SP \geq 3$ up to a density where localization effects set on. In a second hypothesis, the longitudinally decreasing tendency of each individual bending increment is considered. Corresponding to its longitudinal position, a fragment of each individual increment contributes to the strain accumulation in the strain maximum of the arc. This relation is mathematically expressed by a GAUSSian sum function, hence, the hypothesis is denoted "GAUSS strain" in the remainder of this thesis.

In order to practically validate the analytical models for incremental bending described above, an experimental setup according to Table 22 comprises a parameter variation of materials, cross sections of plane strips, press loads, clamping lengths and incremental bending angles. The exemplary case studies are denoted equally to the experiments conducted for forming single increments (Table 16).

Table 22: Experiments to verify the superposition behavior of the forming zones in the ISB process.

Material	s_0	h_0	$l_{c,0}$	F_N	δ	$\frac{1}{2}\gamma$	*SP*	Δf	case
	[mm]	[mm]	[mm]	[kN]	[°]	[°]	[-]	[mm]	
22MnB5	1.4	50	50	500	3.25	45.0	{1…33}	{100…3}	a)
		80	100	816	3.00	44.0	{1…20}	{160…8}	b)
HCT780X	1.5	50	100	816	5.25	47.5	{1…10}	{123…12}	d)
FORTA H800	1.0	50	50	900	2.40	30.0	{1…60}	{60…1}	g_1)
					6.25	40.5	{1…25}	{110…3.5}	g_2)

Plane strips from the materials 22MnB5, HCT780X and FORTA H800 are grid-marked electrolytically and subsequently introduced to incremental bending experiments on the ISB research tool in its revised setup for in-plane bending. The forming zone angles γ shown in the table are calculated from the analytical model of a single bending increment in order to enable the determination of the feeding intervals Δf necessary to achieve a certain superposition *SP* of forming zones according to eq. (91). Consequently, Δf is decreased systematically corresponding to the

expected number of superposed forming zones *SP* and each is carried out on individual specimens until material failure due to cracking at the extrados is observed (cf. Appendix, Figure 122). The bending angle was kept constant within each experimental series. Besides the examination of springback angles, curvature and failure from these experiments, the deformation zone is evaluated by qualitative and quantitative means from strain maps captured by OSM. The deformation zone is understood as the whole accumulation of superposed forming zones caused by incremental bending sequences. The major strain maps captured from the experimental series g_1) are illustrated in Figure 67 for *SP* in between one and twelve; *SP* = {1, 2, 4, 6, 8, 12}.

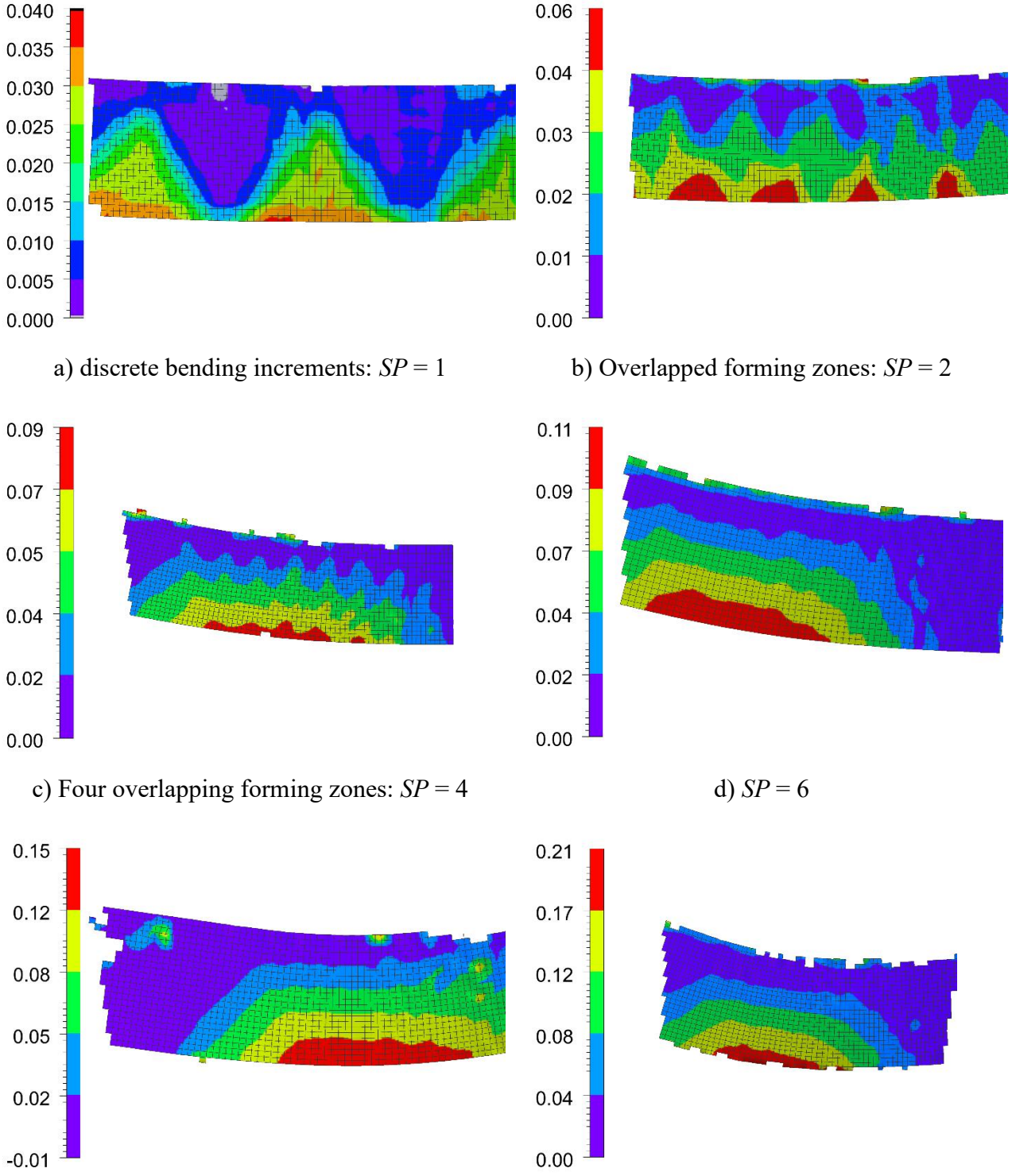

a) discrete bending increments: $SP = 1$

b) Overlapped forming zones: $SP = 2$

c) Four overlapping forming zones: $SP = 4$

d) $SP = 6$

e) $SP = 8$

f) $SP = 12$

Figure 67: Major strain maps, as captured from the surfaces of sheet metal strips which were subjected to incremental in-plane bending. Visualization of the deformation zone of case g_1: FORTA H800, 50 x 1.0 mm² at 900 kN press force at a constant incremental bending angle of 2.4 degrees. a) Three bending increments with a separating incremental feed of $\Delta f = 60$ mm, b) beginning of overlapping forming zones at $\Delta f = 30$ mm, c) $\Delta f = 15$ mm resulting in $SP = 4$, d) $\Delta f = 10$ mm, e) $\Delta f = 7$ mm, f) $\Delta f = 5$ mm.

Evidently, smoother deformation zones are achieved with a higher degree of superposition *SP*. The initial discrete bending increments successively overlap towards an even deformation region in the results with a higher superposition. In addition, strain and curvature increase by the systematic reduction of feed. To quantify these relations for all experiments summarized in Table 22, the strain maxima at the outer arcs are extracted from the optical strain measurements (OSM) and evaluated with respect to *SP*. In the diagrams of Figure 68, these results are compared to the aforementioned hypotheses for strain accumulation of the overlapping forming zones. "Cumulated strain" is based on a constant strain distribution throughout the forming zone, thus linearly adding up the calculated strain maxima of each bending increment by the number of *SP*. The "GAUSS strain" hypothesis takes the longitudinal strain gradient of each increment by the GAUSSian sum function into account.

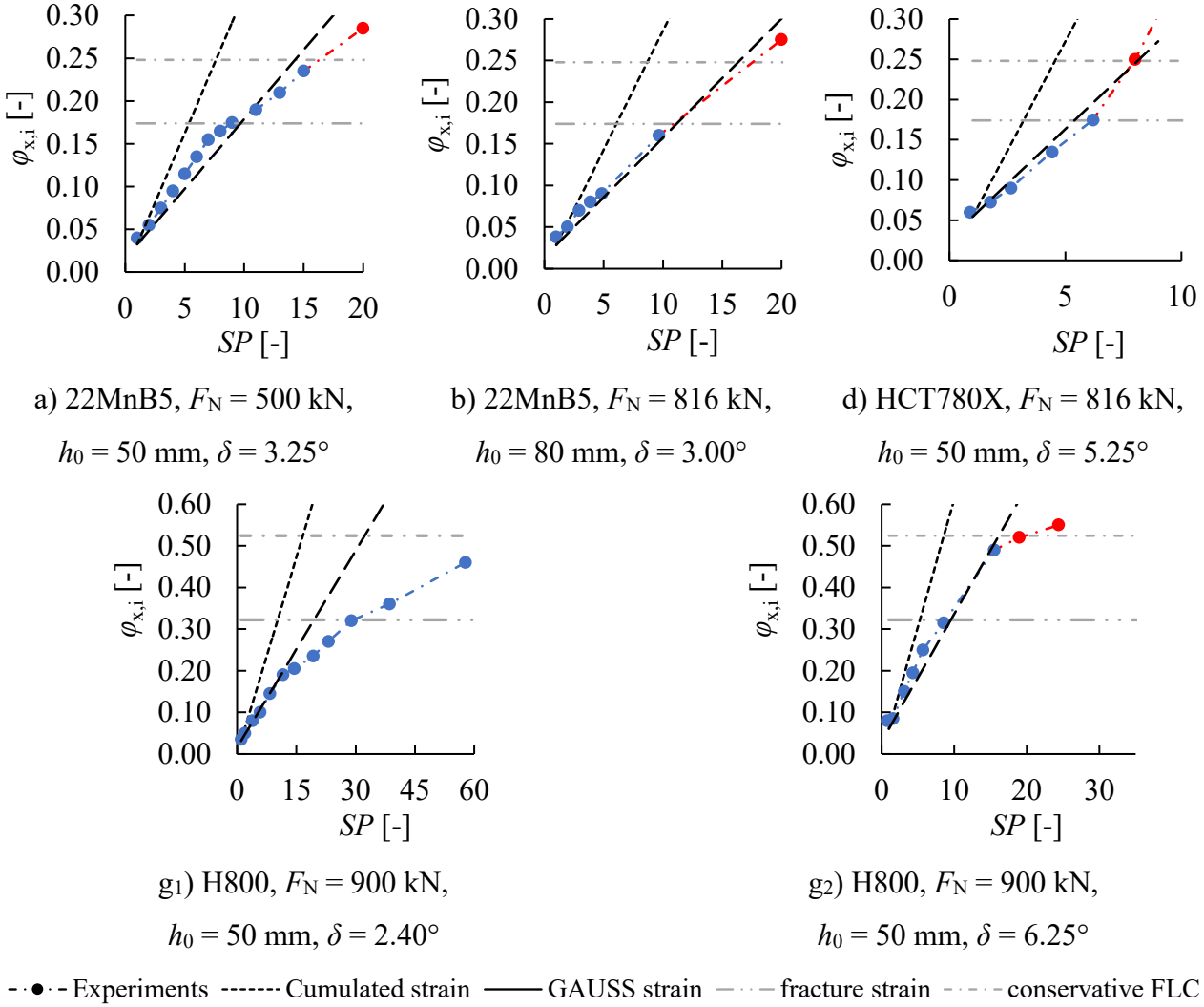

Figure 68: Longitudinal strain maxima $\varphi_{x,i}$ of the incremental bending series plotted over the number of superposed forming zones *SP*. Comparison of two hypotheses for accumulated strain: While a plain linear strain assumption strongly overshoots the experimental observations, the GAUSSian sum function matches the strain values captured from the experiments except for g_1 where very small incremental bending angles were processed. Red sections of the experimental graphs indicate pronounced necking or rupture at the extrados. These highlighted sections are compared to the assumed failure criteria against rupture.

From the quantitative OSM examination, namely the longitudinal strain maxima at the outer arc, a linear trend of increasing strain values over superposition is observed from the experimental series. Regarding the prediction of the applied models, the GAUSSian sum function delivers sufficient strain predictions for *SP*. To determine cracking, the forming limits given by fracture strain and the conservative FLC approach are implemented and compared to those experiments, where cracking (cases d and g_2) or severe necking tendencies with micro cracks (cases a and b) are observed at the extradoses of the bending specimens. The series a and g_1 reveal a kink towards flatter inclination in the otherwise linear trend of strain over superposition. In case g_1, no failure is obtained because FORTA H800 was formed up to the limitation of technical feasibility, i.e., incremental feed of $\Delta f < 1$ mm ($SP > 60$), causing the incrementally curved material to collide with the tool.

The GAUSS superposition strain model is parameterized by

i) initial strain as resulting from a single bending increment and

ii) the amount of overlapping increments *SP*, which results from the incremental feeding distance.

Suitable strain predictions are obtained from this assumption. Incorporating both failure criteria, fracture strain and the conservative FLC approach, the forming zone superpositions and the corresponding feeding distances are expressed for a given ISB process setup according to

$$SP_{\mathrm{crit,l}} = \mathrm{s} \cdot \frac{\ln(\varepsilon_{\mathrm{f}} + 1)}{\varphi_{x,ex}(\delta)} - 1;\ \Delta f_{\mathrm{crit,l}} = \frac{2}{SP_{\mathrm{crit,l}}} \cdot h_0 \cdot \tan\frac{\gamma}{2} \qquad \text{(eq. 98)}$$

and

$$SP_{\mathrm{crit,u}} = 4 \cdot \frac{n}{\varphi_{x,ex}(\delta)} - 1;\ \Delta f_{\mathrm{crit,u}} = \frac{2}{SP_{\mathrm{crit,u}}} \cdot h_0 \cdot \tan\frac{\gamma}{2}\ . \qquad \text{(eq. 99)}$$

The lower critical number of superposed forming zones $SP_{\mathrm{crit,l}}$ and the corresponding lower critical feed $\Delta f_{\mathrm{crit,l}}$ derive from fracture strain ε_{f} while the upper values $SP_{\mathrm{crit,u}}$ and $\Delta f_{\mathrm{crit,u}}$ derive from the conservative FLC model.

The above-described superposition strain model only counts for arcs, which are formed with at least as much incremental steps, as superposed forming zones: *SP* ($n_{\mathrm{ISB}} \geq SP$). This state is referred to as saturated incremental sequence. It is observed, that if a saturated superposition is reached by a corresponding number of increments, strain would no longer increase. In contrary, if a smaller number of increments is formed than *SP*, the superposed strain is considered ascending (e.g., the s-shaped profile specimen no.6, Figure 66). Figure 69 shows graphical interpretations of these scenarios. For

an ascending type of incremental deformation zone, the parameterization of the GAUSSIAN sum function could either be *SP* or n_{ISB}. The first approach would overestimate strain and therefore give a worst-case approximation of strain, while the latter case would underrate the strain maximum.

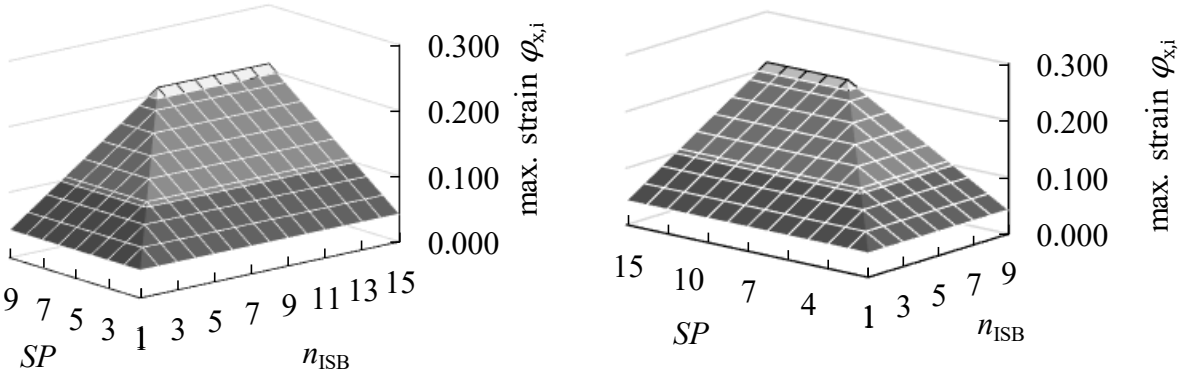

Figure 69: Study of the strain superposition function. a) If a larger number of increments is adjusted, than could overlap, strain would no longer increase and is considered "**saturated**". b) If increments are formed by a very small incremental feed Δf, which would correspond to a higher superposition factor *SP*, than the actual number of increments n_{ISB}, only n_{ISB} deformation zones can overlap thus determining maximum strain in the GAUSSian sum function. This state of superposition is denoted "**ascending**".

In order to assure saturation in the experimental series of Table 22, at least a 10% higher number of incremental steps n_{ISB} are formed than the factor of superposition *SP* (e.g., the last experiment on case g_1 is given by *SP* = 60, so n_{ISB} = 67 steps are conducted to ensure a saturated state of forming).

With regard to crucial geometric features of a product manufactured by profile bending, the total bending angle α and the curvature κ are of key interest. α achieved in incremental swivel bending needs to be derived from the sum of all incremental bending angles after release of process force where elastic springback is approximated by the model of WITTEK et al. (2011). However, as work hardening significantly influences springback according to ENGEL and KERSTEN (2010), yield stress needs to be adjusted by a hardening law according to the incrementally accumulated strain maximum. The average springback angle $\delta_{SB,i}$ of an incremental sequence follows

$$\delta_{\mathrm{SB,i}} = \delta \cdot \frac{3 \cdot R_i}{2 \cdot E \cdot \varphi_x}, \text{with } R_i = kf\left(\varphi_{x,i}\right) \qquad \text{(eq. 100)}$$

using the hardening-justified yield stress R_i and strain, as resulting from a single increment.

For verification, the total bending angles α of the above-mentioned experiments are evaluated by the digital measuring apparatus TUBOCONTROL. α is divided by the number of increments n_{ISB} to obtain

the average unloaded incremental angle $\delta_{u,s}$. For the material and parameter variation of Table 22, $\delta_{u,s}$ are presented over superposition and compared to analytically modelled trends of $\delta_{u,i}$ in Figure 70.

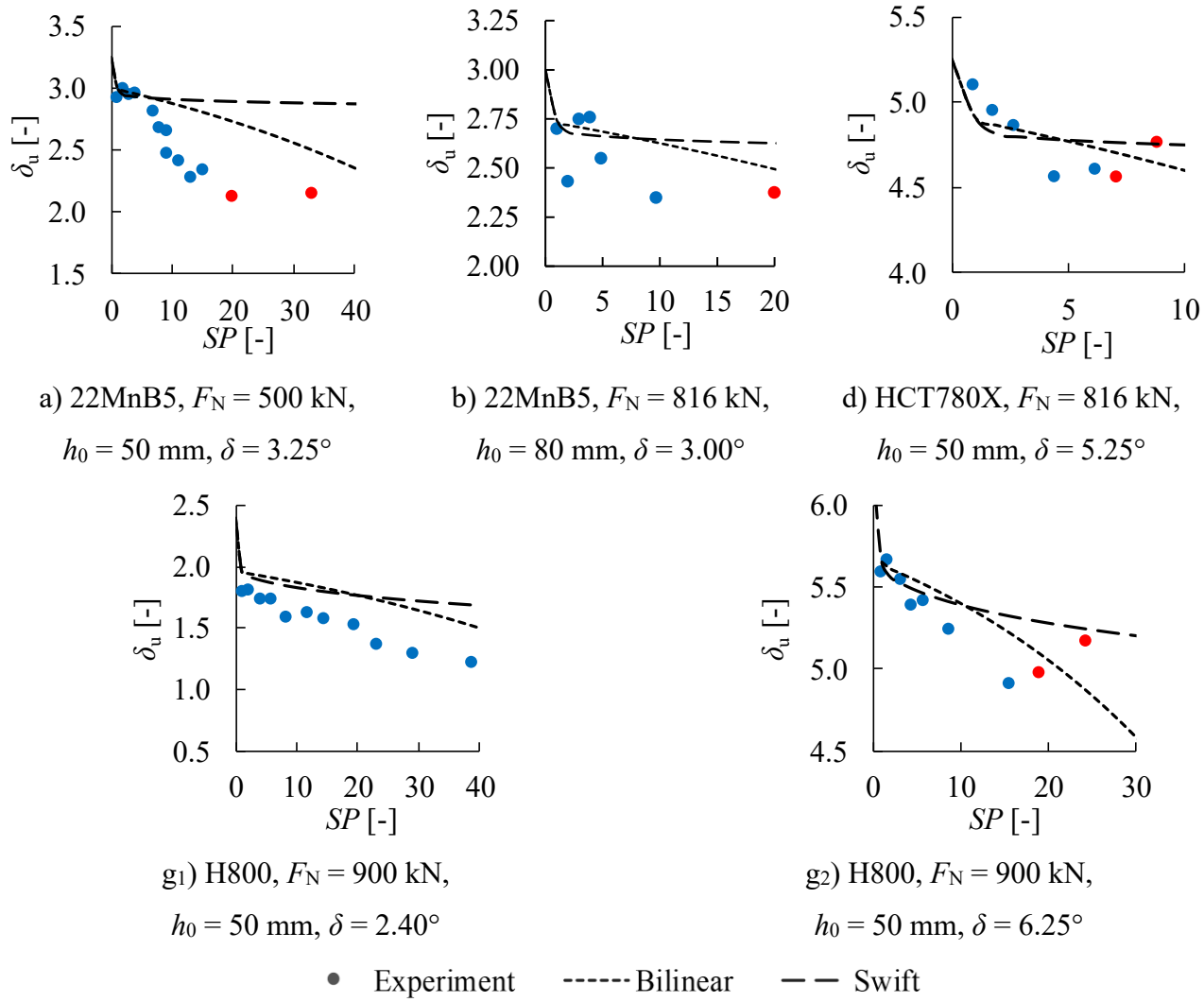

Figure 70: Comparison of the experiments and corresponding calculation models of the average incremental bending angle plotted over incremental density *SP*. By work hardening, yield stress is aligned according to the strain maxima which are achieved in incremental bending.

The unloaded bending angles $\delta_{u,s}$ obtained from the practical experiment are compared to the analytical predictions of $\delta_{u,i}$ over *SP*. The modelling approaches underlie the general concept of an alignment of yield stress according to work hardening which is caused by straining at the extrados. Two hardening laws are implemented and compared out of which the bilinear model delivers a better agreement to the experiments. A remaining tendency towards smaller unloaded bending angles is seen from the comparison of experiments to the model predictions which might be explained by imperfections in practical experiments compared to idealized assumptions in modelling, e.g., friction and stiffness.

In incremental bending processes, curvature inherently relates to the density of forming sequences, as observed in an empirical approach by SCHERER (2014). In the present thesis, density is adjusted by the incremental feed Δf which is related to superposed forming zones SP by profile height and the size of each forming zone. These zones successively sum up to the deformed area of the working piece. Together with the modelling approach for springback, curvature is interpolated trigonometrically from Δf and $\delta_{u,s}$. The specimens of this experimental series (Table 22) are measured by the FAROARM coordinate sampler to obtain the curvature κ_{NF} at the intrados (in this case at the strain-neutral fiber) of the incrementally formed arcs. Figure 71 plots the curvature of the experiments over incremental feed.

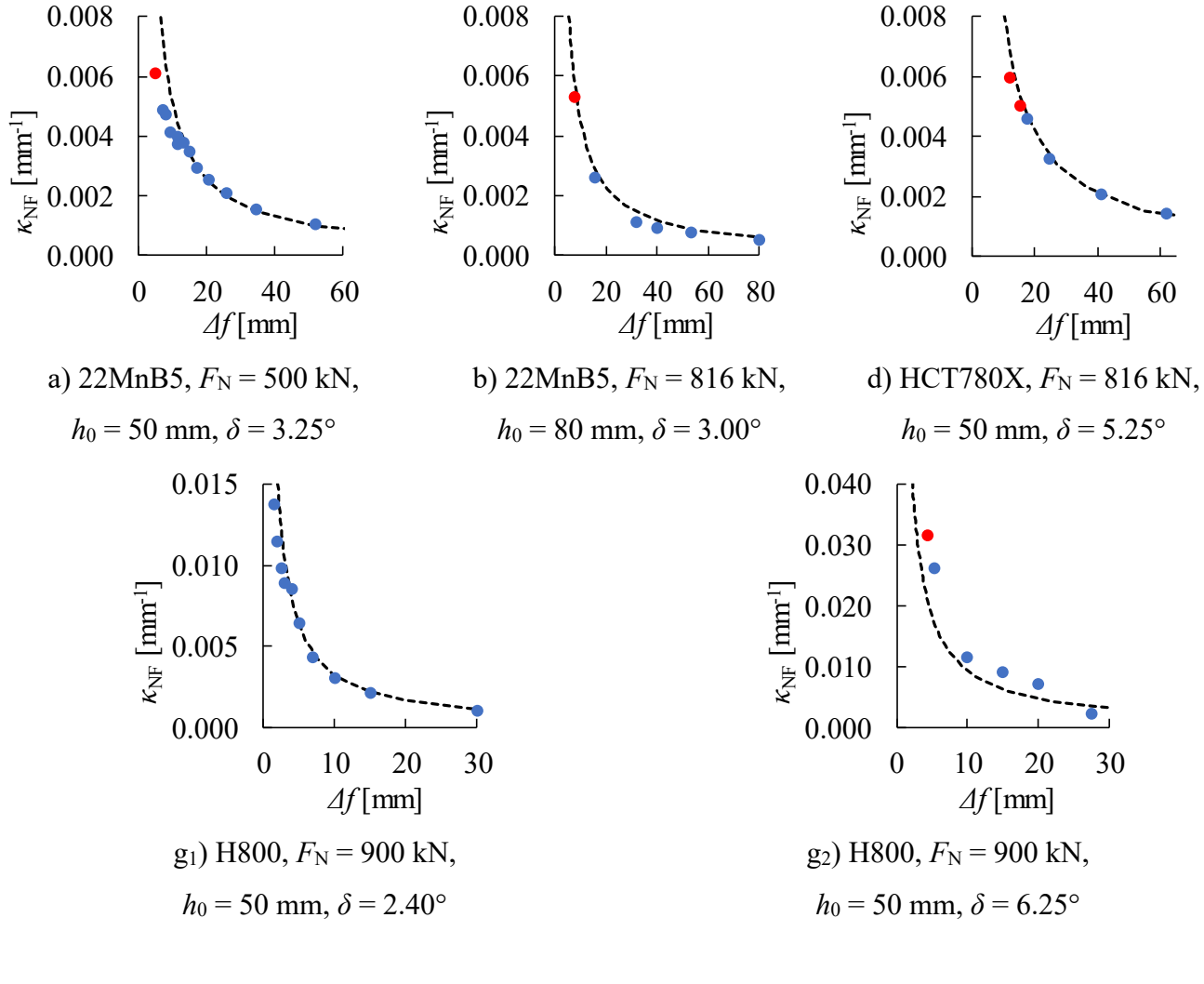

Figure 71: Curvature over incremental feed plots obtained from the bending experiments with successively increasing superposition of forming zones. Comparison to the predictions of the analytical model prediction for each case (dashed lines) reveals a sufficient prediction of curvature obtained from ISB. Red dots indicate failure due to rupture at the extrados.

The predictions of the analytical model exhibit a satisfying compliance to the experiments. Fundamentally, curvature increases sharply at small incremental feeding distances.

In conclusion of the parametrization for the experimental series of this chapter and the models compared in the preceding graphs of Figure 68, Figure 70 and Figure 71, the following modelling steps are utilized:

1) The ISB process parameters F_N, and o are determined from
   i. the mechanical properties of a given material,
   ii. the tribological conditions of the process setup and
   iii. the required cross section and bending geometry.
2) The size of a single forming zone γ as well as the corresponding strain distribution is described as a function of incremental bending angle δ. Moreover, springback is estimated.
3) In relation to the profile height h_0, the forming zone angle γ is used to calculate the superposition SP of forming zones depending on the incremental feed Δf and hence the accumulated strain maximum $\varphi_{x,s}$ at the extrados. Depending on SP and the resulting $\varphi_{x,i}$, work hardening R_i and the average angle of springback δ_{SB} are determined.
4) From the unloaded incremental bending angles $\delta_{u,s}$ and the incremental feed Δf, the circular approximation of the polygonised shape delivers the curvature of formed bending geometry.

To summarize these steps, the ISB process layout method is graphically shown in Figure 72.

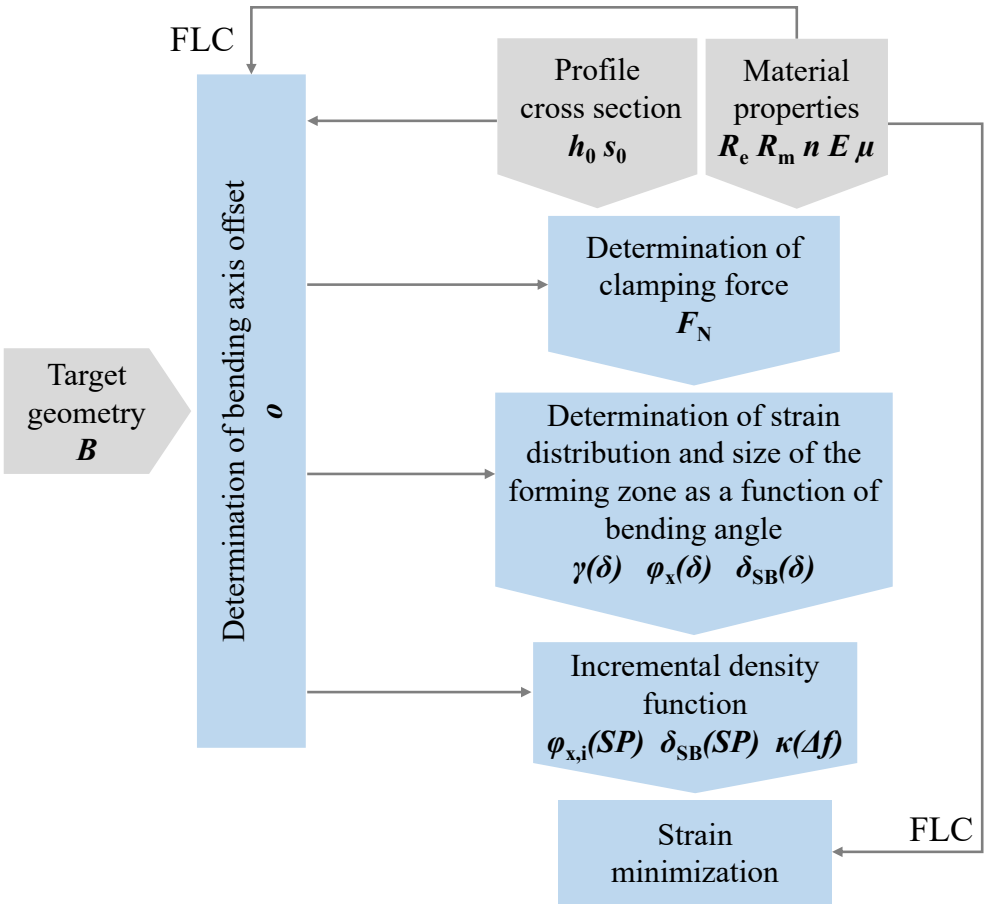

Figure 72: Graphical summary of the ISB layout method.

6.4.5 Validation of the ISB failure criterion against rupture

At this state of ISB process development, the method to estimate a feasible bending geometry with respect to the material's forming capabilities still needs verification and experimental determination of forming limits. In sheet metal forming, forming limit curves (FLCs) are a common tool to determine a given material's failure against necking. The FLC characterizes a material's biaxial formability under plane stress. Besides the presented theoretical approaches to determine FLCs, experimental approaches are pursued.

6.4.5.1 Nakazima experiments

The NAKAZIMA test assembly according to KEELER (1961), KEELER and BRAZIER (1977) and NAKAZIMA et al. (1968) is proposed in the technical standard DIN EN ISO 12004-2 for testing FLCs. At UTS, such an assembly is scaled down by a factor of 2, which includes scaling the specimen dimensions. Since the original test assembly is valid up to an initial blank thickness s_0 of 4 mm for reasons of superimposed bending strain over the hemispherical dome punch, the UTS assembly is assumed to be valid for $s_0 \leq 2$ mm.

In this thesis, forming of ultra- and advanced high-strength steels is focused. Since forming forces are considerably high for these materials, the UTS test assembly is specially reinforcement to be operated on a large press (Müller 2018). The blank holder and die are case-hardened so that their serrated clamping surfaces withstand high contact forces. A tool frame transfers the press force to the blank holders while supporting a system for in-process optical strain measurement (OSM). The stamp is manufactured from tool steel 1.2379, polished and plasma nitrided, which is expected to minimize friction and wear in the lubricated FLC test.

By varying the taper width of the specimens, a range of tested strain ratios is obtained in the experiment. As DIN EN ISO 12004-2 does not explicitly suggest specific widths, the following specimen widths were chosen based on the experience of previous FLC studies on the UTS test assembly (Kotzian 2017; Müller 2018; Pereira Da Costa 2013; Selter 2017): 100 mm square specimens and taper widths of 65 mm, 50 mm, 40 mm and 25 mm (Frohn-Sörensen et al. 2022). Where necessary, additional samples were added to increase FLD coverage. All samples were extracted by micro water jet cutting, carefully sanded at the edges and electrolytically gridded to facilitate OSM.

The NAKAZIMA test includes the following procedure: The specimen's upper surface is clamped by a blank holder which is loaded by the press main axis to fix the specimen flange for bulging. On the lower specimen surface, a complementary blank holder bears the reaction force of clamping. The blank holders are serrated to hinder the clamped material from being drawn into the forming zone. Driven by the lower press axis, the hemispherical stamp forms a half dome in the tapered area of the

specimen until material failure. Friction between punch and specimen was optimized by lubrication with grease and deep drawing foil for all material tests (Frohn-Sörensen et al. 2022). In this way, maximum allowable strains were obtained, judged by an offset of less than 15% from the apex of the dome of the die. According to the width of the specimens, each pair of large and small strains at failure provides a support point for the FLC. The VIALUX AUTOGRID system is attached to the NAKAZIMA test assembly to record strain throughout the test. The last frame prior to visible necking or cracking is selected for evaluation from the recorded test sequence.

DIN EN ISO 12004-2 proposes to evaluate the FLC tests based on location. Perpendicular to the extension of the strain maximum on the blank surface, five line sections are evaluated by strain over the grid length. Due to material localization, a very coarse maximum may be obtained. The maximum is therefore interpolated by a polynomial function. The zeroes of the second derivative of the principal strain next to the crack are the support points of this function. The polynomial's vertex provides the major strain value, while minor strain is obtained directly from the section. At least five valid test replicates were performed to statistically evaluate the major and minor strains for each FLC support point (Frohn-Sörensen et al. 2022).

Figure 73 shows the obtained FLCs in the φ_1 - φ_2 area (FLD). The mean FLC is calculated from the repetitions of each individual tests. The upper and lower interval of 95% confidence determine the FLC's statistical enveloping curves. The tabular values of the FLCs are summarized in the Appendix, Table 28, page 208.

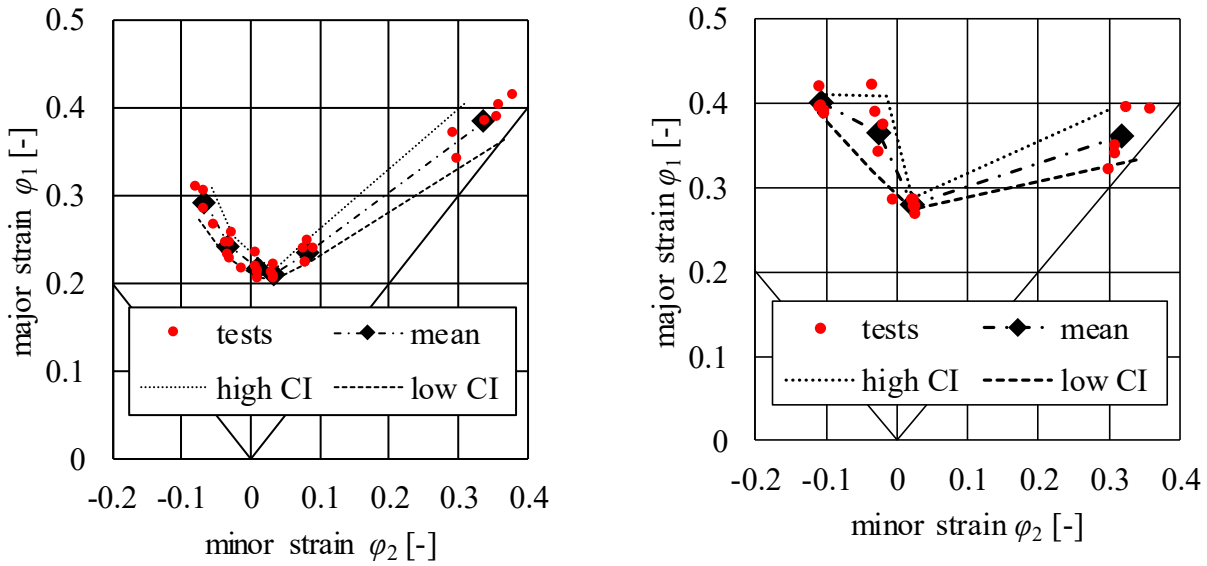

a) HCT780X, s_0 = 1.5 mm

b) 22MnB5, s_0 = 1.4 mm

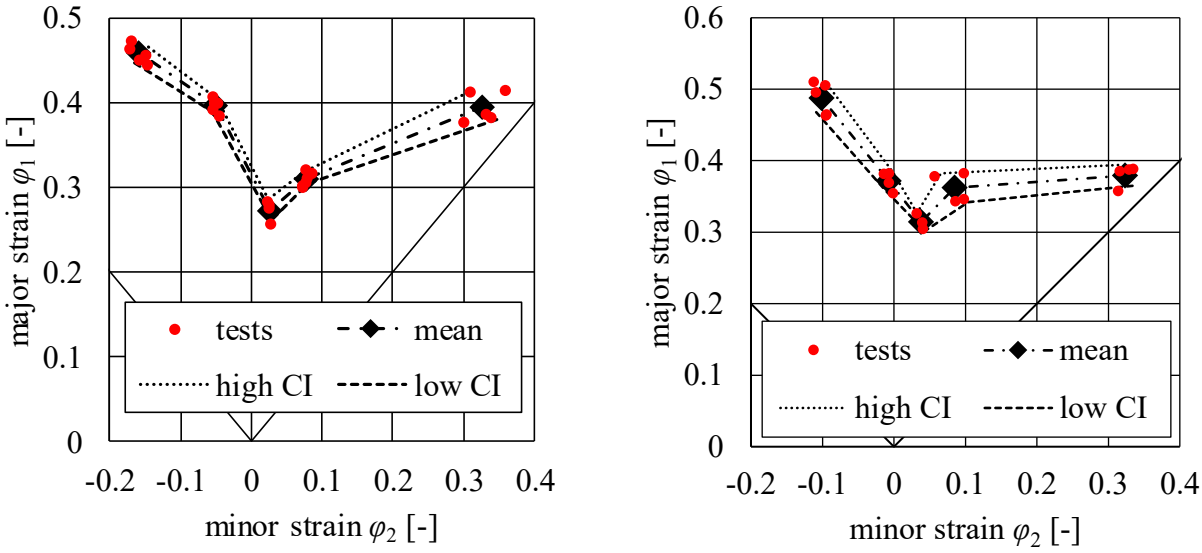

c) 42SiCr, s_0 = 2.0 mm

d) FORTA H800, s_0 = 2.0 mm

Figure 73: FLCs as resulting from the NAKAZIMA experiment for a) HCT780X, b) 22MnB5, c) 42SiCr, d) FORTA H800. All curves were tested on the UTS 1:2 scaled test assembly.

The obtained FLCs show a global average standard strain deviation of 0.015. Valid specimens failed well within the margins of max 15% offset to the spherical dome's apex. The FLC knees of all materials are marginally shifted toward positive values of minor strain.

In the cases of HCT780X, 22MnB5 and 42SiCr, strain measured from the biaxial tension specimens reveal significantly higher scatter of 0.025 compared to the other tapered widths (Frohn-Sörensen et al. 2022). Tapered specimens will give the experiment a favored direction of failure, perpendicular to the length of the taper, which will occur at similar locations. This hypothesis is consistent with the observations of MARCINIAK and KUCZYŃSKI (1967). They concluded that necking would occur perpendicular to a predominant principal strain. A square or circular specimen, on the other hand, has no directionality. This potentially increases the area of possible failure and therefore the range of results. In the case of plane strain testing conditions, 42SiCr and H800 tended to fail in the flange radius instead of the dome's apex. 42SiCr revealed this phenomenon at a tapering width of 50 mm while in the case of H800 it occurred at both widths, 40 mm and 50 mm. To avoid this failure type, the edges of three remaining specimens from each respective experiment where cut, so that simple strips instead of tapered specimens were tested. Even if this procedure might trigger valid failure behavior judging by cracking near the punch's apex, these test results reveal significantly different strain ratios which do not fit reasonably well into the trends of the FLC curves. Thus, those tests with cut specimen edges were excluded from the FLCs. The initial tests, which cracked in the flange, however, cause the significant dips near plain strain of both FLCs. Recapitulatory, a comprehensive investigation between strips and tapered FLC specimens is encouraged.

6.4.5.2 Notched tension tests

For the sheet materials HCT780X, 22MnB5, 42SiCr and FORTA H800, a second approach to investigating failure limit curves was carried out in addition to the NAKAZIMA experimental procedure (Frohn-Sörensen et al. 2022). According to GOODWIN (1968), similar to the variation of the specimen taper width that produces different strain ratios in the NAKAZIMA experiment, the variation of the notch radius in notched tensile test specimens allows the obtained ratio of major and minor strain to be varied. Tensile notching experiments test forming limits in the second quadrant of the FLD, i.e., negative minor strain (Brozzo, Deluca, and Rendina 1972). Similar to hydraulic bulging (Geiger et al. 2013), a key difference with the NAKAZIMA approach is that the influence of friction or lubrication on the experiment is excluded. In addition, the normal pressure exerted by the die in the NAKAZIMA experiment and the heat transfer from the forming zone in the sheet to the die are absent in the notched tensile tests. With the notched tensile tests, a closer resemblance to profile forming is sought, in particular to the ISB forming zone, which has been shown to lose tool contact as soon as plastic deformation starts.

Notched tensile specimens with a taper width of 10 mm and notch radii varying between 2.5, 5, 10, 20 and 40 mm were fabricated from the sheet metal materials (Frohn-Sörensen et al. 2022). To be ready for digital image correlation (DIC) with GOM ARAMIS, the specimens were painted with a stochastic pattern, see Figure 74 a). Based on the physical principle of triangulation, the camera-based system dynamically measures spatial coordinates, displacements and surface strain. For the experiments, the notched specimens were clamped in the ZWICK/ROELL Z250 uniaxial testing machine and subjected to tensile strain. The ARAMIS system (b) was used to record the deformation at the surface of each specimen. Three repetitions were performed for each specimen geometry.

a) b) c)

Figure 74: FLC testing from notched tensile specimens. a) specimen preparation by a stochastic pattern, b) main assembly GOM ARAMIS system, c) resulting major strain map superposed on a radius 20 mm notched specimen of 42SiCr (red to green ranging from $\varphi_1 = 0$ to 0.5), indication of longitudinal and lateral sections and local coordinate system.

For evaluation, longitudinal and lateral sections were arranged in the deformation zone of each specimen, cf. Figure 74 c). The mean, minimum, maximum and standard deviation of the recorded major and minor strain gradients within these sections were calculated and exported over the course of the experiment along with the synchronized force and displacement channels of the testing machine. These data are used to investigate the failure limit within the FLD (Frohn-Sörensen et al. 2022).

While there is no standardized procedure for evaluating the failure of notched specimens, NAKAZIMA FLC tests offer a variety of approaches for determining the unstable forming phase. The major and minor strain trends plotted over a section perpendicular to the developing crack are evaluated in the location-based approach defined in DIN EN ISO 12004-2. Without considering the progression, the evaluation is conducted at the very frame when the first sign of necking is evident by the unaided eye. In contrast, VOLK and HORA (2011) suggest a time-dependent approach. The major strain trend over time is evaluated for a particular coordinate placed in the region of maximum deformation. VOLK and HORA´s theory postulates that there are distinct constant slopes in the regions of stable deformation and in the regions of unstable deformation. Therefore, the transition is located by means of two linear fits at the beginning and the end of the first derivation of the strain, i.e., the major strain rate φ_1', plotted against time. Furthermore, in order to provide an independent and automatable assessment of the stable-unstable transition, KUPPERT (2015) suggests calculating the coefficient of determination from the second derivation of strain over time.

In addition, the maximum of force over time similar to the evaluation of uniaxial tensile tests is considered as alternative approach for evaluating the notched tensile experiments. The major and minor strain values corresponding to this force maximum F_{max} are determined for each specimen. Furthermore, in order to evaluate the FLCs of the sheet materials under consideration, the methods explained above are applied to the notched tensile tests. For HCT780X, Figure 75 (a) shows the resulting strain paths from the notched tensile tests. For all materials these paths lie between plain strain ($\varphi_2 = 0$) and uniaxial stress ($-2\ \varphi_2 = \varphi_1$) in the FLD. Larger radii will give lower values for the minor strains, while smaller radii would be closer to the plane strain. For higher principal strain values, steeper strain path slopes are observed. The longitudinal section is used to identify the location of maximum strain and subsequent material failure by cracking in the GOM ARAMIS software. The cross section data is used for further processing at this location. When these data are taken into account, it is observed that for smaller notch radii there is a significantly greater spread in the major and minor strain values (Frohn-Sörensen et al. 2022).

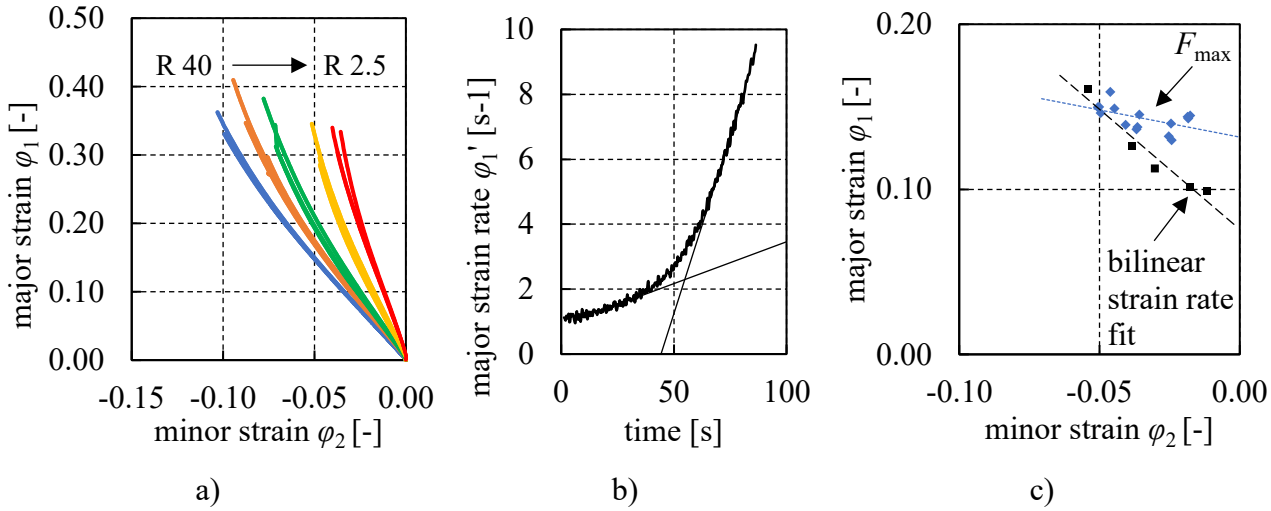

Figure 75: FLC evaluation from notched tensile specimens. a) FLD of the experiments on HCT780X. Colors correspond to individual notch radii which range from 40 to 2.5 mm, b) evaluation of transition from stable to instable forming by bilinear fits to strain rate over time for a R 10 mm specimen, c) linear interpolation of FLCs.

In order to extract FLCs from the experiments, the timestep of maximum force F_{max} is regarded for each specimen to obtain the major/minor strain data pairs form the section's average (Frohn-Sörensen et al. 2022). Moreover, the method of VOLK and HORA (2011) is applied. Two distinct areas of strain rate over time with a constant slope of the trend are identified after calculating the first derivation of strain over time. The location of the stable-unstable transition is obtained by fitting and extrapolating linear functions in these regions. (see Figure 75 b).

6.4.5.3 Comparison of ISB failure prediction

Several model-based and experimental methods to predict failure in biaxial sheet metal forming are applied to the ISB process. All of these failure predictions within major-minor strain plane assume linear strain paths resulting from the forming process. As long as the ISB process is aligned along the longitudinal coordinate of the profile, or on the other hand progressing in the same direction, linear strain paths prevail throughout the superposed forming increments.

In subchapter 6.2, the FLC modelling approaches of KEELER and STEINHEIMER are presented. In addition, the experimental procedures according to DIN EN ISO 12004-2 on the NAKAZIMA assembly as well as notched tension tests are conducted on the sheet metal materials included in this thesis. From these FLC approaches, those with the best prediction compliance to failure against rupture in the ISB process are requested. The accumulated strain maxima, resulting from OSM at the extradoses of the plane strip experiments with successively increasing incremental density are considered for comparison to the FLCs (subchapter 6.4.4). In addition, the strain maxima of the profiles from 42SiCr are compared to the FLCs (subchapter 6.4.3). All experiments and FLCs are plotted in individual graphs for each sheet metal respectively as shown in Figure 76.

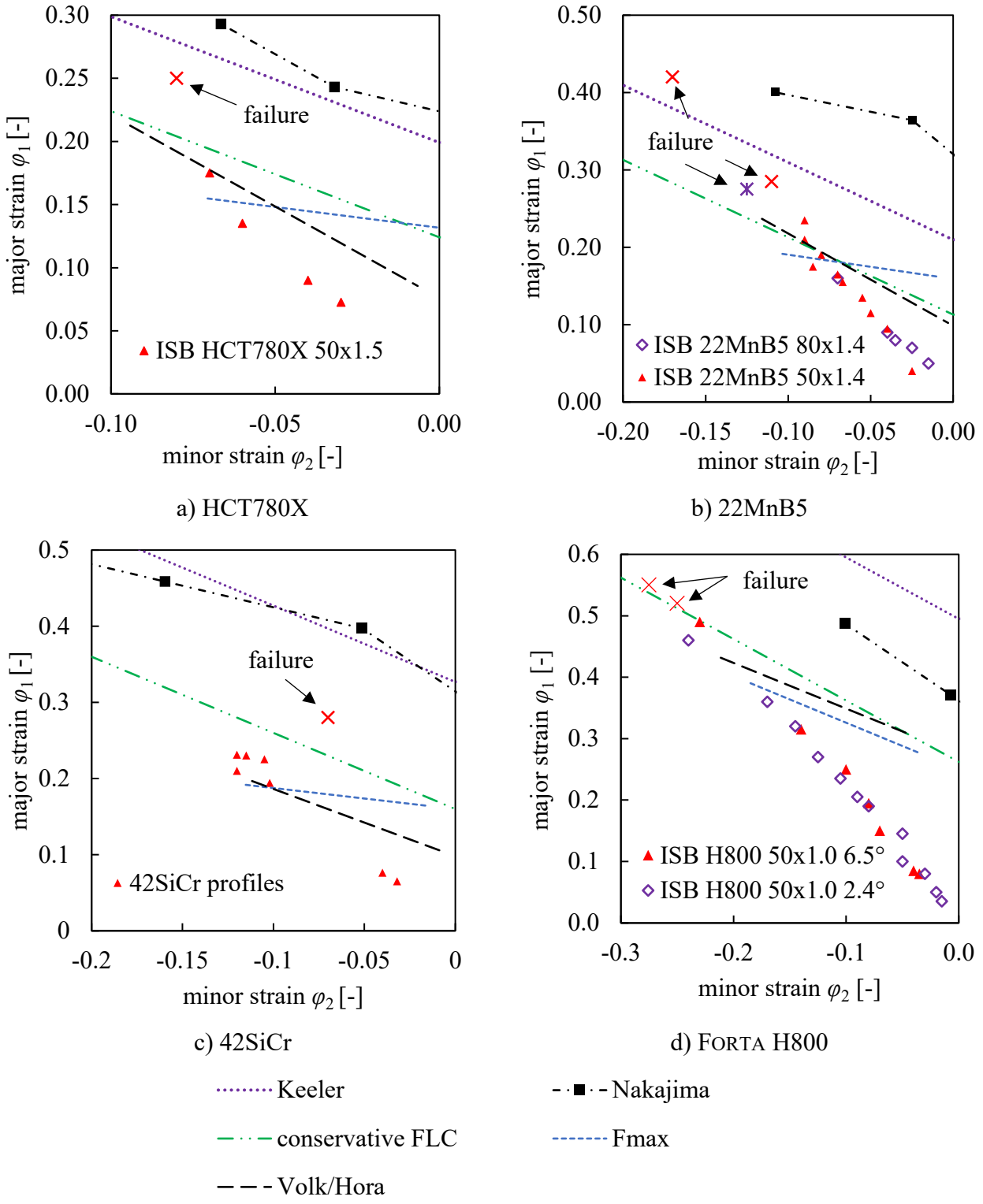

Figure 76: Accumulated strain maxima of bending specimen with increasing incremental density *SP*. Comparison of the experiments to two FLC models (KEELER, conservative) and experimentally measured FLCs (NAKAZIMA, notched tension tests) for failure prediction.

To predict failure, two experimentally determined FLCs are applied. The NAKAZIMA test is a well-established method in sheet metal forming. For all materials, a strong overestimation of the forming potential of an incrementally bent arc is seen by this FLC. In contrast, failure is closely approximated by the results of the notched tension tests (NTT). The FLC is evaluated from the NTT experiments

by two methods, one determines the instability from the force maximum while the method of VOLK and HORA (2011) utilizes a bilinear approximation of strain rate. With regards to the inclination of the linear interpolation of the data points and the accuracy of failure prediction, the VOLK/HORA method is preferred. However, a slight systematic underestimation of the forming potential of all materials still exists.

In addition, two modelling approaches are compared for failure prediction namely the approaches by KEELER and the conservative approach presented by STEINHEIMER. The semi-empirical modelling approach of KEELER was fitted to deep drawing experiments. It therefore closely resembles the NAKAZIMA experiment with regard to the utilized process setup. Thus, the model overestimates the forming potential of all materials significantly. The conservative approach delivers the best overall prediction to the observed failure.

6.5 Strain optimization

With regards to layout, the ISB process might be optimized under various considerations. A given profile bending geometry requires a certain curvature. For an incremental bending method, the most efficient discretization of an arc is required. Firstly, the bending geometry needs to be located within a feasible range of material formability. Secondly, a criterion to determine a valid segmentation in between few but large increments or a higher number of small steps is required. Both sides show distinct benefits and drawbacks. By production-driven considerations, the lowest possible number of bending increments would lead to the shortest cycle time. Moreover, fewer incremental steps mean less accumulations of elastic springback because larger bending angles lead to sufficient plasticizing. Therefore, it is desirable to keep the number of increments small. However, a low superposition of larger bending increments will also lead to pronounced strain maxima as well as a coarser appearance of the whole arc. Contrary, a high density of incremental steps will lead to a smooth strain distribution with less potential for critical strain localization. In addition, the curvature obtained from a dense process setup evidently delivers a flusher geometrical result due to the finer polygonization on the one hand, but also due to reduced local transversal straining on the other hand. However, such a process setup leads to longer processing times and potentially lower manufacturing accuracy due to a larger accumulation of springback errors.

In addition to these considerations, it is hypothesized that tighter bending radii are possible by increasing incremental density or conversely, the cumulated strain maximum decreases with higher incremental discretization. In the following text, this hypothesis is applied to the layout method of the ISB process. Initially, the bending axis offset factor and clamping force are set as process constraints and are calculated on the basis of the cross section and the material of interest. The bending angle and density (i.e., superposition) of increments will determine strain and curvature and can be

chosen in an ambivalent way. To demonstrate this relationship, case f and g are regarded as examples (i.e., H800, 500 and 900kN, 50x1 mm² according to Table 16). As seen in the sections above, strain is influenced by the incremental angle δ and the number of overlapped forming zones (SP or n_{ISB}, depending on saturation, cf. Figure 69). In Figure 77, strain is plotted over the parameters δ and SP.

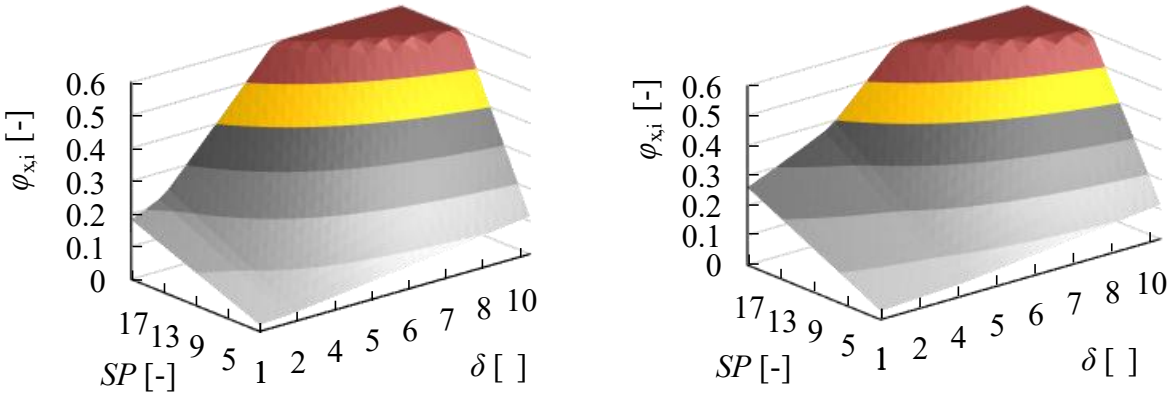

f) FORTA H800, 500 kN g) FORTA H800, 900 kN

Figure 77: Longitudinal strain maxima $\varphi_{x,i}$ plotted over the overlapping forming zones SP and the incremental bending angle δ. A marginal zone of critical forming begins at the lower strain limit, i.e., fracture strain, (yellow surface) and reaches up to the upper strain limit, as given by the conservative FLC. In the red area above, critical strain values occur, which potentially lead to cracking at the extrados. Margins are given for a FORTA H800 strip material (case f and g). An increase of clamping force (f → g) leads to significantly higher strain maxima at a high density of small incremental steps.

The strain maximum resulting from incremental bending is expressed as a function of incremental bending angle and superposition. In the examples shown in Figure 77, the same strain values are achieved when forming at 4° incremental angle and a superposition factor of 17 similarly when forming 10° increments with only 6 overlapping forming zones.

However, apart from strain the process parameters δ and SP moreover determine the curvature. Returning to the polyvalence of the layout of incremental density, the curvature would be required by a given target geometry. As a refinement of the incremental subdivision of an arc is expected to act as the decisive influence for mastering borderline cases, strain needs to be expressed as a function of curvature and incremental subdivision. A given curvature would in this case intrinsically determine the corresponding incremental bending angle. Since the curvature of a given target geometry is normally related to the inner arc, it must first be rearranged to curvature at neutral fiber κ_{NF} by laying out the offset factor according to the ISB strain diagram shown in section 6.1. By calculating the unloaded incremental bending angle for every position of the diagrams shown in Figure 77, curvature can be expressed accordingly, see Figure 78.

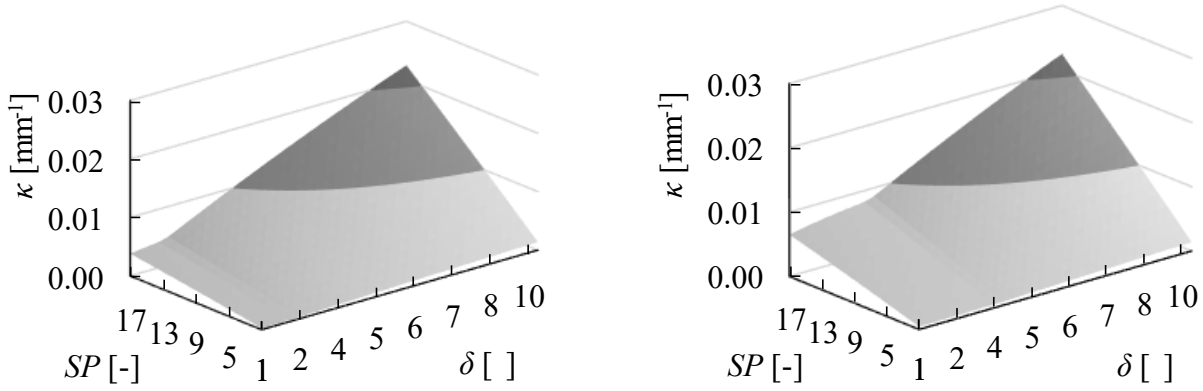

f) FORTA H800, 500 kN g) FORTA H800, 900 kN

Figure 78: Curvature as a function of incremental bending angle and superposition of increments for FORTA H800 at a clamping force of f) 500 kN and g) 900 kN. Compared to strain, considerably small curvature is obtained in the region of small bending angles and a large superposition due to high accumulations of elastic springback. A higher clamping force reveals a suitable compensation in this region.

From both diagrams, Figure 77 and Figure 78, strain caused by the incremental bending process is determined with regards to curvature and superposition factor. By setting fixed values for κ_{NF}, an optimal incremental subdivision is derived with respect to strain, see Figure 79. For given curvatures, the accumulated strain maximum resulting from the incremental procedure shows a distinct minimum over *SP* in case of f). In case of g), where a larger press force is applied, a changing inclination of the curve array is seen at same locations where the minima are observed at the lower press forces. These positions of the curves are regarded as balanced setting of the ISB process between a too coarse subdivision and a too large number of bending steps.

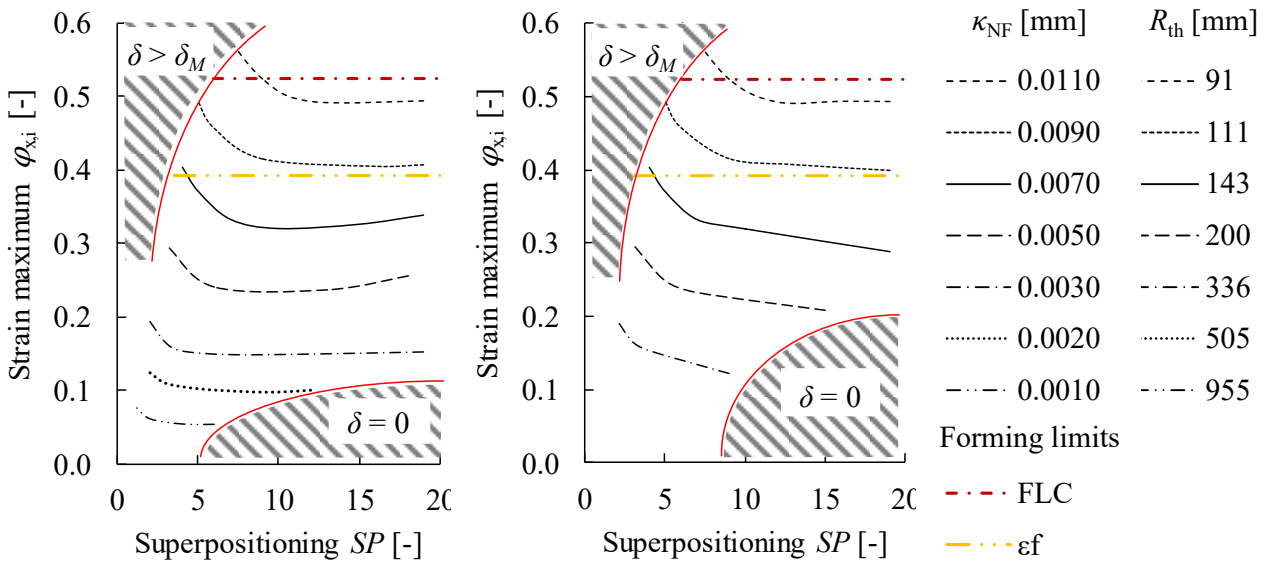

f) FORTA H800, 500 kN g) FORTA H800, 900 kN

Figure 79: Process windows for the incremental bending procedure. Curve families with constant curvature at the neutral fiber are plotted as strain over superposition functions and compared to the ISB forming limits. Two different clamping force values are regarded according to cases f and g (cf. Table 16). Areas of unfeasible values are indicated hatched where the incremental bending angle δ becomes zero or exceeds the bending angle of the tool, δ_M (in this case 10°).

For given curvatures, strain minima are identified over the incremental density function according to Figure 79. At these points, balanced ISB process setups are achieved with respect to the mildest forming while at the same time, preserving a short cycle time. Depending on the material's ductility and the permissible tolerances, a lower incremental subdivision might accelerate the manufacturing method but delivers a more coarse and more polygonised bending geometry. Moreover, pronounced strain maxima appear with an elevated risk of failure due to rupture (left hand side of the diagrams). Interestingly, with finer subdivisions beyond the balanced subdivision and under application of a relatively low clamping force near its minimum requirement $F_{N,min}$ (right hand side of Figure 79 f), strain might even increase again. This observation is explained by pronounced elastic springback which needs to be compensated by bending over-proportionally large incremental steps. This explanation is supported by the areas of high SP and small δ as seen in the diagrams of Figure 77 and Figure 78 (left hand side, each). Moreover, in these cases, poor plasticizing will leave a wide band of purely elastic bending near the neutral fiber. After release of press force, large residual stresses might even lead to elastic out of plane buckling. For compensation, increasing the clamping force helps to sufficiently conduct an ISB process if a very fine subdivision is desired.

Diverse materials are studied in this thesis which are observed to fail due to accumulated longitudinal straining of the incremental forming procedure. For a FORTA H800 strip, the plots of constant curvatures shown in Figure 79 are compared with two failure criteria. A curvature range of

$\kappa_{NF} = 0.009 – 0.010$ lies in between these margins and is therefore considered a borderline case. While a setup of few but large bending increments reaches the upper forming limit (i.e., the conservative FLC approach), the least critical setup is achieved with a subdivision of 9 – 12 superposed forming zones. When increasing *SP*, a higher density of smaller increments is obtained which cannot improve the forming result with respect to strain. The deepest point of these curves is thus suggested as solution for the optimization problem of the incremental process layout in between minimized strain and least number of bending increments. The optimum ISB setup is understood as balance between forming as few steps as possible for saving process time and avoiding excessive springback accumulations and as many steps as necessary to allow safe forming conditions as well as a smooth curvature as summarized graphically in Figure 80.

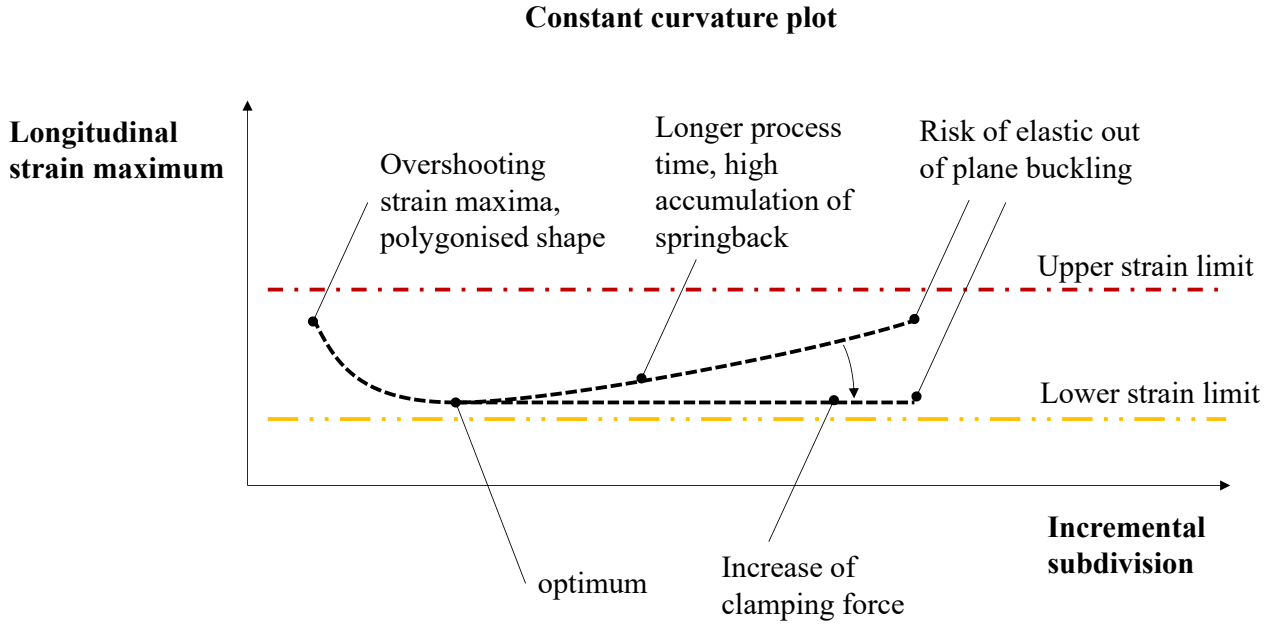

Figure 80: Graphical conclusion of the strain minimization for incremental bending.

6.6 Discussion and conclusions of chapter 6

Modelling and experimental verification of the bending increment density

The density of incremental steps is of key relevance for the ISB process layout to shape a bending geometry. Not only the material but the resulting geometry is also affected by strain in terms of curvature and springback. By the model-based prediction of the forming zone, the number of superposed increments is derived based on feed in between increments. Mathematically, GAUSS' sum function suitably describes the overlapping forming zones. The calculation takes into account the longitudinal transition of the strain gradient of each individual bending increment, as well as its position relative to the location of maximum strain, i.e., the highest number of overlapping zones. Springback is parameterized by the work hardened yield stress of the incrementally processed material. Combined with the feeding distance, a circular approximation of the polygonised shape is

applied to predict the resulting curvature which is validated by the experimental series conducted in section 6.4.4.

The model for the density of bending increments is based on the assumption of the forming zone angle γ being constant throughout the process sequence as derived for a single bending increment. In addition, longitudinal strain gradients are assumed for the superposition of individual bending increments. If these representations of the individual forming zones overlap, the gradients add up linearly. However, in practice, the actual formed increment would partially reach into the previously work hardened and partially untouched material. Therefore, a distorted strain distribution of the whole deformation zone results, as seen from the optical strain measurements of the experiments. The influence of this matter stays an open issue. In this regard it might be worth to investigate altering the order of formed increments. Instead of forming successively one after another increment, density could be raised in multiple cycles to compensate distortion.

From the incremental bending experiments, two distinct behaviors are observed. During larger steps, strain shows a linear trend over superposition until material failure. Correspondingly, curvature follows a steadily increasing trend over incremental feed. However, during forming small bending increments, cases a and g_1 show a kink in the curves of strain and curvature respectively, from where on the inclination of the trends follow a considerably flatter course which is hereby considered as stagnation of the ISB process, see Figure 81.

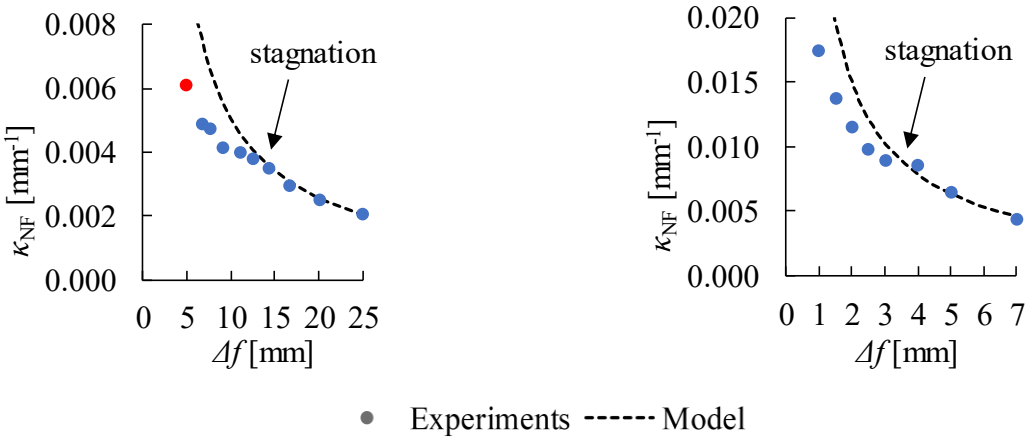

a) 22MnB5, F_N = 500 kN, h_0 = 50 mm, δ = 3.25°

g_1) H800, F_N = 900 kN, h_0 = 50 mm, δ = 2.40°

Figure 81: The effect of stagnation on the incremental bending procedure is observed when forming a large number of small incremental bending steps. In consequence, strain and the corresponding curvature κ_{NF} do not follow the expected trends over incremental feed Δf.

By inspection of the representative bending specimens, a stagnated state of the ISB process hardly reveals any drastic failure appearances at its highest superposition, such as the obvious macroscopic cracks of series d and g_2. In contrast, 22MnB5 delivers multiple areas of pronounced necking and

micro cracks at the extrados in case a, while FORTA H800 was formed up to the limitation of technical feasibility in case g_1.

Multiple explanations are suspected for the stagnation effect and require further investigation. First, the experimental series where stagnation occurred are formed in a range, where the forming zone angle has not reached its upper limitation γ_{ult}. The model for superposed forming zones assumes a constant forming zone angle which is derived based on the initial state of material. If a large superposition is adjusted, the material will be considerably hardened by strain, thus possessing a higher yield stress R_e. Below γ_{ult}, the forming zone angle is highly influenced by R_e which could potentially cause the observed stagnation in cases of small incremental angles. Moreover, a significant change in tribological conditions could be related to the observations. In the cases of stagnation, the material is processed by a large number of steps at the very same location, as given by the superposition. For example, at approximately the same value of accumulated longitudinal strain of $\varphi_{x,i} = 0.46$, the material is processed 15 times in the case of g_1 but 58 times in the case of g_2). Flattening of surface roughness, accompanied by work hardening could potentially lead to larger deviations from any model assumptions based on constant tribological conditions.

Based on a preferably wide range of materials with yet high-strength characteristics, experimental series are conducted to validate the process layout method of this thesis. For constraints, these experiments are restricted to forming under constant incremental parameters with regard to the bending angle δ as adjusted by the forming tool and feed Δf. Apart from forming profiles to validate the ISB assessment scheme of section 6.1, plane strips from sheet metal are bent with the bending axis shifted towards the intrados of an arc in order to obtain uniform and analytically predictable circumstances. In conclusion, reliable model predictions are achieved within the covered range of the experimental study.

ISB failure criterion

For failure prediction, forming limit curves (FLCs) are tested for each material except S235JR which is only intended for theoretical comparison. In the testing procedure according to NAKAZIMA, a variation of specimens is stretched over a spherical punch to test different strain ratios under plane stress conditions. As alternative experimental evaluation, notched tension tests are conducted and evaluated with regard to fitting FLCs. In addition to the experimentally determined curves, the modelling approaches of KEELER and STEINHEIMER are calculated from the mechanical material properties obtained in tensile testing. In the practical ISB experiments conducted in this thesis, material failure due to cracking is provoked. For all cases, the conservative FLC approach of STEINHEIMER and the experimentally determined FLCs from notched tension tests approximate the strain limits of ISB bending specimens closely.

The large overshooting failure prediction in ISB of the NAKAZIMA FLCs can be explained by multiple reasons. Firstly, in the experiment, the beginning instability is under influence of high contact pressure to the hemispherical punch. Even if carefully reducing friction, still friction shear stress will occur at the surfaces in contact. Moreover, due to contact, heat transfer from the plasticized specimen towards tool would occur. In addition to contact-related reasons, the method for evaluating the coordinates of FLCs according to DIN EN ISO 12004-2 leaves yet some uncertainties, especially if multiple necking zones occur (Jocham 2018). Lastly, out of plane bending superposes the evaluated strain ratios in the NAKAZIMA experiment. In contrast, the notched tension tests possess a higher similarity to the forming zone of the ISB process. For evaluation, the approach suggested by VOLK and HORA for linear fitting strain rate during FLC tests led to a satisfying reproducibility to identify the onset of necking from the experimental repetitions (Volk and Hora 2011). A remaining slight underestimation of the failure of ISB processed specimens might result from the incremental forming method.

7 Use case, demonstrator process and process applications

ISB was applied for the first time as an industrial use case by a R&D funded cooperate project named "ISB-ELEKTRO" (Engel, Frohn, Hillebrecht, and André Knappe 2017). The simulations and practical experiments related to this use case are regarded as the first industrial application of the findings of this thesis. The herein developed analytical modelling approaches are applied to layout the required bending geometries. The demonstrator is based on a structural component from a bent profile and represents a show-case validation for the analytics. In the following sections, each analytical model is applied consecutively.

Initially in ISB-ELEKTRO, the substructure of the prototype concept of the electric vehicle STREET SCOOTER COMPACT was re-designed into a profile-intense construction. This type of vehicular assembly offers the benefits of functional integration and provides more manufacturing flexibility with respected to vehicle derivatives because of the structure's suitability for manufacturing by bending (Chatti 1998; Groth 2020). From the re-designed substructure illustrated in Figure 82, the longitudinal members (blue components) were designated for an ISB process.

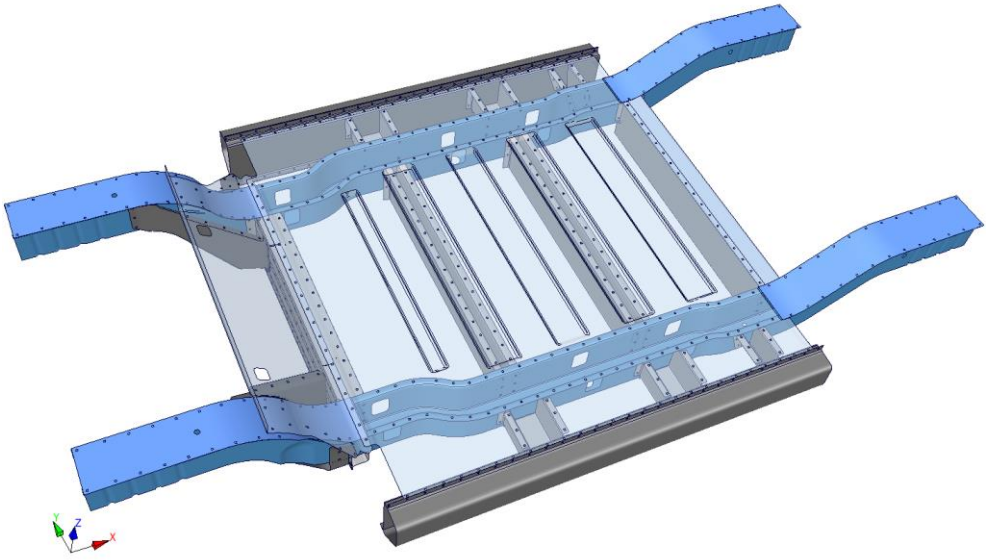

Figure 82: E-car substructure, re-designed for a profile-intense construction by EDAG ENGINEERING GROUP AG. Longitudinal members (blue) are planned from hat-shaped profiles by HILLEBRECHT et al. (2017). By functional integration of a profile intense car substructure, a large number of individual parts are unified.

The longitudinal members required bent arcs in s-shaped alternating sequences about the horizontal and vertical axes with respect to the profile cross section. Therefore, the developed industrial scale ISB tool required two different inserts, one of each to apply the incremental bending procedure in a corresponding bending plane. An economic calculation for a fully automated operation of ISB within the shop floor was documented by ENGELS (2016) based on an annual lot size of 20000 pieces of longitudinal members.

7.1 Application of the ISB layout method

The four steps of the ISB process layout developed in this thesis are applied to layout the incremental bending procedure for the specific bending geometry in which the profile floor lies withing the bending plane, see Figure 83.

Figure 83: Bending geometry of the use-case considered for systematical process layout.

In detail, these layout steps are with regards to the layout scheme presented in Figure 72 ex ante.

1. the determination of the bending axis offset o and the resulting strain distribution,
2. the layout of the clamping force F_N,
3. the parametrization of the forming zone as a function of bending angle $\gamma = f(\delta)$ and
4. the layout of the incremental superposition SP and thereby the incremental feed Δf.

The model predictions of the processing parameters are compared to the bending experiments on the demonstrator profiles.

7.1.1 Bending axis offset

If being unsupported, the profile wall of the hat shaped cross section would buckle within the forming sequence of the ISB process when exposed to compressive stress at the intrados. Therefore, the walls either need to be positioned at the neutral fiber or within the tensile strain distribution of the bending process with respect to the offset of the neutral axis. In these investigations, the axis is positioned over the inner profile wall which corresponds to an offset factor o = 0.5. For the definition of the offset factor, only the floor of the profile is considered because it is the area of the demonstrator which is formed by means of the herein developed process of frictionally engaged in-plane bending. Under consideration of two different materials having 2 mm thickness, i.e., HCT780X and FORTA H800, the ISB strain diagram defines the range of feasible bending geometries, see Figure 84. As a failure criterion, fracture strain is included in the diagrams to give an estimation of the margin where critical ISB arcs begins. In addition, the conservative FLC approach is applied as upper margin where cracking at the extrados is expected.

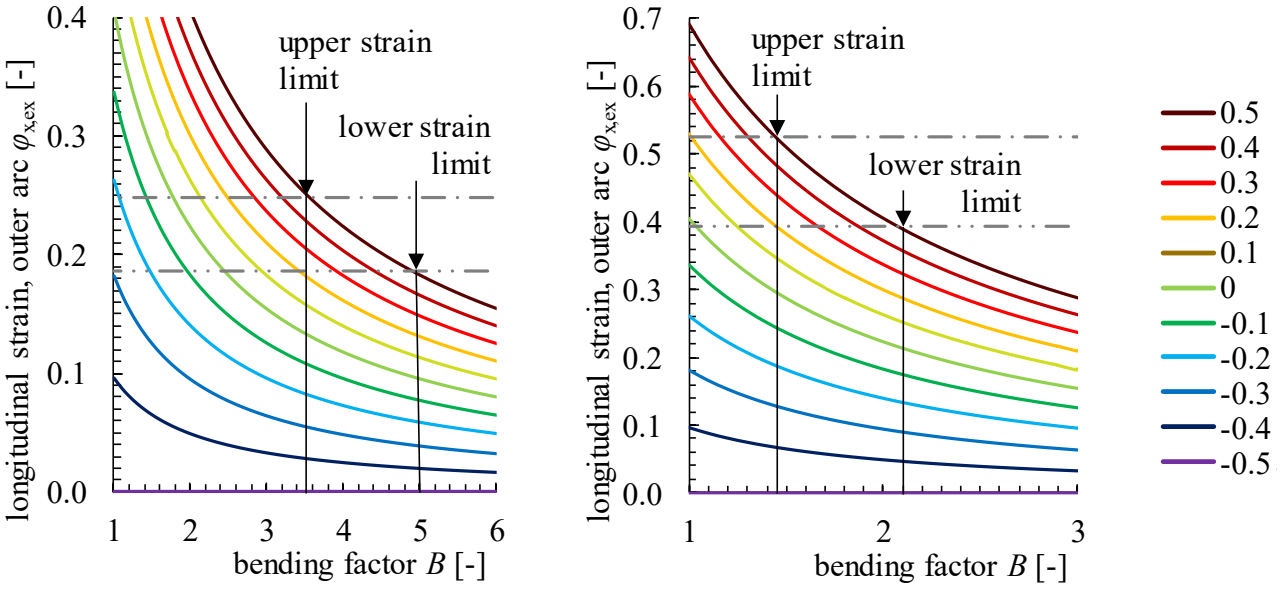

a) HCT780X b) FORTA H800

Figure 84: ISB Strain Diagram, applied to the demonstrator geometry with respect to the materials a) HCT780X and b) FORTA H800.

Feasible bending factors cover a range of $B = 3.5 – 5.0$ and $B = 1.45 – 2.1$ for the materials HCT780X and FORTA H800, respectively. These bending geometries represent the critical area up to maximum feasible curvature of an arc. Analogous, $R_{th} = 315$ mm and $R_{th} = 131$ mm are the minimum feasible bending radii of these profiles. It is pertinent to mention at this stage that the diagrams shown above are based on continuous bending, thus not taking into account the incremental process method.

7.1.2 Clamping force

Firstly, the clamping force is estimated for both materials in the firmly clamped floor area of the profile cross section. If only the floor of the profile is considered, a nominal clamping load of $F_N = 803$ kN and 1679 kN results for the eccentric bending axis position at the intrados based on 2 mm thick sheets of HCT780X and FORTA H800 respectively. The initial static friction coefficients $\mu_{0,ini}$ of both materials (0.293 and 0.190) were deployed to derive these forces. However, as friction of these sheet metals is identified to significantly depend on the applied contact pressure, the coefficients need to be related to the surface of the active die faces of the forming tool. The clamping length of the ISB large scale tool sums up to 90 mm · (300 mm + 600 mm) = 81000 mm² with respect to the rotatory and the stationary clamping unit length respectively. When considering only the bending of the profile floor, the resulting friction coefficients rise moderately due to the large tool surface related to the cross section. The resulting clamping loads are obtained as $F_N = 766$ kN for HCT780X at 9 MPa and 1594 kN for FORTA H800 at 20 MPa.

Secondly, the walls and flanges are included in the calculation of the internal bending moment M_z of the profile by propagating the stress distribution of the bending process on the hat shaped cross

section. Again, the friction coefficients are implemented as a function of pressure to obtain F_N corresponding to the resulting surface pressure given by the contact surface between tool and profile. For the hat shaped cross section of the demonstrator, the necessary clamping forces are calculated as $F_N = 2955$ kN for HCT780X at 36 MPa and $F_N = 6199$ kN for FORTA H800 at 78 MPa.

7.1.3 Forming zone

The forming zone from bending under frictional engagement is calculated for both profile materials. Since no clamping is applied at the walls, only the clamped area at the profile floor needs to be considered for the calculation of the forming zone according to the herein developed analytical models for frictionally engaged bending. Instead, the walls are freely stretched over the bending mandrel as observed from experiments. Figure 85 shows the development of the forming zone angle γ in the profile floor and the corresponding strain maximum at the extrados $\varphi_{x,ex}$ for both materials over the bending angle δ which is applied by the forming tool.

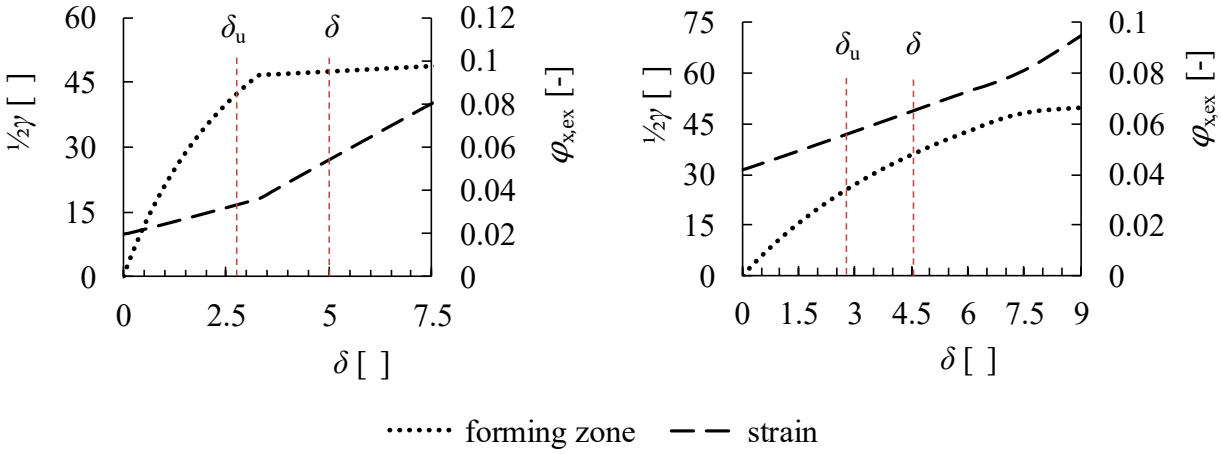

a) HCT780X

at $\delta = 5.0°$: $\gamma = 47°$; $\varphi_{x,ex} = 0.054$

at $\delta_u = 2.7°$: $\gamma = 41°$; $\varphi_{x,ex} = 0.033$

b) FORTA H800

at $\delta = 4.5°$: $\gamma = 36°$; $\varphi_{x,ex} = 0.065$

at $\delta_u = 2.7°$: $\gamma = 25°$; $\varphi_{x,ex} = 0.055$

Figure 85: Forming zone and longitudinal strain maximum for the materials considered for forming the bending geometries of the automotive use case. a) HCT780X and b) FORTA H800, both with 2 mm of sheet metal thickness.

Both materials used for manufacturing the demonstrator component evidently offer quite different forming conditions with respect to the forming zone which develops in an ISB process.

7.1.4 Superposition

The superposition of multiple bending increments is determined based on the calculated forming zone angles and corresponding strain maxima. Superposition as a function of incremental feed combined with the springback angle of each incremental step is incorporated in the model for circular

approximation to ultimately obtain the achieved curvature of the bending geometry as a function of incremental feed, see Figure 86.

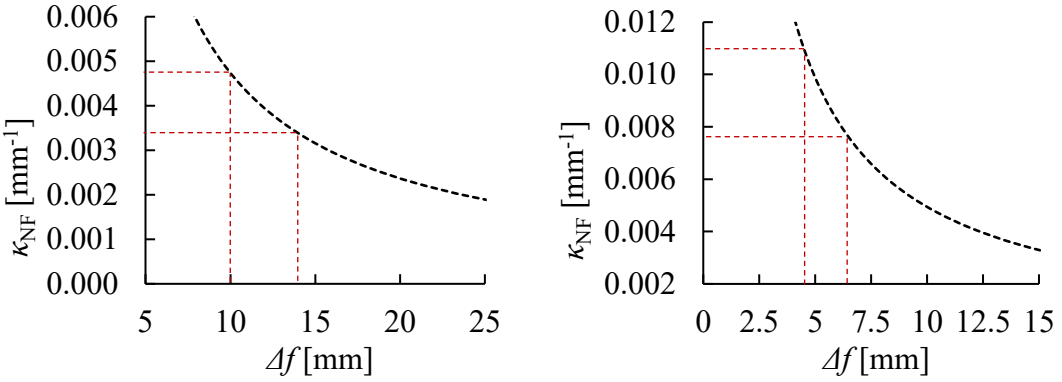

a) HCT780X

Δf_{crit} = 10…14; κ_{max} = 0.0034…0.0047

b) FORTA H800

Δf_{crit} = 4.6…6.3; κ_{max} = 0.0078…0.0106

Figure 86: Curvature, as predicted by the circular approximation from interchanging feed and bending increments. Upper and lower limits of critical curvatures are indicated in the graphs and noted in the subtext.

In addition, the critical feeding distances are calculated for the upper and lower strain limits for both materials. Correspondingly, critical bending radii at the neutral fiber range from

i. R_{th} = {294 … 213} mm for HCT780X
ii. R_{th} = {128 … 94} mm for FORTA H800.

The lower margin for strain maximum as given by fracture strain is considered safe range of ISB operation while the upper margin, given by the conservative FLC, is interpreted as critical. Note, that these margins for the bending radius are lower, than predicted by the strain diagram, where continuous forming is assumed: R_{th} = 315 mm and R_{th} = 131 mm for HCT780X and FORTA H800 respectively.

7.2 Tool development

A longitudinal beam of an electric car is regarded as a use case for the ISB process development. This demonstrator is based on a continuous profile with hat-shaped cross section as semi-finished product which needs to be bent about two perpendicular bending axes, see Figure 87.

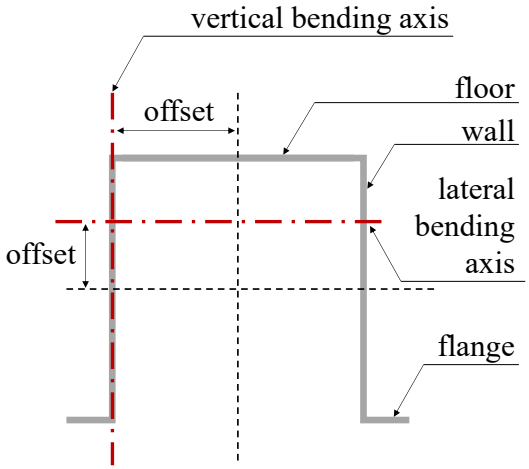

Figure 87: Hat shaped profile cross section with two perpendicular bending axes with the corresponding bending axis offsets indicated by dash-dotted lines.

By means of finite element simulations, a corresponding industrial scale tool is developed which is able to process the demanded cross sections.

7.2.1 FE-Simulations

The incremental bending sequence of an ISB process is simulated in the finite element method (FEM) to develop an industrial sized forming tool. In addition to the presented simulation models for frictionally engaged stretching and bending, this FEM model is used for profile bending instead of plane sheet metal strips. Before considering the profiles of the automotive use case application, an initial validation loop based on ISB profile bending was conducted according to ENGEL, GROTH, and FROHN (2015). Flat U-shaped profiles were bent on the ISB research tool. Based on the ductile sheet metal material DC04 (material number 1.0338), different geometries were bent under variation of axis offset, feed and number of increments. Strain maps were captured by optical strain measurement (OSM) from the surface of these geometries. A corresponding FE-model capable for profile bending was set up according to the ISB research tool. Using the same process parameters as for the bent U-Profiles, the FE-model was validated based on the resulting strain distribution and geometrical features of the profiles (bending radius and angle). This validated simulation model thus assures to dimension an improved and extrapolated version of the ISB tool prototype.

At the beginning of this thesis no sufficient bending of hat shaped profiles was feasible in preliminary try out experiments on the initial stage of the research tool because of cross sectional deformations of the profile walls and flanges. Therefore, the tooling was modified in simulation to facilitate bending

of hat shaped cross sections, see Figure 88. Additional blank holders were introduced which are able to clamp the profile flanges and at the same time, support the walls. This setup was parameterized by F_N, o, δ and n_{ISB} for incremental bending about the vertical axis, as required for the demonstrator. Thereby, the developed active die faces from simulation would be applicable in a realistic forming tool to manufacture the demanded bending geometries for the demonstrator.

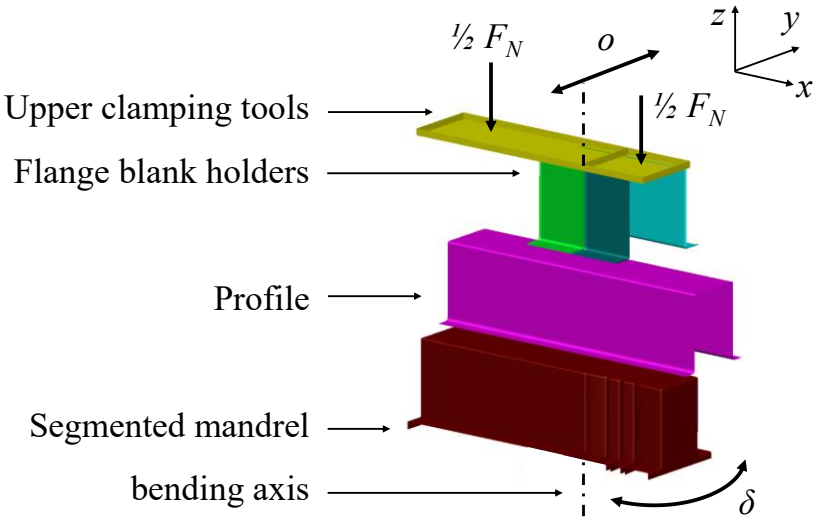

Figure 88: FEM model for ISB profile bending about the cross section's vertical axis. Indication of process parameters, i.e., clamping force F_N, lateral (y) bending axis offset o and incremental bending angle δ.

In addition to this setup, the demonstrator geometry required bends in a perpendicular bending plane (cf. Figure 87). The semi-finished product was assumed to be turned by 90° about its longitudinal axis to facilitate this forming operation by ISB. A second tooling set was planned as inserts for the outer frame of the ISB tool. Again, the effective faces for applying the press load on the walls of an open profile were developed in FEM simulations. A mandrel was positioned in the profile's cavity to transmit the clamping force from top to bottom. Cut-outs in the die faces guide the profile flanges. In longitudinal direction (x - coordinate), two clamping tools implemented according to the process principle of an ISB process. One of these clamping units pivots relative to the other, stationary unit, see Figure 89. In addition, a lateral embossing punch was introduced to the tooling which got activated when the floor of the profile was oriented towards the intrados of the bend. In this forming case, wrinkles would tend to appear at the floor, which are relocated by the punch towards two longitudinal ribs. From a structural point of view, these ribs make the demonstrator stiffer in its use case. Similar to the vertical bending axis, the kinematic parameters (F_N, o, δ, n_{ISB}) for incremental bending about the lateral bending axis were implemented in this FE model.

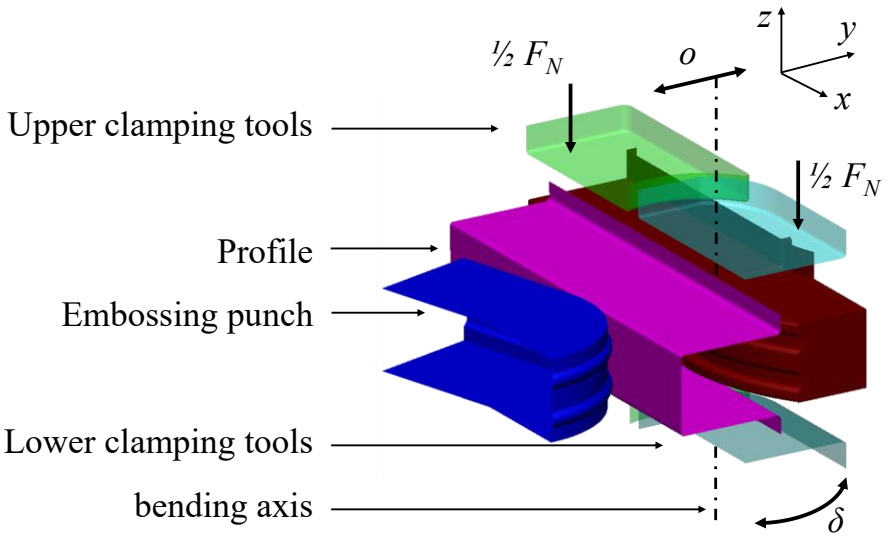

Figure 89: FE model for ISB profile bending about a bending axis orthogonal to the symmetry of the cross section. Indication of process parameters, i.e., clamping force F_N, lateral (y) bending axis offset o and incremental bending angle δ.

From the simulation models, three distinct bending geometries result:

a) Bending about the cross section's vertical axis, without distinction of positive or negative rotation direction according to the model shown in Figure 88.

b_1) Bending about in perpendicular bending plane with the profile floor located at the extrados (positive bending direction according to Figure 89) or

b_2) with the floor at the intrados (negative bending direction with activated embossing punch).

For these simulation cases, the results presented in Figure 90 were achieved.

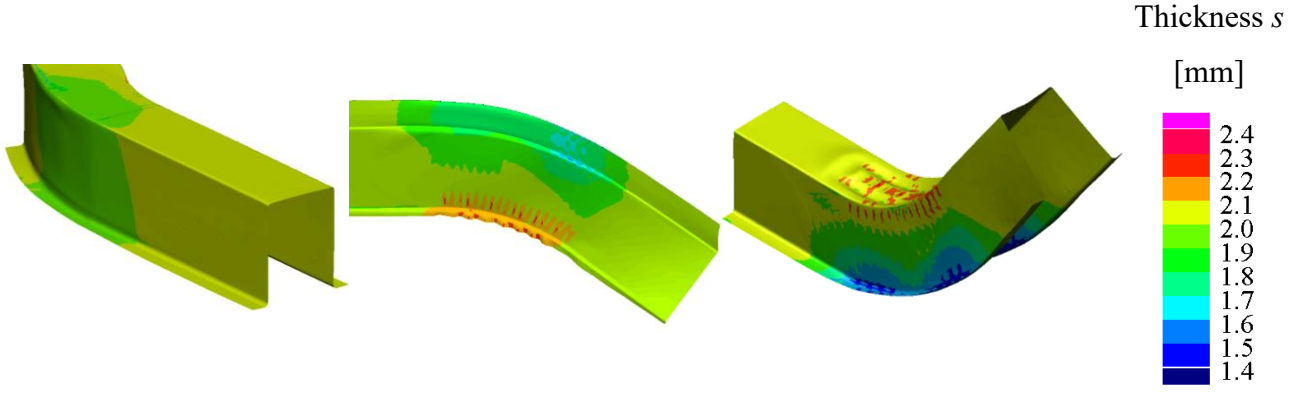

a) b_1) b_2)

Figure 90: FE-Simulations of the bending geometries of the ISB demonstrator.

In case of (b_1), the profile floor is susceptible to cracking which limits the tightness of the bending radius. In turn, the flanges in the inner radius are compressed and have a strong tendency to wrinkle. In the other bending direction (b_2), the material at the profile floor is compressed at the intrados. For bending of tight radii, forming results in a strong compressive stress component so that the inner bend tends to wrinkle sharply. A longitudinal bead die was implemented to deflect the resulting transverse

wrinkles into longitudinal ribs. The disadvantageous wrinkles are thus transformed into an advantageous double bead to stiffen the structure of the longitudinal member and at the same time, tighter arcs become feasible. From the simulations (a), (b_1) and (b_2), the effective die faces were subsequently transferred to the CAD development of the industry scale ISB forming tool.

7.2.2 ISB tool design

The surfaces derived from the aforementioned simulation models were applied to the mandrel, flange holders and clamping units of the ISB process, referred to as industrial-scale ISB tool, see Figure 91 and Figure 92. Because of the high ISB process forces necessary for processing the large profile cross section and the high material strength, the tool was planned for operation on a 10 MN servo electric press. With regards to stiff interlocking of lower and upper tool as well as centric swiveling shafts of the pivoted unit, which rotates over self-lubricated brass sliding plates, many of the improvements of the evolution of the research tool are found in the industrial-scale ISB tool.

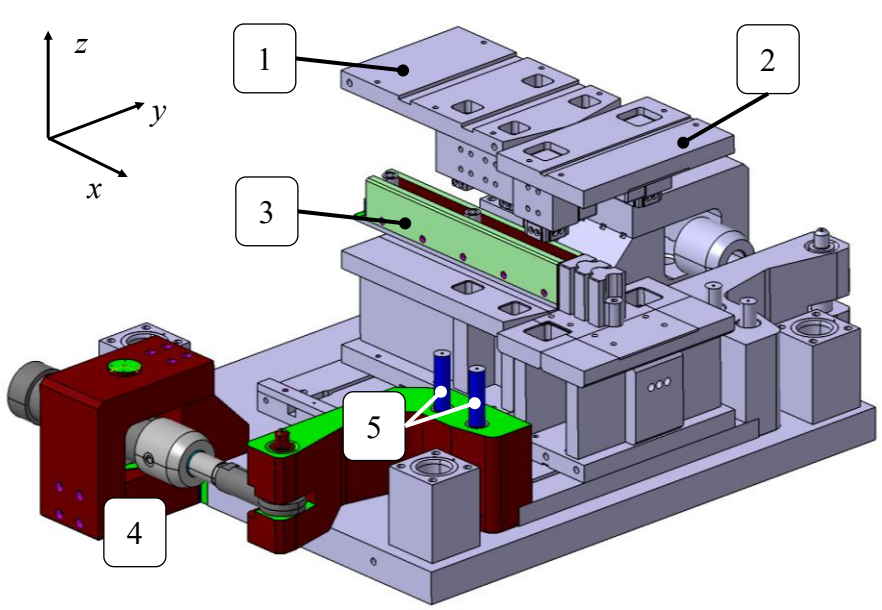

1) Upper stationary tool, with flange holders
2) Upper pivoted tool, flange holder
3) Lower stationary tool, mandrel with internal hydraulic feed axis
4) Hydraulic bending drive
5) Interlocking pillars between upper and lower pivoted tools

Figure 91: Industrial-scale ISB tool, designed for a 10MN servo-electric press (with partially hidden upper tooling). Tool inserts for bending about a vertical axis of a hat-shaped cross section of a profile. Die faces according to FEM: upper tools (1,2) with flange holders and lower tools with mandrel (3).At the attachment consoles of the bending drives (4), interlocking (5) of lower and upper tool assures tool stiffness during bending.

In order to realize both bending planes, two interchangeable active parts according to the die faces from the FEM are designed within a common tool frame. In addition to the hydraulic bending drives, the industrial-scale ISB tool features a hydraulic feeding drive which is mounted within the mandrel shaft. Two spring loaded pistons interlock into precut holes in the profile. These pistons are mounted on a slide attached to a hydraulic piston to longitudinally convey the profile.

For the lateral bending axis (referring to the cross section), the profile is turned 90° and enclosed by a separate tooling. Hereby, the kinematics applied by the ISB tool can be preserved. In detail, the bending direction is applied by the hydraulic drives, the clamping operation is applied by the press, the bending axis is offsettable in lateral (*y*-) direction and feeding progresses longitudinally along the *x*-coordinate. If this bending plane is applied, the profile's cavity is open to the side which means that the tool must feature a vertically lifting mandrel to allow the sequential process steps of ISB, which is implemented by loaded springs. During loading and bending, both walls of the profile must be clamped firmly by the tool units while during tooling reset, and feeding, the clearance of the profile must be guaranteed.

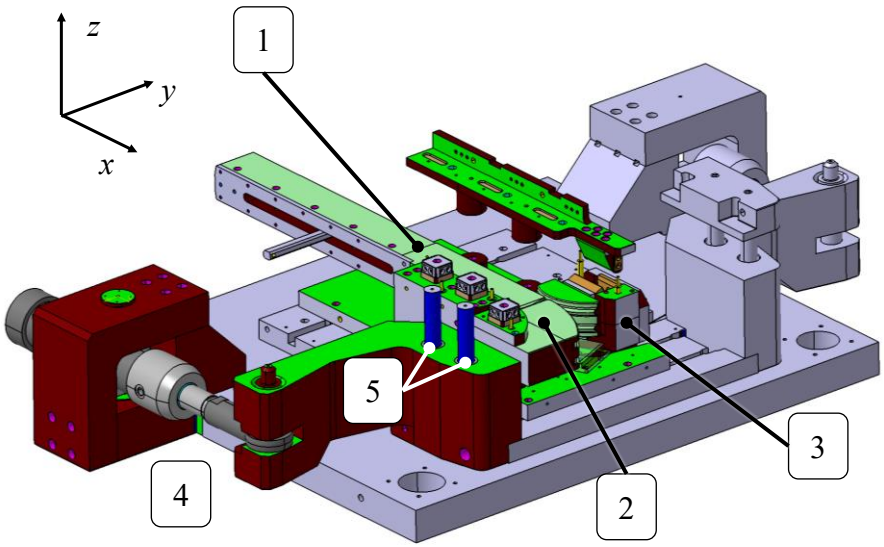

1) Spring loaded stationary tool, with internal hydraulic feed axis
2) Spring loaded pivoted tool
3) Lateral punch, driven by a wedge slide
4) Hydraulic bending drive
5) Interlocking pillars between upper and lower pivoted tools

Figure 92: Industrial-scale ISB tool (hidden upper tooling), equipped with the insert for the perpendicular bending plane. Lifted by spring loads, a mandrel (1) holds the profile in the stationary and pivoted (2) part of the tool. An optional punch is driven by a wedge slide (3) to form stiffening ribs at the base of the profile during each incremental press stroke. The outer frame stays identical to the tooling of the vertical bending axis.

The upper and lower stationary and pivoted tools are flat die faces which enclose the walls of the profile for firm application of the clamping load. Narrow slits in these tools guide and support the flanges of the profile during forming. A unique feature of this tooling variant is the optional lateral punch which is driven by a wedge slide. It has been shown in FEM, that wrinkles would appear if tight arcs were bent incrementally with the cross sections floor being at the intrados. The punch incrementally embosses this area to form two longitudinal ribs instead of letting wrinkles appear, thus stiffening the bent product with regards to the structural application of the profile. With these inserts, the industrial scale ISB tool was put into operation, see Figure 93. The bending geometries demanded by the demonstrator are manufactured as practical validation.

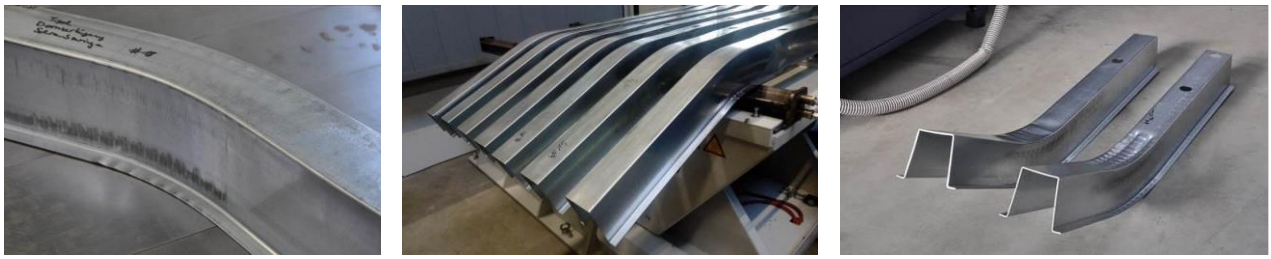

a) b_1) b_2)

Figure 93: Bending geometries achieved by the industrial scale ISB tool. a) Bending about the vertical axis, b_1) bending about the lateral axis with profile floor at the extrados, b_2) with the floor at the intrados. In b_2), variants without (left) and with longitudinal ribs are shown.

7.3 Experiments

7.3.1 Forming machinery

For operation of the industrial-scale ISB tool a servo-mechanical press was utilized. The SCHULER MSE 2-1000-3.5-600 is located at the AUTOMOTIVE CENTER SÜDWESTFALEN GmbH (Figure 94 a). The servo-mechanical eccentric press provides a nominal force of 10 MN. For the ISB process, the nominal lifting of 600 mm of the press was set to 100 mm in pendulum operational mode.

a) b)

Figure 94: a) Servo-mechanical press at the AUTOMOTIVE CENTER SÜDWESTFALEN. b) Clearance of the SCHULER MSE, equipped with the industrial-scale ISB tool.

During manufacturing the ISB process demonstrators (Figure 94 b), the press speed was set to 8 strokes/min which, in case of 100 mm pendulum mode, represents an average closing speed of 28 mm/sec. Apart from regular and pendulum operation modes, the press is able to rest under load in the lower dead spot for a defined time or waiting for a trigger signal. The latter case was utilized to ensure that the ISB process finishes before release of clamping. Further specifications of the press are summarized in Appendix, Table 26. The hydraulic unit WOODTLI used for the laboratory scale ISB experiments in section 5.6.2 was coupled to the SCHULER MSE using the same program in the

LABJACK tool control as for the laboratory experiments. For the experiments associated with the use-case, the feed channel of the hydraulic unit and the tool control was activated. Communication to the press is established by the DA converter, so semi-automatic sequences were achieved during incremental bending.

7.3.2 Bending experiments

Based on the use-case geometry, two distinct experimental series were conducted in the context of an ISB process layout methodology of this thesis. Firstly, the clamping force F_N lasting on the process was successively raised beginning from well below the lower margin of the process window for both materials, see Figure 95. For HCT780X, F_N was varied in between 2000 and 3150 kN while press loads ranging from 2700 up to 6200 kN were applied during bending FORTA H800. The analytical model suggests F_N = 2955 kN for HCT780X and F_N = 6199 kN for FORTA H800.

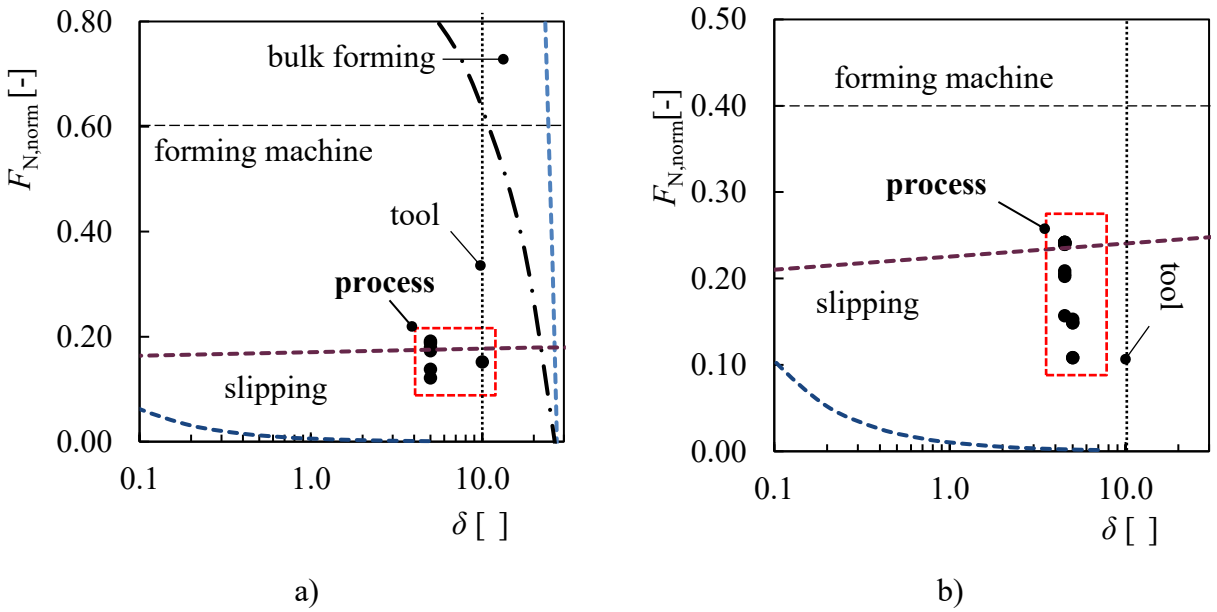

Figure 95: Successive increase of clamping force F_N crossing the border for slipping in the process windows of the materials FORTA H800 and HCT780X.

This approach validates the effects of the transition between material slipping through the clamping area and firm fixation under traction. Forming under traction is defined as crucial premise for the ISB process. Indeed, the calculated clamping forces are confirmed by the experimental series: Only when using the clamping forces predicted by the model, undesired deformations of the profile bends were avoided. In detail torsion (see Figure 96 a) or, more severely, buckling beyond the clamped area occurred when operating the process below the lower clamping force margin. These effects are explained by material slipping through the tool clamping during bending and thus undefined forming conditions.

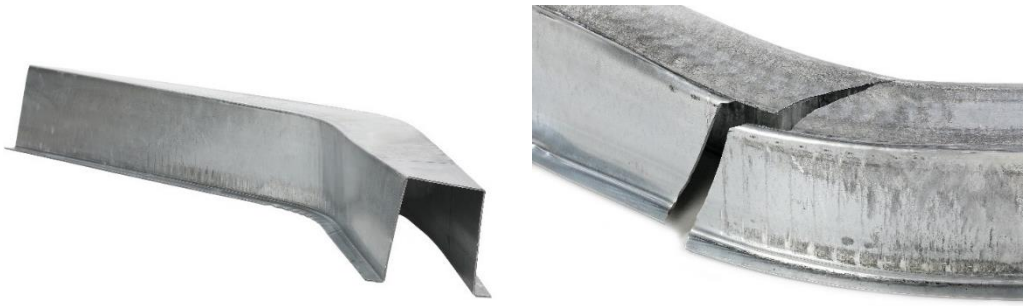

a) b)

Figure 96: Failure during incremental bending hat shaped profiles for the use-case scenario. a) Profile torsion due to insufficient clamping, b) cracking at the extrados due to excessive longitudinal straining.

In a second experimental series, successively decreasing feeding distances Δf were manufactured on both materials within the same bending plane. After bending, the profiled specimens were evaluated with regards to the resulting inner profile radius which is assumed identical to the radius at neutral fiber due to the adjusted offset (see miniature tensile tests in the next section for verification). Profiles from HCT780X and FORTA H800 are deployed for this study according to Table 23.

Table 23: Experimental series of the demonstrator profiles with variation of incremental feed. Experiments base on hat-shaped cross sections from 2 mm sheet metal materials HCT780X and FORTA H800.

Material	Spec. no.	Offset o [-]	Press load F_N [kN]	Incr. angle δ [°]	Incr. feed Δf [mm]	Incr. steps n_{ISB} [-]	Bending radius R_{th} [mm]	Bending angle α [°]	Unloaded incr. angle $\delta_{u,s}$ [°]
HCT780X	DP18	0.5	2950	5	20	10	370	25.0	2.50
HCT780X	DP21	0.5	2950	5	16	7	290	21.0	3.00
HCT780X	DP23	0.5	2950	5	15	7	280	18.5	2.64
HCT780X	DP26	0.5	2950	5	12	7	255	N/A	N/A
HCT780X	DP27	0.5	2950	5	8	7	210 (crack)	N/A	N/A
FORTA H800	H18	0.5	6200	4.5	9	13	N/A	33.0	2.54
FORTA H800	H16	0.5	6200	4.5	9	9	170	25.5	2.83
FORTA H800	H13	0.5	6200	4.5	8	10	160	27.0	2.70
FORTA H800	H12	0.5	6200	4.5	5	7	110 (crack)	23.0	3.29

The profiles of both materials were formed with decreasing incremental feed until initiation of crack at the extrados (see Figure 96 b). Corresponding to the incremental feed adjusted, the bending radius is observed to drop accordingly. The measured radii of the specimens are expressed as curvature over incremental feed and compared to the circular approximation model in Figure 97.

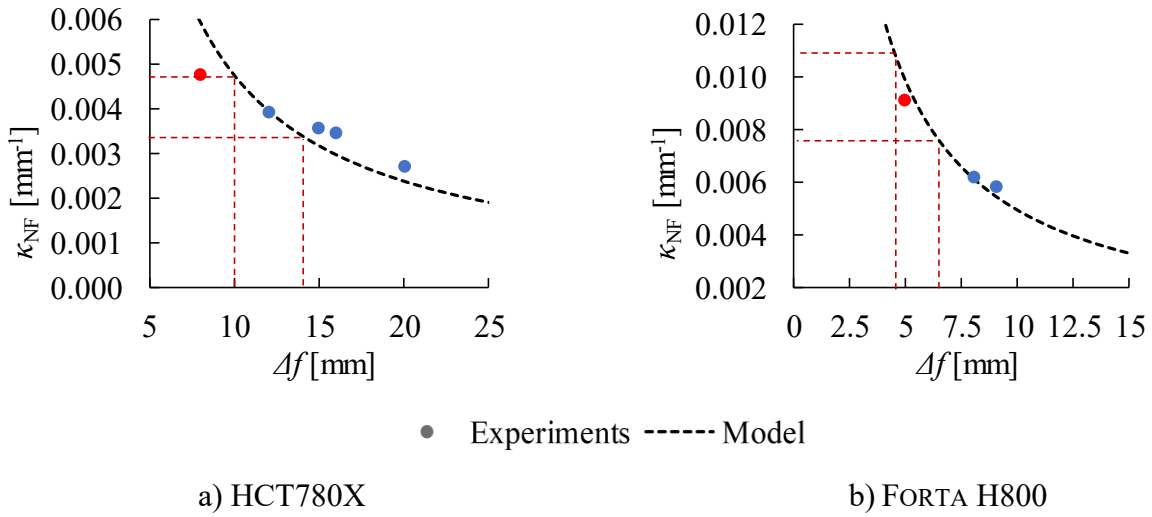

a) HCT780X b) FORTA H800

Figure 97: Curvature over incremental feed as expected by the model and as obtained from incremental forming based on the use case geometry from the materials a) HCT780X and b) FORTA H800. Red points indicate those profiles which failed due to cracking.

The curvatures achieved in the experiments agree reasonably well to the model predictions for curvature over incremental feed. Critical feeding margins calculated from the analytical model for incremental bending are verified by the cracked specimens of both materials. Compared to the limits for feasible bending radii given by the strain diagram – which bases on elementary theory of continuous bending – the limits obtained from the model on incremental forming delivers lower feasible bending radii. This relationship connects to the forming potential of incremental forming methods compared to continuous processes. The incremental bending angles δ for both materials which have been specified based on practical considerations (machine clearance, reasonable plasticizing), may still render some possibility for optimization.

7.3.3 Miniature tensile tests

In order to assure the application of the modelling assumptions with regards to strain distribution and the associated work hardening, miniature test specimens are extracted in a similar way to the profiles from 42SiCr (described in section 6.4.1, Figure 64 and Figure 65). The specimens are oriented in longitudinal profile direction and taken along the extrados of the profile floor as well as in lateral direction over circumference of the bent profile in order to validate the lateral and longitudinal qualitative and quantitative influence of ISB. The specimens are extracted by wire erosion and subsequently subjected to tensile testing for the examination of local mechanical material parameters of the strain hardened profiles. As an example, these investigations are conducted on specimen H16 referring to Table 23. The locations of tensile test extractions as well as the tested strain values and corresponding work hardened stress values are shown in Figure 98 for the longitudinal evaluation at the extrados of the profile floor.

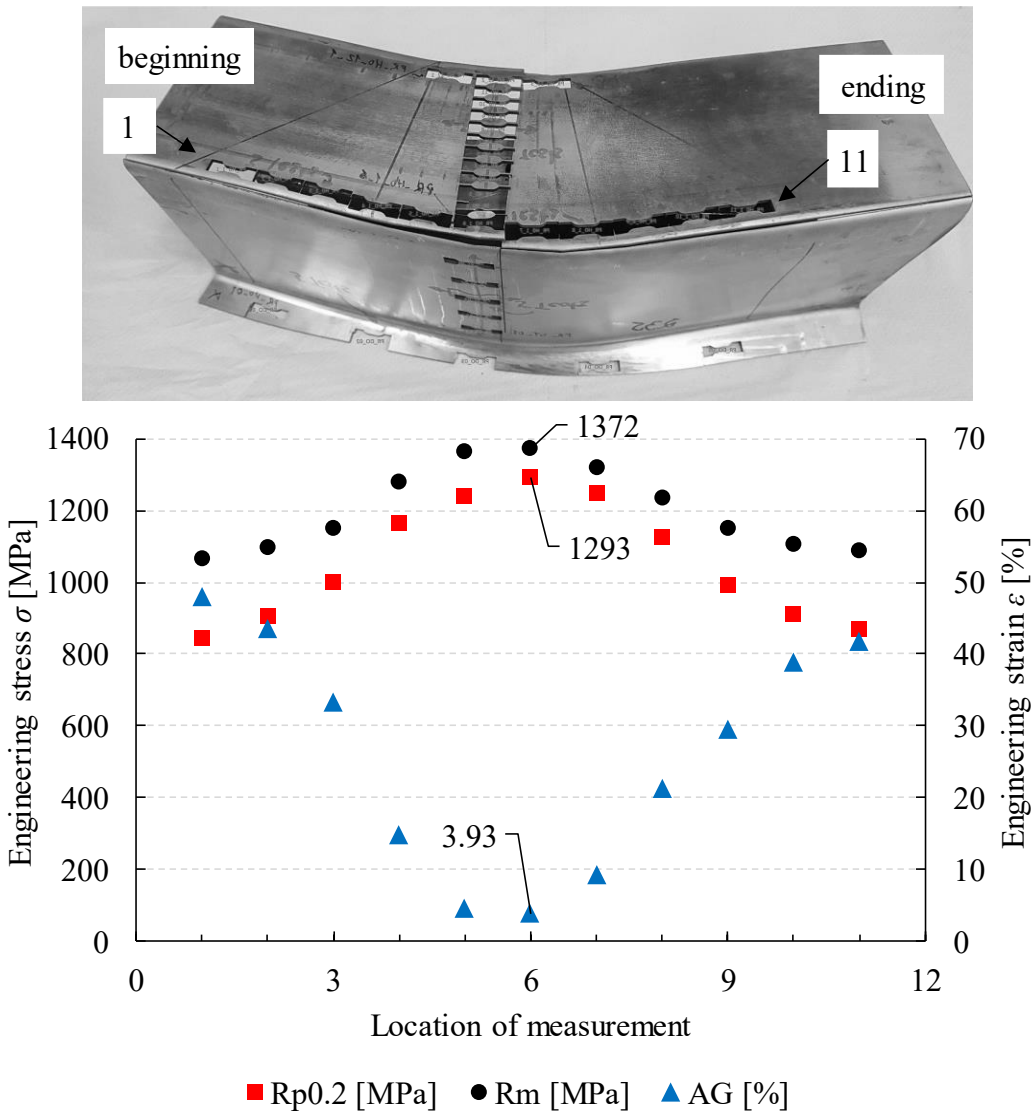

Figure 98: Evaluation of longitudinal strain and work hardening distribution of the demonstrator profile bend from FORTA H800 steel. At distinct locations, miniature specimens are extracted by wire extrusion and subjected tensile testing. The mechanical material parameters from these tests are plotted over the longitudinal coordinate of the extrados at the floor of the profile.

The results reveal smooth longitudinal transition areas from the material's initial state. A strongly work hardened strain maximum is achieved in the central region of specimen no. H16 whose ductility is not yet fully exhausted as it can be judged on A_G. Therefore, profile H13 was bent with an even tighter bending radius without failure. The values obtained from evaluating in lateral profile circumference are presented in Figure 99.

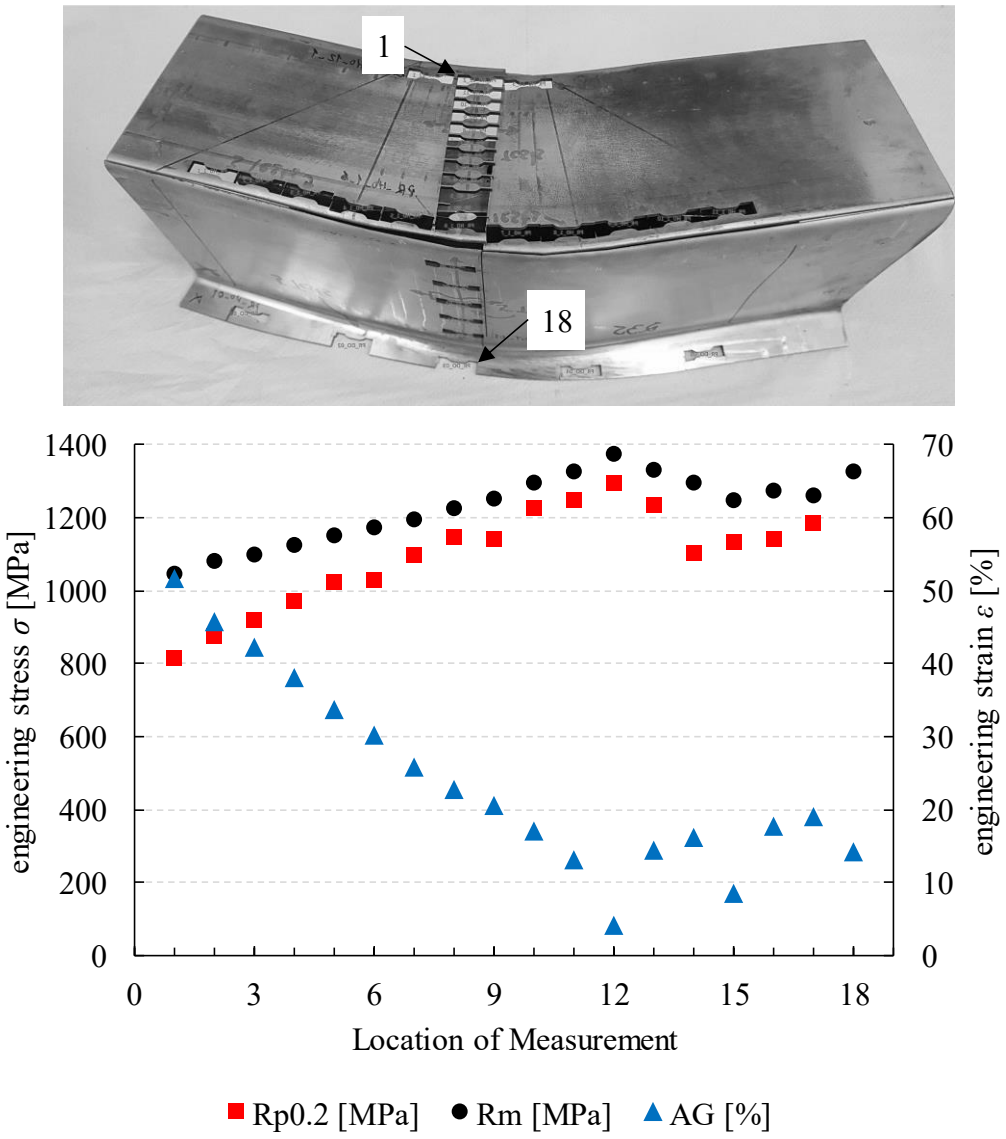

Figure 99: Evaluation of lateral strain and work hardening distribution of the demonstrator profile bend from FORTA H800 steel. At distinct locations, miniature specimens are extracted by wire extrusion and subjected tensile testing. The mechanical material parameters from these tests are plotted over the circumferential coordinate of the profile. Measurement no.12 equals measurement no.6 of the preceding evaluation.

Over the lateral profile coordinate *y*, all mechanical parameters begin at the material's initial state, which confirms the neutral fiber shift towards the intrados by the adjusted bending axis offset. A linear increase of work hardening and corresponding decrease of ductility are observed within the floor area over the profile's lateral coordinate. Strain decreases slightly from its maximum value at the extrados of the floor along the wall of the profile due to the different forming mechanism associated with both areas, i.e., frictionally engaged in-plane bending within the floor and stretch bending at the wall of the profile. Conclusively, the results of testing the local mechanical material properties indicate sufficient applicability of the modelling assumptions developed for in-plane bending.

7.3.4 Manufacture of longitudinal members by an ISB process

The industrial scale tool was designed and subsequently manufactured at LEWA ATTENDORN (Kringe-Schmeck 2017). Once set into operation according to Figure 100, the ISB tool (a) is equipped on the 10 MN servo mechanical press of the AUTOMOTIVE CENTER SÜDWESTFALEN. After conducting the experimental series presented above, the longitudinal members (b) were manufactured by an ISB process as demonstrators of the funded project (Groth 2017).

a) b)

Figure 100: Industrial demonstrator production in the R&D project "ISB-ELEKTRO" according to STÖTZEL (2017). ISB industrial scale tool (a) equipped on the SCHULER MSE 2-1000-3.5-600 press for ISB manufacturing of continuous longitudinal members (b) for the substructure of an electric vehicle. The component features two bending planes (lateral and vertical in relation to the cross section) which are realized by individual tool inserts.

As semi-finished products, hat-shaped profiles were made by continuous roll forming at KRONENBERG PROFIL (Schmitz 2016). The individual bends were formed subsequently from the center of the component towards its foremost and rear ends to avoid any collision of the ISB tool. In detail, the inner s-shaped double bending geometries about the vertical axis were formed firstly before the outer bends about the horizontal profile axis were made. With this procedure, the required bending geometries were successfully manufactured as ultimate goal of the project ISB-ELEKTRO.

7.4 Alternative ISB tool and process concepts

At the end of this thesis the alternative tooling concepts, apart from the herein utilized press tools for the ISB process, are briefly presented. Initially, ISB was applied to a press tool with secondary axes which offers the advantage of having the machinery's main force for clamping. The disadvantages of this approach, however, are that any active secondary axes such as the bending axis and feed axis need to be automated by a tool control if not driven passively, e.g., by wedge slides. Moreover, large parts with high masses (i.e., press ram, upper forming tool) need to be accelerated during press forming, potentially limiting the speed of an ISB process due to inertia. Consequently, alternative

concepts have been pursued throughout the investigations of this thesis which are explained in detail in the following subsections.

Table 24: Summary of the machinery concepts objected in this thesis.

ISB concept	Advantages	Disadvantages
Press tool	• Direct transmission of clamping force • Highest tool stiffness • Universal machinery	• Operation of secondary axes requires tool control • Limited process speed
Bending machine tool	• Direct transmission of bending force • Machine inherent control of all axes without additional tool control unit • Universal machinery	• Indirect application of clamping force • Limited clearance • Limited process speed
Special purpose ISB machine	• Direct transmission of all forces • Optimized for process speed • Fully automatized • Minimized equipping time	• Purpose bound machinery

The stiffness of the press tool is estimated as being the highest because of its dense and compact design in the form of a plate tool.

7.4.1 ISB tool concept for rotary draw bending machines

The main disadvantage of the presented press tools is the need for an exclusive tool control, which needs to be connected by sensors in order to control all secondary axes of the ISB tool, e.g., feeding and bending. Consequently, the implementation of the ISB process on an industrial style rotary draw bending machine (RDBM) was thus considered. UTS' shop floor provides a TRACTO TECHNIK TUBOTRON TT120 which was considered for the conceptual design of an ISB tool capable for the profile of the ISB use case.

The process parameters of the incremental sequence of the demonstrator (feed, incremental bending angle, axis offset, number of increments) where considered as specifications for the RDBM – ISB tool (Janzen 2017; Menn 2019). While the bending kinematics are applied directly on the bending machine, a variation of concepts for the transmission of the clamping force had to be developed because the machine does not provide any out of plane axes. The best energy density applicable by a clamping mechanism is achieved by wedge sliders with regards to permissible clearances within the assembly of the TT120. By FEM, the RDBM ISB tool concept was developed based on the wedge slider principle, see Figure 101.

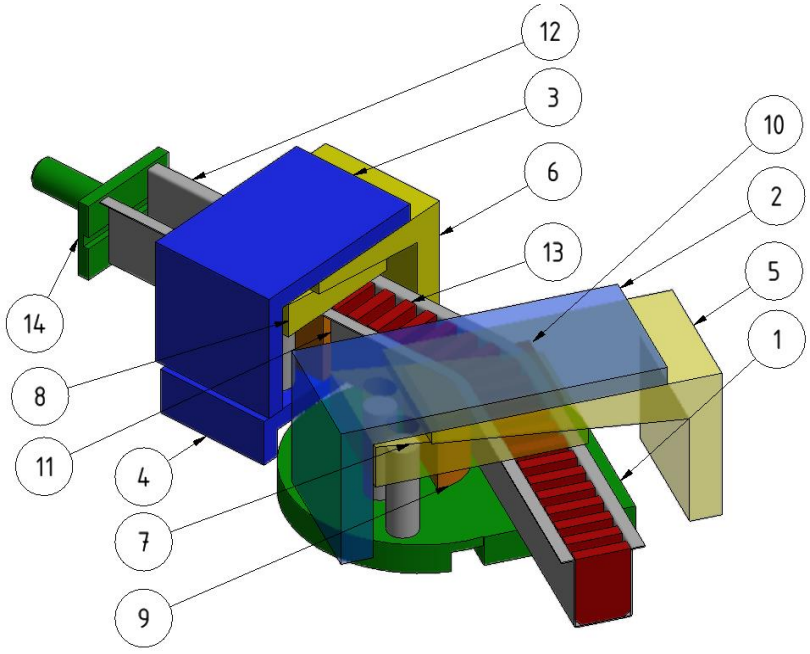

1. Bending support
2. Rotatory frame
3. Stationary frame
4. Lower part of 3.
5. Rotatory wedge counterpart
6. Stationary wedge
7. Rotatory wedge
8. Stationary wedge
9. Inner flange support
10. Outer flange support
11. Inner flange support
12. Hat shaped profile
13. Segmented mandrel
14. Feed

Figure 101: Finite element based simulation model of an ISB tool concept for a rotary draw bending machine. Transmission of clamping force by wedge sliders.

The wedge slider concept transforms the horizontal forces provided by the machine axes of the pressure die and clamping die into vertical clamping forces being applied on stationary and pivoted clamping units respectively. The simulation has revealed similar forming results of the RDBM ISB tool compared to an ISB press tool, evaluated by geometry and strain distribution. However, the capabilities of the RDBM are not utilized sufficiently in this setup because of the comparably high required clamping forces. The ISB process is based on the frictionally engaged principle of force transmission to achieve forming flexibility. As given by the law of friction, very high normal forces are required perpendicular to the bending plane. Moreover, this relation led to very flat wedge sliders in the objected example which need an angle of less than 5°. The lifting stroke for profile clearance during release, reset and feed steps of the incremental sequence was hence strongly limited which raises the risk of jamming of the profile within the tooling during feed.

7.4.2 Special purpose ISB machine concept

A specialized ISB machine concept was developed and designed by JANZEN (2019). The main goal of this development was to improve the state-of-the-art cycle time which has been proposed to be achievable by the industrial-scale ISB tool, when fully automated. With the drives applied in the ISB-specialized machine concept, a cycle time of 1.34 seconds is feasible, which is approximately three times faster than the press tool under assumption of a fully automated process operation.

The special purpose ISB machine is designed for the profile cross section and bending operations according to the use case, i.e., a 120 x 90 mm hat-shaped profile with 20 mm flanges from 2 mm HCT780X steel and the corresponding process forces. Therefore, this machine concept features interchangeable tooling inserts which are held together as package within a cylindrical socket to simplify equipping in between the bending planes. The concept was moreover planned to allow a maximum incremental bending angle of $\delta_M = \pm 12$ degrees and an absolute bending axis offset up to ± 100 mm. Regarding the produced bends, a total bending angle up to 90 degrees is feasible while the minimum distance between two bends is limited to 300 mm.

The clamping force is applied by an excentre driven punch, see Figure 102 (1), which distributes the load evenly on a stationary (3) and a pivoted (4) clamping unit respectively. The feeding unit (5) force-fittingly clamps the profile by the principle of an industrial brake and runs on rails. It is driven by an electric drive via a trapezoidal thread spindle. For bending, a hydraulic piston (6) is intended, while the bending axis is laterally adjustable (y – coordinate) by synchronized linear drives.

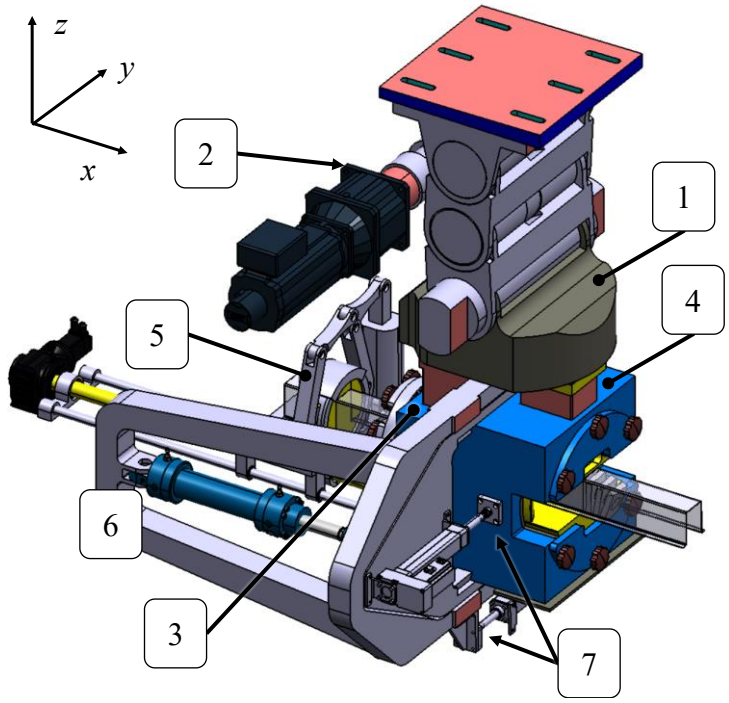

1) Excenter driven clamping punch
2) Thrust crank drive for excenter
3) Stationary clamping unit
4) Pivoted clamping unit
5) Feed unit
6) Hydraulic bending drive
7) Bending axis offset adjustment

Figure 102: Specialized ISB machine concept (hidden machine frame) (Janzen 2019).

All axes are planned within fully automated control, i.e., clamping load, profile feed, adjustment of bending plane and bending angle. The special purpose ISB machine concept is intended to be mounted within a standard o-shaped press frame.

8 Summary and Outlook

Flexible manufacturing techniques are essential to facilitate the paradigm shift from mass production to mass customization as the same is associated with the fourth industrial revolution (Wang et al. 2017). By adjusting the process parameters, kinematic and incremental forming processes allow to shape individual product variants and this is enabled by a large amount of degrees of freedom provided by the process as well as an independent tooling (Yang et al. 2018). However, in order to avoid time and material consuming trial and error approaches, process models are required to tailor the kinematic processing parameters of these methods to the target geometry of a specific product under the constraints of a given material. These models are either based on

a) statistical regression methods, such as VORKOV et al. (2019) applied in a gray-box approach for air bending,
b) analytical plasto-mechanics, for example applied to roller bending by FINCKENSTEIN et al. (1981) or to three-roll push bending by KERSTEN (2013) or,
c) numerical approaches based on the finite element method (FEM), such as SCHERER (2014) provided for power-forming.

The process of Incremental Swivel Bending has been demonstrated by ENGEL, FROHN, HILLEBRECHT, and KNAPPE (2017) as an exemplary study to provide large manufacturing flexibility for structural components manufactured from high-strength steels given by the high number of degrees of freedom provided by incremental forming processes. The processing parameters for the investigated component were however determined using elaborate empirical layout procedures. Fundamentally, the forming mechanism of ISB is identified as frictionally engaged incremental in-plane bending (Frohn et al. 2018). However, up to the state of research and technology, comparable forming mechanisms were only modeled by statistical or numerical approaches (Scherer 2014).

This thesis aims to provide an analytical solution to link the kinematic processing parameters of an ISB process along with the properties of the provided material to the required bending geometry. Moreover, the optimization problem of the density of incremental steps has not yet been addressed. For the practical verification of the ISB process development, various high-strength steels are characterized in detail with respect to mechanical properties, tribological concerns and forming limits. The ISB process is represented by successive analytical models, of which each represents the layout of a specific degree of freedom of the forming process. The appropriate bending strain distribution with regards to the laterally shiftable bending axis is determined based on the material properties and the target bending geometry. The clamping force which is necessary for frictionally engaged transmission of bending moment is derived from tribological and mechanical considerations. Based on the equilibrium of forces throughout the material, the forming zone and strain which result within

an incremental step are determined. Based on the information about the forming zone by quantitative and qualitative means, the superposition of increments is expressed as function of feed and the same is related to strain and curvature resulting from incremental bending. This established concept is the aim of the present study. Corresponding numerical simulation models are also established to complement the analytical predictions. Practical experiments are laid out by the analytical approaches and are conducted on a laboratory scale ISB forming tool. For validation and comparison, optical strain maps are captured from the surfaces of the bending specimens and bending angle and curvature are evaluated by tactile measurements. Based on the initially characterized selection of materials, the experiments and model predictions show the following results:

i. A considerably higher clamping force is necessary for bending with an offset bending axis. By longitudinal strain superposition, the bending axis offset helps to compensate wrinkling problems if shifted towards the intrados of an arc or to suppress instable tensile forming conditions if shifted towards the extrados.
ii. The size of the forming zone increases substantially over the first few degrees of incremental bending angle until it converges to a threshold value. The major influencing factors are identified as friction coefficient, clamping force and the mechanical properties of the material.
iii. Curvature increases in relation to the density of the incremental steps and the average unloaded incremental bending angle after springback.

From the validation of these findings, the general optimization problem of incremental forming techniques is considered and a solution is presented for minimizing strain of the ISB process. For a given curvature, a small amount of large bending increments evidently is the most time efficient solution, but it might lead to material failure as pronounced strain maxima would occur. In turn, multiple small incremental steps potentially cause lower strain maxima thus allowing to achieve higher curvatures. As the effect of strain smoothening of the incremental bending procedure stagnates at specific incremental subdivision, a further increase of incremental density is insufficient as it only raises cycle time. In the utmost case, when large numbers of incremental steps are formed, elastic effects tend to render manufacturing inaccuracy and the risk of out of plane buckling due to accumulated springback. Therefore, the optimum process for an ISB operation is defined at the kink of the strain over density function where the least increments provide smooth straining and efficient process time consumption.

In the end, the achieved methodology is applied to study a use case. As an industrial demonstrator, the longitudinal member of an electric car was manufactured by an ISB process. Sections of this demonstrator were formed from two different high-strength steels according to a systematic process layout and are analyzed with respect to the analytical modelling predictions. The experiments confirm

the analytical model predictions with respect to necessary clamping force for obtaining valid forming results and the curvature which resulted from specific combinations of kinematic process parameters. Incremental profile bending techniques possess an utmost potential for flexible manufacturing in the context of highly variable production demands but the selection of appropriate process settings is not evident due to a large number of degrees of freedom and independent tooling. The present thesis contributes towards understanding the layout of such kinematic and incremental bending techniques by mechanically modelling the ISB process in a comprehensible way. Moreover, the findings allow to tailor the processing parameters of an ISB process to a given bending shape for future applications.

Outlook

Throughout this thesis, the incremental bending procedure has been assumed as constant with respect to the incremental processing parameters in modelling and correspondingly it is validated in a practical experiment and demonstrated as an application. When measuring curvature over profile length, the experiments of this thesis exhibit a similar trend as the findings of GROTH, ENGEL, and LANGHAMMER (2018). It remains an open issue if an adaptive setup of the incremental density is applicable to achieve a more even distribution of the desired curvature trend. In turn, the methodology could moreover be applied to bend nonlinear curvature distributions such as splines. In addition, the increments are aligned in a successive way. It is yet unknown that which effects certain strategies for alternative arrangements could bear on the bending results, such as multiple passes associated with harmonics as shown for single point incremental forming by CARETTE et al. (2018).

Rectangular open cross sections with straight elements are considered for profile bending by an ISB process. The application to profiles with inclined sections, e.g., hexagonal or trapezoid, could be an interesting research application which might reveal yet uncovered effects. On the contrary, trials of an ISB process on tubular profiles is relatively questionable due to the well-established continuous processes. In this context, the benefit of an ISB process is clearly seen in the context of having a large supporting length which compensates the risk of torsion as the torsion becomes a considerably large issue while bending open profiles (Groth and Engel 2018). The foremost benefit of an ISB process is however the manufacturing flexibility associated with this process.

Solid tools are introduced as contact surfaces, in the analytic and simulation models as well as in the manufactured tools. Even more, square shaped tools, which are uniformly loaded with respect to both clamping units are favored. The influence of segmented dies, adapted ones, or such which can be changed actively throughout the process is neglected. First studies have indicated large potentials to influence the forming zone by modified die faces (Frohn-Sörensen, Reuter, and Engel 2021).

9 References

9.1 Technical standards and guidelines; sorted by type and number

Standard type and no.	Title
ASTM E 1876	Dynamic Young's Modulus, Shear Modulus, and Poisson's Ratio by Impulse Excitation of Vibration
DIN 50125	Prüfung metallischer Werkstoffe – Zugproben
DIN 8580 (2003-09-00)	Manufacturing processes - Terms and definitions, division
DIN 8582 (2003-09-00)	Fertigungsverfahren Umformen - Einordnung; Unterteilung, Begriffe, Alphabetische Übersicht
DIN 8586 (2003-09-00)	Manufacturing processes forming by bending - Classification, subdivision, terms and definitions
DIN EN 10027-2	Designation systems for steels – Part 1: Steel names
DIN EN ISO 6892-1	Metallic materials – Tensile testing – Part 1: Method of test at room temperature
DIN EN ISO 12004-2	Metallic materials – Sheet and strip - Determination of forming-limit curves – Part 2: Determination of forming-limit curves in the laboratory
VDI 3430 (2014)	Rotary draw bending of profiles

9.2 Literature

Abbott, Edward J., and Floyd A. Firestone. 1933. "Specifying Surface Quality: A Method Based on Accurate Measurement and Comparison." *Mechanical Engineering (ASME)* 55:569–72.

Abraham, Tim, Günter Bräuer, Felix Kretz, and Peter Groche. 2018. "Observation of the A-C:H Run-in Behaviour for Dry Forming Applications of Aluminium." *MATEC Web of Conferences* 190:14001. doi: 10.1051/matecconf/201819014001.

Adelhof, Alois. 1992. *Komponenten Einer Flexiblen Fertigung Beim Profilbiegen.* Dissertation, Aachen: Shaker Verlag GmbH.

Allwood, J. M., D. R. Shouler, and A. Erman Tekkaya. 2007. "The Increased Forming Limits of Incremental Sheet Forming Processes." *Key Engineering Materials* 344:621–28. doi: 10.4028/www.scientific.net/KEM.344.621.

Ambrogio, Giuseppina, De Napoli Luigi, Letícia Filice, Francesco Gagliardi, and Maurizio Muzzupappa. 2005. "Application of Incremental Forming Process for High Customised Medical Product Manufacturing." *Journal of Materials Processing Technology* 162:156–62. doi: 10.1016/j.jmatprotec.2005.02.148.

Ancellotti, S., V. Fontanari, S. Slaghenaufi, E. Cortelletti, and M. Benedetti. 2019. "Forming Rectangular Tubes into Complicated 3D Shapes by Combining Three-Roll Push Bending,

Twisting and Rotary Draw Bending: The Role of the Fabrication Loading History on the Mechanical Response." *International Journal of Material Forming* 12(6):907–26. doi: 10.1007/s12289-018-1453-0.

Andersen, Ann-Louise, Thomas D. Brunoe, and Kjeld Nielsen. 2015. "Reconfigurable Manufacturing on Multiple Levels: Literature Review and Research Directions." Pp. 266–73 in *Advances in Production Management Systems: Innovative Production Management Towards Sustainable Growth*, *IFIP Advances in Information and Communication Technology*, edited by S. Umeda, M. Nakano, H. Mizuyama, N. Hibino, D. Kiritsis, and G. von Cieminski. Cham: Springer International Publishing.

Bach, Friedrich-Wilhelm, Kai Möhwald, Andreas Laarmann, and Thomas Wenz. 2006. *Moderne Beschichtungsverfahren*. John Wiley & Sons.

Back, Stephan, and Hermann Weigel. 2014. *Design for Six Sigma:-Kompaktes Wissen-Konkrete Umsetzung-Praktische Arbeitshilfen*. München: Carl Hanser Verlag GmbH Co KG.

Becker, Christoph, A. Erman Tekkaya, and Matthias Kleiner. 2014. "Fundamentals of the Incremental Tube Forming Process." *CIRP Annals* 63(1):253–56. doi: 10.1016/j.cirp.2014.03.009.

Borchmann, Linda. 2021. *Regelung Des Werkstoffflusses Zur Erhöhung Der Bauteilqualität Beim Rotationszugbiegen*. Vol. 14. Dissertation: Siegen: Universi Verlag.

Brozzo, P., B. Deluca, and R. Rendina. 1972. "A New Method for the Prediction of Formability Limits in Metal Sheets." in *Proc. 7th biennal Conf. IDDR*.

Cao, Jian, Ekkard Brinksmeier, Mingwang Fu, Robert X. Gao, Biao Liang, Marion Merklein, Michael Schmidt, and Jun Yanagimoto. 2019. "Manufacturing of Advanced Smart Tooling for Metal Forming." *CIRP Annals* 68(2):605–28. doi: 10.1016/j.cirp.2019.05.001.

Carette, Yannick, Hans Vanhove, and Joost Duflou. 2018. "Reducing Workpieces to Their Base Geometry for Multi-Step Incremental Forming Using Manifold Harmonics." *AIP Conference Proceedings* 1960(1):160004. doi: 10.1063/1.5035030.

Chatti, S., Matthias Hermes, A. Tekkaya, and Matthias Kleiner. 2010. "The New TSS Bending Process: 3D Bending of Profiles with Arbitrary Cross-Sections." *CIRP Annals* 59:315–18. doi: 10.1016/j.cirp.2010.03.017.

Chatti, Sami. 1998. *Optimierung der Fertigungsgenauigkeit beim Profilbiegen*. Dissertation, Aachen: Shaker Verlag GmbH.

Clausen, Arild H., Odd S. Hopperstad, and Magnus Langseth. 2000. "Stretch Bending of Aluminium Extrusions for Car Bumpers." *Journal of Materials Processing Technology* 102(1):241–48. doi: 10.1016/S0924-0136(99)00487-2.

Colgan, Mark, and John Monaghan. 2003. "Deep Drawing Process: Analysis and Experiment." *Journal of Materials Processing Technology* 132(1):35–41. doi: 10.1016/S0924-0136(02)00253-4.

Coulomb, Charles Augustin. 1821. *Théorie des machines simples en ayant égard au frottement de leurs parties et à la roideur des cordages*. Bachelier.

Czichos, Horst, and Karl-Heinz Habig. 2010. *Tribologie-Handbuch: Tribometrie, Tribomaterialien, Tribotechnik*. Wiesbaden: Springer Vieweg.

Doege, Eckart, and Bernd-Arno Behrens. 2007. *Handbuch Umformtechnik: Grundlagen, Technologien, Maschinen ; mit 55 Tabellen*. Berlin, Heidelberg: Springer-Verlag.

Dubratz, Markus. 2006. *Entwicklung Eines Werkzeugkonzeptes Zur Inkrementellen Biegeumformung Ebener Bleche*. *Studienarbeit am Lehrstuhl für Umformtechnik der Universität Siegen*.

Duflou, Joost R., Anne-Marie Habraken, Jian Cao, Rajiv Malhotra, Markus Bambach, Dave Adams, Hans Vanhove, Amirahmad Mohammadi, and Jack Jeswiet. 2018. "Single Point Incremental Forming: State-of-the-Art and Prospects." *International Journal of Material Forming* 11(6):743–73. doi: 10.1007/s12289-017-1387-y.

Eckold, Walter. 1958. "Maschine zur spanlosen Formung von handgesteuerten Blechen oder Profilen." (DE969993C).

Eckstein, Johannes. 2009. *Numerische Und Experimentelle Erweiterung Der Verfahrensgrenzen Beim Halbhohlstanznieten Hochfester Bleche*. Dissertation: Universität Stuttgart.

Elmer, Franz-Josef. 1997. "Nonlinear Dynamics of Dry Friction." *Journal of Physics A: Mathematical and General* 30(17):6057–63. doi: 10.1088/0305-4470/30/17/015.

Engel, Bernd, Johannes Buhl, and Christopher Heftrich. 2014. "Modelling and Optimization of Lightweight-Sandwich-Sheets with an Adhesive Interlayer for the Forming Process Die Bending." *Procedia CIRP* 18:168–73. doi: 10.1016/j.procir.2014.06.126.

Engel, Bernd, Peter Frohn, Martin Hillebrecht, and André Knappe. 2017. "Incremental Swivel Bending for Scalable Lightweight Structures." *ATZ Worldwide* 119(5):26–31. doi: 10.1007/s38311-017-0023-2.

Engel, Bernd, Peter Frohn, Martin Hillebrecht, and Andre Knappe. 2017. "Inkrementelles Schwenkbiegen zur kostengünstigen Herstellung von Trägerstrukturen in Elektrofahrzeugen." Pp. 219–34 in *Karosseriebautage Hamburg 2017*, edited by A. Piskun. Wiesbaden: Springer Fachmedien.

Engel, Bernd, Christian Gerlach, and Stefan Cordes. 2008. "Biegemomentenabschätzung Des Dornbiegeverfahrens." *UTF-Science* (2):1–8.

Engel, Bernd, Sebastian Groth, and Peter Frohn. 2015. "Numerische Verfahrensentwicklung Für Das Inkrementelle Schwenkbiegen (ISB) von Komplexeren Profilquerschnitten." Pp. 83–88 in *Tagungsband XXXIV. Verformungskundliches Kolloquium*. Vol. 34. Zauchensee, Austria: Universität Leoben.

Engel, Bernd, and Hassan Raheem Hassan. 2014. "Investigation of Neutral Axis Shifting in Rotary Draw Bending Processes for Tubes." *Steel Research International* 85(7):1209–14. doi: 10.1002/srin.201300333.

Engel, Bernd, and Hassan Raheem Hassan. 2015. "Advanced Model for Calculation of the Neutral Axis Shifting and the Wall Thickness Distribution in Rotary Draw Bending Processes." *International Journal of Materials and Metallurgical Engineering* 9(2):6.

Engel, Bernd, and Sebastian Kersten. 2010. “Sensitivitätsanalyse Beim Freiformbiegen von Rohrprofilen, 30.” P. 138 in *EFB-Kolloquium Blechverarbeitung*. Vol. 123.

Engel, Bernd, Sebastian Kersten, and D. Anders. 2011. “Spline-Interpolation and Calculation of Machine Parameters for the Three-Roll-Pushbending of Spline-Contours.” *Steel Research International* 82(10):1180–86.

Engels, Heiko. 2016. *ISB Elektro - Inkrementelles Schwenkbiegen Zur Kostengünstigen Herstellung von Trägerstrukturen in Elektrofahrzeugen. Teilvorhaben: Entwicklung Der Produktionstechnik Zur Integration Des Inkrementellen Schwenkbiegens in Die Bestehende Fertigungskette, Schlussbericht.* Attendorn: KIRCHHOFF Automotive Deutschland GmbH. doi: 10.2314/GBV:875646999.

Filzek, Jan. 2004. *Kombinierte Prüfmethode Für Das Reib-, Verschleiß-Und Abriebverhalten Beim Tief-Und Streckziehen*. Vol. 62. Dissertation, Aachen: Shaker Verlag GmbH.

Finckenstein, Eberhard von, G. Ludowig, G. Zicke, and G. Stutte. 1981. “Developments in NC-Sheet Metal Bending, Especially in NC-Roll Bending.” *CIRP Annals* 30(1):163–66. doi: 10.1016/S0007-8506(07)60916-0.

Flehmig, Thomas, Klaus W. Blümel, and Martin Kibben. 2001. “Thin Walled Steel Tube Pre-Bending for Hydroformed Components - Bending Boundaries and Presentation of a New Mandrel Design.” *SAE Transactions* 110:567–85.

Franz, Wolf-Dietrich. 1961. “Biegewerkzeuge Und Sonderanwendungen.” Pp. 101–13 in *Das Kalt-Biegen von Rohren*. Berlin, Heidelberg: Springer-Verlag.

Franz, Wolf-Dietrich. 1988. *Maschinelles Rohrbiegen: Verfahren Und Maschinen*. Düsseldorf: VDI Fachmedien GmbH & Co. KG.

Franzke, Martin, Dominik Recker, and Gerhard Hirt. 2008. “Development of a Process Model for Online-Optimization of Open Die Forging of Large Workpieces.” *Steel Research International* 79(10):753–57. doi: https://doi.org/10.1002/srin.200806195.

Frohn, Peter, Bernd Engel, and Sebastian Groth. 2018. “Analytic Description of the Frictionally Engaged In-Plane Bending Process Incremental Swivel Bending (ISB).” *AIP Conference Proceedings* 1960(1):160006. doi: 10.1063/1.5035032.

Frohn, Peter, Hana Jirková, Bohuslav Masek, and Bernd Engel. 2017. “Changes of Plastic Properties of Incremental Formed UHSS Profiles by Subsequent Q-P Processing.” Pp. 4–6 in *Proceedings of the International Conference on Plasticity, Damage and Fracture*. Puerto Vallarta, Mexico.

Frohn-Sörensen, Peter, Clemens Cislo, Hanno Paschke, Martin Stockinger, and Bernd Engel. 2021. “Dry Friction under Pressure Variation of PACVD TiN Surfaces on Selected Automotive Sheet Metals for the Application in Unlubricated Metal Forming.” *Wear* 203750. doi: 10.1016/j.wear.2021.203750.

Frohn-Sörensen, Peter, Wolfram Hochstrate, Dominique Schneider, Michael Schiller, and Bernd Engel. 2020. “Incremental Bending of Conic Profiles on CNC Hydraulic Bending Machines.” *Proceedings of the Institution of Mechanical Engineers, Part B: Journal of Engineering Manufacture* 0954405420982227. doi: 10.1177/0954405420982227.

Frohn-Sörensen, Peter, Bohuslav Mašek, Martin F. X. Wagner, Kateřina Rubešová, Omid Khalaj, and Bernd Engel. 2020. "Flexible Manufacturing Chain with Integrated Incremental Bending and Q-P Heat Treatment for on-Demand Production of AHSS Safety Parts." *Journal of Materials Processing Technology* 275:116312. doi: 10.1016/j.jmatprotec.2019.116312.

Frohn-Sörensen, Peter, Daniel Nebeling, Jonas Reuter, and Bernd Engel. 2022. "A Critical Evaluation of Forming Limit Curves Regarding Layout of Bending Processes." *Key Engineering Materials* 926:1051–60. doi: 10.4028/p-d09adu.

Frohn-Sörensen, Peter, Jonas Reuter, and Bernd Engel. 2021. "Influencing the Forming Zone by Altering the Contact Pressure in a Bending Process." in *Proceedings of the 24th International Conference on Material Forming*. Liege, Belgien: PoPuPS.

Gantner, Peter, Herbert Bauer, David K. Harrison, and Anjali K. M. De Silva. 2005. "Free-Bending—A New Bending Technique in the Hydroforming Process Chain." *Journal of Materials Processing Technology* 167(2):302–8. doi: 10.1016/j.jmatprotec.2005.05.052.

Gatea, Shakir, Hengan Ou, and Graham McCartney. 2016. "Review on the Influence of Process Parameters in Incremental Sheet Forming." *The International Journal of Advanced Manufacturing Technology* 87(1):479–99. doi: 10.1007/s00170-016-8426-6.

Geiger, R., H. Kaiser, H. Höneß, W. Krämer, K. Lange, H. Müller, H. D. Schacher, H. Schelosky, D. Schlosser, H. Wilhelm, and R. Zeller. 2013. *Lehrbuch der Umformtechnik: Band 3: Blechumformung*. Berlin, Heidelberg: Springer-Verlag.

Gerlach, Christian. 2010. *Ein Beitrag Zur Herstellung Definierter Freiformbiegegeometrien Bei Rohren Und Profilen*. Vol. 1. Dissertation: Aachen: Shaker Verlag GmbH.

Ghiotti, Andrea, and Stefania Bruschi. 2011. "Tribological Behaviour of DLC Coatings for Sheet Metal Forming Tools." *Wear* 271(9):2454–58. doi: 10.1016/j.wear.2010.12.043.

Ghosh, Amit K. 1974. "Strain Localization in the Diffuse Neck in Sheet Metal." *Metallurgical Transactions* 5(7):1607–16. doi: 10.1007/BF02646332.

Gibson, T. J., R. M. Hobbs, and P. D. Stewart. 1974. "Development of Tests for Selecting Lubricants Suitable for Press-Forming of Sheet Metals." in *International Conference on Production Technology, Institution of Engineers, Melbourne, Australia. 1974, 328-332*.

Glascott, J., F. H. Stott, and G. C. Wood. 1985. "The Effectiveness of Oxides in Reducing Sliding Wear of Alloys." *Oxidation of Metals* 24(3):99–114. doi: 10.1007/BF00664227.

Glascott, J, G. C. Wood, and F. H. Stott. 1985. "The Influence of Experimental Variables on the Development and Maintenance of Wear-Protective Oxides during Sliding of High-Temperature Iron-Base Alloys." *Proceedings of the Institution of Mechanical Engineers, Part C: Journal of Mechanical Engineering Science* 199(1):35–41. doi: 10.1243/PIME_PROC_1985_199_088_02.

Goodwin, Gorton M. 1968. *Application of Strain Analysis to Sheet Metal Forming Problems in the Press Shop*. *SAE Technical Paper*. 680093. Warrendale, PA: SAE International. doi: 10.4271/680093.

Groche, Peter, Jan Filzek, and Gernot Nitzsche. 2004. "Local Contact Conditions in Sheet Metal Forming and Their Simulation in Laboratory Test Methods." *Wissenschaftliche Gesellschaft Für Produktiontechnik (in Braunschweig)* 11(1):55–60.

Gronostajski, Zbigniew. 2000. "The Constitutive Equations for FEM Analysis." *Journal of Materials Processing Technology* 106(1):40–44. doi: 10.1016/S0924-0136(00)00635-X.

Groth, Sebastian. 2017. *Inkrementelles Schwenkbiegen Zur Kostengünstigen Herstellung von Trägerstrukturen in Elektrofahrzeugen (ISB-Elektro). Teilvorhaben: Entwicklung Der Fertigungstechnik Inkrementelles Schwenkbiegen (EdF-ISB), Schlussbericht.* Siegen: Universität Siegen. doi: 10.2314/GBV:1002787904.

Groth, Sebastian. 2020. *Methode Zur Produktplanung Beim Freiformbiegen*. Vol. 12. Dissertation, Aachen: Shaker Verlag GmbH.

Groth, Sebastian, and Bernd Engel. 2018. "A Method for Manufacturing Bent Profiles with Open Cross-Section by Die-Push-Bending." *ITAtube Journal* (1):44–49.

Groth, Sebastian, Bernd Engel, and Peter Frohn. 2018. "Approach to a Manufacture-Oriented Modeling of Bent Tubes Depending on the Curvature Distribution during Three-Roll-Push-Bending." *AIP Conference Proceedings* 1960(1):110006. doi: 10.1063/1.5034963.

Groth, Sebastian, Bernd Engel, and Kay Langhammer. 2018. "Algorithm for the Quantitative Description of Freeform Bend Tubes Produced by the Three-Roll-Push-Bending Process." *Production Engineering* 12(3):517–24. doi: 10.1007/s11740-018-0795-2.

Gunasekaran, Angappa. 1998. "Agile Manufacturing: Enablers and an Implementation Framework." *International Journal of Production Research* 36(5):1223–47. doi: 10.1080/002075498193291.

Häfner, Tom, Benedict Rothammer, Jennifer Tenner, Kim Krachenfels, Marion Merklein, Stephan Tremmel, and Michael Schmidt. 2018. "Adaption of Tribological Behavior of A-C:H Coatings for Application in Dry Deep Drawing." *MATEC Web of Conferences* 190:14002. doi: 10.1051/matecconf/201819014002.

Hanson, Magnus, Nils Stavlid, Ernesto Coronel, and Sture Hogmark. 2008. "On Adhesion and Metal Transfer in Sliding Contact between TiN and Austenitic Stainless Steel." *Wear* 264(9):781–87. doi: 10.1016/j.wear.2006.11.056.

Hartl, Christoph. 2005. "Research and Advances in Fundamentals and Industrial Applications of Hydroforming." *Journal of Materials Processing Technology* 167(2):383–92. doi: 10.1016/j.jmatprotec.2005.06.035.

Heftrich, Christopher, Rainer Steinheimer, and Bernd Engel. 2018. "Rotary-Draw-Bending Using Tools with Reduced Geometries." *Procedia Manufacturing* 15:804–11. doi: 10.1016/j.promfg.2018.07.410.

Hermes, Matthias. 2011. *Neue Verfahren Zum Rollenbasierten 3D-Biegen von Profilen*. Dissertation, Aachen: Shaker Verlag GmbH.

Heslot, F., T. Baumberger, B. Perrin, B. Caroli, and C. Caroli. 1994. "Creep, Stick-Slip, and Dry-Friction Dynamics: Experiments and a Heuristic Model." *Physical Review E* 49(6):4973–88. doi: 10.1103/PhysRevE.49.4973.

Hetzner, H., J. Koch, S. Tremmel, S. Wartzack, and M. Merklein. 2011. "Improved Sheet Bulk Metal Forming Processes by Local Adjustment of Tribological Properties." *Journal of Manufacturing Science and Engineering* 133(6). doi: 10.1115/1.4005313.

Hillebrecht, Martin, Andre Knappe, Jörg Hülsmann, Sascha Engel, and EDAG Engineering GmbH. 2017. *Inkrementelles Schwenkbiegen Zur Kostengünstigen Herstellung von Trägerstrukturen in Elektrofahrzeugen (ISB Elektro). Teilvorhaben: Lastenhefterstellung/ Erforschung Virtueller Strukturkonzepte Und Produktionsbaukasten, Schlussbericht.* [Fulda]: [EDAG Engineering GmbH]. doi: 10.2314/GBV:1006068570.

Hinkel, Markus. 2013. *Prozessfenster Für Das Spannen von Rohrprofilen Beim Rotationszugbiegen Unter Berücksichtigung Der Tribologie*. Vol. 3. Dissertation, Aachen: Shaker Verlag GmbH.

Hoffmann, Hartmut, Reimund Neugebauer, and Günter Spur. 2012. *Handbuch umformen*. München: Carl Hanser Verlag GmbH Co KG.

Hollomon, John H. 1945. "Tensile Deformation." *Aime Trans* 12(4):1–22.

Hooke, Robert. 1678. *Lectures de Potentia Restitutiva, Or of Spring Explaining the Power of Springing Bodies*. John Martyn.

Hora, Pavel, and Longchang Tong. 2008. "Theoretical Prediction of the Influence of Curvature and Thickness on the FLC by the Enhanced Modified Maximum Force Criterion." P. 7 in *Proceedings of the NUMISHEET 2008 Conference*. Interlaken, Switzerland.

Hortig, Dirk. 2001. *Werkzeugbeschichtungen Mit Trockenschmierstoffeigenschaften Für Das Tiefziehen*. Vol. 47. Dissertation, Aachen: Shaker Verlag GmbH.

Hughes, I. F. 1977. "Evaluation of Steel Galling and Surface Finish." *Sheet Metal Industries* 54(2):147–53.

Janzen, Nico. 2017. *Konstruktion: Anwendung Des ISB Verfahrens Auf Eine Rotationszugbiegemaschine*. *Bachelorarbeit am Lehrstuhl für Umformtechnik der Universität Siegen*.

Janzen, Viktor. 2019. *Entwicklung eines Maschinenkonzepts zur Implementierung des inkrementellen Schwenkbiegens*. *Masterarbeit am Lehrstuhl für Umformtechnik der Universität Siegen*.

Jeswiet, J., F. Micari, G. Hirt, A. Bramley, J. Duflou, and J. Allwood. 2005. "Asymmetric Single Point Incremental Forming of Sheet Metal." *CIRP Annals* 54(2):88–114. doi: 10.1016/S0007-8506(07)60021-3.

Jin, Yingjun, Takashi Kuboki, and Makoto Murata. 2005. "Influence of Strip Materials on Behavior of Incremental In-Plane Bending." *Journal of Materials Processing Technology* 162–163:190–95. doi: 10.1016/j.jmatprotec.2005.02.175.

Jirkova, Hana, and Ludmila Kucerova. 2016. "Q-P Process on Steels with Various Carbon and Chromium Contents." Pp. 819–24 in *Proceedings of the 8th Pacific Rim International Congress on Advanced Materials and Processing*, edited by F. Marquis. Basel: Springer International Publishing.

Jirková, Hana, Ludmila Kučerová, and Bohuslav Mašek. 2012. "Effect of Quenching and Partitioning Temperatures in the Q-P Process on the Properties of AHSS with Various Amounts of

Manganese and Silicon." *Materials Science Forum*. doi: 10.4028/www.scientific.net/MSF.706-709.2734.

Jirková, Hana, Bohuslav Mašek, Martin F. X. Wagner, Danuše Langmajerová, Ludmila Kučerová, Ruth Treml, and Daniel Kiener. 2014. "Influence of Metastable Retained Austenite on Macro and Micromechanical Properties of Steel Processed by the Q&P Process." *Journal of Alloys and Compounds* 615:S163–68. doi: 10.1016/j.jallcom.2013.12.028.

Jocham, David. 2018. "Bestimmung Der Lokalen Einschnürung Nach Linearer Und Nichtlinearer Umformhistorie Sowie Ermittlung Dehnungs-Und Geschwindigkeitsabhängiger Materialkennwerte." PhD Thesis, Technische Universität München.

Jost, H. Peter. 1966. "Lubrication (Tribology) Education and Research." *A Report on the Present Position and Industry Needs, Department of Education and Science, HM Stationary Office, London*.

Jost, H. Peter. 2006. "Tribology: How a Word Was Coined 40 Years Ago." *Tribology & Lubrication Technology* 62(3):24.

Karbasian, H., and A. E. Tekkaya. 2010. "A Review on Hot Stamping." *Journal of Materials Processing Technology* 210(15):2103–18. doi: 10.1016/j.jmatprotec.2010.07.019.

Keeler, Stuart P. 1961. "Plastic Instability and Fracture in Sheets Stretched over Rigid Punches." Dissertation, Massachusetts Institute of Technology.

Keeler, Stuart P. 1965. *Determination of Forming Limits in Automotive Stampings*. SAE Technical Paper.

Keeler, Stuart P. 1966. "Determination of Forming Limits in Automotive Stampings." *SAE Transactions* 74:1–9.

Keeler, Stuart P. 1968. "Circular Grid System—a Valuable Aid for Evaluating Sheet Metal Formability." *SAE Transactions* 371–79.

Keeler, Stuart P., and W. G. Brazier. 1977. "Relationship between Laboratory Material Characterization and Press-Shop Formability." in *Proc. Conf. on Microalloying 75, 1977, 517-528*.

Kersten, Sebastian. 2013. *Prozessmodelle Zum Drei-Rollen-Schubbiegen von Rohrprofilen*. Vol. 2. Dissertation, Aachen: Shaker Verlag GmbH.

Khodayari, Ghafoor. 1993. "Untersuchungen Zum Elastisch-Plastischen Biegen von Stahlprofilen." Dissertation, Universität Siegen.

Klocke, Fritz. 2017. *Fertigungsverfahren 4: Umformen*. Berlin, Heidelberg: Springer-Verlag.

König, Wilfried. 2013. *Fertigungsverfahren: Blechbearbeitung*. Berlin, Heidelberg: Springer-Verlag.

Koren, Y., U. Heisel, F. Jovane, T. Moriwaki, G. Pritschow, G. Ulsoy, and H. Van Brussel. 1999. "Reconfigurable Manufacturing Systems." *CIRP Annals* 48(2):527–40. doi: 10.1016/S0007-8506(07)63232-6.

Kotzian, Tobias. 2017. *Ermittlung von Grenzformänderungskurven Für Unterschiedliche Aluminiumlegierungen*. *Bachelorarbeit am Lehrstuhl für Umformtechnik der Universität Siegen*.

Kringe-Schmeck, Sebastian. 2017. *Inkrementelles Schwenkbiegen Zur Kostengünstigen Herstellung von Trägerstrukturen in Elektrofahrzeugen (ISB-Elektro). Teilvorhaben: Entwicklung Einer Prototypenanlage Zum Inkrementellen Schwenkbiegen (EPISB), Schlussbericht.* Attendorn: [LEWA Attendorn GmbH]. doi: 10.2314/GBV:100872159X.

Kuppert, Andreas. 2015. *Erweiterung und Verbesserung von Versuchs-und Auswertetechniken für die Bestimmung von Grenzformänderungskurven*. Vol. 267. Dissertation, Erlangen: Meisenbach.

Kurz, Rudolf. 1970. "Anwendungsmöglichkeiten des Pulvernitrierens im Vergleich zum Badnitrieren (Tenifer-Verfahren)." *Materialwissenschaft und Werkstofftechnik* 1(3):124–26. doi: 10.1002/mawe.19700010303.

Lange, Kurt. 2002. *Umformtechnik: Grundlagen*. Berlin, Heidelberg: Springer-Verlag.

Liedtke, Dieter, Ulrich Baudis, Joachim Boßlet, Uwe Huchel, Wolfgang Lerche, Heinz-Joachim Spies, and Heinrich Klümper-Westkamp. 2018. *Wärmebehandlung von Eisenwerkstoffen II: Nitrieren und Nitrocarburieren*. Tübingen: expert verlag.

Lindner, Stefan. 2016. "Forta H-Series – Ultimate Lightweight Solutions with High Strength Austenitic Materials." Pp. 891–99 in *16. Internationales Stuttgarter Symposium*, *Proceedings*, edited by M. Bargende, H.-C. Reuss, and J. Wiedemann. Wiesbaden: Springer Fachmedien.

Lorenz, B., Y. R. Oh, S. K. Nam, S. H. Jeon, and B. N. J. Persson. 2015. "Rubber Friction on Road Surfaces: Experiment and Theory for Low Sliding Speeds." *The Journal of Chemical Physics* 142(19):194701. doi: 10.1063/1.4919221.

Ludwik, Paul. 1909. *Elemente der Technologischen Mechanik*. Berlin, Heidelberg: Springer-Verlag.

Macherauch, Eckard, and Hans-Werner Zoch. 2011. "Nitrieren und Nitrocarburieren." Pp. 237–40 in *Praktikum in Werkstoffkunde: 91 ausführliche Versuche aus wichtigen Gebieten der Werkstofftechnik*, edited by E. Macherauch and H.-W. Zoch. Wiesbaden: Springer Vieweg.

Male, A. T., and M. G. Cockroft. 1964. "A Method for the Determination of the Coefficient of Friction of Metals under Conditions of Bulk Plastic Deformation." *Journal of the Institute of Metals* 93:38.

Male, Alan T., and Vincent DePierre. 1970. "The Validity of Mathematical Solutions for Determining Friction From the Ring Compression Test." *Journal of Lubrication Technology* 92(3):389–95. doi: 10.1115/1.3451419.

Marciniak, Zdzislaw, and Kazimierz Kuczyński. 1967. "Limit Strains in the Processes of Stretch-Forming Sheet Metal." *International Journal of Mechanical Sciences* 9(9):609–20. doi: 10.1016/0020-7403(67)90066-5.

Marušić, K., H. Otmačić, D. Landek, F. Cajner, and E. Stupnišek-Lisac. 2006. "Modification of Carbon Steel Surface by the Tenifer® Process of Nitrocarburizing and Post-Oxidation." *Surface and Coatings Technology* 201(6):3415–21. doi: 10.1016/j.surfcoat.2006.07.231.

Mathes, Christian. 2007. *Inkrementelles Schwenkbiegen Mit Innovativem Werkzeugkonzept*. *Studienarbeit am Lehrstuhl für Umformtechnik der Universität Siegen*.

Menn, Philipp. 2019. *FE Simulation von Werkzeugkonzepten Zur Anwendung Des ISB Verfahrens Auf Rotationszugbiegemaschinen*. *Masterarbeit am Lehrstuhl für Umformtechnik der Universität Siegen*.

Merklein, M., J. Lechler, and T. Stoehr. 2008. "Characterization of Tribological and Thermal Properties of Metallic Coatings for Hot Stamping Boron-Manganese Steels." Pp. 9–228 in *Proceedings of the 7th international conference coatings in manufacturing engineering, Chalkidiki, Greece*. Vol. 2.

Merklein, Marion, Michael Schmidt, Stephan Tremmel, Sandro Wartzack, Kolja Andreas, Tom Häfner, Rong Zhao, and Jennifer Steiner. 2015. "Investigation of Tribological Systems for Dry Deep Drawing by Tailored Surfaces." *Dry Met. Forming OAJ FMT* 1:42–56.

Mises, R. v. 1913. "Mechanik der festen Körper im plastisch- deformablen Zustand." *Nachrichten von der Gesellschaft der Wissenschaften zu Göttingen, Mathematisch-Physikalische Klasse* 1913:582–92.

Mössle, Erhard. 1983. *Einfluss Der Blechoberflache Beim Ziehen von Blechteilen Aus Aluminiumlegierungen*. Vol. 72. Dissertation, Berlin, Heidelberg: Springer-Verlag.

Müller, Klaus-Peter. 2013. *Praktische Oberflächentechnik: Vorbehandeln· Beschichten· Prüfen*. Berlin, Heidelberg: Springer-Verlag.

Müller, Norman. 2018. *Erweiterung Des Versuchsstandes Zur FLC Ermittlung Für Dickere Oder Festere Bleche*. *Bachelorarbeit am Lehrstuhl für Umformtechnik der Universität Siegen*.

Nakazima, Koe, Toshio Kikuma, and Kaname Hasuka. 1968. "Study on the Formability of Steel Sheets." *Yawata Technical Report* 264:8517–30.

Navinšek, B., P. Panjan, and I. Milošev. 1997. "Industrial Applications of CrN (PVD) Coatings, Deposited at High and Low Temperatures." *Surface and Coatings Technology* 97(1):182–91. doi: 10.1016/S0257-8972(97)00393-9.

Nazari, Esmaeil, Christian Löbbe, Stefan Gallus, S. Ahmad Izadyar, and A. Erman Tekkaya. 2018. "Design of Process Parameters for the Incremental Tube Forming (ITF) by FEM to Control Product Properties." *AIP Conference Proceedings* 1960(1):160020. doi: 10.1063/1.5035046.

Netsch, Thomas. 1995. *Methode Zur Ermittlung von Reibmodellen Für Die Blechumformung*. Vol. 27. Dissertation, Aachen: Shaker Verlag GmbH.

Neugebauer, R., W. G. Drossel, U. Lorenz, and N. Luetz. 2002. "Hexabend–A New Concept for 3D-Free-Form Bending of Tubes and Profiles to Preform Hydroforming Parts and Endform Space-Frame-Components." *Advanced Technology of Plasticity* 2:1465–70.

Neugebauer, R., F. Schieck, S. Polster, A. Mosel, A. Rautenstrauch, J. Schönherr, and N. Pierschel. 2012. "Press Hardening — An Innovative and Challenging Technology." *Archives of Civil and Mechanical Engineering* 12(2):113–18. doi: 10.1016/j.acme.2012.04.013.

Nitzsche, Gernot. 2007. *Reduzierung Des Adhäsionsverschleißes Beim Umformen von Aluminiumblechen*. Vol. 72. Dissertation, Aachen: Shaker Verlag GmbH.

Oehler, Gerhard. 1963. “Biegen.” *Carl Hanser-Verlag, München*.

Oehler, Gerhard, and Fritz Kaiser. 2013. *Schnitt-, Stanz-Und Ziehwerkzeuge*. Berlin, Heidelberg: Springer-Verlag.

Paul, Surajit Kumar. 2021. “Controlling Factors of Forming Limit Curve: A Review.” *Advances in Industrial and Manufacturing Engineering* 2:100033. doi: 10.1016/j.aime.2021.100033.

Paulsen, Frode, and Torgeir Welo. 2001. “Cross-Sectional Deformations of Rectangular Hollow Sections in Bending: Part II — Analytical Models.” *International Journal of Mechanical Sciences* 43(1):131–52. doi: 10.1016/S0020-7403(99)00107-1.

Pereira Da Costa, Vitor Manuel. 2013. *Werkstoffrelevante Voruntersuchungen Und Definition Der Verfahrensgrenzen Beim Inkrementellen Schwenkbiegen (ISB)*. *Bachelorarbeit am Lehrstuhl für Umformtechnik der Universität Siegen*.

Persson, B. N. J., O. Albohr, U. Tartaglino, A. I. Volokitin, and E. Tosatti. 2004. “On the Nature of Surface Roughness with Application to Contact Mechanics, Sealing, Rubber Friction and Adhesion.” *Journal of Physics: Condensed Matter* 17(1):R1–62. doi: 10.1088/0953-8984/17/1/R01.

Rohleder, Martin. 2002. *Simulation Rückfederungsbedingter Formabweichungen Im Produktentstehungsprozess von Blechformteilen*. Shaker.

Schapitz, Eberhard, and Guenter Levin. 1963. *Elementare Berechnung von Schalen Und Vollwandsystemen*. Düsseldorf: VDI-Verlag.

Scherer, Daniel. 2014. “Methoden Zur Automatisierung Der Inkrementellen Blechumformung.” Dissertation, Technische Universität München.

Schmitz, Frank. 2016. *Inkrementelles Schwenkbiegen Zur Kostengünstigen Herstellung von Trägerstrukturen in Elektrofahrzeugen. Teilvorhaben: Profilentwicklung Zur Anwendung Beim Inkrementellen Schwenkbiegen (PRAIS), Schlussbericht.* Leichlingen: Kronenberg Profil GmbH. doi: 10.2314/GBV:875686346.

Schöler, S., D. Yilkiran, D. Wulff, F. Özkaya, K. Möhwald, B. A. Behrens, and H. J. Maier. 2018. “Selective Oxidation of Tool Steel Surfaces under a Protective Gas Atmosphere Using Inductive Heat Treatment.” *MATEC Web of Conferences* 190:14003. doi: 10.1051/matecconf/201819014003.

Schwarz, Wilhelm, and Bernd Engel. 2009. “Verfahren zum Biegen eines Werkstücks.” (WO2009083609A2).

Selmi, Naceur, and H. Bel Hadj Salah. 2012. “Flexible Multipoint Hydroforming Using Metallic Sheet Medium.” Pp. 19–21 in *Second Tunisian Congress of Mechanics*.

Selter, Oliver. 2017. *Entwicklung Der Verfahrenstechnik Zum Modularen Walzprofilierbiegen*. Vol. 10. Dissertation, Aachen: Shaker Verlag GmbH.

Sengupta, A. K., B. Fogg, and S. K. Ghosh. 1981. “On the Mechanism behind the Punch-Blank Surface Conformation in Stretch-Forming and Deep-Drawing.” *Journal of Mechanical Working Technology* 5(3):181–210. doi: 10.1016/0378-3804(81)90039-5.

Shaw, M. C. 1963. “The Role of Friction in Deformation Processing.” *Wear* 6(2):140–58.

Shaw, Milton C., Abraham Ber, and Pierre A. Mamin. 1960. “Friction Characteristics of Sliding Surfaces Undergoing Subsurface Plastic Flow.” *Journal of Basic Engineering* 82(2):342–45.

Siegert, Klaus. 2015. *Blechumformung: Verfahren, Werkzeuge und Maschinen*. Berlin, Heidelberg: Springer-Verlag.

Speer, J., D. K. Matlock, B. C. De Cooman, and J. G. Schroth. 2003. “Carbon Partitioning into Austenite after Martensite Transformation.” *Acta Materialia* 51(9):2611–22. doi: 10.1016/S1359-6454(03)00059-4.

Staeves, Johannes. 1998. *Beurteilung Der Topografie von Blechen Im Hinblick Auf Die Reibung Bei Der Umformung*. Vol. 41. Dissertation, Aachen: Shaker Verlag GmbH.

Staupendahl, Daniel, and A. Erman Tekkaya. 2017. “The Reciprocal Effects of Bending and Torsion on Springback during 3D Bending of Profiles.” *Procedia Engineering* 207:2322–27. doi: 10.1016/j.proeng.2017.10.1002.

Steinheimer, Rainer. 2005. “Werkstoffmodellierung Für Die Umformtechnik.” in *WKF-Kolloquium*. Siegen.

Steinheimer, Rainer. 2006. *Prozesssicherheit Beim Innenhochdruck-Umformen*. Vol. 66. Shaker.

Stoiber, M., J. Wagner, C. Mitterer, K. Gammer, H. Hutter, C. Lugmair, and R. Kullmer. 2003. “Plasma-Assisted Pre-Treatment for PACVD TiN Coatings on Tool Steel.” *Surface and Coatings Technology* 174–175:687–93. doi: 10.1016/S0257-8972(03)00353-0.

Stott, F. H., and M. P. Jordan. 2001. “The Effects of Load and Substrate Hardness on the Development and Maintenance of Wear-Protective Layers during Sliding at Elevated Temperatures.” *Wear* 250(1):391–400. doi: 10.1016/S0043-1648(01)00601-9.

Stötzel, Christoph. 2017. *Inkrementelles Schwenkbiegen Zur Kostengünstigen Herstellung von Trägerstrukturen in Elektrofahrzeugen (ISB-Elektro). Teilvorhaben: Definition Der Anforderungen an Längsträgerbauteile Für Elektrofahrzeuge (DALE), Schlussbericht.* [Attendorn]: [Automotive Center Südwestfalen GmbH]. doi: 10.2314/GBV:1002661226.

Stribeck, Richard. 1946. “Die Wesentlichen Eigenschaften Der Gleit-Und Rollenlager.” *Zeitschrift Des Vereines Deutscher Ingenieure* 46:180.

Swift, H. W. 1952. “Plastic Instability under Plane Stress.” *Journal of the Mechanics and Physics of Solids* 1(1):1–18. doi: 10.1016/0022-5096(52)90002-1.

Tekkaya, A. Erman. 1998. “State of the Art in Simulation of Sheet Metal Forming.” *Blech Rohre Profile(Germany)* 43(11):62–64.

Vatter, Peter H., and Raoul Plettke. 2013. “Process Model for the Design of Bent 3-Dimensional Free-Form Geometries for the Three-Roll-Push-Bending Process.” *Procedia CIRP* 7:240–45. doi: 10.1016/j.procir.2013.05.041.

Vetter, J. 2014. “60years of DLC Coatings: Historical Highlights and Technical Review of Cathodic Arc Processes to Synthesize Various DLC Types, and Their Evolution for Industrial

Applications." *Surface and Coatings Technology* 257:213–40. doi: 10.1016/j.surfcoat.2014.08.017.

Volk, W., and Pavel Hora. 2011. "New Algorithm for a Robust User-Independent Evaluation of Beginning Instability for the Experimental FLC Determination." *International Journal of Material Forming* 4(3):339–46. doi: 10.1007/s12289-010-1012-9.

Vollertsen, Frank, and Florian Schmidt. 2014. "Dry Metal Forming: Definition, Chances and Challenges." *International Journal of Precision Engineering and Manufacturing-Green Technology* 1(1):59–62. doi: 10.1007/s40684-014-0009-0.

Vorkov, Vitalii, Richard Aerens, Dirk Vandepitte, and Joost R. Duflou. 2015. "Influence of a Single Bend in the Bumping Process of Large Radius Air Bending." *Key Engineering Materials* 651–653:1090–95. doi: 10.4028/www.scientific.net/KEM.651-653.1090.

Vorkov, Vitalii, Richard Aerens, Dirk Vandepitte, and Joost R. Duflou. 2018. "Analytical Prediction of Large Radius Bending by Circular Approximation." *Journal of Manufacturing Science and Engineering* 140(12). doi: 10.1115/1.4041496.

Vorkov, Vitalii, Goncalo Afonso Da Costa Rodrigues, and Joost Duflou. 2019. "Gray Box Approach for Prediction of Air Bending." Pp. 45–50 in *Procedia Manufacturing*. Vol. 27. Elsevier.

Wagner, Stefan. 1996. *3D-Beschreibung der Oberflächenstrukturen von Feinblechen*. DGM-Informationsges., Verlag.

Wagner, Stefan. 1997. "Three-Dimensional Description of Sheet-Metal Surfaces." *Tribotest* 4(2):191–207. doi: https://doi.org/10.1002/tt.3020040207.

Wagner, Stefan. 1999. *Tribology in Drawing Car Body Parts*. *SAE Technical Paper*. 1999-01–3228. Warrendale, PA: SAE International. doi: 10.4271/1999-01-3228.

Wang, Yi, Hai-Shu Ma, Jing-Hui Yang, and Ke-Sheng Wang. 2017. "Industry 4.0: A Way from Mass Customization to Mass Personalization Production." *Advances in Manufacturing* 5(4):311–20. doi: 10.1007/s40436-017-0204-7.

Weihnacht, Volker, Andreas Brückner, and Sven Bräunling. 2008. "ta-C beschichtete Werkzeuge für die Trockenumformung von Aluminiumblechen." *Vakuum in Forschung und Praxis* 20(3):6–10. doi: 10.1002/vipr.200800356.

Whitehouse, David. 2004. *Surfaces and Their Measurement - 1st Edition*. 1st ed. Oxford: Butterworth-Heinemann.

Wittek, A., H. Richter, and Boguslaw Lazarz. 2011. "Tubular Stabilizer Bars-Calculations and Construction." *Transport Problems* 6(3):17–25.

Wolfgarten, Martin, and Gerhard Hirt. 2016. "New Method for the Manufacturing of Curved Workpieces by Open-Die Forging." *CIRP Annals* 65(1):285–88. doi: 10.1016/j.cirp.2016.04.125.

Wu, W. T., J. P. Tang, and G. Li. 2000. "Recent Development of Process Simulation and Its Applications to Manufacturing Processes." *Journal of Shanghai Jiaotong University (Science)* 5(1):235–41.

Yang, D. Y., M. Bambach, J. Cao, J. R. Duflou, P. Groche, T. Kuboki, A. Sterzing, A. E. Tekkaya, and C. W. Lee. 2018. “Flexibility in Metal Forming.” *CIRP Annals* 67(2):743–65. doi: 10.1016/j.cirp.2018.05.004.

Young, Thomas. 1845. *A Course of Lectures on Natural Philosophy and the Mechanical Arts*. Taylor and Walton.

Zöller, Fabian. 2016. *Erarbeitung von Grundlagen zur Abbildung des tribologischen Systems in der Umformsimulation*. Vol. 279. Dissertation, Bamberg: Meisenbach.

9.3 Source of imagery

Figure 1	ECKOLD GmbH & Co. KG.	Sperrluttertal, 37444 St. Andreasberg
Figure 2	Patent WO2009083609A2	Schwarz, Wilhelm, and Bernd Engel
Figure 83:	um werbephotographie	Nikolaus-Seng-Str. 2 36041 Fulda / Maberzell
Figure 94:	um werbephotographie	Nikolaus-Seng-Str. 2 36041 Fulda / Maberzell
Figure 96:	um werbephotographie	Nikolaus-Seng-Str. 2 36041 Fulda / Maberzell

10 Appendix

10.1 Measurement apparatus

Depending on the necessary accuracy, lengths have been measured by standard tools, such as steel rulers (accuracy 0.5 mm), calipers (accuracy 0.1 mm) or outside micrometers (accuracy 0.01 mm). The mass of specimens was measured by a digital laboratory scale, type SARTORIUSLC 4200 S with an accuracy of 0.01 g. Apart from the above mentioned, specific measurement apparatuses have been deployed in the present thesis.

Electrolytical gridding parameters

Table 25: Electrolytical gridding parameters for optical strain measurement of the materials objected in this work.

Material	**Transformer**	**Current**		**Electrolyte**
	Manufacturer, type	Flow type	[Volt]	type
22MnB5	custom	AC	11	E1
HCT780X, zinc coated	custom	AC	14	639
42SiCr	custom	AC	11	6744
FORTA H800	ÖSTLING EU-CLASSIC	AC	8	701/9

10.2 Machinery

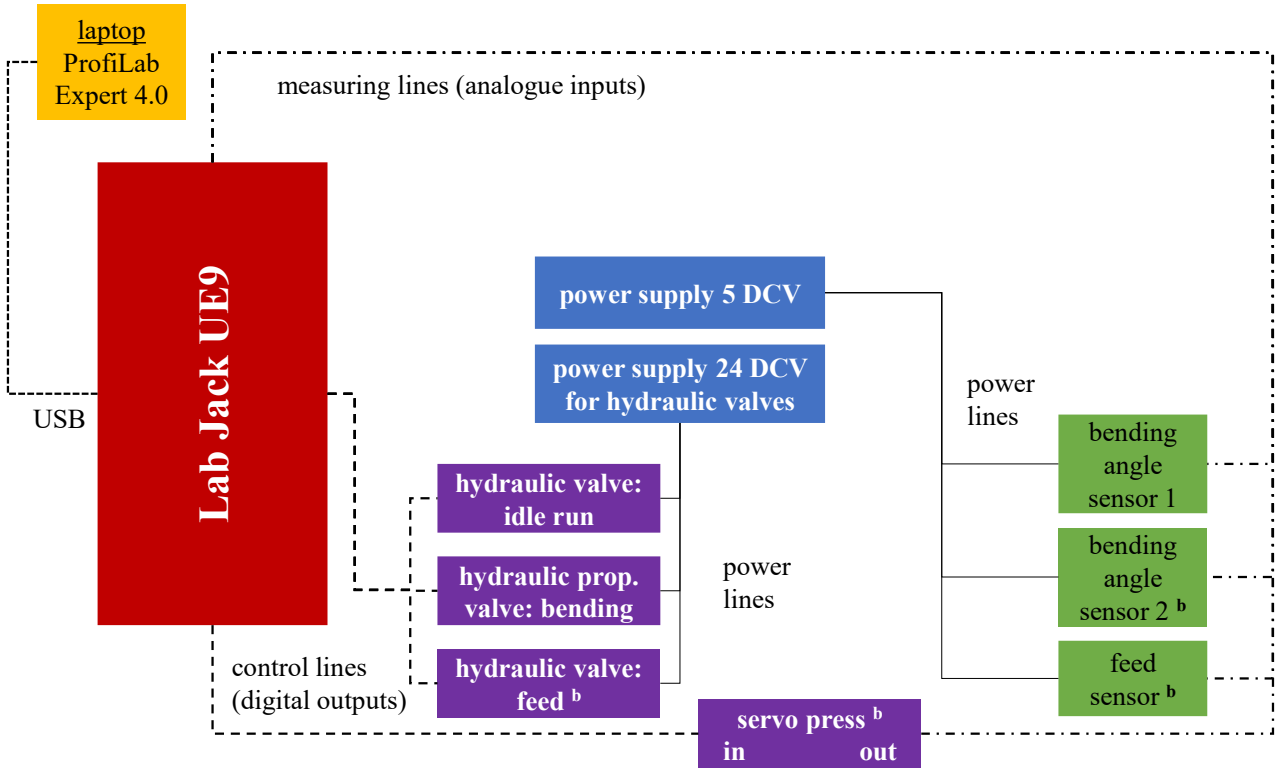

Figure 103: Power and signal linkage of the machine control for incremental swivel bending. The scheme shows a complete summary of all connections of the industrial and research ISB tools. Each tool, however, may only use parts of the illustrated connections ([a] = research tool only; [b] = industrial scale tool only).

SCHULER MSE servo mechanical press

With respect to the ram's lower dead center, the height clearance of the SCHULER MSE can be adjusted between 1900 mm and 1400 mm. The maximum tool surfaces at its table and its ram measures 3500 mm x 2200 mm. The press has an optional servo-mechanical drawing cushion with a nominal force of 1 MN.

Table 26: Further specifications of the MSE 2-1000-3.5-600.

speed	3-60	strokes / min
stiffness of press frame	8330	kN/mm
electrical installed load	1020	kVA
height (above floor)	8.5	m
length at press table height level	5.4	m
width	3.0	m

10.3 Tools

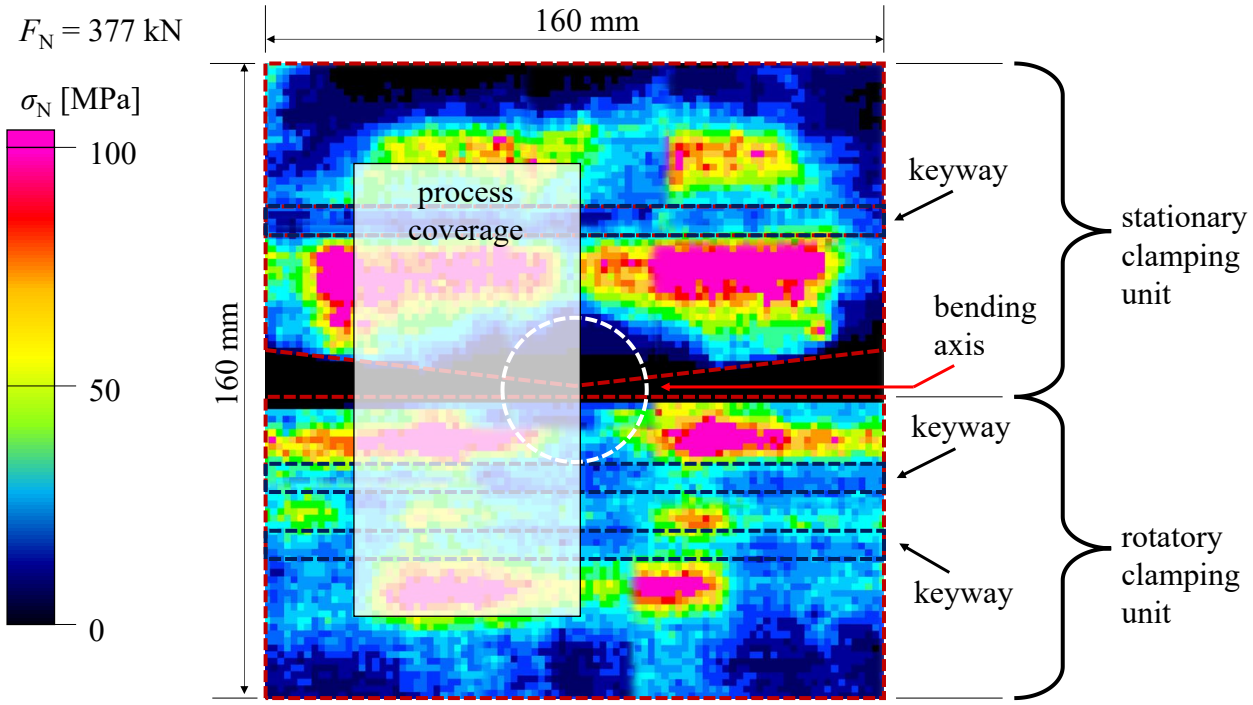

Figure 104: Normal pressure distribution in the revised version of the laboratory sized ISB tool for bending plane metallic strips. Measurements obtained by piezoresistive pressure sensor films type TEKSCAN 5051.

10.4 Materials

Hardening curve parameters

Table 27: Hardening curve parameters used throughout this thesis.

	bilinear model	LUDWIK / HOLLOMON	SWIFT / KRUPKOWSKI		
Material	***m***	C_H	C_{S1}	C_{S2}	C_{S3}
	[MPa]	[MPa]	[MPa]	[-]	[-]
S235JR	849	538	540	0.0073	0.207
42SiCr	1742	1044	1050	0.0067	0.167
22MnB5	1930	729	730	0.0011	0.114
Forta H800	1780	1800	1882	0.0310	0.278
HCT780X	2948	1135	1136	0.0011	0.125

FLC tests

Table 28: Experimentally determined forming limit curves for a) HCT780X (s_0 = 1.5 mm), b) 22MnB5 (s_0 = 1.4 mm), c) 42SiCr (s_0 = 2 mm), d) H800 (s_0 = 2 mm). For each material, major strain φ_1 and minor strain φ_2 values are given with respect to the tapering width. For each test setup, intervals of 95% confidence are calculated. All curves were tested on the UTS 1:2 scaled NAKAZIMA test assembly.

	tapering width											
	15		***25***		***40***		***50***		***65***		***100***	
	[mm]		[mm]		[mm]		[mm]		[mm]		[mm]	
	φ_1	φ_2	φ_1	φ_2	φ_1	φ_2	φ_1	φ_2	φ_1	φ_2	φ_1	φ_2
Material	[-]	[-]	[-]	[-]	[-]	[-]	[-]	[-]	[-]	[-]	[-]	[-]
HCT780X 1.5 mm	0.293 ± 0.020	-0.07 ± 0.010	0.243 ± 0.012	-0.032 ± 0.007	0.218 ± 0.010	0.009 ± 0.002	0.211 ± 0.006	0.034 ± 0.002	0.263 ± 0.009	0.082 ± 0.005	0.385 ± 0.020	0.337 ± 0.028
22MnB5 1.4 mm	-	-	0.400 ± 0.011	-0.108 ± 0.003	0.364 ± 0.045	-0.025 ± 0.010	0.280 ± 0.007	0.023 ± 0.001	-	-	0.362 ± 0.029	0.318 ± 0.020
42SiCr 2.0 mm	-	-	0.459 ± 0.010	-0.160 ± 0.010	0.379 ± 0.007	-0.051 ± 0.004	0.273 ± 0.012	0.026 ± 0.002	0.311 ± 0.007	0.078 ± 0.003	0.395 ± 0.016	0.327 ± 0.020
H800 2.0 mm	-	-	0.487 ± 0.020	-0.101 ± 0.008	0.372 ± 0.013	-0.007 ± 0.005	0.314 ± 0.010	0.038 ± 0.004	0.362 ± 0.020	0.085 ± 0.019	0.379 ± 0.015	0.324 ± 0.010

10.5 Friction

10.5.1 Nitro-carbureted and surface oxidized "TENIFER" friction tools

HCT780X

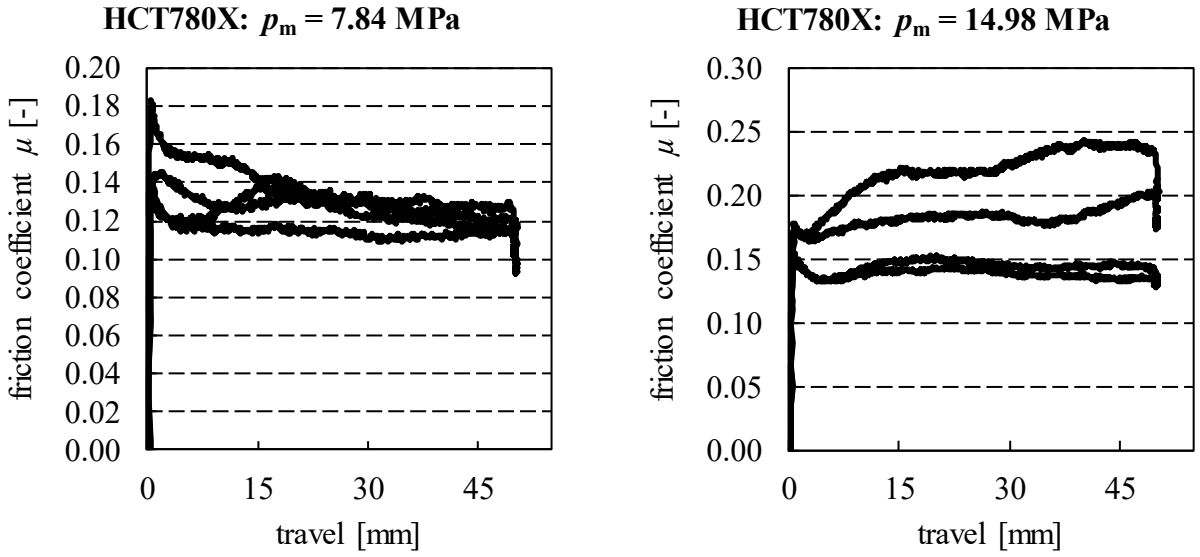

Figure 105: Friction experiments on nitro-carbureted tools with the sheet metal material HCT780X at nominal contact pressure of 6 and 15 MPa.

42SiCr, sanded

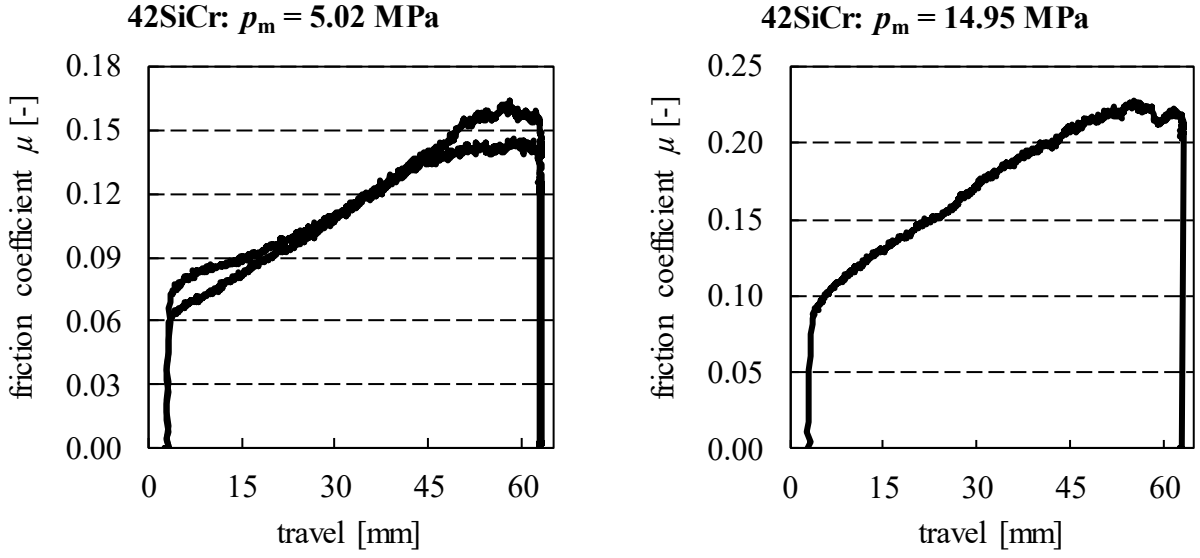

Figure 106: Friction experiments on nitro-carbureted tools with the sheet metal material 42SiCr at nominal contact pressure of 6 and 15 MPa reveal strong adhesion tendencies. Prior to friction tests, tinder was removed by sanding. The combination was abandoned.

Forta H800

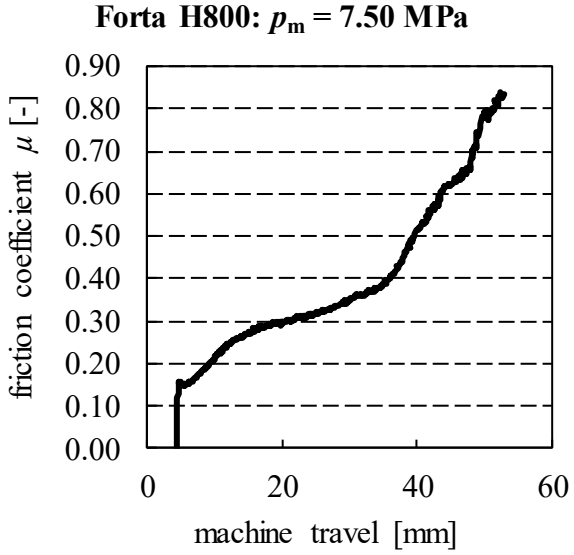

Figure 107: Friction experiment on nitro-carbureted tools with the sheet metal material Forta H800 at a mean contact pressure of 7.5 MPa reveals a strong galling tendency. This combination was abandoned.

10.5.2 Polished and plasma nitrided friction tools

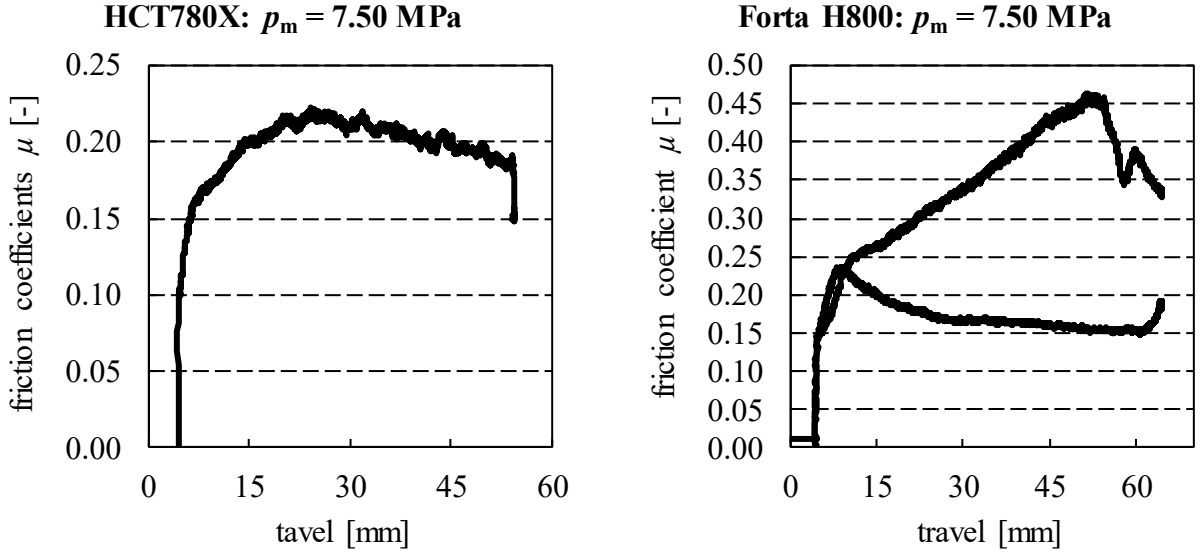

Figure 108: Friction experiment on polished and plasma nitrided tools at a mean contact pressure of 7.50 MPa reveals a tendency towards adhesion (HCT780X) and sporadic galling (Forta H800). The investigations on this coating were thus abandoned.

10.5.3 Physical vapor deposed AlTiN surface layers

HCT780X

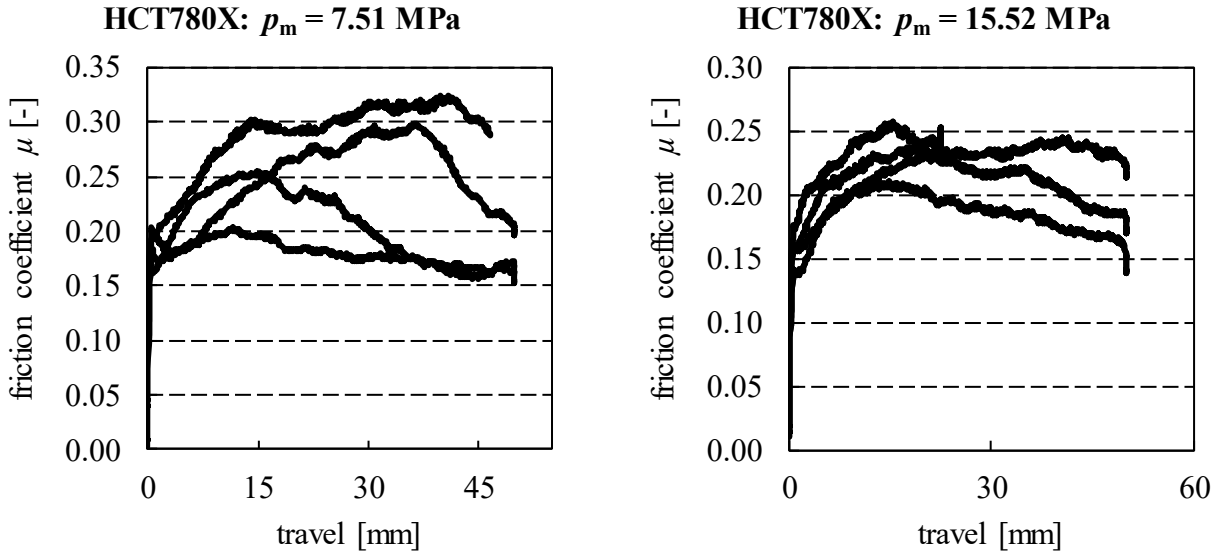

Figure 109: Friction experiments on PVD-AlTiN coated tools with the sheet metal material HCT780X at nominal contact pressures 6 and 15 MPa.

42SiCr

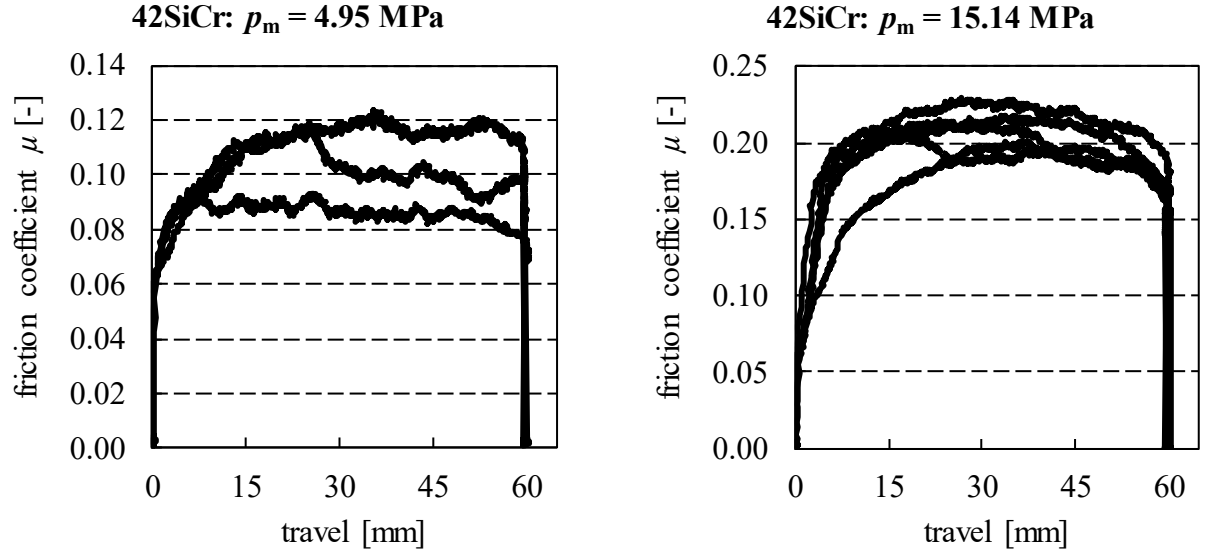

Figure 110: Friction experiments on PVD-AlTiN coated tools with the sheet metal material 42SiCr at nominal contact pressures of 6 and 15 MPa. Prior to friction tests, tinder was removed by sanding.

Forta H800

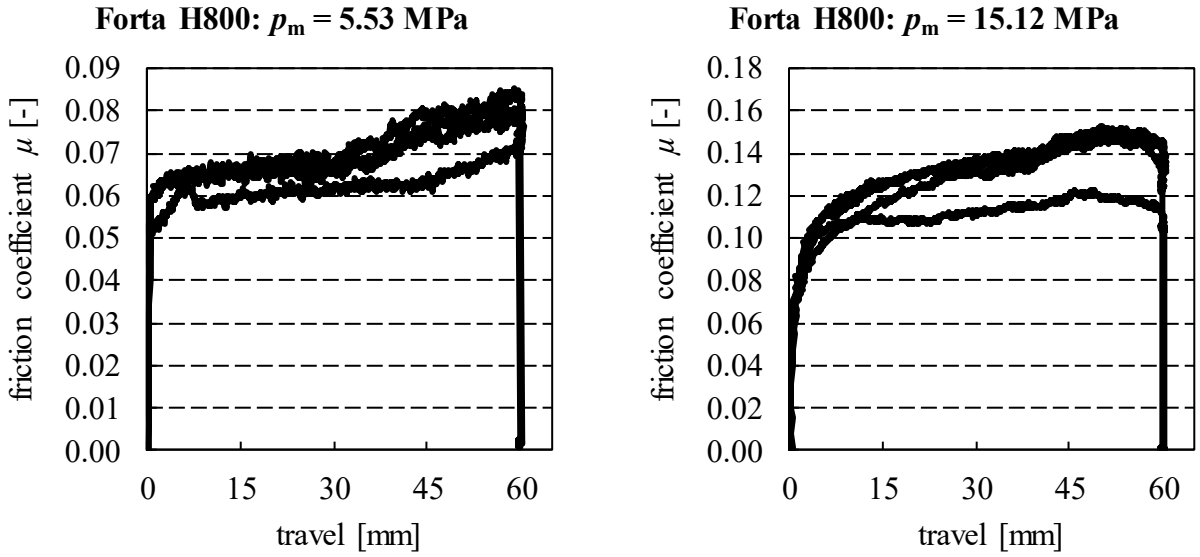

Figure 111: Friction experiments on PVD-AlTiN coated tools with the sheet metal material H800 at nominal contact pressures of 6 and 15 MPa.

10.5.4 Plasma-assisted chemical vapor deposed TiN layers

HCT780X

i) UTS

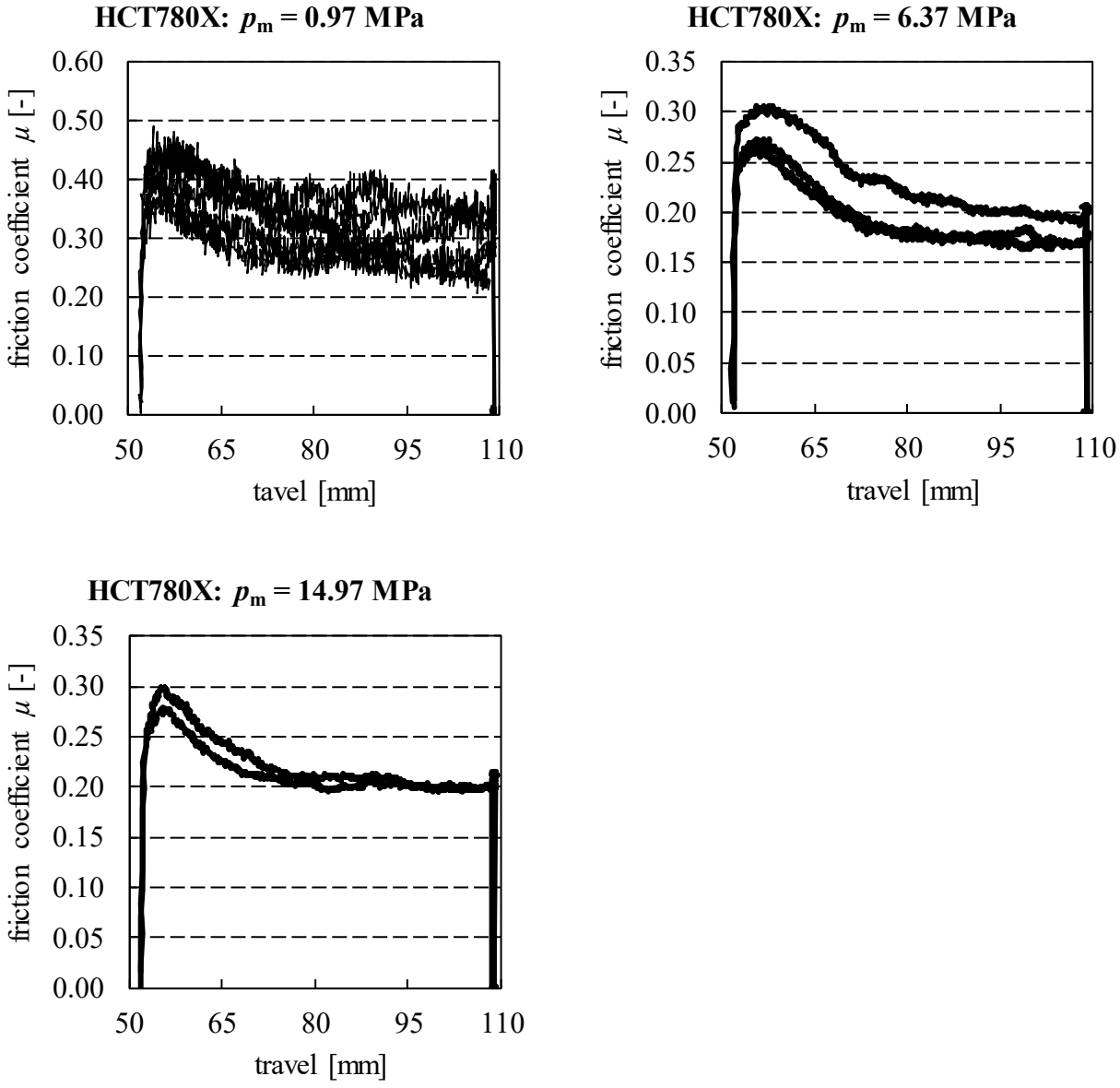

Figure 112: Friction experiments on PACVD-TiN coated tools with the sheet metal material HCT780X at nominal contact pressures 1, 6 and 15 MPa.

ii) LEOBEN

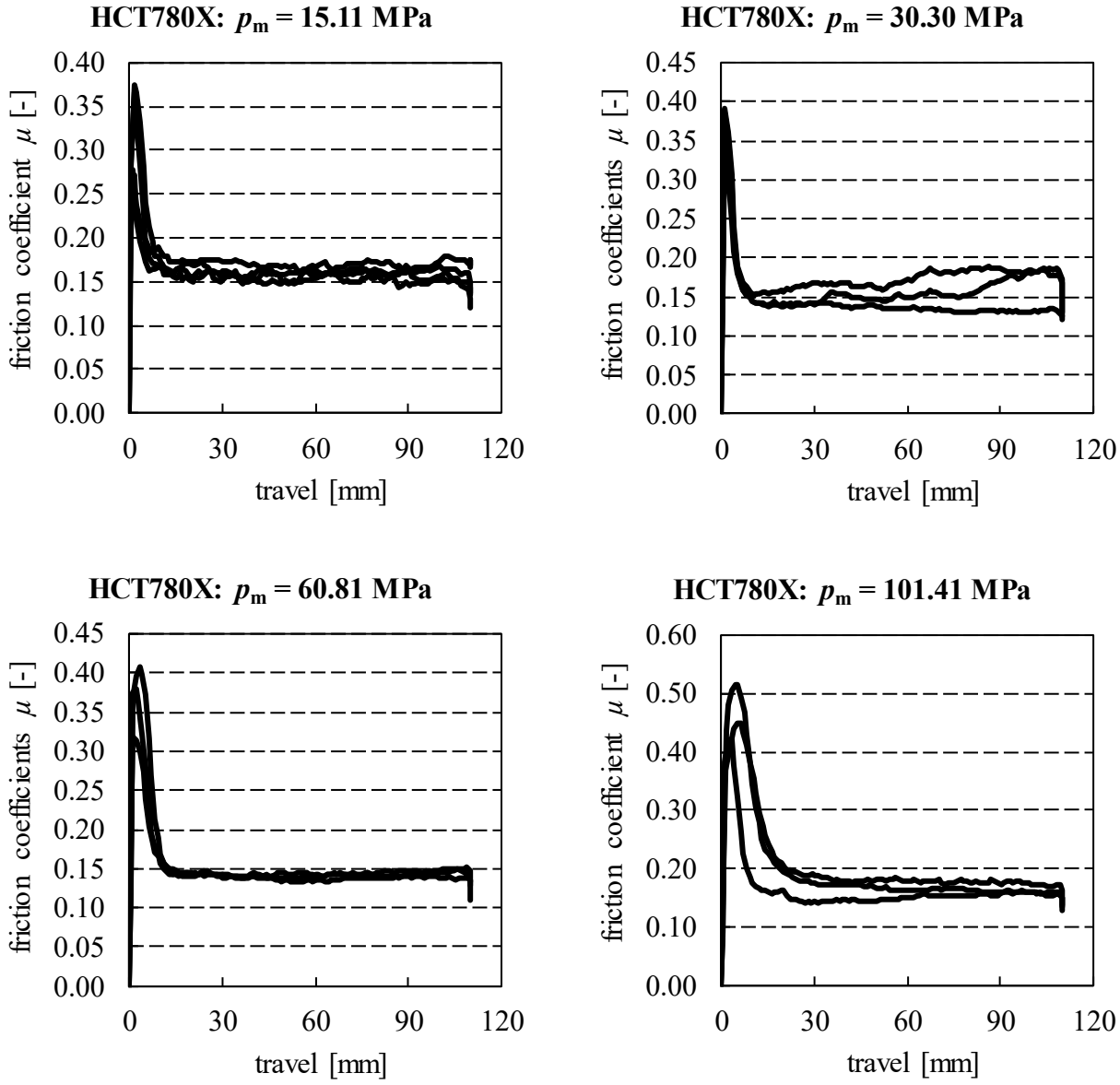

Figure 113: Friction experiments on PACVD-TiN coated tools with the sheet metal material HCT780X at nominal contact pressures of 15 – 100 MPa.

22MnB5

i) UTS

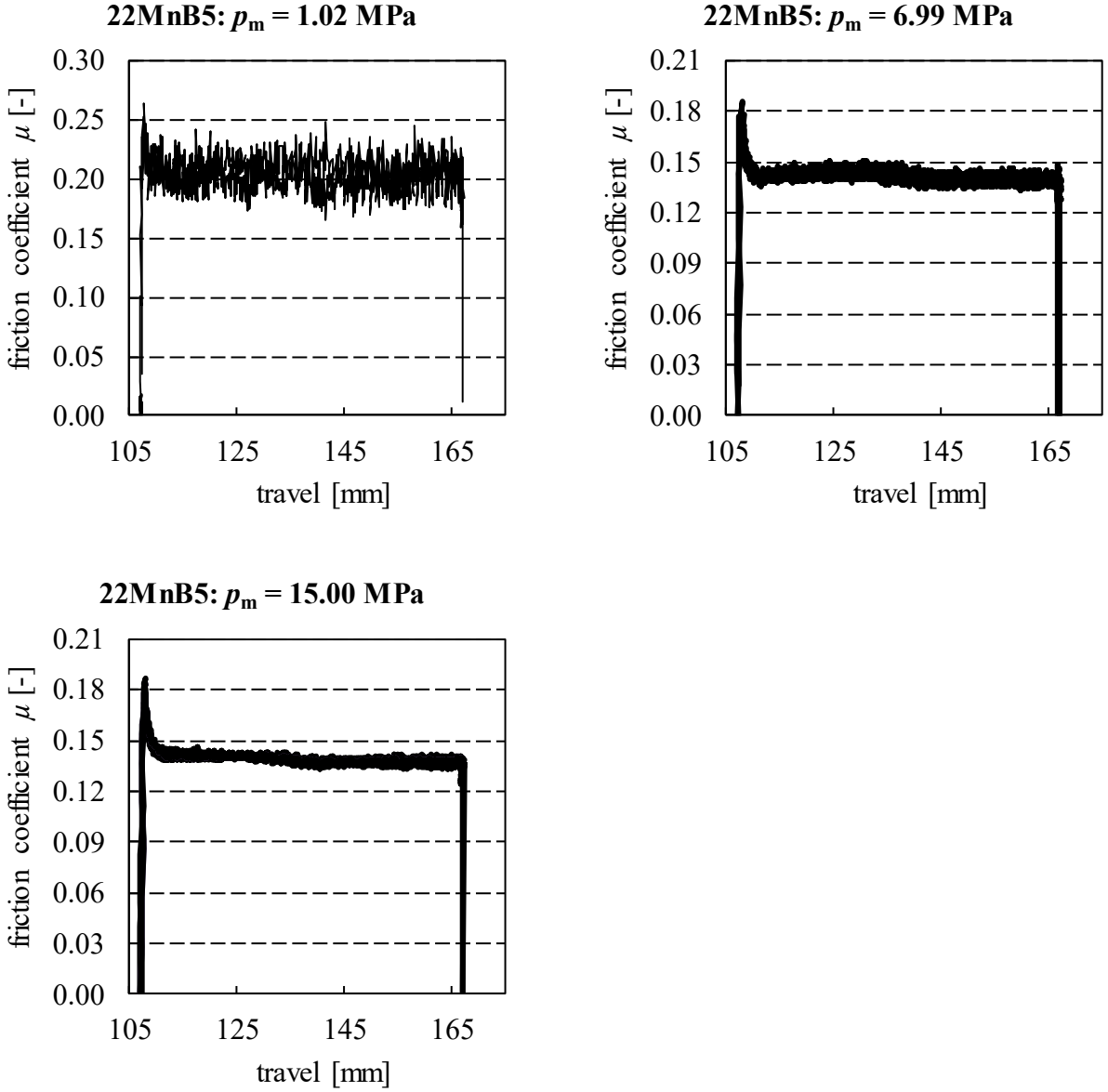

Figure 114: Friction experiments on PACVD-TiN coated tools with the sheet metal material 22MnB5 at nominal contact pressures of 1, 6 and 15 MPa.

ii) LEOBEN

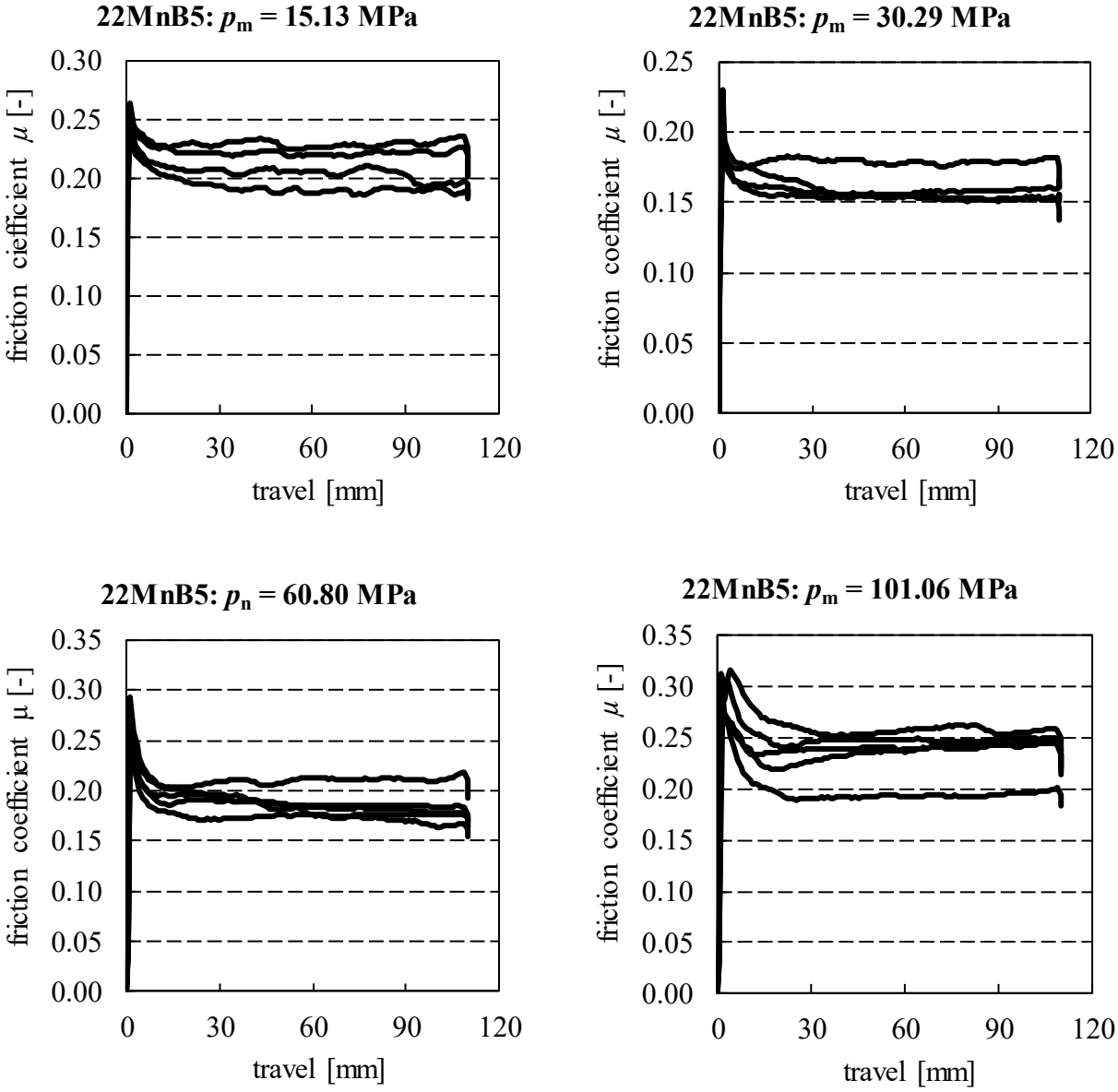

Figure 115: Friction experiments on PACVD-TiN coated tools with the sheet metal material 22MnB5 at nominal contact pressures of 15 – 100 MPa.

42SiCr

i) UTS

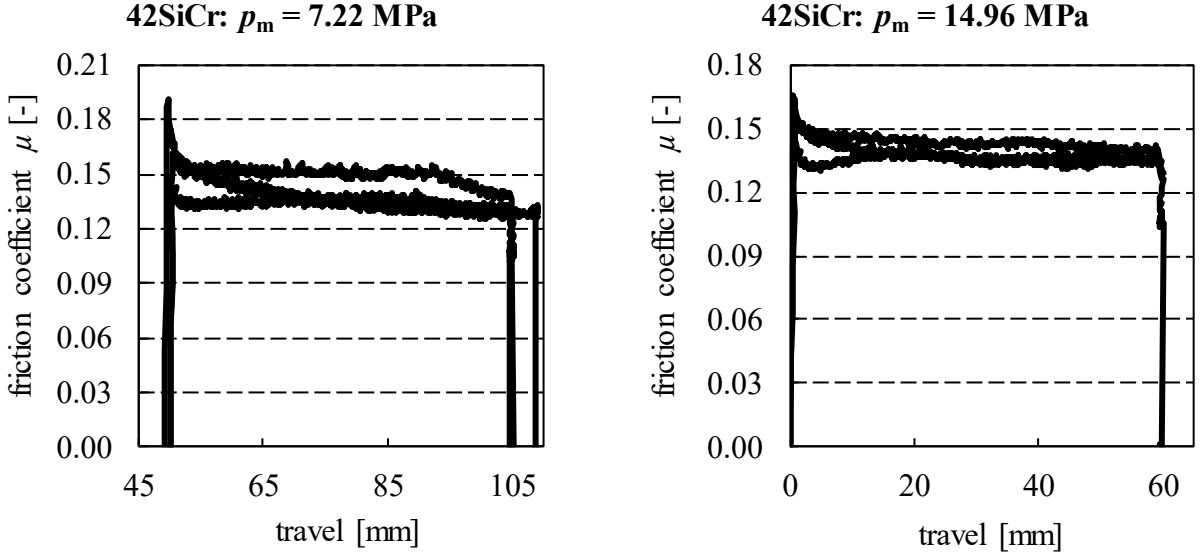

Figure 116: Friction experiments on PACVD-TiN coated tools with the sheet metal material 42SiCr at nominal contact pressures of 6 and 15 MPa. Prior to friction tests, tinder was removed by sanding.

ii) LEOBEN

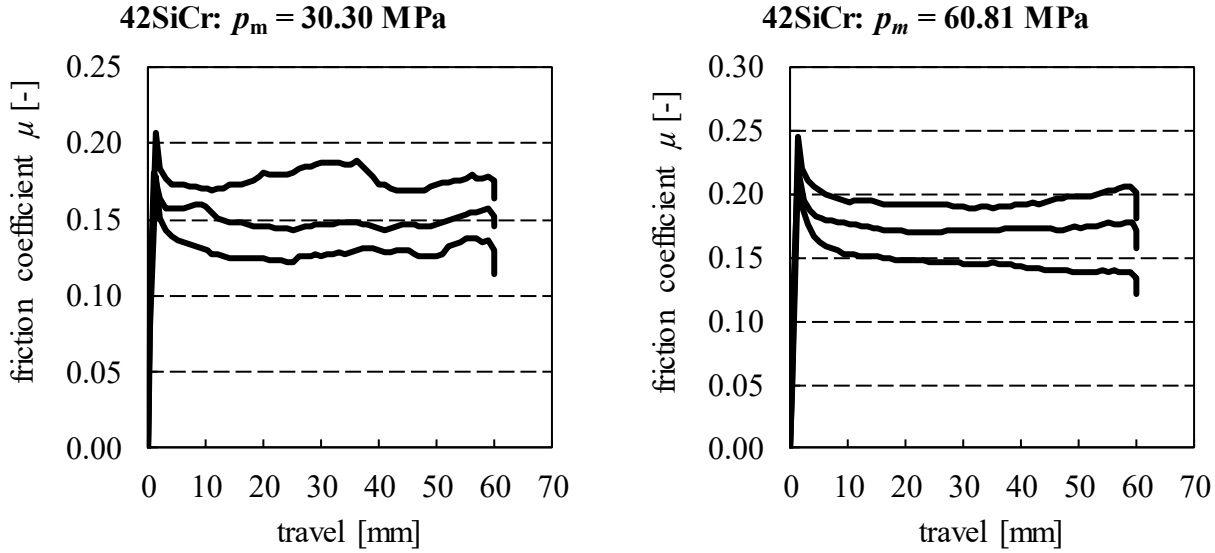

Figure 117: Friction experiments on PACVD-TiN coated tools with the sheet metal material 42SiCr at nominal contact pressures of 30 and 60 MPa. Prior to friction tests, tinder was removed by sanding.

Forta H800

i) UTS

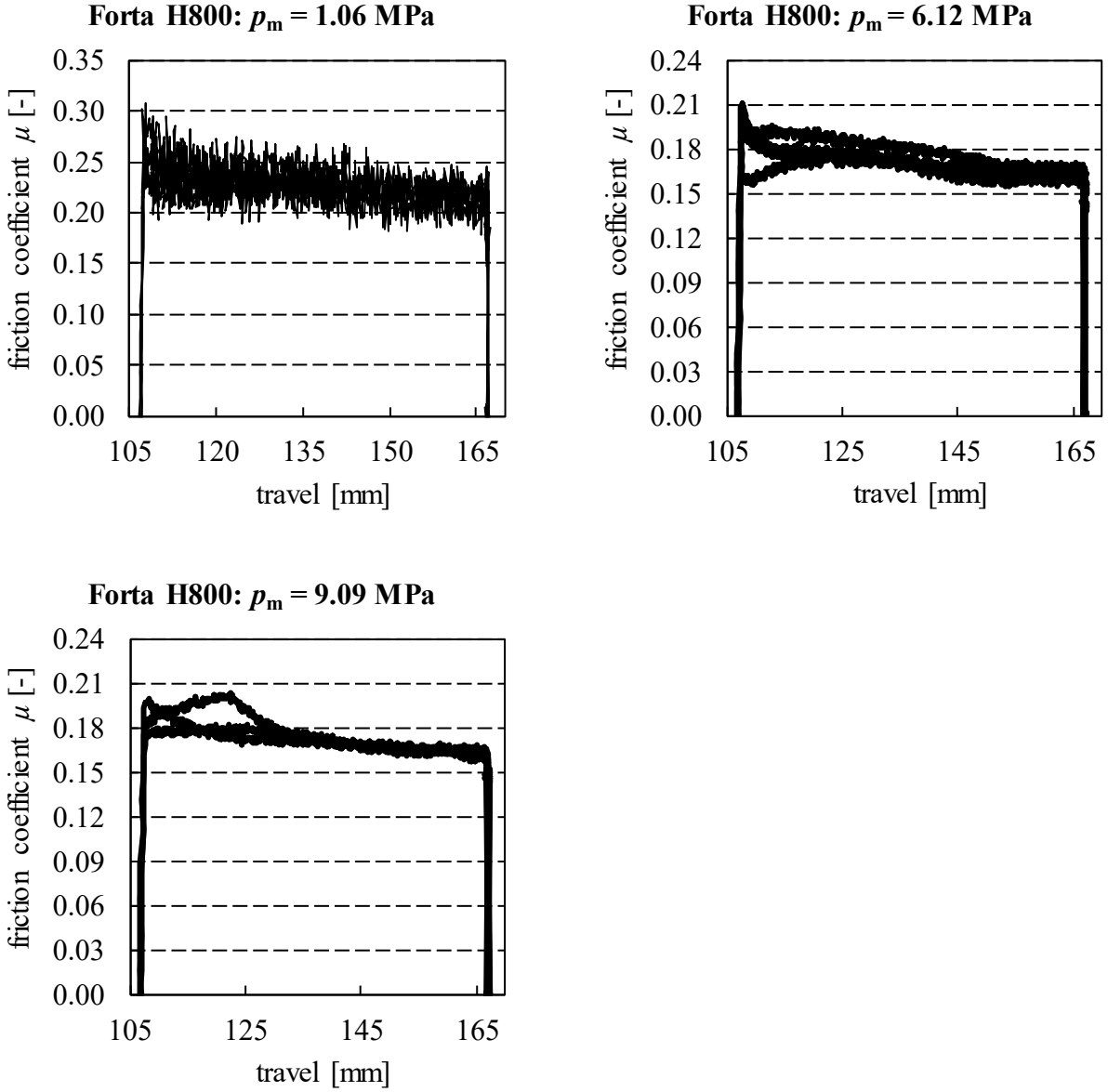

Figure 118: Friction experiments on PACVD-TiN coated tools with the sheet metal material Forta H800 at nominal contact pressures of 1, 6 and 15 MPa.

ii) LEOBEN

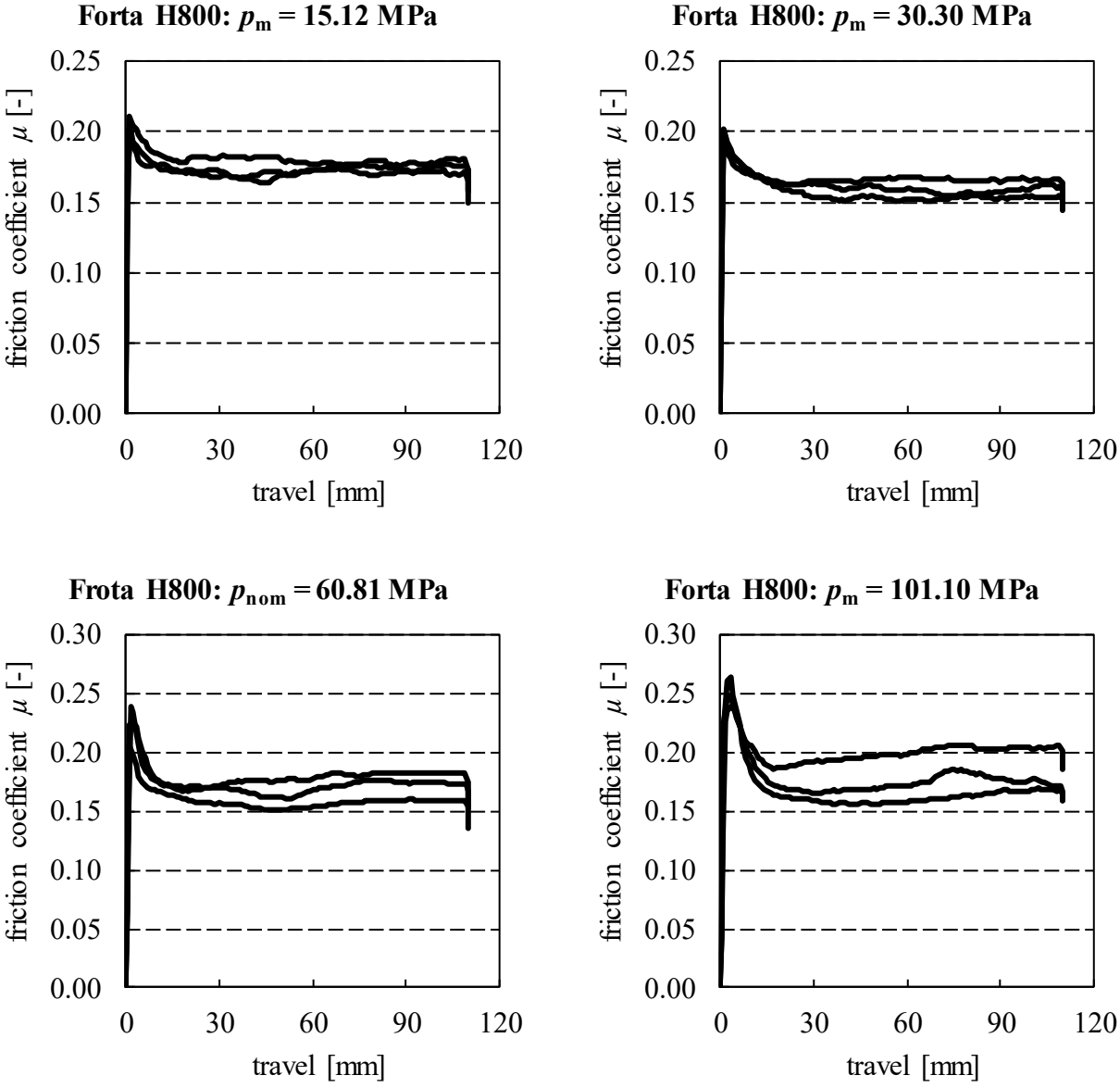

Figure 119: Figure 120: Friction experiments on PACVD-TiN coated tools with the sheet metal material Forta H800 at nominal contact pressures of 15 -100 MPa.

10.6 Validation Experiments

10.6.1 Validation of linear tensile forming under frictional engagement

Figure 121: Strips from HCT780X, Forta H800 and 22MnB5 tested under plastic tensile deformation in strip drawing.

10.6.2 Validation of incremental superposition

Table 29: Unloaded bending angle over of the experiments on superposition of forming zones. Cases are denoted equally to Table 16 and Table 22. Values in brackets indicate necking or cracking.

Material	case	***SP*** [-]													
		1	2	3	4	5	6	7	8	9	10	11	13	15	20
22MnB5	a)	2.9	3.0	3.0	3.0	3.4	3.2	2.8	2.7	2.5	2.2	2.4	2.3	2.4	(2.1)
	b)	2.7		2.4	2.8	2.8	2.6				2.4				(2.4)
HCT780X	d)	5.1		5.0	4.9		4.6		4.6			4.6		4.8	
FORTA H800	g_1)	1.8	1.8		1.7		1.7		1.6			1.6		1.6	1.5
	g_2)	5.6	5.7	5.6	5.4		5.4				5.3			4.9	(5.0)

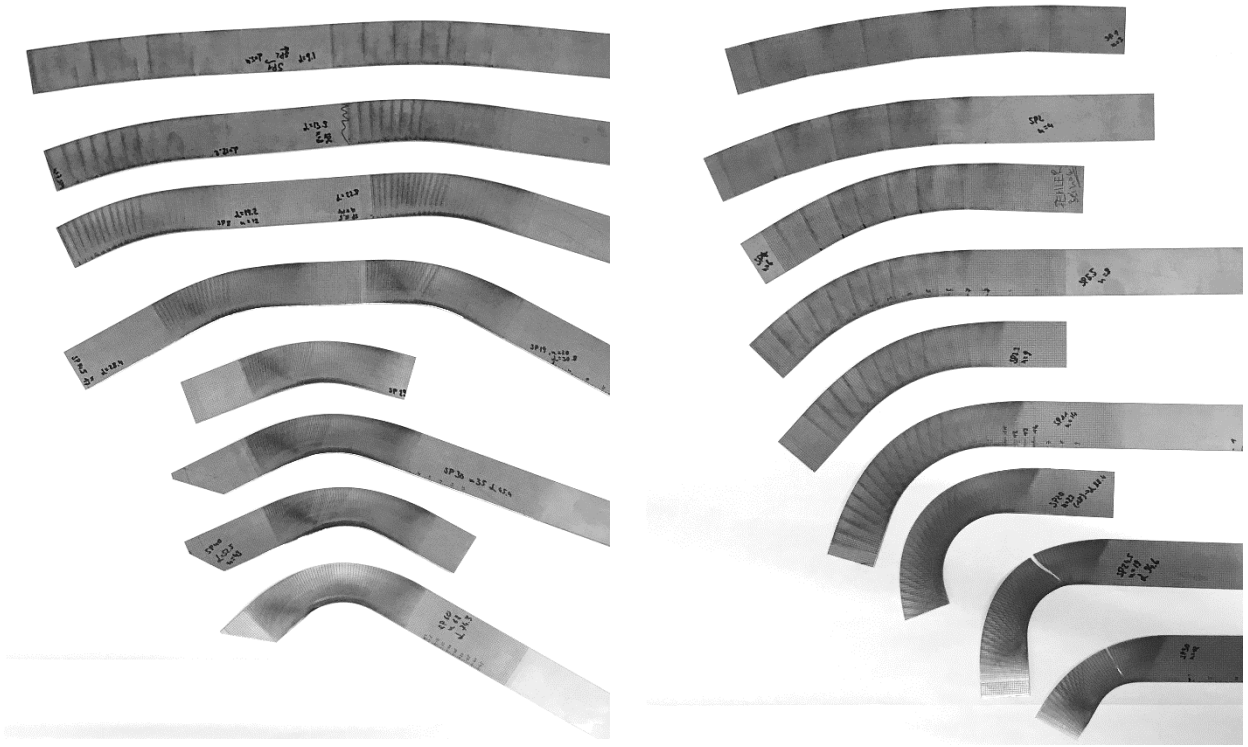

a) b)

Figure 122: FORTA H800 bending specimens for the investigation on incremental densities. a) Incremental bending angle 2.40 degrees and b) 6.25 degrees.

About the volume:

This dissertation presents a methodological approach to the process design of incremental swivel bending. This highly flexible manufacturing process is suitable for bending open profiles and allows to manufacture new product variants with each sequence and, in addition, to compensate production fluctuations in each step. In addition, incremental swivel bending can be used to produce geometries that are very difficult to manufacture with other forming processes with a high potential for lightweight constructions and functional integrations. The reader is provided with the necessary formulae based on mechanical considerations that can be applied to dimension the process parameters to a desired target geometry using a given sheet metal material.

About the author:

After three years of employment as a development engineer in the automotive industry and a preceding mechanical engineering degree with a stay abroad in Sweden, Peter Frohn-Sörensen was a research associate at the Department of Forming Technology at the University of Siegen. As part of his work, he was responsible for sheet metal forming processes and finite element simulations.

ISBN 978-3-96182-145-7
ISSN 2191-0030

universi
UNIVERSITÄTSVERLAG SIEGEN